



# Scatter Radio Relaying & Applications

BY  
GEORGE A. VOUGIOUKAS

A DISSERTATION  
SUBMITTED IN PARTIAL FULFILLMENT OF THE  
REQUIREMENTS FOR THE DEGREE OF

DOCTOR OF PHILOSOPHY  
IN  
TECHNICAL UNIVERSITY OF CRETE  
SCHOOL OF ELECTRICAL AND COMPUTER ENGINEERING

COMMITTEE IN CHARGE:  
PROFESSOR AGGELOS BLETSAS (SUPERVISOR)  
PROFESSOR GEORGE N. KARYSTINOS  
PROFESSOR CONSTANTINOS B. PAPADIAS

DECEMBER 2020

© Copyright by George A. Vougioukas, 2020.  
All rights reserved.

---

## Abstract

Billions of devices are expected to be wirelessly connected in the foreseeable future. Sustaining such connectivity will require simple, elegant, engineering solutions. Based on backscatter radio principles, this dissertation offers novel, *ultra-low-complexity*, *ultra-low-power*, *ultra-low-cost* solutions, for connectivity in the field of narrowband wireless communications.

Methods for achieving wireless communication by “recycling” radio waves, pre-existing in the environment, are offered and analysed. In contrast to generating own signals for transmission, a device (tag) adopting the suggested methods can transmit its information towards *any* conventional FM radio receiver, by recycling *ambient* signals from FM radio stations. That way, it is shown that *batteryless* information transmission can be achieved up to distances of 26 meters, by harvesting energy from the environment. Ultra-low cost prototypes consumed only 24  $\mu$ Watt in continuous (non duty-cycled) operation.

In the case of ambient signals of unknown origin and structure, digital modulation schemes are also offered, accompanied by novel coherent, partially-coherent illumination-agnostic, as well as fully noncoherent, channel-coded or uncoded detection algorithms. It is shown that under certain conditions, modulated and unknown ambient signals, can offer performance gains in the process of recovering tag’s information signal, i.e., modulation of the ambient signal may be helpful. The proposed schemes do not require any cooperation with the ambient transmitter. That way, in sharp contrast to prior art, the tags adopting the proposed techniques are receiver-less; ultra-low-complexity and batteryless operation are also facilitated.

Exploiting the aforementioned methods, originally intended for solving ambient backscatter communication problems, it is demonstrated for the first time that backscattering tags can also be used in an unorthodox way, for *relaying* signals in the frequency domain. *Scatter radio relaying* can be used to solve multi-antenna processing problems: a) *blind* (i.e., zero-feedback) beamforming, offering power gains in the order of 0.4 – 3.7 dB, and b) direction of arrival (DoA) estimation, offering error less than 5 degrees with 8 scattering tags. The proposed methods utilize single antenna radios without any requirement for channel feedback, multi-antenna RF front-ends or expensive controllers.

The proposed techniques extend the solution space for engineers building wireless devices under power, complexity and cost constraints. Hopefully, this work will amplify the recent interest of the research community on backscatter radio and accelerate efforts towards the wide adoption of backscatter radio relaying in current and future commodity wireless systems, sensors and networks.

## Acknowledgements

Besides hard work, creativity and luck, the completion of this endeavour required proper guidance and support. For the last two I'm thankful to Professor Bletsas, a true Professional, for his support throughout the last 5 years of my work in the telecom lab. I hope my bargaining skills at Shanghai didn't scare him too much. I would also like to thank the thesis committee for their valuable time and comments that helped towards significantly improving the work.

Statistics show that,<sup>1</sup> instead of trying to solve a problem on your own (although I am a big fan of that) it is at least 20 dB more interesting & fun to try and solve the problem with others that are equally interested in said problem. The others in my case were all friends and members of the telecom lab., Panos, Michail, Panos, Psaros, kir. Lefteris, Marios. I would also like to thank the rest of the members of the telecom lab and especially Konstantinos, Manos and Vaggelis for all the "environmental" adventures and late summer nights over R6s'. I hope that we will eventually find a garage for our projects.

The joy of solving technical problems led me to undertaking the endeavour that resulted in this thesis. When other, non-technical, problems stood in the way of the interesting ones, I was lucky enough to have both local (Thanasis, Sotiris, Vaggelis, Mihalis, Michail, Dimitris, Panos, kir. Ilias) and distant (Spiros, Nikos, Kostas) close friends and family, that proposed effective solutions.

As stated by a song,<sup>2</sup> no money  $\Rightarrow$  no honey. Financial support for this work was provided by HFRI and GSRT and I'm grateful to them for providing the support required so as to solve the problems that I was interested in. The formal acknowledgement follows:

The work was supported by the Hellenic Foundation for Research and Innovation (HFRI) and the General Secretariat for Research and Technology (GSRT), under the HFRI PhD Fellowship grant (GA. no. 2263).



---

<sup>1</sup>There is high probability that they actually do.

<sup>2</sup>Fidlar-No Money No Honey

*We have to continually be jumping off cliffs  
and developing our wings on the way down.*

*—Kurt Vonnegut*

# Contents

Abstract . . . . .	iii
Acknowledgements . . . . .	iv
<b>1 Introduction</b>	<b>1</b>
1.1 Applications Of Backscatter Radio . . . . .	2
1.1.1 Ultra-Low-Power Wireless Devices . . . . .	2
1.1.2 Distributed & Passive Beamforming . . . . .	6
1.1.3 Virtual Antenna Arrays . . . . .	8
1.2 Motivation & Contribution . . . . .	9
1.2.1 Motivation . . . . .	9
1.2.2 Contribution . . . . .	10
1.3 Roadmap . . . . .	14
1.4 Notation . . . . .	15
<b>2 Fundamentals Of Backscatter Radio</b>	<b>16</b>
2.1 Modulation in the Passband . . . . .	16
2.2 Scattering Antenna . . . . .	17
2.3 A Communications' Perspective . . . . .	18
2.3.1 Wireless Signal Model . . . . .	19
2.3.2 Homodyne Reception . . . . .	21
2.4 Implementing Backscatter Radio . . . . .	23
2.4.1 Variable Antenna Loading . . . . .	23
2.4.2 Load Control . . . . .	24
2.5 Backscatter Radio Architectures . . . . .	24
<b>3 Recycling Radio Waves: A Digital Tag Approach</b>	<b>27</b>
3.1 Communication with Ambient Backscatter . . . . .	27
3.1.1 Carriers from the Air . . . . .	27
3.1.2 Hitchhiking on Strangers' Signals . . . . .	28

---

3.2	Engineering Tag's Waveforms . . . . .	29
3.2.1	Antenna Loading for Frequency Shifting . . . . .	29
3.2.2	Mapping Information on Tag's Waveform . . . . .	31
3.3	Processing . . . . .	34
3.3.1	Received Signal . . . . .	34
3.3.2	Correlation . . . . .	35
3.4	Detection Algorithms . . . . .	38
3.4.1	Coherent Detection . . . . .	38
3.4.2	Partially Coherent Detection . . . . .	41
3.4.3	Noncoherent Detection . . . . .	45
3.5	Performance Evaluation . . . . .	46
3.6	Comparison with State of The Art . . . . .	50
3.6.1	Backscatter OOK . . . . .	51
3.6.2	OOK Detection . . . . .	51
3.6.3	Results . . . . .	52
<b>4</b>	<b>Recycling Radio Waves: An Analog Tag Approach</b>	<b>57</b>
4.1	FM Remodulation: Principle & Analysis . . . . .	58
4.1.1	Operating Principle . . . . .	58
4.1.2	Impact of Noise . . . . .	61
4.1.3	Ambient Selection Diversity . . . . .	72
4.1.4	Multiple Access . . . . .	75
4.2	Implementation . . . . .	75
4.2.1	Implementation with Discrete Components . . . . .	76
4.2.2	Custom IC Implementation . . . . .	78
4.3	Who needs batteries? . . . . .	79
4.3.1	Energy Harvesting . . . . .	79
4.3.2	A Simple PSU for a Simple Tag . . . . .	88
4.4	Recovering a Sensor's Value . . . . .	89
4.4.1	Sensor Readout Options . . . . .	90
4.4.2	Communication Range . . . . .	90
4.5	Prototype Development . . . . .	94
<b>5</b>	<b>Tags as an Antenna Array: Direction of Arrival Estimation</b>	<b>97</b>
5.1	System Model . . . . .	97
5.2	Processing . . . . .	100
5.2.1	Emulating a Multi-Antenna Receiver . . . . .	100

5.2.2	MUSIC Processing . . . . .	101
5.3	Simulation Results . . . . .	102
<b>6</b>	<b>Tags as an Antenna Array: Beamforming</b>	<b>107</b>
6.1	Basic Idea and Signal Model . . . . .	108
6.2	Analysis . . . . .	110
6.2.1	Compound Wireless Channel . . . . .	110
6.2.2	Phase Alignment . . . . .	111
6.2.3	Probability of Alignment . . . . .	111
6.2.4	Achievable Gain . . . . .	115
6.3	Implementation . . . . .	116
6.3.1	Assistive Tag Design . . . . .	116
6.3.2	Phase Control . . . . .	117
6.4	Experimental Results . . . . .	119
6.4.1	RFID Tag Interrogation . . . . .	119
6.4.2	Channel Measurements . . . . .	121
<b>7</b>	<b>Conclusion</b>	<b>128</b>
7.1	Wireless Transmission of Information . . . . .	129
7.1.1	FM Remodulation . . . . .	129
7.1.2	Digital Modulation Schemes . . . . .	129
7.2	Virtual Antenna Array . . . . .	130
7.2.1	Emulating a Multi-Antenna Receiver . . . . .	130
7.2.2	Beamforming with Single Antenna Transmitter & Receiver . . . . .	131
7.3	Future Work . . . . .	131
<b>8</b>	<b>Appendix</b>	<b>133</b>
8.1	Supplementary Material for Chapter 3 . . . . .	133
8.1.1	SBPSK Decision Rule Derivation . . . . .	133
8.2	Supplementary Material for Chapter 4 . . . . .	134
8.2.1	Bandwidth of $J_0\left(2\rho \sin\left(\frac{\omega_{\text{sens}} t}{2}\right)\right)$ . . . . .	134
8.2.2	Expectation of The Absolute Value of a Gaussian R.V . . . . .	136
8.2.3	Probability of Outage Under Ambient Selection Diversity . . . . .	136
8.2.4	Details on Simulations and Experiments . . . . .	139
8.3	Supplementary Material for Chapter 5 . . . . .	140
8.3.1	Expected Value of $\cos^2(\varphi_m)$ . . . . .	140
8.4	Supplementary Material for Chapter 6 . . . . .	140

8.4.1 Average Number of Alignment Events . . . . . 140  
8.4.2 Simulation Parameters . . . . . 140

**Bibliography** . . . . . **142**

# Chapter 1

## Introduction

It is August 4, 1945. A group of children from the Vladimir Lenin All-Union Pioneer organization, present a wooden, hand-carved replica of the Great Seal of the United States to W. Averell Harriman, the US Ambassador to the Soviet Union, as a “gesture of friendship” towards their allies.

After passing the x-ray inspection and believing it was a merely friendly gesture to their allies, the seal was hung at the ambassador’s office. Unbeknown to anyone in the Embassy, the seal contained a bug,<sup>1</sup> which was subsequently called “The Thing”. The “Thing” allowed the Soviet Union to spy on the United States. The bug hung in the ambassador’s office, until it was detected in 1952. But how did a bug remain undetected and operational for such a long period of time?

In 1951, a British radio operator accidentally overhears American conversations on his radio. Sweeps in the Embassy did not reveal anything. The offices were routinely checked for bugs and microphones, while the great seal was checked a number of times but nothing suspicious was noted about it. Another sweep in 1952, provoked by a second accidental overhearing of conversations, revealed the bug in the great seal.

It consisted of a cylindrical cavity connected to a wire and nothing more [1]. Initially, the Americans were confused by the bug. Because of its simplicity, they were not sure if it was an actual bug. How could a simple cavity and wire transmit voice? The answer was *backscatter radio*.

In simple terms, the bug acted as a mirror, a mirror whose ability to reflect “light” was controlled by the sound on it. It modulated information (analog, voice) on top of an impinging (on its wire/antenna) RF signal. The modulation was performed by alternations of the loading of its antenna [2], caused by appropriate design of the cavity [1]. Voice/sound was captured by a diaphragm (part of the cavity). Soviets needed

---

<sup>1</sup>Covert listening device.

only to provide an illuminating RF signal (the “light”) and tune their radios to the appropriate frequency, in order to receive the backscattered signal embedding the voice (the reflection). Like a mirror, in the absence of RF illumination, the bug does not transmit/reflect anything. That is the reason why it stood undetected under conventional (receiving) radio-sweeps.

The story of the “Thing” demonstrates the feasibility of solving communication problems in an elegant, ultra-low-complexity, ultra-low-power (in the case of the “Thing”, zero power) manner, exploiting reflection radio principles. If backscatter radio is good enough for the world of international espionage, why not consider it as a solution for less adventurous communication problems?

## 1.1 Applications Of Backscatter Radio

Despite all those years, 2020 finds backscatter radio to still be a choice for transmitting information, while consuming miniscule amounts of energy.

The prominent example of a commercial application where backscatter radio finds extensive use, is radio frequency identification (RFID) tags [3–5]. Commercially available readers/interrogators provide an illuminating signal to an RFID tag, while the latter modulates its information on top of said signal using backscatter radio [2]. At the same time, due to its ultra-low-power consumption, the RFID operates by harvesting energy from the impinged signal allowing for the batteryless transmission of its information. RFIDs transmit a unique ID and, as the name suggests, are mainly used for identification purposes.

Apart from the RFID industry, an extensive amount of research has been conducted, to address the problems inherent in backscatter radio communication technology. The results of the relevant literature have lead to a wide area of applications where the benefits of backscatter radio can be fully exploited.

### 1.1.1 Ultra-Low-Power Wireless Devices

Having as objective the design of a device that can wirelessly transmit information, the design space usually includes as solutions conventional wireless communication protocols like, Bluetooth, LoRa or even WiFi. Due to their complexity, the aforementioned solutions require significant energy for the transmission of information. The last, further complicates the overall circuitry required for building a wireless device, which in turn increases the cost.

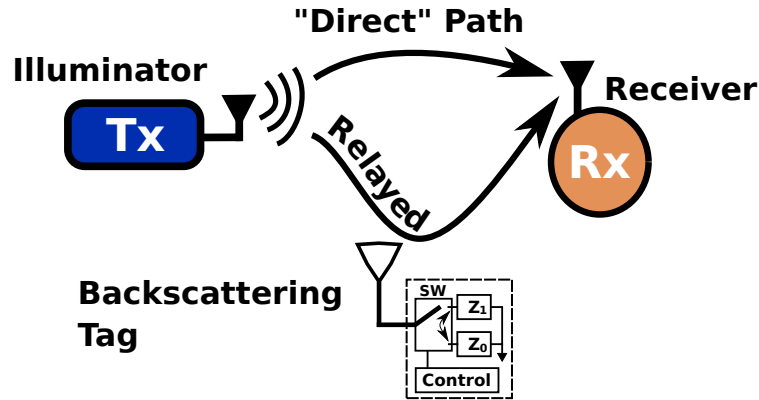


Figure 1.1: Backscatter radio setup. A backscattering tag relays a modified version of an illuminating signal. The receiver receives the superposition of signals from direct (transmitter-to-receiver) and relayed (transmitter-to-tag-to-receiver) paths.

While for some cases overall complexity may not be a serious problem (e.g., smartphones), there exist applications where it may be. Designing wireless sensors is such an application. Wireless sensors can be used in a wide spectrum of activities, ranging from home automation to telemetry systems and precision agriculture. Irrespective of the application, a wireless sensor must be robust and require the minimum amount of maintenance (e.g., battery replacements); minimizing cost is always a design constraint. Minimizing the system's complexity and power consumption, automatically satisfies the aforementioned constraints.

Recent studies have demonstrated the applicability of backscatter radio, for solving the problems emerging in wireless sensing applications [6,7]. The *narrowband* character of most wireless sensing applications, further enhances the suitability of ultra-low-complexity solutions like backscatter radio (in contrast to WiFi or Bluetooth).

As it will be explained in detail in Chapter 2, information transmission can be achieved using just an appropriately controlled RF switch, alternating the termination of an antenna. Given RF illumination, varying an antenna's loading causes (controlled) reflection of said illuminating signal. The reflected/backscattered signal attains certain characteristics, which can be controlled by the antenna's loading. In simple terms, varying the termination of an antenna, passively modifies and re-radiates an impinged signal.

Information can be thus modulated on the illuminating signal, using appropriate control of the termination of an antenna. Besides reaching an intended receiver via "direct" propagation paths, the illuminator's signal is *relayed* towards said receiver through additional "virtual" paths, realized by the backscattering operation. The relayed signal is a "copy" of the illuminator's signal "modified" by the backscattering operation, so as to

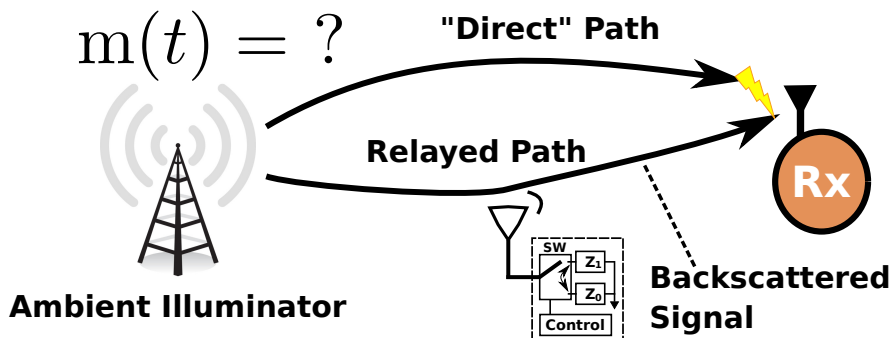


Figure 1.2: Ambient backscatter communication setup. A tag uses an unknown, modulated and time-varying signal as its carrier, so as to backscatter its information. The illuminator’s “direct” signal interferes with the backscattered signal.

carry the tag’s information (Fig. 1.1). The receiver must be able to “discriminate” the signal component that carries tag’s information and decode it efficiently.

Using just an RF switch for communication purposes (accompanied by an appropriate controller and RF illumination), eliminates the need for high-power active elements like amplifiers, mixers or high frequency oscillators. Due to the lower complexity, both the energy and monetary costs are significantly reduced.

#### a) Wireless Communication with Bistatic & Ambient Backscatter

Any backscatter communication system consists of the backscatter tag (including the RF switch, its controller and the backscattering antenna), a receiver and an illuminator. The illuminator is an active RF transmitter, which provides the backscattering antenna of the tag, with the necessary RF illumination. The receiver and the illuminator may be co-located (monostatic setup, as in RFID) or can be separate units, located at different, possibly distant points (bistatic setup [4], [8], [9]).

Bistatic setups offer flexibility and improved communication range [8], [9], [10] while more than 1 illuminators in *multistatic* setups, can significantly increase coverage [11], at the expense of additional installation costs. However, the requirement for an additional device (unmodulated RF transmitter/illuminator), may limit the variety of possible applications of backscatter radio.

The need for a dedicated transmitter providing illumination/carrier is omitted in the case of *ambient backscatter*. In contrast to dedicated, unmodulated illuminating signals, *ambient* backscatter, a special case of bistatic backscatter, exploits for RF illumination ambient *modulated* signals, already present “in the air” [12], as shown in Fig. 1.2.

While solving the problem of requiring a dedicated device for continuous wave (CW) RF illumination, the idea of ambient backscatter generates a number of new problems. The ambient signals are modulated, time-varying and more importantly, *unknown*.

Another problem emerging in an ambient backscatter radio setup is the fact that due to double fading (illuminator-to-tag-to-receiver), the relayed signal is subject to severe interference from the direct signal at the receiver (Fig. 1.2). To effectively decode the tag's information, the interference must be mitigated or, ideally, cancelled. Additionally, the ambient signals, in the general case, "travel" a significant distance prior to impinging on the tag's antenna and thus, are significantly attenuated.

### b) Addressing the Problems of Ambient Backscatter

The unavailability of any information regarding the modulated and time-varying ambient signal, poses a significant barrier towards the reception and effective decoding of information transmitted by a backscattering tag.

Recently, numerous studies have proposed solutions for coping with the limitations of ambient backscatter communication. The studies focus on backscatter on-off keying (OOK), where information is backscattered on the amplitude of the ambient signal (e.g., [13, 14] and references therein). The problem of deriving receivers and detectors is mitigated using the assumption of a normally distributed illuminating signal: the complex baseband samples of ambient signals are modelled as samples drawn from a circularly symmetric complex normal distribution. That way, binary hypotheses (for digital communication) are easily formed and respective detectors are derived.

Other studies consider OOK in conjunction with some form of differential coding at the tag, requiring perfect synchronization with the ambient carrier. Such requirement for synchronization can be only satisfied by equipping the tag with an appropriate receiver structure for the ambient RF signal [15].

Ambient backscatter, utilizing quadrature phase-shift keying (QPSK) and quaternary amplitude shift keying (4-ASK) at the tag, was studied from an information-theoretic point of view in [16]. It was shown that backscattering operation may offer performance gains to the reception of ambient signal from the legacy receiver.

The finding of [16] demonstrates that backscatter radio can be used for purposes different than achieving ultra-low-power communication. More specifically, given proper thought and design, a backscattering tag may be able of offering gains to "third-party" communication systems that "host" it.

Detailed surveys of the (growing) ambient backscatter literature can be found in [7, 17].

### c) Ambient Backscatter-System Implementations

Ambient signals may originate from digital television (DTV) broadcasters, FM radio transmitters or other, non-dedicated sources (such as WiFi [18]). In [12] illumination from DTV transmissions was exploited and tag-to-tag, digital communication was demonstrated based on simple envelope detection principles, achieving ranges in the order of 60 cm. In [19] multi-antenna and spread spectrum concepts were implemented in an analog, low power manner. Taking advantage of interference cancellation due to exploiting multi antenna techniques, communication rates up to 1 Mbps (for a tag-to-tag communication range of 2 m) were achieved, exploiting an impinged (at the tag antenna) DTV signal of  $-10$  dBm. In a similar manner, using spread spectrum techniques, a communication range of 6 m was achieved at a rate of 3.3 bps for an impinged DTV signal of  $-15$  dBm.

Ambient FM illumination from radio stations was exploited in [20], achieving experimental range of 18 m (for analog audio transmission). The tag was a computer connected to a function generator, which in turn drove the RF switch. Digital 2 & 4 audio FSK and analog audio backscatter transmission were demonstrated. Ambient FM illumination was also considered in [21] to showcase properties of specially designed waveforms (perfect pulses), employed at the tag's side.

#### 1.1.2 Distributed & Passive Beamforming

It was stated in the previous paragraphs that given proper design, a backscattering tag may be able to offer gains at a communication system that “hosts” it: the transmitter of said system provides illumination while the receiver receives the superposition of:

- The transmitter's signal propagating through “direct” paths offered from features of the propagation environment (physical reflections from objects and walls).
- The transmitter's signal as relayed from the backscattering operation of the tag (artificial, controlled reflection). The relayed signal is also subject to reflections from the environment.

An illustration of the propagation “routes” described above is offered in Fig. 1.1. By discriminating those two branches of signal at the receiver, the tag's information can be recovered from the second branch, while the first acts as strong interference; the relayed version of the transmitter's signal contains the tag's information. In the context of recovering tag's information, discrimination of those two signal components is a problem that is usually overlooked by the literature and will be addressed in Chapter 3.

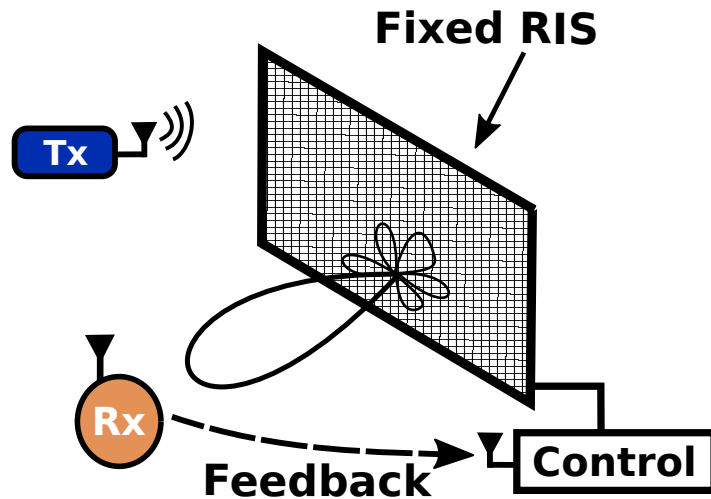


Figure 1.3: A reconfigurable intelligent surface (RIS) setup. A large number of reflective elements are deployed in a large surface. The elements are controlled so as the reflected signals constructively interfere at the location of a receiver.

What if the receiver does not discriminate those signal components? What if the tag, instead of loading information, modifies the impinged signal—using backscatter radio—so as the aforementioned signal components interfere constructively at the receiver? In that case, power gain is offered at the receiver through *passive beamforming*. Solving beamforming problems using backscatter radio techniques, omits the need for complex, high-power (due to multiple RF front-ends) antenna arrays at the transmitter (or the receiver).

### a) Reconfigurable Intelligent Surfaces

Literature has recently offered methods for backscatter-inspired, backscatter-based, passive beamforming using distinct devices in the environment, rather than the transmitter or the receiver units. That is the case of re-configurable intelligent surfaces (RIS) [22–25].

RISs (Fig. 1.3) are surfaces whose electromagnetic behavior can be controlled electronically. Thus, the propagation environment can be altered and beamforming can be realized. Such surfaces may be implemented, among other ways, using reconfigurable reflectarrays [26] and programmable meta-surfaces [27]. In [28], an algorithm was designed for maximizing the received signal strength at target areas, by placing highly reflective metallic surfaces in specific spots.

In [29], a large array of dual-antenna elements, connected through phase shifters, was considered. Propagation was altered by controlling the phase shifters. Using channel feedback from a Wi-Fi access point, the phase shifters of the array were controlled in a way that specific performance goals could be achieved at a receiver (e.g., Shannon capacity).

In [30], an array of column-wise metallic patches, connected through RF switches, altered the reflective area of a large surface. Exploiting received signal strength indication (RSSI) feedback from the receiver, a controller could assign appropriate states at each switch so that power at the receiver’s location could be maximized.

Binary reconfigurable, large metasurfaces, able to enhance the reception of RF signals on a communication system are also proposed in [31]. The control of the said metasurfaces is performed through custom optimization algorithms, utilizing channel feedback from a secondary receiver connected to the controller; a transmitter of the said communication system may also be connected (through network infrastructure) to the controller of the surface [32]. A similar technique was presented in [33].

## b) Parasitic Arrays

An alternative solution to the complexity and cost of multiple RF front ends is based on parasitic arrays, such as switched parasitic antennas (SPAs) and electronically steerable passive array radiators (ESPARs) [34–36]. In such systems, a number of parasitic elements terminated with variable loads, are placed near a single active element. To ensure sufficient coupling, the parasitic elements are placed at distances of less than  $\lambda/2$  from the active element.

By altering the loads of the parasitics for a given stimulation of the single active element, different radiation patterns can be realized. The operation resembles backscattering with the difference lying in the level of coupling between the transmitter (driven elements) and the tag (parasitic elements).

Besides beamforming [37], using such antenna systems, MIMO communication [35,36] and other problems requiring statistical signal processing [38], can also be solved without multiple RF front ends. An SPA for an RFID reader was designed in [39]. The circuitry of the parasitic element was wirelessly powered by the driven element, altering the parasitic load periodically.

### 1.1.3 Virtual Antenna Arrays

Using a single RF front-end (“illuminator”) and a number of parasitic elements (“tags”), parasitic arrays have demonstrated the capability of solving problems requiring high complexity, multi RF front-end arrays, in a low complexity (and cost) manner.

The problem of direction of arrival estimation was solved in [38] using a single active element (single receiving front-end) and a number of parasitics. MIMO gains were demonstrated in [36, Chap. 5], using a virtually rotating antenna. Due to the Doppler

effect, a virtually rotating antenna leads to multiple “copies” of an impinged signal in the frequency domain, converting spatial diversity or multiplexing (offered by a conventional antenna array) to frequency diversity (or multiplexing).

## 1.2 Motivation & Contribution

### 1.2.1 Motivation

#### a) Ultra-Low-Power Backscatter Communication

Most of the practical implementations of ambient backscatter systems listed above, offer short communication ranges and require specially designed receivers for tag interrogation/reception. In most cases, only tag-to-tag communication is offered, while other solutions may involve complex, laboratory-level, tag implementations including complex receiving structures (e.g., [40]), defeating the purpose of exploiting backscatter radio principles.

Most implementations suggested by the literature, while exploiting backscatter radio principles, due to their implementation complexity, do not pose as viable solutions for the problems emerging in modern wireless sensing.

Literature suggests theoretical solutions for the problems of ambient backscatter, that are mainly based on OOK modulation. OOK, due to its simplicity allows for minimum power consumption at the tag. However, as it will be subsequently shown in detail, OOK does not solve the problem of direct signal interference. Simplified, complex normal assumptions, in conjunction with OOK, lead to detectors that, though of low complexity, do not combat direct signal interference thus limiting the communication performance.

#### b) Passive and Distributed Antenna Arrays

Towards lowering the complexity, cost and power consumption of problems requiring antenna arrays, methods using passive (parasitic arrays) and distributed (RIS) systems have been proposed.

For the problem of beamforming, shifting the functionality required from the radio ends to the environment, may suggest large surfaces/RIS, requiring additional installation effort, as well as custom controllers with elaborate algorithms. The last, require channel feedback so as to appropriately control the surface. Cooperation with the legacy communication system, i.e., the system to be assisted by the beamforming operation, or in some cases with an additional, secondary, receiver is required for the said feedback, which may not be an option for many practical scenarios.

Parasitic arrays cope with a number of problems that would otherwise require conventional arrays, using just a single RF front-end. Despite lowering the complexity of multiple RF front-ends, such systems require modifications in either the transmitter and/or the receiver of a communication system.

### 1.2.2 Contribution

Motivated by the limitations of the solutions provided by the current literature, this dissertation attempts to solve the problems of ambient backscatter communication.

The dissertation offers both analog & digital hybrid (in the sense of combining benefits from different modulations) backscatter modulation schemes to be exploited in ambient backscatter setups. A common denominator for all proposed techniques is the control of the switching frequency with which the tag switches the antenna load between two values. These modulation schemes allow for discriminating the direct and relayed signals in the frequency domain, allowing for easy cancellation of direct signal interference. The proposed switching techniques also allow for easy multiplexing of tags/sensors at the frequency domain [6], [9], [41].

Coherent, partially coherent and fully noncoherent detection schemes are provided for the suggested, digital modulation schemes, even though the illuminating signal is modulated and time varying. Contrary to prior art, no cooperation with the ambient transmitter is assumed, leading to receiver-less, ultra-low-complexity tags; signal structure is either explicitly considered for designing fully coherent and fully noncoherent detectors, or is completely ignored for deriving illumination-agnostic, partially coherent detectors.

Using the same switching principles, the proposed, analog *FM remodulation* scheme, allows for recovery of a batteryless tag's backscattered information using any commodity FM radio receiver, from the old radio set with tubes, to a modern FM-radio equipped smartphone (Fig. 1.4).

Tag operation is modeled in detail by incorporating all related parameters. Principles from dedicated illumination, bistatic backscatter communication [9, 41, 42], cannot be directly applied to ambient, *modulated* illumination scenarios, and new detection schemes are carefully designed, escorting details of tag operation. In summary, Chapter 3 and Chapter 4 of the dissertation will offer the following:

- A digital, hybrid modulation scheme, which will be referred to as pseudo frequency shift keying (PFSK), exploiting the multiple access benefits of backscatter FSK and the limited bandwidth requirements of OOK. Under certain assumptions, fully coherent detectors will be offered for PFSK.

- A digital, hybrid of backscatter FSK and binary-PSK (BPSK) modulation scheme, which will be referred to as shifted BPSK (SBPSK). Contrary to prior art, the scheme does not require *any* information regarding the ambient carrier or its structure for performing detection. Partially coherent as well as fully noncoherent, illumination-agnostic detectors are offered. In contrast to the previously mentioned coherent scheme, due to its illumination-agnostic character, SBPSK can cope with narrowband illuminating signals attaining various modulation schemes.
- Exploiting SBPSK, short packet coding will be utilized for the first time under an ambient backscatter scenario and a soft decision structure will be derived. Utilizing the derived detectors under a Bose-Chaudhuri-Hocquenghem (BCH) code, high performance gains will be demonstrated, suggesting that the nature of ambient backscatter may be beneficial under certain conditions and improve performance instead of degrading it. The last is a different point of viewing results from recent studies [16].
- An analog modulation scheme based on backscatter, (analog) FM along with results for the effect of noise and interference at the output of a commodity FM receiver.<sup>2</sup> The scheme will be subsequently referred to as *FM remodulation* (Chapter 4, Fig. 1.4).
- A complete prototype (contrary to laboratory setups presented in prior art) of an ultra-low power tag employing the suggested analog, ambient backscatter scheme, built with ultra-low-cost, off-the-shelf components, achieving tag-to-receiver ranges in the order of **26** meters outdoors, able to be interrogated by *any* conventional FM receiver (including FM radio equipped (smart)phones), while consuming **24**  $\mu$ Watts in continuous operation.
- Based on the FM remodulation technique, multiple prototype wireless soil moisture sensing tags were built, targeting applications in precision agriculture and environmental sensing. Their simplicity, cost and power consumption, allow for the widespread adoption of sensing technology within empirical farming practices.
- The proposed modulation schemes, due to the inherent switching operation, allow for ultra-low-complexity, receiver-less tags with easy reception and frequency-based multiple access, at the expense of slightly increased power consumption (compared to OOK).

---

<sup>2</sup>The same method was independently offered by [20].

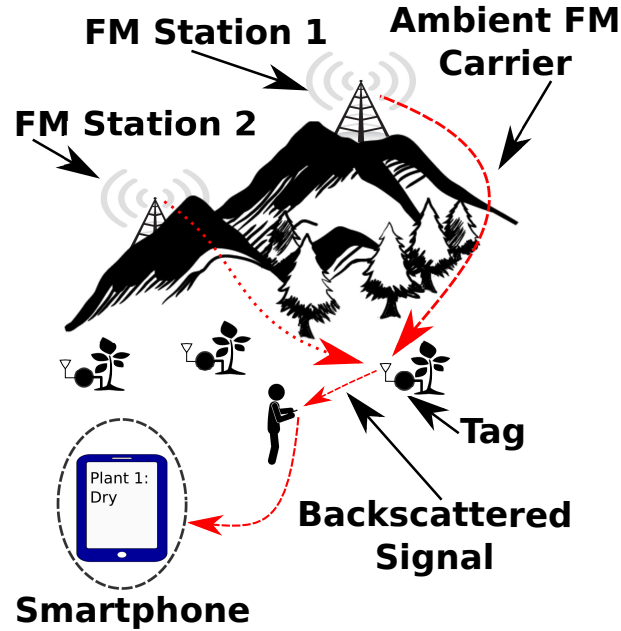


Figure 1.4: Recycling FM radio signals for transmitting the value of a soil moisture sensor. While consuming  $24\mu\text{Watts}$ , the value of the sensor can be recovered at distances in the order of 20 meters by *any* FM radio receiver, including those found in modern smartphones.

While solving the problems inherent in ambient backscatter communication, the switching techniques provided in the listing above, also apply to problems that literature attempts to solve using parasitic arrays or RISs.

As it will be shown in Chapters 3 – 5, multiple switching tags result in copies of the illuminating signal in the frequency domain. Spatial diversity offered by a conventional antenna array, is transformed to frequency diversity through the switching techniques originally intended for solving ambient backscatter problems. Thus, instances of problems requiring multi-antenna processing can be solved in an ultra-low-power, ultra-low-complexity manner with the proposed switching backscatter radio techniques (Chapter 5).

While the switching techniques were inspired by the problem of direct signal interference in ambient backscatter, as discussed earlier, looking said problem as a feature instead, allows for passive beamforming. A method for blindly controlling the relayed channel (using backscatter radio, Fig. 1.5), without any feedback from the intended receiver will be offered in Chapter 6, allowing for opportunistic, instantaneous, beamforming gains. The contributions of the dissertation in the field of passive beamforming and array signal processing are summarized below:

- In contrast to modifying the transmitter or receiver, a number of backscattering tags, utilizing the switching methods originally intended for ambient backscatter

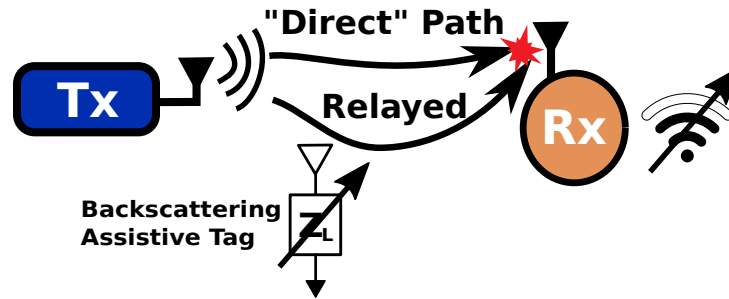


Figure 1.5: Using a backscatter radio tag to assist the reception of a signal at a receiver.

communication, will be used to solve a *DoA* estimation problem, a problem that would otherwise require antenna arrays with multiple RF front-ends (Chapter 5, Fig. 1.6). With the proposed method, backscattering tags act as a virtual antenna array.

- In contrast to deploying large RISs, associated with feedback structures & control algorithms, the dissertation will offer a simple, *zero-feedback*, backscatter radio-based, fading mitigation/beamforming technique & prototype, for coping with the effects of multipath (Chapter 6).
- Due to the blind/zero-feedback, instantaneous nature of the proposed beamforming system, an expression will be derived for the probability of enjoying beamforming gain.
- An analytical expression for the average power gain offered by a (given) number of *assistive* (beamforming) backscattering tags, will be also derived, verified and corroborated by simulation and experimental results.
- Despite the passive nature of the proposed beamforming tags, extensive measurements showed that considerable gains (in the order of 3 dB) can be enjoyed, even when utilizing a single backscattering tag.
- The feasibility and effectiveness of the proposed beamforming technique, is highlighted with experiments and measurements utilizing the commercial Gen2 protocol; RFID tags were successfully interrogated multiple times only after the aid of the proposed, assistive, backscattering tags.
- The simple, passive (no amplification) character of the beamforming tag(s), allows for future, wirelessly powered (beamforming) tags, to aid the interrogation of other, adjacent, RFID tags that could not otherwise operate due to the effects of multipath.

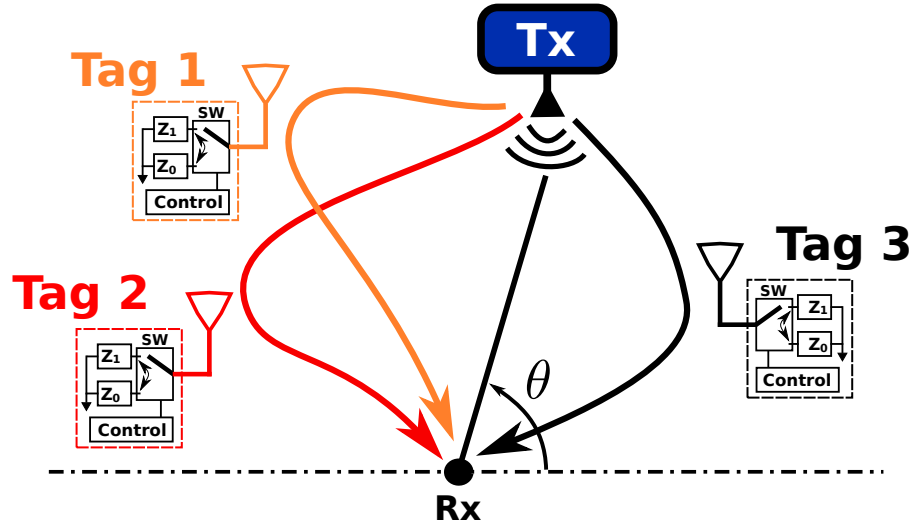


Figure 1.6: DoA ( $\theta$ ) estimation of a RF source, using tags around a single antenna receiver. Multiple backscatter tags introduce new propagation paths for a signal to follow. Using the proposed switching techniques, the transmitter’s observations through the tags can be discriminated in the frequency domain and be subsequently used in relevant algorithms.

### 1.3 Roadmap

- Chapter 2 introduces the reader to the concept of backscatter radio and demonstrates how it can be exploited for solving a number of communication problems.
- Exploiting backscatter radio principles, Chapter 3 will present the digital, ambient backscatter modulation schemes.
- FM remodulation, allowing for batteryless transmission of a sensor’s information by recycling FM radio signals, will be described and analysed in Chapter 4.
- Using the switching methods presented in Chapters 3 – 4, in Chapter 5, scatter radio relaying will be exploited for emulating a multi-antenna receiver and solving a DoA estimation problem.
- Inspired by the results of Chapter 5 and turning the interference problems faced in Chapters 3 – 4 into features, methods for blind (zero-feedback) beamforming using a number of backscattering tags, will be offered in Chapter 6.
- Conclusions are drawn in Chapter 7, while supplementary material is provided in Chapter 8.

## 1.4 Notation

Lowercase, letters will denote scalars. Bold lowercase letters will denote vectors, while bold uppercase letters matrices. The complex conjugate, conjugate transpose (Hermitian) and simple transpose operations on a vector or matrix, will be denoted by  $(\cdot)^*$ ,  $(\cdot)^H$ ,  $(\cdot)^T$ , respectively. The real part of complex number  $z$  will be given by  $\Re\{z\}$ , while its phase by  $\angle z$ .

The probability density function (PDF) of a random variable (r.v.)  $\chi$  evaluated at  $x$ , will be denoted as  $f_\chi(x)$ , while its cumulative distribution function (CDF) by  $F_\chi(x)$ . The expected value of  $\chi$  will be given by  $\mathbb{E}[\chi]$ .

$\chi \sim \mathcal{N}(\mu, \sigma^2)$  expresses the fact that  $\chi$  is distributed according to the Gaussian distribution of mean  $\mu$  and variance  $\sigma^2$ , while  $\chi \sim \mathcal{CN}(\mu, \sigma^2)$  the fact that  $\chi$  is a proper complex Gaussian r.v., of mean  $\mu$  and variance  $\sigma^2$ . For the special case of  $\mu = 0$ , the complex Gaussian distribution is characterized as *circularly symmetric*.

# Chapter 2

## Fundamentals Of Backscatter Radio

This chapter introduces the reader to the concept of backscatter radio. Starting from the basic principles allowing for an antenna to reflect a signal in a controlled manner, a high level, wireless signal model is derived. The derived model allows for a multitude of wireless communication problems to be projected onto it and be solved in a low power, complexity and cost manner, exploiting the beauty and simplicity of backscatter radio.

### 2.1 Modulation in the Passband

In backscatter radio, a device varies the impedance terminating its antenna. Under illumination from an RF signal  $c(t)$  and assuming a load causing imperfect termination, the antenna reflects (part of) the impinged signal.

By altering the loads terminating the device's antenna, the characteristics of the reflected signal can be manipulated (Fig. 2.1). As it will be shown in the next sections, the signal backscattered by the antenna attains the following form:

$$x_{sc}(t) = c(t) (A_s - \Gamma_L(t)), \quad (2.1)$$

where  $\Gamma_L(t)$  is the reflection coefficient associated with the load terminating the antenna at time  $t$ , while  $A_s$  is an antenna related parameter that will be subsequently defined. Eq. 2.1 shows that by just altering the loads terminating an antenna, an impinged signal can be modified and “re-radiated” in a passive manner. Proper design of  $\Gamma_L(t)$  can lead to ultra-low-complexity solutions for common communication problems.

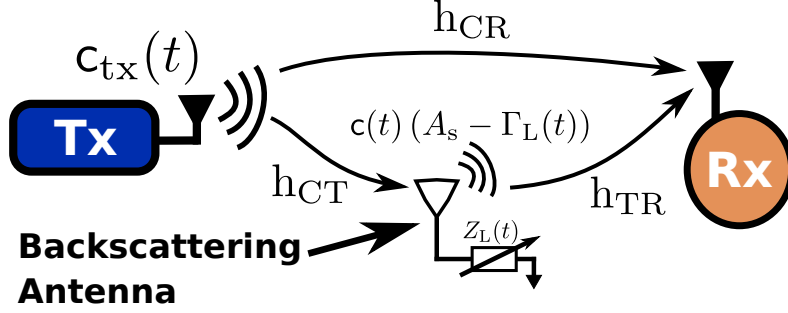


Figure 2.1: A backscattering antenna with means for variable loading at its terminals, passband-modulates an impinging signal  $c(t)$  (originating from a transmitter Tx).

## 2.2 Scattering Antenna

Any antenna illuminated by an incident field  $\vec{\mathcal{E}}_{\text{inc}}$  will, to an extent defined by its design, scatter the said field; currents induced on the antenna by the incident field, will force the former to “re-radiate” [43]. In particular, the scattered field will consist of two components. The first, *structural mode* component, is independent of antenna’s loading, while the second, *antenna scattering mode* component, is strongly connected to the loading [44]. Mathematically, the backscattered electric field at  $(r, \phi, \theta)$  can be expressed as follows [45]:

$$\vec{\mathcal{E}}_{\text{sc}}(r, \phi, \theta; Z_L) = \vec{\mathcal{E}}_{\text{sc}}^{\text{str}}(r, \phi, \theta) + \vec{\mathcal{E}}_{\text{sc}}^{\text{am}}(r, \phi, \theta; Z_L) = \vec{\mathcal{E}}_{\text{sc}}^{\text{str}}(r, \phi, \theta) - I_R \Gamma_L \frac{\vec{\mathcal{E}}_a(r, \phi, \theta)}{I_{\text{in}}}, \quad (2.2)$$

where  $\vec{\mathcal{E}}_{\text{sc}}^{\text{str}}(r, \phi, \theta)$  denotes the field due to the structural mode scattering, while  $\vec{\mathcal{E}}_{\text{sc}}^{\text{am}}(r, \phi, \theta; Z_L)$  the backscattered field due to the load dependent, antenna scattering mode.  $I_R$  is the current induced on the antenna by the incident field  $\vec{\mathcal{E}}_{\text{inc}}$ , when the former is terminated at a reference load  $Z_R = Z_A^*$ , where  $Z_A$  the antenna’s impedance. The *power wave reflection coefficient*  $\Gamma_L$  is defined for load  $Z_L$  as:

$$\Gamma_L = \frac{Z_L - Z_A^*}{Z_L + Z_A}. \quad (2.3)$$

For a current  $I_{\text{in}}$  at its terminals,  $\vec{\mathcal{E}}_a$  is the electrical field radiated by the antenna in the absence of an incident field. It can be shown [46] that the term  $\frac{\vec{\mathcal{E}}_a(r, \phi, \theta)}{I_{\text{in}}}$  is independent of both the loading of the antenna and the current  $I_{\text{in}}$ .<sup>1</sup> Eq. (2.2) can be then rewritten

<sup>1</sup>For free-space propagation in a lossless medium, the expression for  $\vec{\mathcal{E}}_a(r, \phi, \theta)$  can be found in [46].

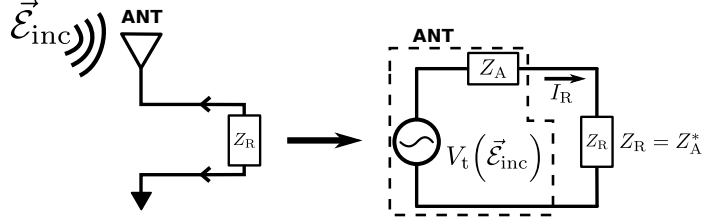


Figure 2.2: An incident field  $\vec{\mathcal{E}}_{\text{inc}}$  induces a current  $I_R$  when the load at the antenna's terminals is  $Z_R$ .

as follows:

$$\vec{\mathcal{E}}_{\text{sc}}(r, \phi, \theta; Z_L) = I_R \frac{\overbrace{\vec{\mathcal{E}}_a(r, \phi, \theta)}^{\vec{\mathcal{E}}_p}}{I_{\text{in}}} (A_s - \Gamma_L) = I_R \vec{\mathcal{E}}_p (A_s - \Gamma_L), \quad (2.4)$$

where  $A_s = \frac{\vec{\mathcal{E}}_{\text{sc}}^{\text{str}}(r, \phi, \theta) I_{\text{in}}}{\vec{\mathcal{E}}_a(r, \phi, \theta) I_R}$  which will be subsequently referred to as the *antenna structural mode parameter*.  $A_s$  is a load-independent parameter that depends on the antenna's physical characteristics [44].

Based on the antenna's equivalent circuit shown in Fig. 2.2, by definition, current  $I_R$  is given as follows:

$$I_R = \frac{V_t(\vec{\mathcal{E}}_{\text{inc}})}{Z_A + Z_R} = \frac{V_t(\vec{\mathcal{E}}_{\text{inc}})}{Z_A + Z_A^*} = \frac{V_t(\vec{\mathcal{E}}_{\text{inc}})}{2\Re\{Z_A\}} = \frac{V_t(\vec{\mathcal{E}}_{\text{inc}})}{2R_A}. \quad (2.5)$$

Given independence in antenna's loading and current  $I_{\text{in}}$ ,  $\vec{\mathcal{E}}_p$  can be absorbed in  $V_{\text{rx}}(\vec{\mathcal{E}}_{\text{inc}}(t))$ . Details on the form of  $V_t(\vec{\mathcal{E}}_{\text{inc}}(t))$  can be found in [44, 46]. It must be noted that, as it was shown in [45], simplified antenna equivalent circuits, can not fully capture the operation of a backscattering tag. Combining Eqs. (2.4) – (2.5) results in the aforementioned (see Eq. (2.1)), representation of the backscattered signal:

$$\mathbf{x}_{\text{sc}}(t) = \mathbf{c}(t) (A_s - \Gamma_L(t)), \quad (2.6)$$

## 2.3 A Communications' Perspective

Provided means for varying the termination load  $Z_L(t)$  of an antenna (and by extension  $\Gamma_L(t)$ ), passband modulation occurs. As a result, the signal backscattered by the antenna is signal  $\mathbf{c}(t)$ , modulated by  $A_s - \Gamma_L(t)$  (Eq. (2.1)).

As it will be shown in the next chapters, a number of problems in the context of wireless communications can be reduced to problems of designing  $\Gamma_L(t)$ . Given a properly

designed  $\Gamma_L(t)$  and appropriate processing at a receiver, the backscattered signal has a specific form, a form which solves the problem at hand. To allow the casting of different problems into problems of designing  $\Gamma_L(t)$ , a universal model for a backscatter radio setup will be subsequently derived.

### 2.3.1 Wireless Signal Model

A backscatter radio setup is depicted in Fig. 2.1. A transmitter (Tx) is assumed, emitting, in the general case, a modulated signal in the form [47]:

$$\Re \{c_{\text{tx}}(t)\} = \Re \left\{ m(t) e^{j2\pi F_c t} \right\}, \quad (2.7)$$

where  $m(t)$  is the complex envelope of the transmitter's signal and  $F_c$  the carrier's frequency. Through its propagation in the environment, the signal is subjected to both large-scale (path loss) and small-scale (multipath) fading [48]; the transmitter's signal reaches the backscattering antenna from a direct, line-of-sight (LOS) path as well as through "delayed" paths due to reflections from scatterers. Thus, the transmitter's signal impinging on the backscattering antenna can be expressed as follows:

$$\begin{aligned} \Re \{c(t)\} &= \Re \left\{ \sum_{i=0}^{L_s} a_{\text{CT},(i)} m(t - \tau_{\text{CT},(i)}) e^{j2\pi F_c (t - \tau_{\text{CT},(i)})} \right\} \\ &= \Re \left\{ \sum_{i=0}^{L_s} a_{\text{CT},(i)} e^{-j\phi_{\text{CT},(i)}} m(t - \tau_{\text{CT},(i)}) e^{j2\pi F_c t} \right\}, \end{aligned} \quad (2.8)$$

where  $L_s$  is the number of scatterers (or clusters of scatterers) and index  $i = 0$  is reserved for the LOS path, while  $\phi_{\text{CT}} = 2\pi F_c \tau_{\text{CT},(i)}$ ;  $a_{\text{CT},(i)}$  and  $\tau_{\text{CT},(i)}$  denote the amplitude attenuation and time delay, respectively, introduced to the signal when the latter propagates through the  $i^{\text{th}}$  path. Subscript CT is used to denote the family of paths starting at the transmitter and leading to the backscattering antenna.

The set of problems addressed by this work, involve narrowband signals. In addition, block fading is considered (except where otherwise noted), i.e., path parameters remain constant for a specific time duration (block). Assuming a narrowband  $m(t)$  propagating through paths with limited delay spread (flat fading wireless channel [48]), for every path  $i$  it holds that  $m(t) \approx m(t - \tau_{\text{CT},(i)})$ . Thus, Eq. (2.8) becomes:

$$\Re \{c(t)\} = \Re \left\{ m(t) \sum_{i=0}^{L_s} a_{\text{CT},(i)} e^{-j\phi_{\text{CT},(i)}} e^{j2\pi F_c t} \right\} = \Re \left\{ m(t) h_{\text{CT}} e^{j2\pi F_c t} \right\}, \quad (2.9)$$

where  $h_{\text{CT}} = \sum_{i=0}^{L_s} a_{\text{CT},(i)} e^{j\phi_{\text{CT},(i)}} = a_{\text{CT}} e^{-j\phi_{\text{CT}}} \in \mathbb{C}$ . Exploiting the results of the previous section, the backscattered signal can be then expressed as follows:

$$\Re \{x_{\text{sc}}(t)\} = \Re \left\{ m(t) h_{\text{CT}} s (A_s - \Gamma_L(t)) e^{j2\pi F_c t} \right\}, \quad (2.10)$$

where  $s \in (0, 1)$  is a parameter related to the radar cross-section (RCS) of the backscattering antenna and quantifies the latter's ability to scatter the impinged power [45]. In the remainder of the text,  $s$  will be referred to as *scattering efficiency*.

In the absence of a backscattering antenna, the transmitter's signal would reach the receiver only via the aggregate of paths starting from the said transmitter and leading to the receiver. In such case, the signal at the receiver's antenna would be:

$$\Re \{y_{\text{d}}(t)\} = \Re \left\{ m(t) h_{\text{CR}} e^{j2\pi F_c t} \right\}. \quad (2.11)$$

Similarly to the previous paragraphs, the contribution of the aforementioned paths is described by the wireless channel parameter  $h_{\text{CR}} = a_{\text{CR}} e^{-j\phi_{\text{CR}}} \in \mathbb{C}$ .

However, due to the existence of the backscattering antenna, the signal impinging on the receiver's antenna is the aggregate of the transmitter's signal as propagated by the "direct" paths  $h_{\text{CR}}$  and the transmitter's signal as "relayed" via the backscattering antenna:

$$\begin{aligned} \Re \{y(t)\} &= \Re \left\{ y_{\text{d}}(t) + m(t) h_{\text{CT}} s (A_s - \Gamma_L(t - \tau_{\text{TR}})) h_{\text{TR}} e^{j2\pi F_c t} \right\} \\ &= \Re \left\{ m(t) h_{\text{CR}} e^{j2\pi F_c t} + m(t) h_{\text{CT}} s (A_s - \Gamma_L(t - \tau_{\text{TR}})) h_{\text{TR}} e^{j2\pi F_c t} \right\} \\ &= \Re \left\{ m(t) h_{\text{CR}} e^{j2\pi F_c t} + m(t) h_{\text{CT}} s A_s h_{\text{TR}} e^{j2\pi F_c t} + m(t) h_{\text{CT}} s \Gamma_L(t - \tau_{\text{TR}}) h_{\text{TR}} e^{j2\pi F_c t} \right\} \\ &= \Re \left\{ m(t) h_{\text{d}} e^{j2\pi F_c t} + m(t) h_{\text{CT}} s \Gamma_L(t - \tau_{\text{TR}}) h_{\text{TR}} e^{j2\pi F_c t} \right\}, \end{aligned} \quad (2.12)$$

where  $h_{\text{TR}} = a_{\text{TR}} e^{-j\phi_{\text{TR}}} \in \mathbb{C}$  the wireless channel parameter describing the backscattering antenna-to-receiver propagation paths and  $h_{\text{d}} = h_{\text{CR}} + h_{\text{CT}} s A_s h_{\text{TR}}$ . It is important to note that the backscattering antenna contributes to the direct path as well. That is due to the  $A_s$  term. The last is frequently ignored in the backscatter radio literature.

Tag-to-receiver (LOS path) propagation delay  $\tau_{\text{TR}}$  is included for completeness. As long as the narrowband assumption for  $m(t)$  holds, any delay introduced to  $m(t)$  can be ignored, as it is not critical to its subsequent use.

While the  $A_s$  part of the backscattered signal contributes only as an additional, "virtual" propagation path, by casting a communications' problem to Eq. (2.12), an engineer may appropriately design  $\Gamma_L(t)$  (and appropriate processing algorithms at the receiver),

so as to solve the problem by just changing loads at the terminals of an antenna. As will be shown in the next chapters (and already discussed at Chapter 1), choosing to solve a problem in such a manner significantly reduces the solution's cost, complexity and power requirements.

### 2.3.2 Homodyne Reception

Following reception from the receiver's antenna and the first stages of passband filtering, the signal at the receiver can be expressed as follows:

$$y_{\text{rx,p}}(t) = \Re \left\{ m(t) h_{\text{d}} e^{j2\pi F_c t} + m(t) h_{\text{CT}} s\Gamma_{\text{L}}(t) h_{\text{TR}} e^{j2\pi F_c t} \right\} + w(t), \quad (2.13)$$

where  $w(t)$  is a band-limited, zero-mean, Gaussian noise process. The first stages of filtering include a band-pass filter, centered at  $F_c$ , of bandwidth  $2W_{\text{SDR}}$ . Thus, the power spectral density (PSD) of  $w(t)$  is defined as follows:

$$S_w(f) = \begin{cases} \frac{N_0}{2}, & |f \pm F_c| \leq W_{\text{SDR}}, \\ 0, & \text{otherwise,} \end{cases} \quad (2.14)$$

In a receiver where homodyne conversion is utilized, the signal (after the first stages of filtering) is directly downconverted to baseband; the components of the complex baseband representation of the said signal, are offered at the output of the homodyne conversion stage for further processing. The conversion is performed by mixing the signal in two separate branches [8]:

$$I(t) = \text{LPF} \{ y_{\text{rx}}(t) \cos(2\pi (F_c + \Delta F) t + \Delta\phi_{\text{R}}) \}, \quad (2.15)$$

$$Q(t) = \text{LPF} \{ -y_{\text{rx}}(t) \sin(2\pi (F_c + \Delta F) t + \Delta\phi_{\text{R}}) \}, \quad (2.16)$$

where  $\Delta F$  denotes the carrier's frequency offset (CFO) from the local oscillator (LO) of the receiver, while  $\Delta\phi_{\text{R}}$  is the respective carrier phase offset (CPO). LPF denotes the application of a (baseband) low-pass filter with bandwidth  $W_{\text{SDR}}$ . By obtaining the *in-phase*  $I(t)$  and *quadrature*  $Q(t)$  components from Eqs. (2.15), (2.16), the signal model of

Eq. (2.12) can be used for processing in the complex baseband domain [8]:

$$\begin{aligned}
I(t) + jQ(t) &= \frac{1}{2} \mathbf{y}(t) e^{-j(2\pi(F_c + \Delta F)t + \Delta\phi_R)} + n(t) \\
&= \mathbf{m}(t) h_d e^{-j(2\pi\Delta F t + \Delta\phi_R)} + \mathbf{m}(t) h_{CT} s\Gamma_L(t) h_{TR} e^{-j(2\pi\Delta F t + \Delta\phi_R)} + n(t) \\
&= [\mathbf{m}(t) h_d + \mathbf{m}(t) h_{CT} s\Gamma_L(t) h_{TR}] e^{-j(2\pi\Delta F t + \Delta\phi_R)} + n(t), \tag{2.17}
\end{aligned}$$

where  $n(t) = n_I(t) + jn_Q(t)$  and  $n_I(t)$ ,  $n_Q(t)$  are the noise components after homodyne conversion, while the  $1/2$  factor can be absorbed in wireless channel parameters. It can be shown that the PSD of the aforementioned noise components is [47]:

$$S_{n_{I/Q}}(f) = \begin{cases} \frac{N_0}{4}, & |f| \leq W_{SDR} \\ 0, & \text{otherwise,} \end{cases} \tag{2.18}$$

The variance of the noise components is given by  $\sigma_{n_{I/Q}}^2 = \mathbb{E}[n_I^2(t)] = \mathbb{E}[n_Q^2(t)] = \frac{N_0}{2} W_{SDR}$  and  $\sigma_n^2 = \mathbb{E}[n^2(t)] = 2\sigma_{n_{I/Q}}^2$ . Finally, after sampling at a rate  $F_s = 1/T_s$ , the discrete baseband equivalent model takes the following form:

$$\begin{aligned}
\mathbf{y}[k] &= I(kT_s) + jQ(kT_s) \\
&= [\mathbf{m}(kT_s) h_d + \mathbf{m}(kT_s) h_{CT} s\Gamma_L(kT_s) h_{TR}] e^{-j(2\pi\Delta F kT_s + \Delta\phi_R)} + n(kT_s) \\
&= [\mathbf{m}[k] h_d + \mathbf{m}[k] h_{CT} s\Gamma_L[k] h_{TR}] e^{-j(2\pi\Delta F kT_s + \Delta\phi_R)} + n[k]. \tag{2.19}
\end{aligned}$$

where  $n[k] \sim \mathcal{CN}(0, \sigma_n^2)$ .

Various methods exist for correcting-ideally cancelling-the CFO term  $e^{-j2\pi\Delta F kT_s}$ . Such methods include maximum-likelihood (ML) estimation techniques (periodogram-based estimation of  $\Delta F$  and subsequent correction of the CFO term) [49] or phase locked loop (PLL)-based CFO tracking and cancellation [50]. The CFO corrected (assuming perfect CFO cancellation) signal can be then used for further digital signal processing (DSP) in the following form:

$$\mathbf{y}_c[k] = \mathbf{m}[k] h_d + \mathbf{m}[k] h_{CT} s\Gamma_L[k] h_{TR} + n[k]. \tag{2.20}$$

It is noted that in the case of periodogram-based CFO correction, the noise samples are in the form  $e^{+j2\pi\widehat{\Delta F} kT_s} n[k]$ , where  $\widehat{\Delta F}$  is the ML estimate of  $\Delta F$ . Due to the circular symmetry of the distribution of  $n[k]$ , the statistical properties of the latter are preserved. That is the reason why the notation for the noise samples is not altered when going from Eq. (2.19) to Eq. (2.20).

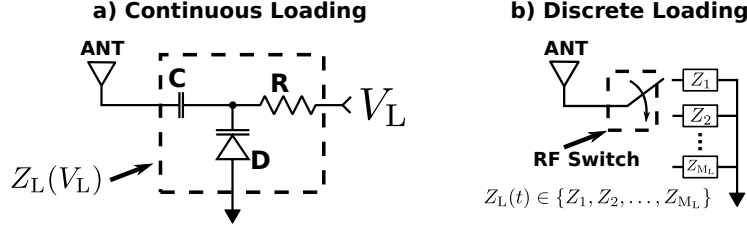


Figure 2.3: Altering the termination of an antenna with a) continuously-variable (using, e.g., a reverse biased varactor) load(s), and b) with  $M_L$  discrete loads (using an RF switch).

Compared to a conventional communication system, comprising of just a receiver and a transmitter, where the discrete baseband equivalent would be given by [51]:

$$y_c[k] = \mathbf{m}[k] h_{CR} + n[k], \quad (2.21)$$

Eq. (2.20) clearly demonstrates the power of backscatter radio. Proper design of  $\Gamma(t) \in \mathbb{C}$ , can allow for different backscatter modulations to occur (see Chapters 3 – 4), using a “foreign” signal  $\mathbf{m}(t)$  as a carrier. Beamforming can be realized when backscatter term  $\mathbf{m}[k] h_{CT} s \Gamma_L[k] h_{TR}$  constructively interferes with  $\mathbf{m}[k] h_d$ , thus aiding the receiver without the need of complex antenna arrays (Chapter 6). Designing  $\Gamma(t)$  to be a sinusoidal waveform, results in frequency shifting of  $\mathbf{m}(t)$  due to mixing. The aforementioned frequency shifting will be utilized in Chapters 3 – 4, to mitigate interference from  $\mathbf{m}[k] h_d$ . The backscatter radio-based mixing, will be also used for transforming spatial diversity offered by a conventional array to frequency diversity, in order to solve a direction of arrival problem in Chapter 5.

## 2.4 Implementing Backscatter Radio

### 2.4.1 Variable Antenna Loading

Up until this point, the ability of varying the loading of an antenna was assumed. Altering the termination of an antenna can be achieved using either a continuously variable load or a number of discrete loads.

The termination of an antenna can be varied in a controlled and continuous manner using, for example, voltage controlled variable capacitors, connected at its terminals. Such capacitors can be implemented using varactor diodes (Fig. 2.3). When the diode is reverse biased, the capacitive loading of said antenna is a function of the bias voltage. The range of values attained by  $Z_L(t)$  as a result of diode’s operation, can be tuned by appropriate

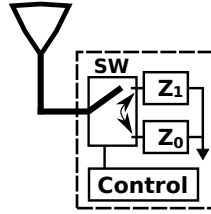


Figure 2.4: A backscattering tag, comprising of an RF switch which, based on the commands of a control circuit, alternatively terminating the antenna at two loads ( $Z_0$ ,  $Z_1$ ). The architecture will be used extensively in the following chapters.

selection of control voltage and circuit architecture. Continuous loading with varactors will be exploited in Chapter 6 for solving fading-related problems.

For applications where it is not required for  $Z_L(t)$  to attain values within a continuous range, an RF switch can be used to alternatively terminate the antenna to a number of discrete loads. An architecture comprising an RF switch alternating the termination of an antenna between 2 discrete loads, will be extensively used in the following chapters for backscatter radio-based communication and emulation of multi-antenna receivers.

### 2.4.2 Load Control

Besides the element(s) allowing for variable loading, means for controlling the said element(s) should be provided. Such means include appropriately designed control circuitry such as a microcontroller unit (MCU) or a reconfigurable digital device e.g., a programmable digital matrix or a field programmable gate array (FPGA). Custom analog circuitry may also be used to control the load, as will be subsequently shown in Chapter 4.

The apparatus allowing for the backscattering operation to occur, including the backscattering antenna, the means for varying the loading of the said antenna and the circuitry controlling the loading, will be subsequently referred to as “tag” or “backscattering tag”. Such an apparatus is depicted in Fig. 2.4. To exploit the benefits offered by backscatter radio in solving problems of wireless communications, the tag(s) should be designed under the “umbrella” of ultra-low-power, cost and complexity constraints.

## 2.5 Backscatter Radio Architectures

Depending on how the transmitter, the receiver and the backscattering tag are used and set up in space, two architectures are defined for backscatter radio systems. These are the *monostatic* architecture and the *bistatic* backscatter radio architecture. A third

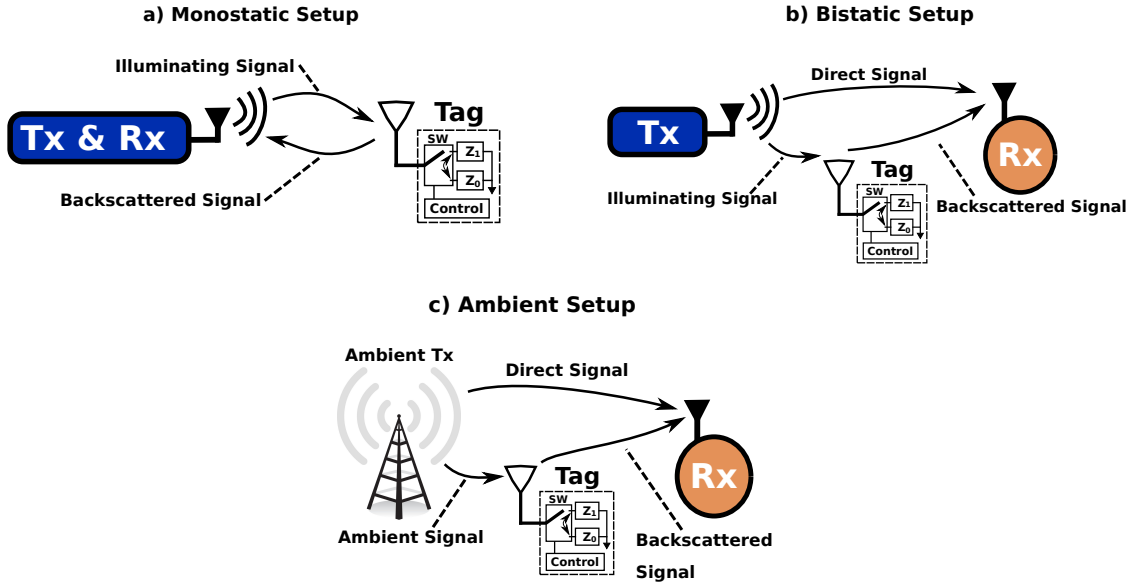


Figure 2.5: Depending on the setup of the transmitter, the tag and the receiver, three architectures are defined for backscatter radio systems.

architecture, *ambient* backscatter radio is also defined and can be thought of as an extension of bistatic backscatter radio. An illustrated description of the architectures, is provided in Fig. 2.5. The reader familiar with radar literature, will recognise the aforementioned architecture definitions as they do also appear, with the same notion, in the field of radar research.

**Monostatic Backscatter Radio** When the transmitter and the receiver of a backscatter radio setup (Fig. 2.1) are co-located, the setup is referred to as a monostatic backscatter radio setup. In a monostatic setup, the transmit and receive chains may also share a common LO and/or a single antenna (through an RF circulator, for example). Sharing an LO leads to a zero CFO ( $\Delta F = 0$ , see Eq. (2.19)).

Commercial RFID tag(s) are the prominent example of an application where backscatter radio finds extensive use; tag's binary information is encoded in  $\Gamma_L(t) \in \{\Gamma_0, \Gamma_1\}$  and is backscattered from the RFID tag(s) towards a reader. For the interrogation of RFID tags, a monostatic setup is traditionally utilized (though recent work has demonstrated significant benefits when using a bistatic setup for interrogation of Gen2 RFIDs [52]).

Due to the nature of the setup (transmitter and receiver in the same location/device), it can be shown that a monostatic setup offers the worst-case attenuation for the backscattered signal thus limiting the achievable communication range [11].

**Bistatic Backscatter Radio** In contrast to the monostatic architecture, in a bistatic backscatter radio setup, the transmitter providing illumination to the backscattering tag and the receiver of the tag's backscattered signal, are separate devices. Such a setup offers flexibility in the way the units are placed in space. Additionally, the wireless channel parameters are independent and diversity is offered, increasing the achievable communication range [11] (given a specific constraint, e.g., BER, to be satisfied at the receiver).

In a bistatic setup, a constant wave (CW) emitter is utilized. Due to the separation of the devices, in contrast to a monostatic setup, extra processing should be applied in order to cancel the inherent in the setup-CFO term.

Bistatic backscatter radio setups can find extensive use, as an alternative to conventional communication standards (e.g., LoRa, Bluetooth), in wireless sensor networks (WSNs) and relevant IoT devices [6, 7], due to their inherent ability to offer large communication ranges with ultra low power consumption [10]. The main drawback of bistatic setups is the need for a dedicated device (transmitter) to provide illumination to the backscattering tag(s).

**Ambient Backscatter Radio** Ambient backscatter is a special type of bistatic setup. In an ambient backscatter setup, *ambient* signals from the environment are utilized as illuminating signals for the backscattering operation. Such signals may be signals from digital television (DTV) transmitters, FM radio stations, Wi-Fi access points, transmissions of cellular systems and others; omitting the dedicated transmitter reduces the installation effort, monetary cost of the system and the energy requirements.

The signals exploited for illumination in an ambient backscatter radio setup are, in the general case, modulated and unknown. Thus, extra difficulties arise in the process of designing  $\Gamma_L(t)$  and/or signal processing algorithms for the receiver. Additionally, due to the involved distances (the ambient transmitter may be kilometers away from the tag), the signals impinging on the tag's antenna are severely attenuated.

In the following chapters, solutions to problems in the context of wireless communications are addressed by proper design of tag's  $\Gamma_L(t)$  and/or appropriate signal processing algorithms at the receiver. The inherent drawbacks of ambient backscatter are addressed in order to provide effective solutions to the aforementioned problems; as already stated, the solutions are offered under the constraints of ultra-low-power, cost and complexity.

# Chapter 3

## Recycling Radio Waves: A Digital Tag Approach

The goal of this chapter is to offer methods for digital communication, realized through ambient backscatter radio. A backscattering tag modulates its digital information “on-top” of ambient signals (utilized as carriers), while a receiver tries to recover the tag’s information, in the presence of interference caused by said ambient carrier. The signals utilized as carriers are modulated, unknown and severely attenuated. The methods that will be subsequently presented, effectively address the problems arising from the aforementioned limitations.

### 3.1 Communication with Ambient Backscatter

#### 3.1.1 Carriers from the Air

In order for a backscattering tag to “transmit” information, an illuminating signal, to be utilized as a carrier, is required. Given an impinging signal  $c(t)$ , due to the backscattering operation of the tag, the backscattered signal takes the form  $c(t)(A_s - \Gamma_L(t))$  (see Chap. 2).

In a conventional transmitter the symbols would be mapped onto appropriately designed waveforms. Using a mixer, a locally generated, high frequency signal (carrier) would be then modulated by said waveforms. The modulated signal would drive an amplifier, which in turn would drive the transmitter’s antenna. The form of the backscattered signal allows for a signal  $A_s - \Gamma_L(t)$  to modulate a high frequency carrier  $c(t)$  using nothing but an appropriately terminated antenna.

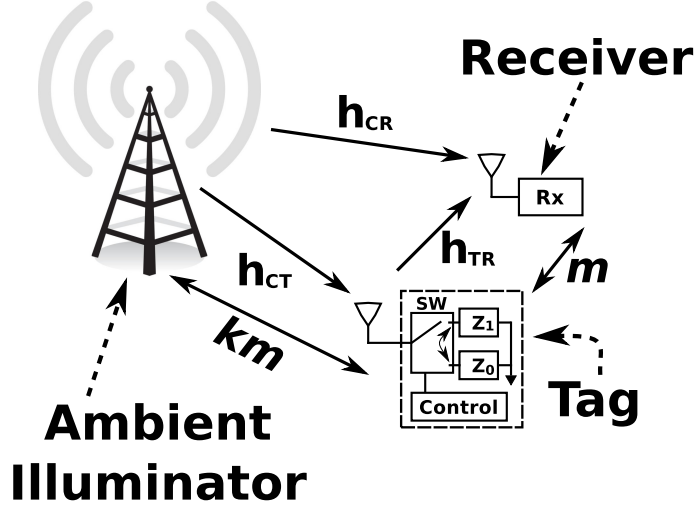


Figure 3.1: Loading information of top of ambient, unknown signals. A tag solves the problem of transmitting its information by using an ambient carrier.

By omitting high frequency oscillators, mixers and relevant circuitry, a backscattering tag can transmit digital information with substantially reduced energy consumption, complexity and overall cost. Although communication in that form can occur with a dedicated illuminator (dedicated device providing a carrier signal, as found in a bistatic setup), exploiting signals that already exist in the environment reduces installation effort and can further reduce energy requirements and monetary cost.

### 3.1.2 Hitchhiking on Strangers' Signals

$\Gamma_L(t)$  is designed so as to carry tag's digital information. A tag modulates its information-bearing waveform  $A_s - \Gamma_L(t)$ , "on-top" of an already modulated, unknown signal  $c(t) = m(t) h_{CT}$  (Fig. 3.1), impinging on the former's antenna. Given homodyne reception, the receiver's output can be expressed as (see Sec. 2.3.2, Eq. (2.17)):

$$I(t) + jQ(t) = [m(t) h_d + m(t) h_{CT} s \Gamma_L(t) h_{TR}] e^{-j(2\pi\Delta F t + \Delta\phi_R)} + n(t), \quad (3.1)$$

The goal of the receiver is to recover the information that is mapped onto  $\Gamma_L(t)$ . Towards achieving that goal, the following problems must be first addressed:

- The backscattered signal, due to double fading (mathematically expressed through product  $h_{CT} h_{TR}$ ) and the non-ideal scattering (quantified by scattering efficiency parameter  $s$ ), is subject to interference by the "stronger" direct signal component  $m(t) h_d$ .

For effective recovery of the tag's information from the received signal, the interference caused by the direct signal component  $\mathbf{m}(t) \mathbf{h}_d$ , which will be subsequently referred to as direct signal interference (DSI), must be mitigated.

- In the general case,  $\mathbf{m}(t)$  is modulated and time-varying and thus, the tag's waveform is affected by a time-dependent "fading" term  $\mathbf{m}(t)$ . Additionally, no information regarding  $\mathbf{m}(t)$  or its structure, is available at the receiver.

The unavailability of any information regarding  $\mathbf{m}(t)$ , poses difficulties in both the main problem (recovering tag's information) at hand, as well as in the problems (mitigation of DSI) arising from trying to solve the main problem.

In the following sections, the aforementioned problems will be treated by fully exploiting the mixing of signals resulting from the backscattering operation;  $\Gamma_L(t)$  will be designed so as to both carry the tag's digital information and, in conjunction with processing at the receiver, cancel the DSI component in the received signal.

## 3.2 Engineering Tag's Waveforms

The tag's waveform  $\Gamma_L(t)$ , irrespective of the symbol to be backscattered, must be designed so as to aid separation of the DSI term  $\mathbf{m}(t) \mathbf{h}_d$  from the tag's signal term  $\mathbf{m}(t) \mathbf{h}_{CT} s \Gamma_L(t) \mathbf{h}_{TR}$ . The hint on how the interference can be cancelled is given by the fact that,  $\mathbf{m}(t) \mathbf{h}_d$  appears in the interference term subject to stationary fading from compound, block constant parameter  $\mathbf{h}_d$ , while in the signal term as the product  $\mathbf{m}(t) \Gamma_L(t)$ .

The interference term can be removed by discriminating it from the signal term in the frequency domain. If antenna loading is implemented such that  $\Gamma_L(t)$  is a (co)sinusoidal waveform of frequency  $F_{sw}$ , then, due to mixing  $\mathbf{m}(t) \Gamma_L(t)$ , the signal term will be "shifted away" from the clutter of  $\mathbf{m}(t) \mathbf{h}_d$  by an amount  $\pm F_{sw}$ . By occupying different frequency bands, filtering can then be used to separate the interference from the useful signal.

### 3.2.1 Antenna Loading for Frequency Shifting

In the simplest case, two loads  $Z_0, Z_1$ , are utilized to alternatively terminate the antenna. The reflection coefficients corresponding to  $Z_0, Z_1$  are given by  $\Gamma_0$  and  $\Gamma_1$ , respectively. Thus, the tag's signal  $\mathbf{x}_{tag}(t)$  can be expressed as follows:

$$\mathbf{x}_{tag}(t) = A_s - \Gamma_L(t), \quad \Gamma_L(t) \in \{\Gamma_0, \Gamma_1\}. \quad (3.2)$$

Using Eq. (3.2),  $x_{\text{tag}}(t)$  can be also expressed as follows:

$$x_{\text{tag}}(t) = \left( A_s - \frac{\Gamma_0 + \Gamma_1}{2} \right) + \frac{\Gamma_0 - \Gamma_1}{2} b(t), \quad b(t) \in \{-1, 1\}. \quad (3.3)$$

Function  $b(t)$  is used as a mathematical representation of the signal controlling which load ( $Z_0, Z_1$ ) terminates the tag's antenna at time instant  $t$ . To select which load is connected to the antenna, a simple RF switch is used. The RF switch is driven by a 50% duty-cycle square wave signal of (fundamental) frequency  $F_{\text{sw}}$ . In that case,  $b(t)$  can be seen as the mathematical representation of the square wave driving the RF switch.  $b(t)$  can be then represented by its Fourier series as follows [7]:

$$b(t) = \frac{4}{\pi} \sum_{k=0}^{+\infty} \frac{1}{2k+1} \cos(2\pi(2k+1)F_{\text{sw}}t + \varphi). \quad (3.4)$$

The tag may begin switching between its loads at an arbitrary time. With respect to a reference, “zero”-phase waveform (which is defined as a square wave beginning at a rising edge), that time can be modelled through the random phase offset  $\varphi$ .

To conserve bandwidth, processing at the receiver focuses on the backscattered signal resulting from just the first harmonic of  $b(t)$ . It can be easily shown that the first harmonic of  $b(t)$  holds  $\approx 80\%$  of the power of the backscattered signal [6]. Thus, including the backscattered signal resulting from the higher order harmonics of  $b(t)$ , would lead to limited gains that would not justify the utilization of significantly more bandwidth at the receiver. Therefore,  $b(t)$  can be substituted by its fundamental component:

$$b(t) \triangleq \frac{4}{\pi} \cos(2\pi F_{\text{sw}}t + \varphi). \quad (3.5)$$

The tag's signal can be then expressed as follows:

$$\begin{aligned} x_{\text{tag}}(t) &= \left( A_s - \frac{\Gamma_0 + \Gamma_1}{2} \right) + \frac{2(\Gamma_0 - \Gamma_1)}{\pi} \cos(2\pi F_{\text{sw}}t + \varphi) \\ &= m_{\text{dc}} e^{j\theta_{\text{dc}}} + m_{\text{tag}} e^{j\theta_{\text{tag}}} \cos(2\pi F_{\text{sw}}t + \varphi), \end{aligned} \quad (3.6)$$

where  $m_{\text{dc}} e^{j\theta_{\text{dc}}} = A_s - \frac{\Gamma_0 + \Gamma_1}{2} \in \mathbb{C}$  and  $m_{\text{tag}} e^{j\theta_{\text{tag}}} = \frac{2(\Gamma_0 - \Gamma_1)}{\pi} \in \mathbb{C}$ .

By constantly switching between two loads at a rate  $F_{\text{sw}}$ , the signal term:

$$\mathbf{m}(t) \mathbf{h}_{\text{CT}} \mathbf{s} \Gamma_{\text{L}}(t) \mathbf{h}_{\text{TR}} = \mathbf{m}(t) \mathbf{h}_{\text{CT}} \mathbf{s} m_{\text{tag}} e^{j\theta_{\text{tag}}} \cos(2\pi F_{\text{sw}}t + \varphi) \mathbf{h}_{\text{TR}}, \quad (3.7)$$

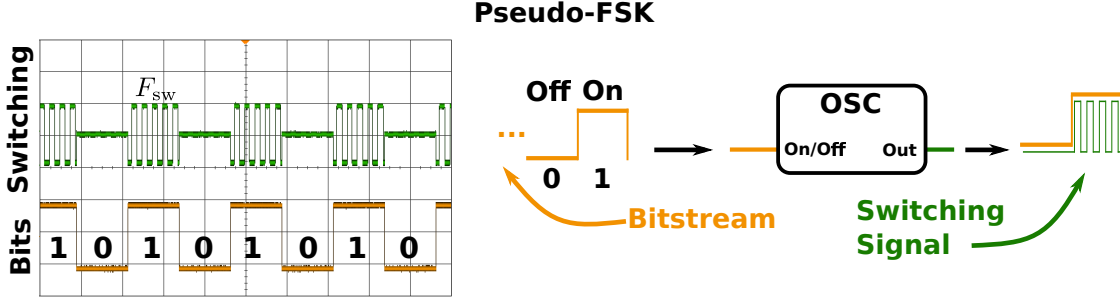


Figure 3.2: (Left) Switching according to PFSK modulation; the 3rd state between  $Z_0$ ,  $Z_1$  denotes that any of the two loads can be used for terminating the antenna (for the bit's duration). (Right) An indicative implementation of PFSK.

represents a relayed in the frequency domain version of  $m(t)$ . Specifically, due to the proposed backscattering, switching technique,  $m(t)$  is “copied” from  $F_c$  and “pasted” at  $F_c - F_{sw}$  and  $F_c + F_{sw}$ . In the baseband domain, filtering can be applied to remove the signal  $m(t)$  centered at DC ( $m(t)h_d$ ), while keeping the backscatter-originated copies (centered at [assuming perfect CFO cancellation]  $0 \pm F_{sw}$ , Eq. (3.7)).

The operation described in this section will be extensively utilized in Chapter 5; independent observations of a signal  $m(t)$  in the frequency domain, offered by a number of backscattering tags, will be exploited for emulating a multi-antenna receiver.

### 3.2.2 Mapping Information on Tag's Waveform

With a way for cancelling the interference available, methods for modulating digital information into the tag's switching signal must be provided. Two modulation methods will be subsequently offered. The first, is a hybrid form of backscatter FSK [8] and OOK, which will be referred to as Pseudo-FSK (PFSK). A slightly more complex (with respect to tag's implementation), second modulation scheme will be also provided, which will be referred to as Shifted BPSK (SBPSK). SBPSK is a hybrid form of backscatter FSK and BPSK.

The proposed modulation schemes can be seen as conventional OOK (PFSK) and BPSK (SBPSK) that modulate a subcarrier, which subsequently modulates a carrier. The subcarrier is the tag's switching signal  $x_{tag}(t)$ , while the main carrier is the ambient signal  $m(t)$ .

#### a) Pseudo-FSK

In the proposed PFSK scheme, to backscatter bit “1”, tag continuously alternates between the two loads at a rate  $F_{sw}$  (Eq. (3.6)), for the duration of the bit ( $T_{bit}$ ). To transmit bit

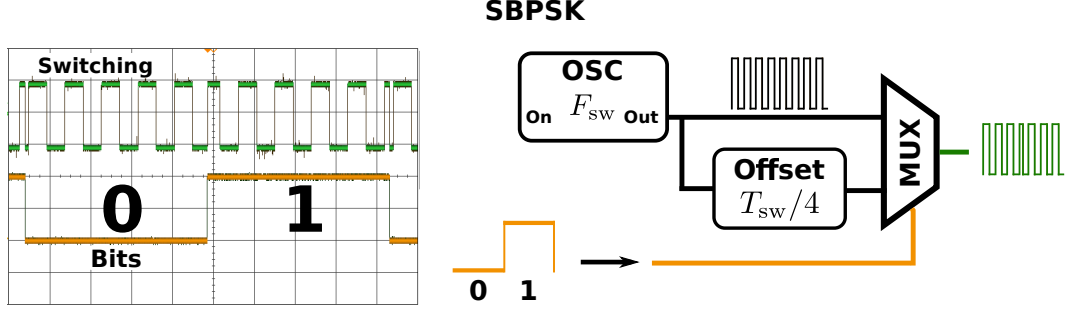


Figure 3.3: (Left) Switching according to SBPSK modulation. (Right) An indicative implementation of SBPSK for  $\Phi_0 = 0$ ,  $\Phi_1 = \Phi_0 + \pi/2$ .

“0”, tag simply terminates its antenna at one of the loads for the same amount of time ( $T_{\text{bit}}$ ). Tag modulation is not pure FSK, since during bit “0”, the tag simply terminates its antenna at one load and thus, bandwidth is reserved. Eq. (3.6) can be used to model the operation by setting  $F_{\text{sw},1} = F_{\text{sw}}$  and  $F_{\text{sw},0} = 0$ . Thus, the tag’s switching signal for bit  $i \in \{0, 1\}$  takes the form:

$$\mathbf{x}_{\text{tag}}^{\text{PF},i}(t) = \begin{cases} m_0 e^{j\theta_0}, & i = 0, \\ m_{\text{dc}} e^{j\theta_{\text{dc}}} + m_{\text{tag}} e^{j\theta_{\text{tag}}} \cos(2\pi F_{\text{sw}} t + \varphi), & i = 1. \end{cases} \quad (3.8)$$

It is assumed that for bit “0” the antenna is connected to load  $Z_0$  and thus  $m_0 e^{j\theta_0} = A_s - \Gamma_0$ . Fig. 3.2-Left depicts the described operation, as captured by an oscilloscope.

Pseudo-FSK can be implemented using an oscillator producing a squarewave of frequency  $F_{\text{sw}}$ . A controller can activate the oscillator whenever a bit “1” is to be backscattered, and keep it activated for the duration of the bit ( $T_{\text{bit}}$ ), as shown in Fig. 3.2. Gating the output of a continuously running oscillator is also possible but such operation would result in unnecessarily high energy consumption. Oscillator’s output is then used to drive the RF switch.

Operation of PFSK results in intermittent (depending on the bitstream to be backscattered), “appearances” of the relayed versions of  $\mathbf{m}(t)$  in the spectrum.

### b) Shifted BPSK

The modulation scheme suggested in this section involves encapsulating information in the phase of the tag’s switching signal. More specifically, given bit  $i \in \{0, 1\}$ , a specific phase offset  $\phi_i(t)$  can be introduced in Eq. (3.6), for the duration of a single bit:

$$\mathbf{x}_{\text{tag}}^{\text{SB},i}(t) = m_{\text{dc}} e^{j\theta_{\text{dc}}} + m_{\text{tag}} e^{j\theta_{\text{tag}}} \cos(2\pi F_{\text{sw}} t + \varphi + \phi_i(t)), \quad (3.9)$$

with:

$$\phi_i(t) = \begin{cases} \Phi_0, & i = 0, \\ \Phi_1 = \Phi_0 + \Delta\phi, & i = 1. \end{cases} \quad (3.10)$$

Tag's signal in Eq. (3.9) can be realized by driving the RF switch by a BPSK modulated subcarrier ( $F_{\text{sw}}$ ), adhering to the deviation constraints of Eq. (3.10).

Similarly to the implementation of PFSK, SBPSK can be implemented using an oscillator producing a square wave subcarrier of frequency  $F_{\text{sw}}$ . In order for the signal driving the tag to adhere to the deviation constraints of Eq. (3.10), delay blocks can be utilized in order to introduce the necessary phase offsets. For example, for the set of  $\Phi_0 = 0$  &  $\Phi_1 = \pi/2$ , the circuit shown in Fig. 3.3, can produce the signal that will be subsequently used to drive the RF switch. Depending on the bit to be backscattered, the multiplexer drives the RF switch either directly (bit "0") or (for bit "1") by introducing a  $T_{\text{sw}}/4$  offset to the oscillator's waveform (where  $T_{\text{sw}} = 1/F_{\text{sw}}$ ).

The modulation can be also realized using an analog, phase modulator driven by a pulse train. The pulse train corresponds to the bitstream to be backscattered. The amplitude of the pulses and the sensitivity of the phase modulator are configured so as Eq. (3.10) is satisfied. The modulator's output drives the RF switch.

A reasonable question could be raised at this point: what is the purpose of offering two modulation schemes?

At the expense of a slightly more complex tag, as it will be subsequently shown, SBPSK allows for the reception of tag's information without requiring any knowledge of  $\mathbf{m}(t)$  or, as a matter of fact, any other wireless channel parameter. In contrast, PFSK operates under fully coherent detection that requires certain assumptions regarding the structure of  $\mathbf{m}(t)$ . Thus, depending on the level of information available regarding the ambient carrier, a choice can be made.

### 3.3 Processing

#### 3.3.1 Received Signal

##### Received Signal-PFSK

For the case of backscattering bit “0” with PFSK, based on Eq. (3.8) and using Eq. (2.12), the following model describes the signal at the receiver:

$$\begin{aligned}
y_0^{\text{PF}}(t) &= \left[ m(t) h_{\text{CR}} + m(t) h_{\text{CT}} h_{\text{TR}} s m_0 e^{j\theta_0} \right] e^{-j(2\pi\Delta F t + \Delta\phi_{\text{R}})} + n(t) \\
&= m(t) \left[ h_{\text{CR}} + h_{\text{CT}} h_{\text{TR}} s m_0 e^{j\theta_0} \right] e^{-j(2\pi\Delta F t + \Delta\phi_{\text{R}})} + n(t) \\
&= m(t) \left( h_{\text{CR}} + \widehat{m}_0 e^{j\theta_0} \right) e^{-j(2\pi\Delta F t + \Delta\phi_{\text{R}})} + n(t), \tag{3.11}
\end{aligned}$$

where  $\widehat{m}_0 e^{j\theta_0} = h_{\text{CT}} h_{\text{TR}} s m_0 e^{j\theta_0}$ .  $h_{\text{d}}$  is not used as, for the case of bit “0”, the tag’s contribution to the signal is solely represented by  $m_0 e^{j\theta_0}$ . Similarly, if the tag backscatters bit “1”, the model for the received signal becomes:

$$\begin{aligned}
y_1^{\text{PF}}(t) &= \left[ m(t) h_{\text{CR}} \right. \\
&\quad \left. + m(t) h_{\text{CTS}} \left( m_{\text{dc}} e^{j\theta_{\text{dc}}} + m_{\text{tag}} e^{j\theta_{\text{tag}}} \cos(2\pi F_{\text{sw}}(t - \tau_{\text{TR}}) + \varphi) \right) h_{\text{TR}} \right] e^{-j(2\pi\Delta F t + \Delta\phi_{\text{R}})} + n(t) \\
&= \left[ m(t) h_{\text{d}} + m(t) h_{\text{CT}} h_{\text{TR}} s m_{\text{tag}} e^{j\theta_{\text{tag}}} \cos(2\pi F_{\text{sw}} t + \Phi_{\text{t}}) \right] e^{-j(2\pi\Delta F t + \Delta\phi_{\text{R}})} + n(t) \\
&= \left[ m(t) h_{\text{d}} + m(t) \widehat{m}_{\text{tag}} e^{j\theta_{\text{tag}}} \cos(2\pi F_{\text{sw}} t + \Phi_{\text{t}}) \right] e^{-j(2\pi\Delta F t + \Delta\phi_{\text{R}})} + n(t) \\
&= \left[ m(t) h_{\text{d}} + \frac{1}{2} m(t) \widehat{m}_{\text{tag}} e^{j\theta_{\text{tag}}} e^{j(2\pi F_{\text{sw}} t + \Phi_{\text{t}})} \right. \\
&\quad \left. + \frac{1}{2} m(t) \widehat{m}_{\text{tag}} e^{j\theta_{\text{tag}}} e^{-j(2\pi F_{\text{sw}} t + \Phi_{\text{t}})} \right] e^{-j(2\pi\Delta F t + \Delta\phi_{\text{R}})} + n(t), \tag{3.12}
\end{aligned}$$

where  $h_{\text{d}} = h_{\text{CR}} + h_{\text{CT}} h_{\text{TR}} s m_{\text{dc}} e^{j\theta_{\text{dc}}}$  and  $\widehat{m}_{\text{tag}} e^{j\theta_{\text{tag}}} = h_{\text{CT}} h_{\text{TR}} s m_{\text{tag}} e^{j\theta_{\text{tag}}}$ . Phase  $\Phi_{\text{t}}$  is defined as  $\Phi_{\text{t}} = \varphi - 2\pi F_{\text{sw}} \tau_{\text{TR}}$ . The trigonometric identity  $\cos(x) = \frac{e^{jx} + e^{-jx}}{2}$  was also used.

##### Received Signal-SBPSK

Following the same derivation path as with PFSK, it can be easily shown that when SBPSK is utilized at the tag, the received signal for the duration of a bit  $i \in \{0, 1\}$ , takes

the following form:

$$y_i^{\text{SB}}(t) = \left[ m(t) h_d + \frac{1}{2} m(t) \widehat{m}_{\text{tag}} e^{j\widehat{\theta}_{\text{tag}}} e^{j(2\pi F_{\text{sw}} t + \Phi_t + \Phi_i)} + \frac{1}{2} m(t) \widehat{m}_{\text{tag}} e^{j\widehat{\theta}_{\text{tag}}} e^{-j(2\pi F_{\text{sw}} t + \Phi_t + \Phi_i)} \right] e^{-j(2\pi \Delta F t + \Delta \phi_R)} + n(t). \quad (3.13)$$

### 3.3.2 Correlation

Prior to detecting tag's information, a correlation structure will be used. The correlation receiver is widely used for the demodulation and detection of FSK modulated signals [47, 51]. The samples of the received signal are correlated with a set of basis functions. Assuming perfect synchronization, the correlators' output is identical to the output of a matched filter (with the same basis functions), sampled at precisely the right time.

Besides constituting the basis for subsequent detection of the tag's bits, the correlation structure acts as the filter for removing the DSI. In order for the correlators to cancel the DSI, for both PFSK and SBPSK, it will be assumed that the complex envelope of the ambient, modulated signal “varies” much slower compared to a complex exponential of frequency  $F_{\text{sw}}$ . Mathematically,

$$\text{BW}(m(t)) \ll F_{\text{sw}}, \quad (3.14)$$

where  $\text{BW}(m(t))$  denotes the largest frequency component of  $m(t)$ . For example, in the context of illumination from FM radio stations (or other, narrowband signals), where each FM station signal's bandwidth is approximately 100 kHz, switching frequency should be in the order of 1 MHz. Even with existing, off-the-shelf technology, such switching rates may be achieved with small power consumption in the order of 20  $\mu\text{Watt}$  [53, 54]. The requirement in Eq. (3.14) can be relaxed, if pre-filtering (of known response) is applied in order to remove DSI. Due to switching and frequency shifting, the adjacent bands must be “clear” of interference, which is a limitation of the shifting techniques. For narrowband applications, however, e.g., backscattering within conventional sensor network systems (utilizing proprietary, multi-channel, low bandwidth protocols) this is not a problem.

Based on the form of the waveforms utilized at the tag (for both PFSK and SBPSK), for the duration of a bit, the following set of correlators will be used:

$$\begin{aligned} r^+ &= \sum_{k=0}^{L-1} y_c[k] \left( e^{j2\pi F_{\text{sw}} k T_s} \right)^* = \sum_{k=0}^{L-1} y_c[k] \left( e^{-j2\pi F_{\text{sw}} k T_s} \right), \\ r^- &= \sum_{k=0}^{L-1} y_c[k] \left( e^{-j2\pi F_{\text{sw}} k T_s} \right)^*, \end{aligned} \quad (3.15)$$

where  $y_c[k]$  is the CFO corrected, discrete baseband signal provided by the homodyne receiver (see Eq. (2.20)). Perfect synchronization is assumed and  $L = T_{\text{bit}}/T_s$  is the bit duration measured in number of samples;  $r^\pm$  is offered after correlating the samples of the received signal corresponding to a single bit, with  $e^{\mp j2\pi F_{\text{sw}}kT_s}$ .

It is noted that with a number of distinct  $F_{\text{sw}}$  switching frequencies and a corresponding number of correlator-sets (see Sec. 5), multiple access can be facilitated by exploiting the benefits of frequency domain multiple access (FDMA).

The exact form of  $r^\pm$ , for when utilizing either PFSK or SBPSK at the backscattering tag, is derived in the following sections.

## Correlator Outputs-PFSK

Using the correlation structure of Eq. (3.15) and assuming the adoption of PFSK modulation at the tag, a model for the output of the correlators will be subsequently provided.

Given that the tag backscatters bit “0” (hypothesis  $H_0$ ), the received signal (prior to CFO correction and sampling) follows the form of Eq. (3.11). Following sampling, CFO correction and synchronization, signal  $y_0^{\text{PF}}[k]$  is used for correlation and the result takes the following form:

$$\begin{aligned} r^+|H_0 &= \sum_{k=0}^{L-1} y_0^{\text{PF}}[k] e^{-j2\pi F_{\text{sw}}kT_s} = \left( h_{\text{CR}} + \widehat{m}_0 e^{j\widehat{\theta}_0} \right) \underbrace{\sum_{k=0}^{L-1} \mathbf{m}[k] e^{-j2\pi F_{\text{sw}}kT_s}}_{\approx 0, \text{ (Eq. (3.14))}} + \underbrace{\sum_{k=0}^{L-1} n[k] e^{-j2\pi F_{\text{sw}}kT_s}}_{\triangleq n^+} \\ &= n^+, \end{aligned} \quad (3.16)$$

where  $n^+ \sim \mathcal{CN}(0, L\sigma_n^2)$ . Using the assumption of Eq. (3.14), a relatively “slow”  $\mathbf{m}[k]$  modulates a “fast” exponential (i.e.,  $F_{\text{sw}}$  is greater than the frequency span of  $\mathbf{m}[k]$ ) and thus, the integral of their product tends to zero [47, Chap. 3.2]. In the same way, it can be shown that under  $H_0$ ,  $r^-|H_0 = n^-$ , with  $n^- \sim \mathcal{CN}(0, L\sigma_n^2)$ .

When the tag backscatters the bit “1” (hypothesis  $H_1$ ), the received signal is given by Eq. (3.12). The output of  $r^+$  can be then expressed as follows:

$$\begin{aligned}
r^+|H_1 &= h_d \underbrace{\sum_{k=0}^{L-1} m[k] e^{-j2\pi F_{sw}kT_s}}_{\approx 0, \text{ (Eq. (3.14))}} + \frac{\widehat{m}_{\text{tag}}}{2} e^{j\widehat{\theta}_{\text{tag}}} e^{j\Phi_t} \sum_{k=0}^{L-1} m[k] e^{j2\pi F_{sw}kT_s} e^{-j2\pi F_{sw}kT_s} \\
&\quad + \frac{\widehat{m}_{\text{tag}}}{2} e^{j\widehat{\theta}_{\text{tag}}} e^{-j\Phi_t} \underbrace{\sum_{k=0}^{L-1} m[k] e^{-j2\pi 2F_{sw}kT_s}}_{\approx 0, \text{ (Eq. (3.14))}} + n^+ \\
&= \frac{\widehat{m}_{\text{tag}}}{2} e^{j\widehat{\theta}_{\text{tag}}} e^{j\Phi_t} \sum_{k=0}^{L-1} m[k] + n^+. \tag{3.17}
\end{aligned}$$

The same reasoning (based on Eq. (3.14)) as with  $H_0$  is applied to the above equation, so as to eliminate the DSI terms. The output  $r^-$  of second correlator can be calculated in a similar manner:

$$r^-|H_1 = \frac{\widehat{m}_{\text{tag}}}{2} e^{j\widehat{\theta}_{\text{tag}}} e^{-j\Phi_t} \sum_{k=0}^{L-1} m[k] + n^-. \tag{3.18}$$

### Correlator Outputs-SBPSK

Using the SBPSK modulation at the tag, exploiting the same correlation structure and following the same procedure as with PFSK, under hypothesis  $H_i$ ,  $i \in \{0, 1\}$ , the output of  $r^+$  becomes:

$$\begin{aligned}
r^+|H_i &= h_d \underbrace{\sum_{k=0}^{L-1} m[k] e^{-j2\pi F_{sw}kT_s}}_{\approx 0, \text{ (Eq. (3.14))}} + \frac{\widehat{m}_{\text{tag}}}{2} e^{j\widehat{\theta}_{\text{tag}}} e^{j\Phi_t} e^{j\Phi_i} \sum_{k=0}^{L-1} m[k] e^{j2\pi F_{sw}kT_s} e^{-j2\pi F_{sw}kT_s} \\
&\quad + \frac{\widehat{m}_{\text{tag}}}{2} e^{j\widehat{\theta}_{\text{tag}}} e^{-j\Phi_t} e^{-j\Phi_i} \underbrace{\sum_{k=0}^{L-1} m[k] e^{-j4\pi F_{sw}kT_s}}_{\approx 0, \text{ (Eq. (3.14))}} + n^+ \\
&= \frac{\widehat{m}_{\text{tag}}}{2} e^{j\widehat{\theta}_{\text{tag}}} e^{j\Phi_t} e^{j\Phi_i} \sum_{k=0}^{L-1} m[k] + n^+, \tag{3.19}
\end{aligned}$$

Calculation of  $r^-$  for the SBPSK case, can be performed in a similar manner:

$$r^-|H_i = \frac{\widehat{m}_{\text{tag}}}{2} e^{j\widehat{\theta}_{\text{tag}}} e^{-j\Phi_t} e^{-j\Phi_i} \sum_{k=0}^{L-1} m[k] + n^-. \tag{3.20}$$

### 3.4 Detection Algorithms

Depending on the amount of information available for the ambient carrier (and the rest of the involved parameters), coherent, partially coherent or even fully noncoherent detection can be applied. Under certain assumptions, PFSK can be utilized for adopting a coherent detection scheme at the receiver, while SBPSK can operate in conjunction with partially coherent detection. SBPSK can also operate with fully noncoherent detection under certain assumptions.

#### 3.4.1 Coherent Detection

##### a) Assumptions

Using Eqs. (3.16) – (3.18), the correlators' output for the  $n^{\text{th}}$  bit at the receiver, when adopting PFSK modulation at the tag, can also take the following form:

$$\begin{aligned} r_n^+ | \mathbf{H}_1 &= \gamma e^{j\Phi_t} \mu_c^{(n)} + n^+, & r_n^+ | \mathbf{H}_0 &= n^+, \\ r_n^- | \mathbf{H}_1 &= \gamma e^{-j\Phi_t} \mu_c^{(n)} + n^-, & r_n^- | \mathbf{H}_0 &= n^-, \end{aligned} \quad (3.21)$$

where  $\gamma = \frac{\widehat{m}_{\text{tag}}}{2} e^{j\widehat{\theta}_{\text{tag}}} \in \mathbb{C}$  and  $\mu_c^{(n)} = \sum_{k=0}^{L-1} \mathbf{m}[k] \in \mathbb{C}$ .<sup>1</sup> It is assumed that the wireless and tag related parameters remain constant for the duration of a few bits. More specifically, the compound parameter  $\gamma$ , remains constant for  $N_p$  bits/integration slots. The same holds for the tag-related phase  $\Phi_t$ , which has been observed to vary only between successive packet transmissions. Mathematical definitions in Eq. (3.21), correspond to studying bits within a packet. Thus, index  $n$  is omitted from  $\gamma$ .

In the general case,  $\mathbf{m}[k]$  is modulated and unknown. Thus, the parameter  $\mu_c^{(n)}$ , is unknown and varies among successive bits, which is the reason for including the index  $n$  in its notation. However, there may be cases, where the structure of  $\mathbf{m}[k]$  allows for the parameter  $\mu_c^{(n)}$  to be considered invariant for a number of consecutive bits.

A case allowing for such consideration can be the case of a constant-envelope modulated, ambient signal. In such case,  $\mathbf{m}[k] = A_c e^{j\phi_c[k]}$ , i.e., while the amplitude  $A_c$  of the signal is constant, its phase  $\phi_c[k]$  varies with time. Given a large  $L$  and representing the samples of  $\phi_c[k]$  as samples drawn from a random variable  $\phi_c$ , the law of large numbers (LLN) can be exploited so as to end up with the following:

$$\mu_c^{(n)} = \sum_{k=0}^{L-1} \mathbf{m}[k] = A_c \sum_{k=0}^{L-1} e^{j\phi_c[k]} = LA_c \frac{1}{L} \sum_{k=0}^{L-1} e^{j\phi_c[k]} \approx LA_c \mathbb{E}[e^{j\phi_c}]. \quad (3.22)$$

<sup>1</sup>For each bit  $n$ , index  $k$  represents the (sample) offset from the beginning of that bit.

Given the narrowband assumption for  $\mathbf{m}[k]$ , it can be assumed that  $\mathbb{E}[\mathbf{e}^{j\phi_c}]$  will not vary for a number of consecutive bits and  $\mu_c^{(n)} \Rightarrow \mu_c \triangleq LA_c \mathbb{E}[\mathbf{e}^{j\phi_c}]$  for the duration of a packet. Thus, exact information ( $\mathbf{m}[k]$ ) from the ambient illuminator does not need to be estimated (for analog ambient illuminator) or detected (for digital ambient illuminator), as long as the sum in Eq. (3.22) remains constant throughout the tag-backscattered packet.

### b) Statistics

For the  $n^{\text{th}}$  bit  $i_n \in \{0, 1\}$ , Eq. (3.21) can be expressed in a vector form as follows:

$$\mathbf{r}_n | H_{i_n} = \begin{bmatrix} r_n^+ \\ r_n^- \end{bmatrix} = \gamma \mu_c \begin{bmatrix} \mathbf{e}^{j\Phi_t} \\ \mathbf{e}^{-j\Phi_t} \end{bmatrix} i_n + \begin{bmatrix} n_n^+ \\ n_n^- \end{bmatrix} = \boldsymbol{\mu}_r i_n + \mathbf{n}_n, \quad \boldsymbol{\mu}_r = \gamma \mu_c \begin{bmatrix} \mathbf{e}^{j\Phi_t} \\ \mathbf{e}^{-j\Phi_t} \end{bmatrix}. \quad (3.23)$$

Given that  $n^\pm \sim \mathcal{CN}(0, L\sigma_n^2)$  (See Eq. (3.16)),  $\mathbf{r}_n$  can be statistically described as follows [55]:

$$\begin{aligned} \mathbf{r}_n | H_0 &\sim \mathcal{CN}(\mathbf{0}_2, L\sigma_n^2 \mathbf{I}_2), \\ \mathbf{r}_n | H_1, \boldsymbol{\mu}_r &\sim \mathcal{CN}(\boldsymbol{\mu}_r, L\sigma_n^2 \mathbf{I}_2), \end{aligned} \quad (3.24)$$

### c) ML Detection

Given perfect information about parameter  $\boldsymbol{\mu}_r$  and equiprobable signaling, the symbol-by-symbol, BER-optimal maximum likelihood (ML) detector is given by [51]:

$$\mathcal{L}(\mathbf{r}) = \frac{f_{\mathbf{r}|H_1, \boldsymbol{\mu}_r}(\mathbf{r}|H_1, \boldsymbol{\mu}_r)}{f_{\mathbf{r}|H_0}(\mathbf{r}|H_0)} \stackrel{H_1}{\geq} 1. \quad (3.25)$$

According to Eq. (3.24), the above can be easily simplified to:

$$\|\mathbf{r} - \boldsymbol{\mu}_r\|_2^2 \stackrel{H_1}{\leq} \|\mathbf{r}\|_2^2 \quad (3.26)$$

As it will be shown in Sec. 3.6.3, in cases (e.g., standard BPSK) where the sum of Eq. (3.22) attains values close to zero, the detector will offer high bit error rates. In the case that the sum is approximately zero, the parameter  $\boldsymbol{\mu}_r$  will also be approximately zero and the detector will not work effectively.

### d) Analytical Probability of Error

If the channel fading parameters ( $a_{CT} = |h_{CT}|$ ,  $a_{TR} = |h_{TR}|$ ) are Rayleigh distributed, it can be easily shown that the total probability of error of the detector in Eq. (3.26), is

given by:

$$\Pr(e) = \mathbb{E}_{|\tilde{\mu}_c|} \left[ \Pr(e | |\tilde{\mu}_c|) \right] = \mathbb{E}_{|\tilde{\mu}_c|} \left[ \mathbf{Q} \left( \frac{|\tilde{\mu}_c|}{\sqrt{L\sigma_n^2}} \right) \right] \stackrel{(a)}{=} \frac{1}{2} - \frac{\sqrt{\pi}}{4} U \left( \frac{1}{2}, 0, \frac{2}{\text{SNR}} \right), \quad (3.27)$$

where  $\tilde{\mu}_c = \gamma\mu_c$  and  $\mathbf{Q}(\cdot)$  is the Q-function [56]. SNR is the average signal-to-noise ratio, defined as follows [57]:

$$\text{SNR} = \frac{\mathbb{E}[|\tilde{\mu}_c|^2]}{L\sigma_n^2}. \quad (3.28)$$

In Eq. (3.27),  $U(\cdot, \cdot, \cdot)$  is the confluent hypergeometric function [58, Eq. (13.4.4)]. Point (a) involves calculating the expectation of  $\mathbf{Q} \left( \frac{|\tilde{\mu}_c|}{\sqrt{L\sigma_n^2}} \right)$  over the product of Rayleigh distributed r.v.s  $a_{\text{CT}}, a_{\text{TR}}$ . Analytical derivation of the expression can be found in [9, App. II].

### e) Estimation of $\boldsymbol{\mu}_r$

The detector of Eq. (3.26) requires knowledge of  $\boldsymbol{\mu}_r$  for its operation. As already stated, parameter  $\boldsymbol{\mu}_r$  is assumed constant through the transmission of  $N_p$  bits. Thus, a portion of the total  $N_p$  tag-backscattered bits, the first  $N_{\text{tr}}$  bits, can be allocated as a training sequence for estimation of  $\boldsymbol{\mu}_r$ .

By vertically concatenating all the correlators' (Eq. (3.23)) vectors corresponding to the first  $N_{\text{tr}}$  bits, the vector  $\mathbf{r}_{\text{tr}}$  can be defined as:

$$\mathbf{r}_{\text{tr}} = \begin{bmatrix} \mathbf{r}_1 \\ \mathbf{r}_2 \\ \vdots \\ \mathbf{r}_{N_{\text{tr}}} \end{bmatrix} = \begin{bmatrix} i_1 \mathbf{I}_2 \\ i_2 \mathbf{I}_2 \\ \vdots \\ i_{N_{\text{tr}}} \mathbf{I}_2 \end{bmatrix} \boldsymbol{\mu}_r + \begin{bmatrix} \mathbf{n}_1 \\ \mathbf{n}_2 \\ \vdots \\ \mathbf{n}_{N_{\text{tr}}} \end{bmatrix} = \mathbf{T} \boldsymbol{\mu}_r + \tilde{\mathbf{n}} \in \mathbb{C}^{2N_{\text{tr}}}, \quad (3.29)$$

where matrix  $\mathbf{T}$  is known to the receiver and  $\tilde{\mathbf{n}} \sim \mathcal{CN}(\mathbf{0}_{2N_{\text{tr}}}, L\sigma_n^2 \mathbf{I}_{2N_{\text{tr}}})$ .

Given  $\mathbf{T}$  and correlator samples  $\mathbf{r}_{\text{tr}}$ , an estimate  $\hat{\boldsymbol{\mu}}_{r,\text{ls}}$  of  $\boldsymbol{\mu}_r$  is given by solving the least squares (LS) problem:

$$\hat{\boldsymbol{\mu}}_{r,\text{ls}} = \arg \min_{\boldsymbol{\mu}_r \in \mathbb{C}^2} \|\mathbf{r}_{\text{tr}} - \mathbf{T} \boldsymbol{\mu}_r\|_2^2. \quad (3.30)$$

Setting the respective gradient of Eq. (3.30) equal to zero, the LS-solution takes the form [49, pp. 521]:

$$\hat{\boldsymbol{\mu}}_{r,\text{ls}} = (\mathbf{T}^H \mathbf{T})^{-1} \mathbf{T}^H \mathbf{r}_{\text{tr}}. \quad (3.31)$$

With an estimate  $\hat{\boldsymbol{\mu}}_{r,ls}$  of  $\boldsymbol{\mu}_r$  available, ML detection can be applied using the detector of Eq. (3.26).

### 3.4.2 Partially Coherent Detection

#### a) Assumptions

For coherent detection, a certain structure was assumed for  $\mathbf{m}[k]$ . Additionally, it was assumed that the averaging operation resulting from the correlation, lead to considering parameter  $\mu_c$  constant for a number of consecutive bits. While the aforementioned assumptions are applicable for a number of scenarios (e.g., exploiting ambient FM signals for illumination), they do not cover the problem in the general case, where  $\mathbf{m}[k]$  is unknown and no assumptions for  $\mu_c^{(n)}$  can be safely made.

SBPSK will be exploited in order to derive an illumination-agnostic detector. Similarly to PFSK, using Eqs. (3.19) – (3.20), the correlators' outputs for when SBPSK is utilized at the tag, can take for the  $n^{\text{th}}$  bit  $i_n \in \{0, 1\}$ , the following form:

$$\begin{aligned} r_{s,n}^+ &= \gamma e^{j(\Phi_t + \Phi_{i_n})} \mu_c^{(n)} + n_n^+, \\ r_{s,n}^- &= \gamma e^{-j(\Phi_t + \Phi_{i_n})} \mu_c^{(n)} + n_n^-. \end{aligned} \quad (3.32)$$

Eq. (3.32) can be re-expressed in a more compact, vector form as follows:

$$\mathbf{r}_{s,n} = \begin{bmatrix} r_{s,n}^+ \\ r_{s,n}^- \end{bmatrix} = \tilde{\mu}_c^{(n)} \begin{bmatrix} e^{j(\Phi_t + \Phi_{i_n})} \\ e^{-j(\Phi_t + \Phi_{i_n})} \end{bmatrix} + \begin{bmatrix} n_n^+ \\ n_n^- \end{bmatrix} = \tilde{\mu}_c^{(n)} \mathbf{x}_{i_n}(\Phi_t) + \mathbf{n}_n \in \mathbb{C}^2, \quad (3.33)$$

where  $\tilde{\mu}_c^{(n)} = \gamma \mu_c^{(n)} \in \mathbb{C}$ . The average SNR is then defined as follows [57]:

$$\text{SNR} = \frac{\mathbb{E}[|\tilde{\mu}_c^{(n)}|^2]}{L\sigma_n^2}. \quad (3.34)$$

#### b) Statistics

Given perfect knowledge of  $\tilde{\mu}_c^{(n)}$ ,  $\Phi_t$ , based on the distribution of noise  $\mathbf{n}_n$  (see below Eq. (3.23)), the statistical description of Eq. (3.33) is:

$$\mathbf{r}_{s,n} | \mathbf{H}_{i_n}, \tilde{\mu}_c^{(n)}, \Phi_t \sim \mathcal{CN}(\tilde{\mu}_c^{(n)} \mathbf{x}_{i_n}(\Phi_t), \tilde{\sigma}_n^2 \mathbf{I}_2), \quad (3.35)$$

where  $\tilde{\sigma}_n^2 = L\sigma_n^2$ . The PDF of  $\mathbf{r}_{s,n}$  can be then defined as follows [49, pp. 504]:

$$\mathbf{f}_{\mathbf{r}_{s,n}|\mathbf{H}_{i_n}, \tilde{\mu}_c^{(n)}, \Phi_t}(\mathbf{r}_{s,n}|\mathbf{H}_{i_n}, \tilde{\mu}_c^{(n)}, \Phi_t) = \frac{1}{\pi^2 \tilde{\sigma}_n^4} e^{-\frac{1}{\tilde{\sigma}_n^2} \|\mathbf{r}_{s,n} - \tilde{\mu}_c^{(n)} \mathbf{x}_{i_n}(\Phi_t)\|_2^2}. \quad (3.36)$$

### c) Partially Coherent, Uncoded, Detection

If variables  $\tilde{\mu}_c^{(n)}$  were known, the BER-optimal detector, given equiprobable signaling, would be the ML detector.  $\Phi_t$ , as stated earlier is considered random, but constant through the duration of a packet, thus it is possible to estimate it using a known training sequence within the packet. Unlike  $\Phi_t$ ,  $\tilde{\mu}_c^{(n)}$  contains information from the ambient carrier<sup>2</sup> and in the general case, varies between successive bits. Thus, a training sequence can not be used, and coherent detection can not be applied.

To overcome this problem, generalized likelihood ratio test (GLRT) will be utilized in the same way as in [41], while (in contrast to [41]) considering a modulated carrier and a different modulation scheme at the tag.  $\tilde{\mu}_c^{(n)}$  is considered an unknown parameter and maximization of Eq. (3.36) over that parameter will be performed. Thus, using the above, the log decision rule becomes [55, pp. 200]:

$$\mathcal{L}_G(\mathbf{r}_{s,n}) = \frac{\max_{\tilde{\mu}_c^{(n)}} \ln \left[ \mathbf{f}_{\mathbf{r}_{s,n}|\mathbf{H}_1, \tilde{\mu}_c^{(n)}, \Phi_t}(\mathbf{r}_{s,n}|\mathbf{H}_1, \tilde{\mu}_c^{(n)}, \Phi_t) \right]}{\max_{\tilde{\mu}_c^{(n)}} \ln \left[ \mathbf{f}_{\mathbf{r}_{s,n}|\mathbf{H}_0, \tilde{\mu}_c^{(n)}, \Phi_t}(\mathbf{r}_{s,n}|\mathbf{H}_0, \tilde{\mu}_c^{(n)}, \Phi_t) \right]} \stackrel{\mathbf{H}_1}{\geq} 1. \quad (3.37)$$

It can be easily shown (see Sec. 8.1) that the aforementioned decision rule can be simplified to the following expression:

$$i_n = \arg \max_{i_n \in \{0,1\}} |\mathbf{r}_n^H \mathbf{x}_{i_n}(\Phi_t)|^2, \quad (3.38)$$

which can also take the following form (Sec. 8.1):

$$\begin{aligned} & \Re \left\{ \left( r_{s,n}^+ \right)^* \left( r_{s,n}^- \right) e^{j2(\Phi_t + \Phi_1)} \right\} \stackrel{\mathbf{H}_1}{\geq} \Re \left\{ \left( r_{s,n}^+ \right)^* \left( r_{s,n}^- \right) e^{j2(\Phi_t + \Phi_0)} \right\} \\ \Leftrightarrow & \Re \left\{ e^{j\theta_{p,n}} e^{j2(\Phi_t + \Phi_0)} \left( e^{j2\Delta\phi} - 1 \right) \right\} \stackrel{\mathbf{H}_1}{\geq} 0, \end{aligned} \quad (3.39)$$

---

<sup>2</sup>Additionally  $\tilde{\mu}_c^{(n)}$  contains wireless channel and tag related parameters, which, as already stated, can be considered constant for the duration of a packet.

where  $|r_{p,n}|e^{j\theta_{p,n}} = (r_{s,n}^+)^* (r_{s,n}^-)$ . If  $\Phi_0 = 0$  and  $\Delta\phi = \frac{\pi}{2}$  are chosen, the decision rule of Eq. (3.39) can be expressed as:

$$\cos(2\Phi_t + \theta_{p,n}) \stackrel{H_1}{\leq} 0. \quad (3.40)$$

The detector of Eq. (3.40) demonstrates that given  $\Phi_t$ , detection can be performed without *any* information regarding the ambient carrier. The detector is partially coherent due to the need for the tag-related phase  $\Phi_t$ .

#### d) Estimation of $\Phi_t$

In order for the detector of Eq. (3.40) to offer a decision,  $\Phi_t$  is necessary. A heuristic estimation scheme utilizing a number of training bits at the start of the packet will be used. Assuming that a single, “0”-valued training bit is used and ignoring the noise, the noiseless output of the correlators is given by:

$$r_1^+ = \tilde{\mu}_c^{(1)} e^{j\Phi_t}, \quad r_1^- = \tilde{\mu}_c^{(1)} e^{-j\Phi_t}. \quad (3.41)$$

The product  $r_1^+ (r_1^-)^*$  is considered, which results to  $r_1^+ (r_1^-)^* = |\tilde{\mu}_c^{(1)}|^2 e^{j2\Phi_t}$  and  $2\hat{\Phi}_t = \angle r_1^+ (r_1^-)^*$ . In the case where  $N_{\text{tr}}$ , zero-valued, training bits are available, two  $1 \times N_{\text{tr}}$  vectors are formed:  $\mathbf{r}_{1:N_{\text{tr}}}^+ = [r_1^+ r_2^+ \dots r_{N_{\text{tr}}}^+]$  and  $\mathbf{r}_{1:N_{\text{tr}}}^- = [r_1^- r_2^- \dots r_{N_{\text{tr}}}^-]$ . Then the estimate of  $2\Phi_t$  is evaluated as  $2\hat{\Phi}_t = \angle \mathbf{r}_{1:N_{\text{tr}}}^+ (\mathbf{r}_{1:N_{\text{tr}}}^-)^H$ . To avoid phase ambiguity issues, estimate  $2\hat{\Phi}_t$  is directly used in the detector of Eq. (3.40) (or Eq. (3.39), in place of  $2\Phi_t$ ).

#### e) Partially Coherent, Coded Detection

Due to the variation of  $\tilde{\mu}_c^{(n)}$  among consecutive bits, a form of “natural” interleaving is offered. Thus, a channel code can be utilized to increase the bit error rate performance. However, to conform to the ultra-low-power constraints, the utilized code should be a short-block code.

The tag is assumed to utilize an error correcting code  $\mathcal{C}$ . Each sequence of  $k$  bits is mapped by the code to a new, coded sequence  $\mathbf{c} \in \mathcal{C}$  of  $N_c$  bits. When such coded transmission is utilized, in the same way as presented in [41], the following decision rule can be utilized:

$$\hat{\mathbf{c}} = \arg \max_{\mathbf{c} \in \mathcal{C}} \left\{ \max_{\tilde{\mu}_c \in \mathbb{C}^{N_c}} \ln \left[ \mathbf{f}_{\mathbf{r}_{s,1:N_c} | \mathbf{c}, \tilde{\mu}_c, \Phi_t} (\mathbf{r}_{s,1:N_c} | \mathbf{c}, \tilde{\mu}_c, \Phi_t) \right] \right\}, \quad (3.42)$$

where  $\tilde{\boldsymbol{\mu}}_c = [\tilde{\mu}_c^{(1)} \tilde{\mu}_c^{(2)} \dots \tilde{\mu}_c^{(N_c)}]^T$  and:

$$\mathbf{r}_{s,1:N_c} = \begin{bmatrix} \mathbf{r}_{s,1} \\ \mathbf{r}_{s,2} \\ \vdots \\ \mathbf{r}_{s,N_c} \end{bmatrix} = \begin{bmatrix} \tilde{\mu}_c^{(1)} \mathbf{x}_1(\Phi_t) \\ \tilde{\mu}_c^{(2)} \mathbf{x}_2(\Phi_t) \\ \vdots \\ \tilde{\mu}_c^{(N_c)} \mathbf{x}_{N_c}(\Phi_t) \end{bmatrix} + \begin{bmatrix} \mathbf{n}_1 \\ \mathbf{n}_2 \\ \vdots \\ \mathbf{n}_{N_c} \end{bmatrix}. \quad (3.43)$$

Assuming that variables  $\tilde{\mu}_c^{(1)} \dots \tilde{\mu}_c^{(N_c)}$  are independent and exploiting the conditional independence of each  $\mathbf{r}_{s,n}$  (given  $\mathbf{c}$ ,  $\tilde{\mu}_c^{(n)}$  and  $\Phi_t$ ) the right-most maximization in Eq. (3.42) can be expressed as follows:

$$\begin{aligned} \max_{\tilde{\boldsymbol{\mu}}_c \in \mathbb{C}^{N_c}} \ln \left[ \mathbf{f}_{\mathbf{r}_{s,1:N_c} | \mathbf{c}, \tilde{\boldsymbol{\mu}}_c, \Phi_t}(\mathbf{r}_{s,1:N_c} | \mathbf{c}, \tilde{\boldsymbol{\mu}}_c, \Phi_t) \right] &= \sum_{n=1}^{N_c} \max_{\tilde{\mu}_c^{(n)}} \ln \left[ \mathbf{f}_{\mathbf{r}_{s,n} | H_{c_n}, \tilde{\mu}_c^{(n)}, \Phi_t}(\mathbf{r}_{s,n} | H_{c_n}, \tilde{\mu}_c^{(n)}, \Phi_t) \right] \\ &\stackrel{(a)}{=} \sum_{n=1}^{N_c} 2 \ln \left( \frac{1}{\pi \tilde{\sigma}_n^2} \right) - \frac{1}{2 \tilde{\sigma}_n^2} \|\mathbf{r}_{s,n}\|_2^2 + \frac{1}{\tilde{\sigma}_n^2} \Re \left\{ (r_{s,n}^+)^* (r_{s,n}^-) e^{j2(\Phi_t + \Phi_{c_n})} \right\}, \quad c_n \in \{0, 1\}, \end{aligned} \quad (3.44)$$

where in (a), results from Sec. 8.1 were utilized. Following the same method as in [41, Sec.III-C], Eq. (3.44) can be expressed as follows:

$$\begin{aligned} \sum_{n=1}^{N_c} \max_{\tilde{\mu}_c^{(n)}} \ln \left[ \mathbf{f}_{\mathbf{r}_{s,n} | H_{c_n}, \tilde{\mu}_c^{(n)}, \Phi_t}(\mathbf{r}_{s,n} | H_{c_n}, \tilde{\mu}_c^{(n)}, \Phi_t) \right] &= \sum_{n=1}^{N_c} K^{(n)} + (1 - c_n) \Lambda_0^{(n)} + c_n \Lambda_1^{(n)} \\ &= \sum_{n=1}^{N_c} K^{(n)} + \Lambda_0^{(n)} + c_n (\Lambda_1^{(n)} - \Lambda_0^{(n)}), \end{aligned} \quad (3.45)$$

where  $K^{(n)} = 2 \ln \left( \frac{1}{\pi \tilde{\sigma}_n^2} - \frac{1}{2 \tilde{\sigma}_n^2} \|\mathbf{r}_{s,n}\|_2^2 \right)$  and:

$$\Lambda_{c_n}^{(n)} = \frac{1}{\tilde{\sigma}_n^2} \Re \left\{ (r_{s,n}^+)^* (r_{s,n}^-) e^{j2(\Phi_t + \Phi_{c_n})} \right\}. \quad (3.46)$$

Neglecting the terms that do not affect the left-most maximization in Eq. (3.42), assuming  $\Phi_0 = 0$ ,  $\Delta\phi = \frac{\pi}{2}$  and exploiting Eq. (3.45), after calculations, the decision rule of Eq. (3.42) becomes:

$$\hat{\mathbf{c}} = \arg \max_{\mathbf{c} \in \mathcal{C}} \sum_{n=1}^{N_c} w_n c_n, \quad (3.47)$$

where  $w_n = -|r_{p,n}| \cos(2\Phi_t + \theta_{p,n})$  and  $|r_{p,n}| e^{j\theta_{p,n}} = (r_{s,n}^+)^* (r_{s,n}^-)$ .

### 3.4.3 Noncoherent Detection

The detector of Eq. (3.40), requires  $\Phi_t$ . As stated earlier, phase  $\Phi_t$  is considered random but *constant* throughout the transmission of a specific number of bits. Thus, multiple bits are affected by the same value of  $\Phi_t$ .

As shown earlier, when signal processing using correlators is applied to the received signal, under certain assumptions for the illuminating signal, coherent detection can be utilized with PFSK. The feasibility of coherent detection (under, e.g., FM illumination), dictates that throughout a certain number of bits, the parameters affecting the tag's signal, including the illuminating signal, do not vary significantly. Thus, correlation is introduced between the received statistics. Having stated the above and assuming that the wireless channel parameters also remain constant for a specific number of bits, sequence based detection techniques may be applied, using SBPSK.

The following steps are performed to achieve noncoherent detection.

1. The receiver uniformly samples the range  $(0, \dots, 2\pi]$  and acquires  $M$  values for  $\Phi_t$ , namely  $\tilde{\Phi}_{t,1}, \tilde{\Phi}_{t,2}, \dots, \tilde{\Phi}_{t,M}$ .
2. For each sampled phase  $\tilde{\Phi}_{t,k}$ ,  $k \in \{1, \dots, M\}$ , using the detector of Eq. (3.38), symbol-by-symbol detection is performed for  $N_p$  bits. That way a total of  $M$   $N_p$ -bit sequences are generated. The  $k$ th sequence is acquired as follows:

$$\begin{aligned} i_1^k &= \arg \max_{i \in \{0,1\}} |\mathbf{r}_1^H \mathbf{x}_i(\tilde{\Phi}_{t,k})|^2, \\ &\vdots \\ i_{N_p}^k &= \arg \max_{i \in \{0,1\}} |\mathbf{r}_{N_p}^H \mathbf{x}_i(\tilde{\Phi}_{t,k})|^2. \end{aligned} \quad (3.48)$$

3. For each one of the  $M$  resulting sequences, receiver stores the value of metric  $\delta_k = |\mathbf{r}_{1:N_p}^H \mathbf{x}_{\mathbf{i}^k}(\tilde{\Phi}_{t,k})|$ , where vector definitions follow:

$$\mathbf{r}_{1:N_p} = [\mathbf{r}_1^T \ \mathbf{r}_2^T \ \dots \ \mathbf{r}_{N_p}^T]^T \in \mathbb{C}^{2N_p}, \quad (3.49)$$

$$\mathbf{x}_{\mathbf{i}^k}(\tilde{\Phi}_{t,k}) = [\mathbf{x}_{i_1^k}^T(\tilde{\Phi}_{t,k}) \ \dots \ \mathbf{x}_{i_{N_p}^k}^T(\tilde{\Phi}_{t,k})]^T \in \mathbb{C}^{2N_p}. \quad (3.50)$$

4. As a final step, receiver selects the sequence  $\mathbf{i}^{k^*} = [i_1^{k^*}, \dots, i_{N_p}^{k^*}]$ , which satisfies:

$$k^* = \arg \max_{k \in \{1, \dots, M\}} \{\delta_k\}. \quad (3.51)$$

### 3.5 Performance Evaluation

The performance of the suggested ambient backscatter, digital communication methods was evaluated through simulations. Both PFSK and SBPSK were tested with respect to the achievable BER as a function of the received SNR. The two modulation schemes were also compared to each other.

Channel coefficients were created such that  $h_q \sim \mathcal{CN}(0, 1)$ ,  $q \in \{\text{CR}, \text{CT}, \text{TR}\}$ , corresponding to Rayleigh fading parameters  $a_q$  with  $\mathbb{E}[a_q^2] = 1$ . It is noted that while for the CR, CT links Rayleigh fading is a reasonable assumption, given the fact that the tag is located near the receiver (due to the significant attenuation), in the context of a typical ambient backscatter setup, Rayleigh fading represents a worst-case scenario for the TR link.

#### a) PFSK Performance

Bitrate and sampling rate were set to  $R = 1$  kbps and  $F_s = 2$  MHz, respectively, resulting to  $L = 2000$ . Packet size was fixed at  $N_p = 100$  bits. Tag RF-related parameters were set to  $\Gamma_0 = 1$ ,  $\Gamma_1 = -1$ ,  $A_s = 0.6047 + j0.5042$  and scattering efficiency of  $s = \sqrt{0.1}$  was assumed. Station's received RF power was set to  $P_c = -40$  dBm. Stations' information signal  $\phi(t)$  was modeled as a zero mean Gaussian process, which is in compliance with modeling performed for FM analysis (see e.g., [47], Chap. 4); phase samples  $\phi[k]$  are IID and are drawn from  $\mathcal{N}(0, P_\phi)$ , where  $P_\phi$  is the average power of signal  $\phi(t)$ , set to  $P_\phi = 1$ . Utilizing the aforementioned assumption:

$$\mathbb{E}[e^{j\phi}] = M_\phi(j) = e^{-\frac{P_\phi}{2}}, \quad (3.52)$$

where  $M_\phi(\nu j) = e^{-\frac{\nu^2 P_\phi}{2}}$  is the characteristic function of  $\phi$  (see Sec. 8.3.1). Monte Carlo experiments were performed using a total of 1.5 million bits per SNR value.

Fig. 3.4-Left quantifies the BER performance of the coherent detector. It can be seen that the analytical BER of Eq. (3.27) matches simulation results of Eq. (3.26), under perfect channel state information (CSI). It can also be observed that under perfect CSI, compared to  $N_{\text{tr}} = 4$  ( $N_{\text{data}} = 96$ ), the detector offers a performance gain of  $\sim 2$  dB, compared to using the estimated channel. Allocating more bits for channel estimation purposes, lowers the difference between the ML-detector with perfect CSI and the ML detector using the channel estimate. Specifically, for the chosen values and for 6 more training bits (6 less data bits/packet) the difference drops from  $\sim 2$  dB to  $\sim 1$  dB.

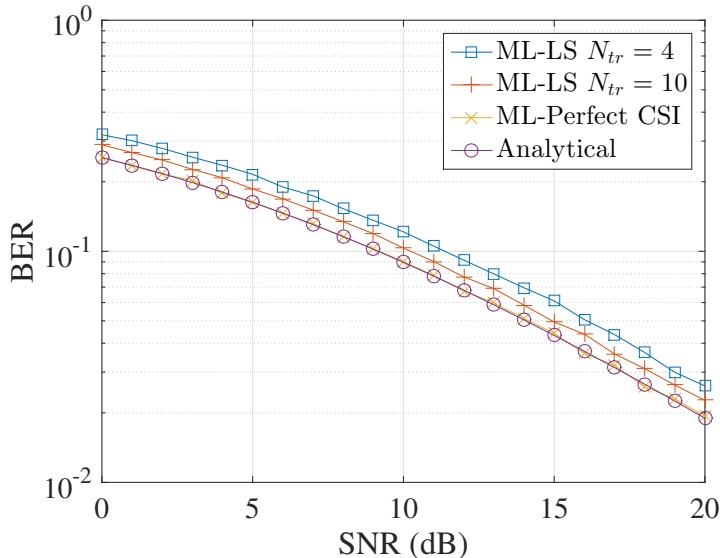


Figure 3.4: BER of PFSK scheme vs average received SNR, for Rayleigh fading.

### b) SBPSK Performance

The same parameters as with PFSK evaluation (see previous section) were used (except for  $R = 0.5$  kbps). Due to the detector being illumination-agnostic, in the context of simulations it was assumed that  $\mathbf{m}[k] \sim \mathcal{CN}(0, P_a)$  with  $P_a = 1$  and the SNR was defined as per Eq. (3.34), with  $\mathbb{E}[|\mu_c^{(n)}|^2] = LP_a$ . It is noted that the derivation of SBPSK detectors does not assume any information (besides assumption of Eq. (3.14)) regarding the ambient carrier.

Complex normal illumination is considered only for simulation purposes to ensure an independently and continuously varying, ambient signal. The detector has also been successfully tested, when the illuminator adopts MSK, BPSK, QPSK or FM modulations (see Sec. 3.6). For the coded case, BCH code was used with codeword length  $N_c = 31$  and uncoded word length  $k = 11$ . The wireless channel parameters were considered constant for the duration of  $N_c$  coded bits (except where otherwise noted).

Fig. 3.5 demonstrates the performance of the detector in Eq. (3.40), compared to ML detector utilizing full (and perfect) information regarding  $\tilde{\mu}_c^{(n)} \mathbf{x}_{i_n}(\Phi_t)$ . The partially coherent detector is also evaluated for the following cases: 1) available knowledge of  $\Phi_t$  and 2) estimate of  $\Phi_t$ ,  $\hat{\Phi}_t$ , for  $N_{tr} = 1, 5, 10$ . It can be observed that the partially coherent, illumination agnostic rule of Eq. (3.40) with perfect information regarding  $\Phi_t$ , offers 4 dB worst performance than the perfect CSI ML. When no information about  $\Phi_t$  is available, it is observed that for 10 training bits, the difference between the partially coherent rule utilizing perfect  $\Phi_t$  and the same rule using  $\hat{\Phi}_t$  instead, is approximately 0.5 dB. When

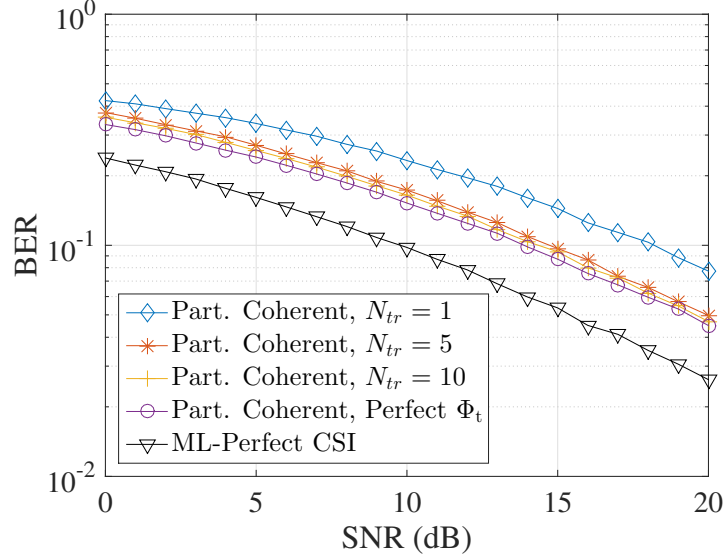


Figure 3.5: BER vs average received SNR for the SBPSK/partially coherent scheme, under Rayleigh fading, while  $\Phi_0 = 0$  and  $\Phi_1 = \frac{\pi}{2}$ .

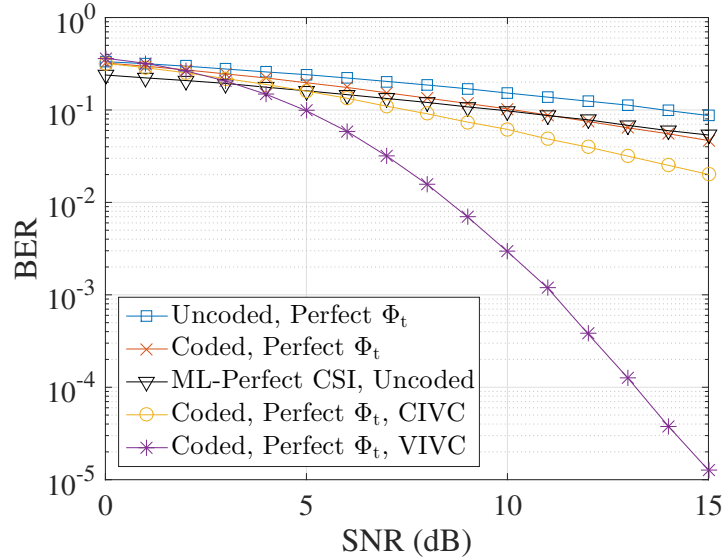


Figure 3.6: BER vs average received SNR utilizing (31, 11) BCH coding under Rayleigh fading for the partially coherent scheme with  $\Phi_0 = 0$  and  $\Phi_1 = \frac{\pi}{2}$ . CIVC denotes the case of packet-constant illumination-related parameter  $\mu_c$  with bit varying wireless channel parameters. VIVC denotes the case of varying both  $\mu_c^{(n)}$  and  $\gamma$  between successive bits. Complex normal illumination is assumed for the simulations.

1 training bit is used, the difference increases to  $\approx 4$  dB, resulting to an overall loss of 8 dB, compared to perfect CSI ML.

Fig. 3.6 shows the performance of the detector in Eq. (3.47). All depicted cases assume modulated illuminator. For the special case of CIVC explained below,  $\mu_c^{(n)}$  is assumed

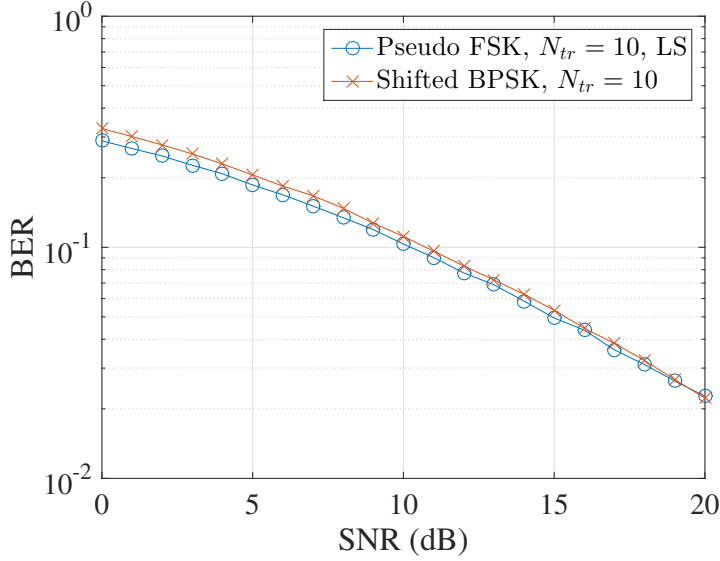


Figure 3.7: Comparison of the suggested digital modulation schemes.

constant for the duration of the tag packet (i.e.,  $\mu_c^{(n)} \equiv \mu_c$ ), while in all other cases, it changes across consecutive tag bits. It is clear that the detector for the coded case outperforms the detector used, when no coding is utilized. It is also observed that in the high SNR regime, the detector offers slightly better performance, compared to perfect CSI ML detector, when no coding is used.

Two cases are additionally demonstrated in Fig. 3.6, namely the case where both ambient signal parameter  $\mu_c^{(n)}$  and the wireless channels vary between successive bits (i.e.,  $\gamma \equiv \gamma^{(n)}$ ), which will be referred to as varying illuminator varying channel (VIVC) and the case where  $\mu_c^{(n)}$  remains constant during the packet but the channels vary among consecutive bits, resulting to varying  $\gamma$  (constant illuminator, varying channel-CIVC). In the last case,  $\mu_c^{(n)}$  was held constant for the duration of a packet (each bit within the same packet was affected by the same  $\mu_c$  value) while variables  $\mathbf{m}[k]$  were created as described earlier.

The performance gain offered when both parameters  $\mu_c^{(n)}, \gamma$  ( $\gamma^{(n)}$ ) vary between successive bits, is the result of the channel code being fully utilized. Constant wireless channel parameters during the transmission of multiple bits may introduce correlation between the received statistics. Thus the code may not be able to offer its best performance. When the ambient carrier's parameter  $\mu_c^{(n)}$  remains constant for the duration of the packet while the channels vary (CIVC), the same reasoning can be applied. Interestingly, Fig. 3.6 shows that modulation at the ambient signal assists the coded sequence detector of tag's information and radically improves performance, even though the sequence detector requires minimal information.

### c) SBPSK vs PFSK

In order to compare the two digital modulation schemes, the ambient carrier is assumed to be a constant envelope-modulated signal. In that way, both schemes can be compared in a fair manner, given that the proposed PFSK coherent detection is derived based on a constant envelope modulated signal, while SBPSK scheme can accept any modulated carrier as illuminating source (as long as Eq. (3.14) holds). Additionally, the same tag and wireless channel related parameters as well as bit rate ( $R = 1$  kbps) are assumed. The average received SNR is defined using Eq. (3.52), Eq. (3.34) (or, equivalently, Eq. (3.28)).

It can be seen in Fig. 3.7 that the fully coherent, PFSK scheme outperforms SBPSK, at the low SNR regime, for approximately 1 dB. As the SNR increases, the gap between the two schemes decreases, while for SNR  $\simeq 20$  dB, the gap vanishes. This behaviour may be explained by the fact that the estimation method for  $\Phi_t$  in the partially coherent SBPSK scheme, is a heuristic based on the assumption of the absence of noise. Additionally, the heuristic estimation used for partially coherent detection in SBPSK, only deals with  $\Phi_t$ , while the LS estimation used in coherent detection of PFSK, deals with the compound channel, which except  $\Phi_t$ , includes tag, wireless channel and ambient carrier related parameters, which are assumed constant for  $N_p$  bits (for the coherent PFSK scheme), thus able to be estimated through short training.

The performance of the fully noncoherent SBPSK detector, will be evaluated in the next section.

## 3.6 Comparison with State of The Art

To showcase the effectiveness of the proposed modulation and detection techniques, SBPSK will be compared against backscatter OOK-based detectors, offered by recent studies on the field of ambient backscatter communications.

Backscatter OOK is extensively used in the literature as it simplifies the derivation of detectors, while ignoring the structure of the underlying illuminating signal. The derivation of detectors for backscatter OOK, is usually performed by modelling the samples of the illuminating signal  $\mathbf{m}[k]$ , as samples of a circularly symmetric, complex normal distribution, i.e.,  $\mathbf{m}[k] \sim \mathcal{CN}(0, \sigma_c^2)$ . Explicitly assuming a certain structure for the illuminating signal (e.g., complex normal  $\mathbf{m}[k]$ ) can significantly limit the performance, in the case that a signal of a different structure is used for backscattering.

For deriving effective detectors it is important to take into account any information that is available regarding the ambient carrier. When no such information is available,

detector derivation should be made in a mathematically sound manner, i.e., without oversimplifications.

At the expense of limited performance, OOK significantly simplifies tag's implementation: for backscattering a bit, the tag's controller simply selects a load to terminate the tag's antenna throughout the bit duration. Besides simplifying implementation, compared to the switching schemes discussed in the previous sections, OOK requires less power for its operation.

### 3.6.1 Backscatter OOK

In the case of Backscatter OOK, for backscattering bit "0", the tag terminates its antenna at  $Z_0$  for the duration of the bit ( $T_{\text{bit}}$ ); for backscattering "1" the tag terminates its antenna at  $Z_1$  for the same duration. The two loads result in two reflection coefficients,  $\Gamma_0$ ,  $\Gamma_1$ , respectively. For the duration of bit  $i_n$ , the tag's signal can then take the following form:

$$\mathbf{x}_{\text{OOK}}^{i_n}(t) = A_s - \Gamma_{i_n}, \quad i_n \in \{0, 1\}, \quad (3.53)$$

Assuming  $\Gamma_0 = 0$  and  $\Gamma_1 = -1$  (as per the representative study in [14]), the received signal (after sampling, CFO cancellation and synchronization) for bit  $i_n$  can be described by the following, discrete baseband model [14, 59]:

$$y_{\text{OOK}}^{i_n}[k] = m[k] h_{i_n} + \mathbf{w}[k], \quad (3.54)$$

where  $\mathbf{w}[k] \sim \mathcal{CN}(0, \sigma_w^2)$ .  $h_{i_n}$  is defined as follows:

$$h_{i_n} = \begin{cases} \frac{1}{2} (h_{\text{CR}} + a_{\text{tag}} A_s), & i_n = 0, \\ \frac{1}{2} (h_{\text{CR}} + a_{\text{tag}} (A_s + 1)), & i_n = 1, \end{cases} \quad (3.55)$$

where  $a_{\text{tag}} = h_{\text{CT}} h_{\text{TR}}$ . One can infer the limited performance that an OOK scheme can offer by observing the signal model in Eqs. (3.54) – (3.55): the discrimination between the tag's states is only due to term  $A_s + 1$ .

### 3.6.2 OOK Detection

For the detection of OOK, detectors offered by a representative study [14] will be utilized. The samples  $m[k]$  of  $m(t)$ , are assumed to be drawn from a circularly symmetric complex Gaussian distribution, i.e.,  $m[k] \sim \mathcal{CN}(0, \sigma_c^2)$  [14], where  $\sigma_c^2$  denotes the ambient carrier's transmit power. Under the CN assumption and based on Eq. (3.54), two hypotheses

$H_0, H_1$  are formed [14]:

$$H_{i_n} : \mathbf{y}_{\text{OOK}}^{i_n} \sim \mathcal{CN}(0, \sigma_{i_n}^2 \mathbf{I}_L), \quad i_n \in \{0, 1\}, \quad (3.56)$$

where  $\mathbf{y}_{\text{OOK}}^{i_n} = [y_{\text{OOK}}^{i_n}[0], \dots, y_{\text{OOK}}^{i_n}[L-1]]^T$  and  $L$  is the oversampling factor, i.e.,  $L = T_{\text{bit}}/T_s$ . As it can be seen, the derivation of the detectors depends on the assumption of a carrier whose baseband samples are distributed according to a specific distribution. It will be shown in Sec. 3.6.3 that such an act limits the performance, when the said samples attain a different (than assumed) structure. Variances  $\sigma_{i_n}^2$  are given by:

$$\sigma_{i_n}^2 = |h_{i_n}|^2 \sigma_c^2 + \sigma_w^2. \quad (3.57)$$

Assuming perfect knowledge of parameters  $\sigma_{i_n}^2$ , the maximum likelihood (ML) detector takes the form of the following decision rule [14]:

$$\delta(\mathbf{y}_{\text{OOK}}) = Z \stackrel{H_0}{>} T_h^{\text{CG/ML}}, \quad \text{if } \sigma_0^2 > \sigma_1^2, \quad (3.58)$$

where  $Z = \|\mathbf{y}_{\text{OOK}}\|_2^2$  and threshold  $T_h^{\text{CG/ML}}$  is given by:

$$T_h^{\text{CG/ML}} = \frac{L \sigma_0^2 \sigma_1^2}{\sigma_1^2 - \sigma_0^2} \ln \frac{\sigma_1^2}{\sigma_0^2}. \quad (3.59)$$

In the case of  $\sigma_0^2 \leq \sigma_1^2$ , an inversion of the decision is performed, i.e.,  $1 - \delta(\mathbf{y}_{\text{OOK}})$ .

Authors of [14], also provide a second decision threshold that is derived under the assumption of a PSK illuminating source. Under the PSK assumption, the decision rule takes the form of Eq. (3.58) with, however, a different threshold [14]:

$$\tilde{T}_h^{\text{PSK}} = L \sigma_0 \sigma_1. \quad (3.60)$$

It can be seen that for both the aforementioned detection schemes, knowledge of  $\sigma_{i_n}^2$  is necessary. A method for estimating those parameters using a short training sequence is provided in [14] and is subsequently utilized in the purposes of comparison.

### 3.6.3 Results

Bit error rate (BER) was considered as the metric of interest. All results are offered using a sequence of  $N_{\text{tr}} = 10$  training bits (for parameter estimation) and  $N_{\text{data}} = 50$  payload bits. For the case of the fully noncoherent SBPSK detector, the total payload was  $N_p = N_{\text{data}} = 50$  (no training bits) bits with  $M = 50$ . Bit duration was fixed through

$L$ , which was set to  $L = 1000$ . Assuming a sampling rate  $F_s = 5$  MHz, the chosen value for  $L$  represents a bit rate of  $R = 1/T_{\text{bit}} = 5$  kbps. Scattering efficiency was set to  $s = \sqrt{0.1}$ , while structural mode parameter to  $A_s = 0.6047 + j0.5042$ .

Channel coefficients were created such that:

$$h_q \sim \mathcal{CN}\left(\sqrt{\frac{k_q}{k_q + 1}}\sigma_q, \frac{\sigma_q^2}{k_q + 1}\right), \quad q \in \{\text{CT}, \text{TR}, \text{CR}\}. \quad (3.61)$$

Eq. (3.61) can be used to model both Rician and Rayleigh fading. Under Rician fading, factor  $k_q$  expresses the power ratio of the dominant path over the scattered paths ( $k_q > 0$ ). Rayleigh fading can be obtained by setting  $k_q = 0$ . The tag is located close to the receiver and a strong line of sight path is probable. Thus, Rician fading is assumed for the tag-to-receiver (TR) link. On the other hand, the ambient illuminator is typically located far from both the tag and the receiver. Thus, the corresponding links (CT, CR) are potentially amenable to rich scattering conditions, so Rayleigh fading is assumed ( $k_{\text{CR}} = k_{\text{CT}} = 0$ ).

Large scale pathloss is also taken into account through variances  $\sigma_q^2 = L_q\sigma_h^2 = L_q$ .  $L_q$  is defined as [48]:

$$L_q = \left(\frac{\lambda}{4\pi}\right)^2 \frac{1}{d_q^\nu}. \quad (3.62)$$

Pathloss exponent  $\nu$ , was set to  $\nu = 2.2$ , representing an “optimistic” scenario. The distances were set to  $d_{\text{CR}} = 6$  km,  $d_{\text{TR}} = 6$  m and  $d_{\text{CT}} = d_{\text{CR}} - d_{\text{TR}}$ .

Given that the vast majority of literature on theoretical ambient backscatter communication considers as signal-to-noise ratio  $P_{\text{tx}}/\sigma_w^2$ , i.e., the ratio of transmitter’s power to the power of complex baseband noise (referred to as transmit SNR), the carrier-to-noise ratio (CNR) is reported:

$$\text{CNR} \triangleq \frac{P_{\text{rx}}}{\sigma_w^2} = \frac{\sigma_c^2 \mathbb{E}[|h_{\text{CR}}|^2]}{\sigma_w^2} = \frac{\sigma_c^2 L_{\text{CR}}}{\sigma_w^2}. \quad (3.63)$$

The definition of CNR in Eq. (3.63) expresses the power ratio of the received ambient carrier signal, from the direct CR link, to the complex baseband noise. It noted that such a definition favours the proposed, DSI-cancelling schemes, however the definition is a middle-ground between transmit SNR and the actual, bit SNR.

Depending on the scenario,  $10^5$ ,  $5 \times 10^6$  or  $8 \times 10^6$  Monte Carlo experiments were performed per CNR value. The channel parameters were assumed *constant* for each Monte Carlo run, i.e., for  $N_{\text{tr}} + N_{\text{data}} = 60$  bits, with  $k_{\text{TR}} = 20$ . It has to be noted that

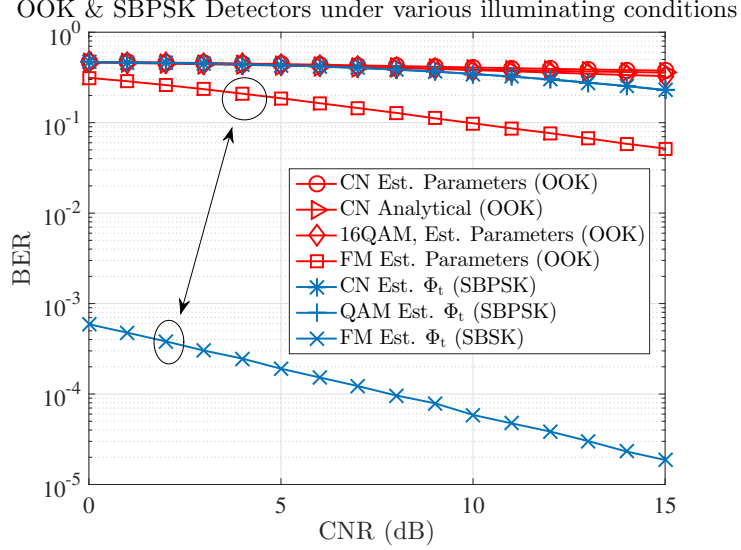


Figure 3.8: Evaluation of the OOK (CN threshold) detectors from [14] and SBPSK detectors (Eq. (3.40)), under different ambient carrier modulations (CN, 16-QAM, FM).

the SBPSK detector can work even when the wireless channel parameters vary between successive bits. Analytical BER expressions are drawn from the results of [14].

The closed form bit error probability for the detector of Eq. (3.58) utilizing the CN or the PSK threshold, is given by [14, Eq. (10)] and [14, Eq. (47)], respectively. Both expressions require exact knowledge of  $\sigma_0^2$ ,  $\sigma_1^2$ . Hence, in every Monte Carlo experiment, each expression was evaluated for the experiment's (exact) channel parameters and an average value was obtained at the end of all experiments (averaged over the different channel realizations). That way, an average value for the closed form probability of error is obtained for each CNR. Illuminating signal was assumed to attain different modulations, namely FM, CN, BPSK and 16-QAM.

In Fig. 3.8 the performance of the OOK detector with the CN threshold, is evaluated for different illuminating conditions; performance of the SBPSK detector for the same conditions is also offered. For OOK with CN illumination, the detector of Eq. (3.58) using perfect and estimated channel parameters  $\sigma_0^2, \sigma_1^2$ , was evaluated along with the closed form expression for the case ([14, Eq. (10)]). The detector is also evaluated, using parameter estimates, under FM and 16-QAM illumination.

Considering CN illumination, the performance of the detectors is similar, with the SBPSK slightly outperforming OOK. However, while for 16-QAM the performance offered by both detectors is identical to CN illumination, if FM illumination is considered, the performance gap compared to CN is significant, for both OOK and SBPSK. The last finding dictates that neglecting the structure of the illuminator's signal, may lead to sig-

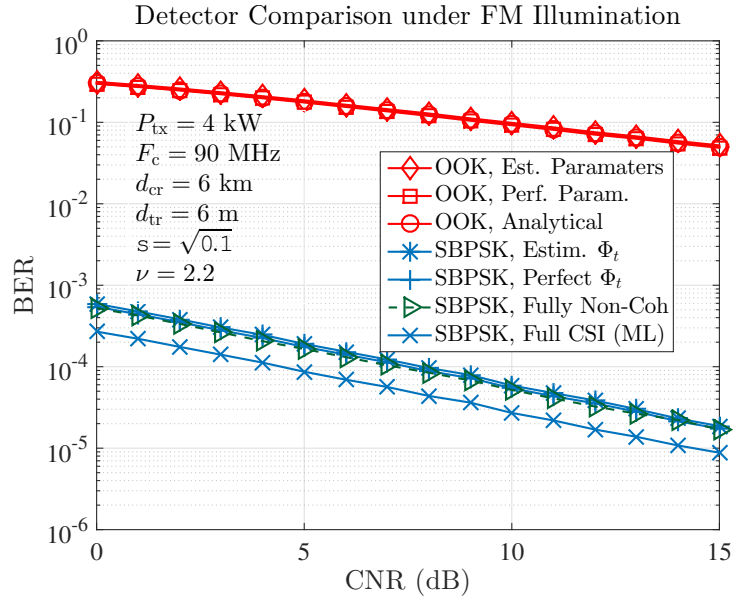


Figure 3.9: Evaluation of the OOK (PSK threshold) detectors from [14] and SBPSK detectors, under FM illumination. SBPSK partially coherent detector is demonstrated for conditions of perfect, estimated  $\Phi_t$  and ML-based full CSI detection. The performance of the proposed fully noncoherent detector, is also demonstrated.

nificant performance loss. It is also observed that SBPSK outperforms OOK, when FM illumination is considered. SBPSK is evaluated using an estimate of  $\Phi_t$ . For the performance of the OOK detectors under simplified signal models, reader is kindly encouraged to see [14].

Performance under FM and BPSK illumination is given in Figs. 3.9 and 3.10, respectively. Under FM illumination (Fig. 3.9) and realistic channel conditions (summarized in the left side of the figure), it can be seen that SBPSK detector outperforms OOK.

The performance gain is offered at the expense of increased complexity at the tag due to switching during each bit duration (as explained earlier). It can be also seen that the proposed SBPSK-based fully noncoherent detector, performs slightly better than the partially coherent detector, with the latter utilizing perfect information of  $\Phi_t$ . This behaviour can be explained by the nature of the detector, which is sequence-based (see Sec. 3.4.3). SBPSK is also evaluated for perfect channel state information (CSI, related to wireless channel, ambient carrier and tag parameters), with ML detection (using Eq. (3.36)).

Under BPSK illumination (Fig. 3.10), the OOK scheme with the PSK threshold outperforms the SBPSK detector. This may be explained by the fact that the OOK detector is derived under the assumption of a PSK illuminating signal, while SBPSK detector does not assume any information regarding ambient carrier's modulation. This finding underlines the importance of the illuminator's signal structure.

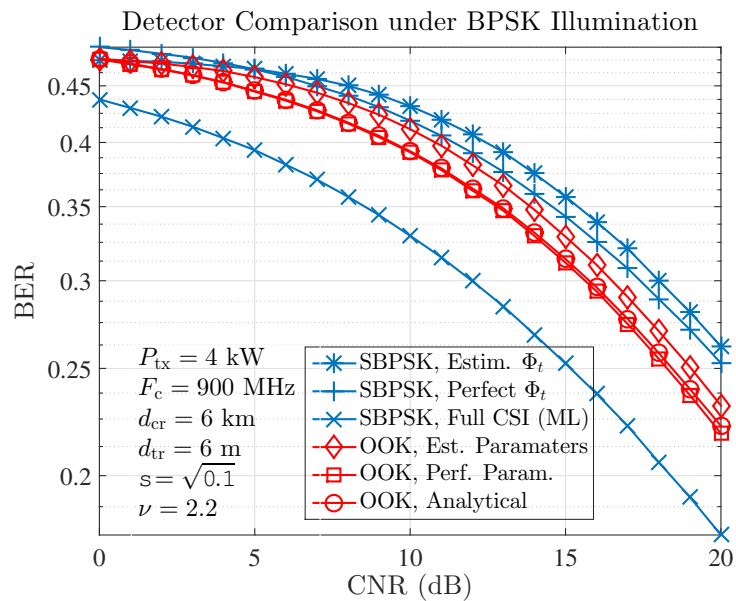


Figure 3.10: Evaluation of the OOK (PSK threshold) detectors from [14] and SBPSK detectors, under BPSK illumination. SBPSK partially coherent detector is demonstrated for the cases of perfect, estimated  $\Phi_t$  and (ML-based) full CSI detection.

# Chapter 4

## Recycling Radio Waves: An Analog Tag Approach

In the previous chapter, methods for exploiting ambient signals for achieving ultra-low-power (digital) communication were offered. Those methods, though effective for transmitting digital information, required a user to be equipped with a receiver able to perform a set of specific signal processing tasks (e.g., SDR). In this chapter, assuming exploitation of ambient FM radio signals, a method for transmitting analog information, consuming 1000 times less power than conventional protocols (e.g., Bluetooth, conventional FM analog transmission) will be presented. The method will be subsequently referred to as *FM Remodulation* (Sec. 4.1).

FM remodulation allows for the information of the tag to be recovered using *any* conventional FM radio receiver, ranging from old vacuum tube radio sets to modern, FM-radio equipped smartphones. The tag implementing such functionality can be built (Sec. 4.2) at a unit cost of  $< 5$  euros, while not requiring any additional infrastructure for recovering its information (besides FM radio coverage & receiver).

The power consumption attained by a tag adopting FM remodulation, allows for the latter to be powered using energy harvesting from various sources (Sec. 4.3). Such sources might be daylight, artificial light, thermal gradients or radio signals (RF energy harvesting). Operating using just energy from the environment, eliminates the need for a battery.

Wireless sensor nodes can be built using batteryless tags that adopt the FM remodulation technology, without the maintenance and environmental cost associated with battery replacements, at an ultra-low-cost ( $< 5$  euro/wireless sensor) and without the need for any special infrastructure (assuming access to an FM radio receiver or FM radio-equipped smartphone).

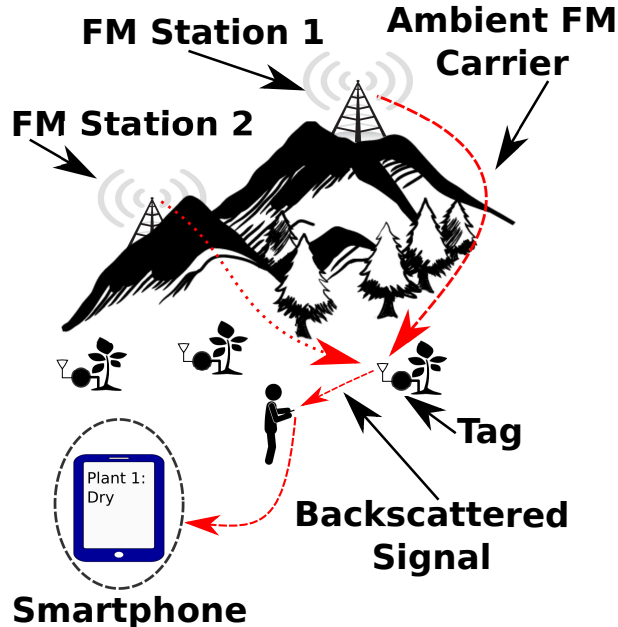


Figure 4.1: FM remodulation for transmitting sensor information towards any FM radio receiver. A FM radio-equipped smartphone is used to recover sensor’s information from tag’s backscattered signal.

## 4.1 FM Remodulation: Principle & Analysis

In this section, the principle allowing the information of a backscattering tag to be remodulated on top of ambient FM radio signals and be subsequently recovered by any FM radio receiver, will be described. The performance of the method with respect to the noise level at a (conventional) FM radio receiver, as well as the diversity gains offered as a by-product of FM remodulation, will be also studied.

Fig. 4.1 demonstrates the concept of exploiting ambient FM radio signals for ultra-low-power, infrastructure-less, batteryless communication; a FM radio-equipped smartphone is used to recover tag’s information, which is the value of a soil moisture sensor.

### 4.1.1 Operating Principle

A FM radio signal, originating from a FM radio station  $s$ , can be mathematically modelled as follows (see Eq. (2.7)) [47]:

$$\begin{aligned} \Re \{c_{\text{tx},s}(t)\} &= \Re \left\{ m(t) e^{j2\pi F_s t} \right\} = \Re \left\{ A_s e^{2\pi k_s \int_0^t \phi_s(\tau) d\tau} e^{j2\pi F_s t} \right\} \\ &= A_s \cos \left( 2\pi F_s t + 2\pi k_s \int_0^t \phi_s(\tau) d\tau \right), \end{aligned} \quad (4.1)$$

where  $A_s, F_s$  is the carrier amplitude and center frequency of radio station  $s$ , respectively and  $k_s$  is the modulator's frequency sensitivity, measured in Hz/V. FM modulation index is given by  $\beta_s = \Delta f_{\max}/W = k_s \max |\phi_s(t)|/W$ , where  $W$  is the (baseband) bandwidth of  $\phi_s(t)$ . If  $\max |\phi_s(t)| = 1$ , then  $\Delta f_{\max} = k_s$ . Signal model in Eq. (4.1) applies to any FM radio station and thus,  $\phi_s(t)$  includes station's audio information (mono or stereo) plus, where applicable, any additional digital information about the station (RDS).

The station's signal propagates towards a backscattering tag and is subjected to amplitude attenuation ( $a_{CT}$ ) and delay (expressed through phase  $\phi_{CT}$  (Eq. (2.9)). The signal impinging at the tag can be then expressed as follows:

$$\Re \{c_s(t)\} = A_s a_{CT} \cos \left( 2\pi F_s t + 2\pi k_s \int_0^t \phi_s(\tau) d\tau - \phi_{CT} \right). \quad (4.2)$$

The backscattering tag is assumed able to perform the switching operation described in Chap. 3, Sec. 3.2.1. Additionally, tag's switching subcarrier is frequency modulated by the tag's information-bearing signal  $\mu(t)$ . Therefore, the tag's signal can be mathematically described by the following expression:

$$x_{\text{tag,FM}}(t) = m_{dc} e^{j\theta_{dc}} + m_{\text{tag}} e^{j\theta_{\text{tag}}} \cos \left( 2\pi F_{sw} t + 2\pi k_{sw} \int_0^t \mu(\tau) d\tau + \varphi \right), \quad (4.3)$$

where  $k_{sw}$  is the frequency sensitivity of the tag's modulator. Details on how such a signal can be created in an ultra-low-power manner by the tag, are given in Sec. 4.2.

Due to the backscattering operation of the tag (Chap. 2), the radio station's FM signal (Eq. (4.2)), is "remodulated" by the tag's FM modulated signal (Eq. (4.3)). Thus, the backscattered signal, impinging on the receiver's antenna, takes the following form (Eq. (2.12)):

$$\begin{aligned} \Re \{y(t)\} &= \Re \{c_s(t) x_{\text{tag,FM}}(t)\} = a_d A_s \cos \left( 2\pi F_s t + 2\pi k_s \int_0^t \phi_s(\tau) d\tau - \varphi_d \right) \\ &+ \frac{1}{2} A_s \widehat{m}_{\text{tag}} \cos \left( 2\pi (F_s + F_{sw}) t + 2\pi k_s \int_0^t \phi_s(\tau) d\tau + 2\pi k_{sw} \int_0^t \mu(\tau) d\tau + \Phi_t + \widehat{\theta}_{\text{tag}} \right) \\ &+ \frac{1}{2} A_s \widehat{m}_{\text{tag}} \cos \left( 2\pi (F_s - F_{sw}) t + 2\pi k_s \int_0^t \phi_s(\tau) d\tau - 2\pi k_{sw} \int_0^t \mu(\tau) d\tau - \Phi_t + \widehat{\theta}_{\text{tag}} \right), \end{aligned} \quad (4.4)$$

where the trigonometric identity  $\cos(a) \cos(b) = \frac{1}{2} [\cos(a+b) + \cos(a-b)]$  was used. Variables  $a_d, \varphi_d$  represent the attenuation and delay introduced to the station's signal by the compound channel, due to the carrier-to-receiver propagation path and the virtual path created by tag's structural mode/"DC" term ( $A_s, m_{dc} e^{j\theta_{dc}}$ ).

Parameters  $\widehat{m}_{\text{tag}}$ ,  $\widehat{\theta}_{\text{tag}}$  express the effect of the channel (and tag characteristics) on the backscattered signal. Phase  $\Phi_t$  is defined as in Chap. 3, Sec. 3.3.1. The aforementioned parameters do not affect subsequent analysis and thus will be omitted for notational simplicity.

Eq. (4.4) shows that, if a conventional FM radio receiver is tuned to either of  $F_s \pm F_{\text{sw}}$  the signal at its speaker(s) will be  $\phi_s(t) \pm \mu(t)$ , respectively. DSI is “naturally” removed due to switching in conjunction with tuning the FM radio receiver at either of  $F_s \pm F_{\text{sw}}$  (Chap. 3, Sec. 3.2.1). Moreover, the station’s signal at  $F_s$  can be clearly heard, without interference from the tag’s signal  $\mu(t)$ , as the tag’s contribution at  $F_s$  acts as an additional, virtual, propagation path. In order for  $\mu(t)$  to be clearly “heard” at a conventional FM radio receiver, the following must hold:

1.  $\mu(t)$  bandwidth must be limited to the audible spectrum (20 Hz to 20 kHz).
2. At least one of  $F_s \pm F_{\text{sw}}$  must fall within the FM radio frequency band (88 MHz to 108 MHz, in Greece),
3. Audio level of the backscattered, demodulated tag signal (given that it’s limited to the audible spectrum), is above a required threshold for successful FM reception. Remember that  $\phi_s(t)$  acts as interference in the reception of  $\mu(t)$ .

If the above statements hold, *any* FM radio receiver can be used to recover the tag’s information signal, which comes in the form of audio. But how can information be encoded into sound? In this work, analog information will be encapsulated in the frequency of an audio tone  $\mu(t)$ . More specifically, a sensor’s value will be translated to the pitch of the said tone (see Sec. (4.2)).

Due to being limited in the audible spectrum,  $\mu(t)$  is potentially amenable to FM station’s interference, while  $k_{\text{sw}} \neq k_s$ . To reduce interference from the FM station signal on the tag backscattered signal, the frequency band of  $\mu(t)$  may be placed on areas that are not occupied by frequency components of  $\phi_s(t)$ . For example, if the chosen FM radio station has only voice content,  $\mu(t)$  can be designed to occupy a higher frequency band. Increasing the frequency deviation of the switching signal (up to a certain value, to avoid excessive noise power due to increased bandwidth), higher audio levels of  $\mu(t)$  are offered compared to interference (see Sec. 4.4.2 and Eq. (4.51)). Such method does not eliminate interference but reduces its effect, allowing for successful sensor interrogation.

### 4.1.2 Impact of Noise

In this section, analysis will be performed so as to study the impact of noise in the backscattered, FM remodulated signal. The analysis performed in order to examine the effect of noise at the output of the FM receiver (when the input is the remodulated backscattered signal), is based on similar analysis performed in [47, 60]. Contrary to the methods followed in [47, 60], this work studies the performance of a FM receiver, when excited by an FM remodulated signal; the tag's information-bearing, deterministic signal is affected by stochastic FM interference, as well as thermal noise.

A conventional, discrimination-based FM radio receiver is considered, tuned at  $F_t = F_s + F_{\text{sw}}$ . The received signal after passband filtering around  $F_t$  can be expressed as follows:

$$y_b(t) = \gamma_b \cos(2\pi F_t t + \phi_d^t + \mu_d^t) + n(t), \quad (4.5)$$

where  $\phi_d^t = 2\pi k_s \int_0^t \phi_s(\tau) d\tau$ ,  $\mu_d^t = 2\pi k_{\text{sw}} \int_0^t \mu(\tau) d\tau$ ,  $\gamma_b = \frac{1}{2} A_c \widehat{m}_{\text{tag}}$  and  $n(t)$  zero-mean, wide sense stationary (WSS) Gaussian process. Assuming the filter to have a bandwidth equal to  $B$ , the PSD of  $n(t)$  is given by:

$$S_n(f) = \begin{cases} \frac{N_0}{2}, & |f \pm F_t| \leq \frac{B}{2} \\ 0, & \text{otherwise,} \end{cases} \quad (4.6)$$

Noise  $n(t)$  is a passband signal (centered at  $F_t$ ) of bandwidth  $B$ . As with any passband signal,  $n(t)$  can be expressed through its baseband components  $n_I(t)$ ,  $n_Q(t)$  [47]:

$$\begin{aligned} n(t) &= n_I(t) \cos(2\pi F_t t) - n_Q(t) \sin(2\pi F_t t) \\ &= \sqrt{n_I^2(t) + n_Q^2(t)} \cos\left(2\pi F_t t + \tan^{-1}\left(\frac{n_Q(t)}{n_I(t)}\right)\right) \\ &= V_n(t) \cos(2\pi F_t t + \Phi_n(t)), \end{aligned} \quad (4.7)$$

$n_Q(t)$ ,  $n_I(t)$  are independent, baseband, band limited, zero mean WSS Gaussian processes with  $R_{n_I}(\tau) = R_{n_Q}(\tau) = R_{n_b}(\tau)$ . The power spectral density of  $n_I(t)$ , is given by [47]:

$$S_{n_b}(f) = S_{n_I}(f) = S_{n_Q}(f) = \begin{cases} N_0, & |f| \leq \frac{B}{2} \\ 0, & \text{otherwise.} \end{cases} \quad (4.8)$$

$R_{\text{nb}}(\tau)$  can then be acquired by  $R_{\text{nb}}(\tau) = \mathcal{F}^{-1} \{S_{\text{nb}}(f)\}$  as follows:<sup>1</sup>

$$\begin{aligned} R_{\text{nb}}(\tau) &= \int_{-\infty}^{+\infty} S_{\text{nb}}(f) e^{j2\pi f\tau} df = \int_{-B/2}^{+B/2} N_0 e^{j2\pi f\tau} df \\ &= N_0 \left[ \frac{e^{j2\pi f\tau}}{j2\pi f\tau} \right]_{-B/2}^{B/2} = N_0 B \text{sinc}(\tau). \end{aligned} \quad (4.9)$$

Thus, the power of noise at the input of the receiver (after filtering) is given by  $P_n = R_{\text{nb}}(0) = N_0 B$ , while the power of the signal is  $P_c = \frac{\gamma_b^2}{2}$ . The SNR at the input of the receiver can be then defined as follows:

$$\text{SNR} = \frac{P_c}{P_n} = \frac{\gamma_b^2/2}{N_0 B}, \quad (4.10)$$

By combining Eq. (4.5) and Eq. (4.7) and performing vector addition, the received signal can be expressed as:

$$\begin{aligned} y_b(t) &= \sqrt{\gamma_b^2 + V_n^2(t) + 2\gamma_b V_n(t) \cos(\Phi_n(t) - \phi_d^t - \mu_d^t)} \\ &\quad \cdot \cos\left(2\pi F_t t + \phi_d^t + \mu_d^t + \tan^{-1}\left(\frac{V_n(t) \sin(\Phi_n(t) - \phi_d^t - \mu_d^t)}{\gamma_b + V_n(t) \cos(\Phi_n(t) - \phi_d^t - \mu_d^t)}\right)\right). \end{aligned} \quad (4.11)$$

The transformation of Eq. (4.5) into Eq. (4.11) was made in order for the noise terms to appear within the signal's phase, which holds the information. That allows for analysing the effect of input noise at the output of the receiver.

### a) High SNR Case

For simplifying the analysis, in this section,  $\gamma_b \gg V_n(t)$  is assumed, which translates to  $\text{SNR} > 10$  dB (high SNR regime). Below that 10 dB threshold, the output SINR, considering the station's demodulated signal as interference and the tag's information signal as useful, drops rapidly with respect to input SNR (as it will be later shown), dictating the need for ambient selection diversity, explained in Sec. 4.1.3.

Considering  $\gamma_b \gg V_n(t)$  ( $\text{SNR} > 10$  dB), the following approximation can be used:

$$\sqrt{\gamma_b^2 + V_n^2(t) + 2\gamma_b V_n(t) \cos(\Phi_n(t) - s(t))} \approx \gamma_b + V_n(t) \cos(\Phi_n(t) - s(t)) \approx \gamma_b, \quad (4.12)$$

<sup>1</sup>Where  $\mathcal{F}$  the Fourier transform and  $\mathcal{F}^{-1}$  its inverse.

where  $s(t) = \phi_d^t + \mu_d^t$ . Using the above approximation and the fact that  $\tan(\phi) \approx \phi \Leftrightarrow \phi \approx \tan^{-1}(\phi)$ , for small  $\phi$ , Eq. (4.11) can be expressed, in the high SNR-regime, as follows:

$$y_b(t) = a(t) \cos(2\pi F_t t + s(t) + n_{\text{out}}(t)) = \Re \left\{ a(t) e^{+j(s(t)+n_{\text{out}}(t))} e^{+j(2\pi F_t t)} \right\}, \quad (4.13)$$

with  $a(t) = \gamma_b + V_n(t) \cos(\Phi_n(t) - s(t)) \approx \gamma_b$  and  $n_{\text{out}}(t) = \frac{V_n(t)}{\gamma_b} \sin(\Phi_n(t) - s(t))$ .

The receiver has to obtain the tag's signal  $\mu(t)$ , which is superimposed to the station's signal  $\phi_s(t)$ . To achieve this, the signal of Eq. (4.13) is first downconverted to baseband and then the complex envelope is obtained:

$$y_b^{\text{dc}}(t) = a(t) e^{+j(s(t)+n_{\text{out}}(t))}. \quad (4.14)$$

The phase of the complex envelope is then extracted:

$$\begin{aligned} y_b^{\text{arg}}(t) &= \angle y_b^{\text{dc}}(t) = s(t) + n_{\text{out}}(t) \\ &= 2\pi k_s \int_0^t \phi_s(\tau) d\tau + 2\pi k_{\text{sw}} \int_0^t \mu(\tau) d\tau + n_{\text{out}}(t). \end{aligned} \quad (4.15)$$

As a final step, the receiver derivates and divides by  $2\pi$ ,  $y_b^{\text{arg}}(t)$  to obtain:

$$r(t) = \frac{1}{2\pi} \frac{d}{dt} y_b^{\text{arg}}(t) = k_{\text{sw}} \mu(t) + k_s \phi_s(t) + \frac{1}{2\pi} \frac{d}{dt} \overbrace{\left[ \frac{V_n(t)}{\gamma_b} \sin(\Phi_n(t) - s(t)) \right]}^{w_n(t)}. \quad (4.16)$$

In Eq. (4.16), term  $k_{\text{sw}} \mu(t)$  is considered as useful signal (tag's signal). Term  $k_s \phi_s(t)$  is interference to tag's signal and the last term ( $w_n(t)$ ) is noise. In order to obtain closed form expression for the SINR at the output of the FM receiver, the characteristics of the noise term,  $\frac{1}{2\pi} \frac{d}{dt} \left[ \frac{V_n(t)}{\gamma_b} \sin(\Phi_n(t) - s(t)) \right]$  must first be derived. Notice that the signal ( $s(t)$ ), appears within the noise term.  $w_n(t)$  can be rewritten as:

$$\begin{aligned} w_n(t) &= \frac{V_n(t)}{\gamma_b} \sin(\Phi_n(t) - s(t)) \\ &\stackrel{*}{=} \frac{V_n(t)}{\gamma_b} \left[ \sin(\Phi_n(t)) \cos(\phi_d^t + \mu_d^t) - \cos(\Phi_n(t)) \sin(\phi_d^t + \mu_d^t) \right], \end{aligned} \quad (4.17)$$

where in \* the identity  $\sin(a - b) = \sin(a) \cos(b) - \cos(a) \sin(b)$  was used. Using Eq. (4.7),  $w_n(t)$  becomes:

$$w_n(t) = \frac{1}{\gamma_b} \left[ n_Q(t) \cos(\phi_d^t + \mu_d^t) - n_I(t) \sin(\phi_d^t + \mu_d^t) \right]. \quad (4.18)$$

The expected value of  $w_n(t)$  can be calculated as follows:

$$\mathbb{E}[w_n(t)] = \frac{1}{\gamma_b} \left( \mathbb{E}[\mathbf{n}_Q(t)] \cos(\phi_d^t + \mu_d^t) - \mathbb{E}[\mathbf{n}_I(t)] \sin(\phi_d^t + \mu_d^t) \right) = 0. \quad (4.19)$$

In Eq. (4.19), the facts that the thermal noise components  $\mathbf{n}_I(t)$ ,  $\mathbf{n}_Q(t)$  are independent of the signal and  $\mathbb{E}[\mathbf{n}_I(t)] = \mathbb{E}[\mathbf{n}_Q(t)] = 0$ , were used. With  $\mathbb{E}[w_n(t)]$  available, the autocorrelation function of  $w_n(t)$  can be calculated as follows:

$$\begin{aligned} R_{w_n}(t + \tau, t) &= \mathbb{E}[w_n(t + \tau) w_n(t)] \\ &= \frac{1}{\gamma_b^2} \mathbb{E} \left[ \left( \mathbf{n}_Q(t + \tau) \cos(\phi_d^{t+\tau} + \mu_d^{t+\tau}) - \mathbf{n}_I(t + \tau) \sin(\phi_d^{t+\tau} + \mu_d^{t+\tau}) \right) \right. \\ &\quad \left. \cdot \left( \mathbf{n}_Q(t) \cos(\phi_d^t + \mu_d^t) - \mathbf{n}_I(t) \sin(\phi_d^t + \mu_d^t) \right) \right]. \end{aligned} \quad (4.20)$$

By definition,  $\mathbb{E}[\mathbf{n}_Q(t + \tau) \mathbf{n}_Q(t)] = \mathbb{E}[\mathbf{n}_I(t + \tau) \mathbf{n}_I(t)] = R_{\text{nb}}(\tau)$ . Using the fact that  $R_{\mathbf{n}_I \mathbf{n}_Q}(\tau) = 0$ , Eq. (4.20) takes the following form:

$$\begin{aligned} R_{w_n}(t + \tau, t) &= \frac{1}{\gamma_b^2} R_{\text{nb}}(\tau) \mathbb{E} \left[ \cos(\phi_d^{t+\tau} + \mu_d^{t+\tau}) \cos(\phi_d^t + \mu_d^t) \right. \\ &\quad \left. + \sin(\phi_d^{t+\tau} + \mu_d^{t+\tau}) \sin(\phi_d^t + \mu_d^t) \right]. \end{aligned} \quad (4.21)$$

Taking advantage of the trigonometric identity  $\cos(a - b) = \cos(a) \cos(b) + \sin(a) \sin(b)$ , Eq. (4.21) becomes:

$$R_{w_n}(t + \tau, t) = \frac{1}{\gamma_b^2} R_{\text{nb}}(\tau) \mathbb{E} \left[ \cos(\phi_d^{t+\tau} - \phi_d^t + \mu_d^{t+\tau} - \mu_d^t) \right]. \quad (4.22)$$

The signal  $\phi_d^t$  (representing the integral of the station's signal), is assumed to be a zero mean, WSS Gaussian process. That way, at any time instant  $t$ ,  $\phi_d^{t+\tau}, \phi_d^t$ , are zero mean, jointly Gaussian random variables [61, Def. 2.1] and the variance of  $q^{t,\tau} = \phi_d^{t+\tau} - \phi_d^t$  can be calculated as:

$$\begin{aligned} \sigma_q^2 &= \mathbb{E} \left[ (q^{t,\tau})^2 \right] = \mathbb{E} \left[ (\phi_d^{t+\tau} - \phi_d^t)^2 \right] = \mathbb{E} \left[ (\phi_d^{t+\tau})^2 \right] - 2R_{\phi_d}(\tau) + \mathbb{E} \left[ (\phi_d^t)^2 \right] \\ &= 2R_{\phi_d}(0) - 2R_{\phi_d}(\tau). \end{aligned} \quad (4.23)$$

$R_{w_n}(t + \tau, t)$  can be then rewritten as follows:

$$\begin{aligned} R_{w_n}(t + \tau, t) &= \frac{1}{\gamma_b^2} R_{\text{nb}}(\tau) \mathbb{E} \left[ \cos(q^{t,\tau} + \mu_d^{t+\tau} - \mu_d^t) \right] \\ &= \frac{1}{\gamma_b^2} R_{\text{nb}}(\tau) \mathbb{E} \left[ \Re \left\{ e^{jq^{t,\tau}} e^{j(\mu_d^{t+\tau} - \mu_d^t)} \right\} \right]. \end{aligned} \quad (4.24)$$

The tag's information is mapped into the frequency ( $F_{\text{sens}}$ ) of an audio tone. It is assumed that  $\mu(t)$  is a deterministic signal (audio tone), more specifically  $\mu(t) = -\sin(2\pi F_{\text{sens}} t)$ . That way  $\mu_d^t = 2\pi k_{\text{sw}} \int_0^t \mu(\tau) d\tau = \frac{k_{\text{sw}}}{F_{\text{sens}}} \cos(2\pi F_{\text{sens}} t) + c$  and Eq. (4.24) becomes:

$$\begin{aligned} R_{w_n}(t + \tau, t) &= \frac{1}{\gamma_b^2} R_{\text{nb}}(\tau) \Re \left\{ \mathbb{E} \left[ e^{jq^{t,\tau}} \right] e^{j(\mu_d^{t+\tau} - \mu_d^t)} \right\} \\ &\stackrel{*}{=} \frac{1}{\gamma_b^2} R_{\text{nb}}(\tau) \Re \left\{ e^{-\frac{\sigma_q^2}{2}} e^{j(\mu_d^{t+\tau} - \mu_d^t)} \right\} \\ &= \frac{1}{\gamma_b^2} R_{\text{nb}}(\tau) e^{-\frac{\sigma_q^2}{2}} \cos(\mu_d^{t+\tau} - \mu_d^t), \end{aligned} \quad (4.25)$$

where in point \* the characteristic function of the Gaussian random variable  $q^{t,\tau}$  was used (see Sec. 8.3.1). In Eq. (4.25), the fact that  $\mathbb{E}[\Re\{z\}] = \Re\{\mathbb{E}[z]\}$  with  $z \in \mathbb{C}$ , was also used. Finally, the autocorrelation function of  $w_n(t)$  can be expressed as:

$$R_{w_n}(t + \tau, t) = \mathbb{E}[w_n(t + \tau) w_n(t)] = \frac{1}{\gamma_b^2} R_{\text{nb}}(\tau) e^{R_{\phi_d}(\tau) - R_{\phi_d}(0)} \cos(\mu_d^{t+\tau} - \mu_d^t). \quad (4.26)$$

Due to dependence of  $R_{w_n}(t + \tau, t)$  on  $t$ ,  $w_n(t)$  can not be characterized as a WSS process. However,  $\mu_d^t$  is a periodic function with period  $T_{\text{sens}} = \frac{1}{F_{\text{sens}}}$ . That way  $\mu_d^{t+T_{\text{sens}}} = \mu_d^t$  and:

$$\begin{aligned} R_{w_n}(t + T_{\text{sens}} + \tau, t + T_{\text{sens}}) &= \frac{1}{\gamma_b^2} R_{\text{nb}}(\tau) e^{R_{\phi_d}(\tau) - R_{\phi_d}(0)} \cos(\mu_d^{t+T_{\text{sens}}+\tau} - \mu_d^{t+T_{\text{sens}}}) \\ &= \frac{1}{\gamma_b^2} R_{\text{nb}}(\tau) e^{R_{\phi_d}(\tau) - R_{\phi_d}(0)} \cos(\mu_d^{t+\tau} - \mu_d^t) \\ &= R_{w_n}(t + \tau, t). \end{aligned} \quad (4.27)$$

Eq. (4.27) and Eq. (4.19), show that process  $w_n(t)$  is cyclostationary with period  $T_{\text{sens}}$ . The  $t$ -averaged, autocorrelation function is given by:

$$\bar{R}_{w_n}(\tau) = \frac{1}{\gamma_b^2} R_{\text{nb}}(\tau) e^{R_{\phi_d}(\tau) - R_{\phi_d}(0)} \frac{1}{T_{\text{sens}}} \int_{T_{\text{sens}}} \cos(\mu_d^{t+\tau} - \mu_d^t) dt. \quad (4.28)$$

Next, the integral involved in Eq. (4.28) will be calculated:

$$\int_{T_{\text{sens}}} \cos(\mu_d^{t+\tau} - \mu_d^t) dt = \int_{T_{\text{sens}}} \cos \left[ \frac{k_{\text{sw}}}{F_{\text{sens}}} [\cos(2\pi F_{\text{sens}} t + 2\pi F_{\text{sens}} \tau) - \cos(2\pi F_{\text{sens}} t)] \right] dt. \quad (4.29)$$

Using the trigonometric identity  $\cos(a) - \cos(b) = -2\sin\left(\frac{a-b}{2}\right)\sin\left(\frac{a+b}{2}\right)$ , Eq. (4.29) becomes:

$$\begin{aligned} \int_{T_{\text{sens}}} \cos(\mu_d^{t+\tau} - \mu_d^t) dt &= \int_{T_{\text{sens}}} \cos \left( -2 \frac{k_{\text{sw}}}{F_{\text{sens}}} \sin(\pi F_{\text{sens}} \tau) \sin(2\pi F_{\text{sens}} t + \pi F_{\text{sens}} \tau) \right) dt \\ &= \int_{T_{\text{sens}}} \cos(\tau_0 \sin(2\pi F_{\text{sens}} t + \tau_1)) dt, \end{aligned} \quad (4.30)$$

where

$$\tau_0 \stackrel{*}{=} 2\rho \sin(\pi F_{\text{sens}} \tau), \quad \rho = \frac{k_{\text{sw}}}{F_{\text{sens}}}, \quad (4.31)$$

$$\tau_1 = \pi F_{\text{sens}} \tau, \quad (4.32)$$

where in \* the symmetry of cosine function was exploited. Applying equation [62, 9.1.42]:

$$\cos(z \sin(\theta)) = J_0(z) + 2 \sum_{k=1}^{\infty} J_{2k}(z) \cos(2k\theta), \quad z \in \mathbb{C}, \quad (4.33)$$

where  $J_k(z)$  is the Bessel function of the first kind of order  $k$ , to Eq. (4.30):

$$\begin{aligned} \int_{T_{\text{sens}}} \cos(\tau_0 \sin(2\pi F_{\text{sens}} t + \tau_1)) dt &= \int_{T_{\text{sens}}} J_0(\tau_0) + 2 \sum_{n=1}^{\infty} J_{2n}(\tau_0) \cos(2n(2\pi F_{\text{sens}} t + \tau_1)) dt \\ &= \int_{T_{\text{sens}}} J_0(\tau_0) dt + \int_{T_{\text{sens}}} 2 \sum_{n=1}^{\infty} J_{2n}(\tau_0) \cos(2n(2\pi F_{\text{sens}} t + \tau_1)) dt \\ &= J_0(\tau_0) \int_{T_{\text{sens}}} dt + 2 \sum_{n=1}^{\infty} J_{2n}(\tau_0) \overbrace{\int_{T_{\text{sens}}} \cos(2n(2\pi F_{\text{sens}} t + \tau_1)) dt}^{=0} \\ &\stackrel{*}{=} J_0(\tau_0) T_{\text{sens}}. \end{aligned} \quad (4.34)$$

$\bar{R}_{w_n}(\tau)$  is thus given by:

$$\begin{aligned}\bar{R}_{w_n}(\tau) &= \frac{1}{\gamma_b^2} R_{\text{nb}}(\tau) e^{R_{\phi_d}(\tau) - R_{\phi_d}(0)} J_0(\tau_0) \\ &= \frac{1}{\gamma_b^2} R_{\text{nb}}(\tau) e^{R_{\phi_d}(\tau) - R_{\phi_d}(0)} J_0(2\rho \sin(\pi F_{\text{sens}}\tau)).\end{aligned}\quad (4.35)$$

The spectral density of  $w_n(t)$  is given by:

$$S_w(f) = \mathcal{F} \left\{ \bar{R}_{w_n}(\tau) \right\} = \frac{1}{\gamma_b^2} e^{-R_{\phi_d}(0)} \mathcal{F} \left\{ R_{\text{nb}}(\tau) e^{R_{\phi_d}(\tau)} J_0(2\rho \sin(\pi F_{\text{sens}}\tau)) \right\}. \quad (4.36)$$

The product in the time domain can be expressed as convolution in the frequency domain. By denoting  $p(\tau) = e^{R_{\phi_d}(\tau)}$ ,  $P(f) = \mathcal{F} \{p(\tau)\}$  and  $M_J(f) = \mathcal{F} \{\mu_J(\tau)\}$  with  $\mu_J(\tau) = J_0(2\rho \sin(\pi F_{\text{sens}}\tau))$ , Eq. (4.36) becomes:

$$S_w(f) = \frac{1}{\gamma_b^2} e^{-R_{\phi_d}(0)} [S_{\text{nb}}(f) * P(f) * M_J(f)]. \quad (4.37)$$

$S_{\text{nb}}(f)$  is defined in Eq. (4.8) as a rectangular window, band limited within  $[-\frac{B}{2}, \frac{B}{2}]$ .  $P(f)$  is considered a signal with most of its power concentrated around zero, with its tails near  $-\frac{B}{2}, \frac{B}{2}$ , attaining negligible values. Thus, the convolution of these terms can be evaluated as follows:

$$\begin{aligned}S_{\text{nb}}(f) * P(f) &= \int_{-\infty}^{+\infty} S_{\text{nb}}(\xi) P(f - \xi) d\xi = N_0 \int_{-\frac{B}{2}}^{\frac{B}{2}} P(f - \xi) d\xi \\ &\stackrel{u=f-\xi}{=} N_0 \int_{f-\frac{B}{2}}^{f+\frac{B}{2}} P(u) du.\end{aligned}\quad (4.38)$$

Let  $W_m$  denote the (baseband) bandwidth of the signal at the output of the receiver (or the bandwidth of the filter used at the output of the receiver), i.e the bandwidth of  $r(t)$ . Both interference  $\phi_s(t)$  and tag's  $\mu(t)$  signals are considered band limited within  $[-W_m, W_m]$ . Thus frequencies of interest (for SINR calculation) are the ones satisfying  $|f| \leq W_m$ . Additionally, it is assumed that  $W_m \ll \frac{B}{2}$ , which holds in case of large modulation index  $\beta_s$  (wideband FM).<sup>2</sup> Under those assumptions, it can be seen that the area calculated for frequency shifts  $|f| \leq W_m$  (see Fig. 4.2), is approximately constant.

<sup>2</sup>Remodulated signal attains such an index due to both large modulation index utilized at the tag and illumination from FM stations being wideband FM.

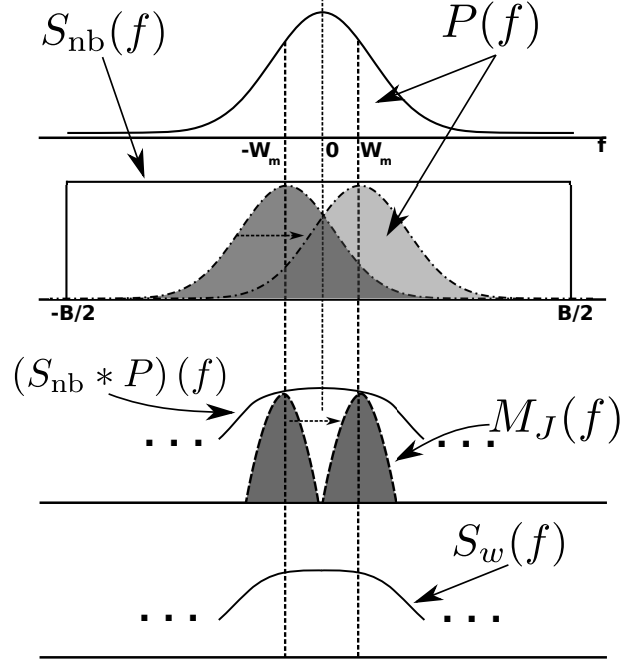


Figure 4.2: Qualitative illustration of the convolutions involved in calculating the spectral density of noise at the output of the receiver.

Because  $P(f)$  takes negligible values at its tails, it follows that for  $|f| \leq W_m$  :

$$\begin{aligned}
 S_{nb}(f) * P(f) &= N_0 \int_{f-\frac{B}{2}}^{f+\frac{B}{2}} P(u) du \\
 &\approx N_0 \int_{-\infty}^{+\infty} P(u) du = p(0) = N_0 e^{R_{\phi_d}(0)}, \text{ for } |f| \leq W_m.
 \end{aligned} \tag{4.39}$$

Using the above result, Eq. (4.37) becomes:

$$S_w(f) = \left( \frac{1}{\gamma_b^2} e^{-R_{\phi_d}(0)} N_0 e^{R_{\phi_d}(0)} \right) * M_J(f) = \left( \frac{N_0}{\gamma_b^2} \right) * M_J(f), \text{ for } |f| \leq W_m \tag{4.40}$$

As it is shown, both analytically & via simulations in Sec. 8.2.1,  $M_J(f)$  is band-limited within  $[-W_m, W_m]$ .<sup>3</sup> Because of the large value of  $B$  compared to  $W_m$ , function  $\alpha(f) = (S_{nb} * P)(f)$  can be safely assumed to attain value  $N_0 e^{R_{\phi_d}(0)}$  for  $|f| \leq W_m$ . That

<sup>3</sup>For the values of  $\rho$  utilized in this work.

way, the convolution in Eq. (4.40) can be derived as follows:

$$\begin{aligned}
S_w(f) &= \frac{1}{\gamma_b^2} e^{-R_{\phi_d}(0)} \int_{-\infty}^{\infty} M_J(\nu) \alpha(f - \nu) d\nu \stackrel{(a)}{=} \frac{1}{\gamma_b^2} e^{-R_{\phi_d}(0)} \int_{-W_m}^{W_m} M_J(\nu) \alpha(f - \nu) d\nu \\
&\stackrel{(b)}{=} \frac{N_0}{\gamma_b^2} \int_{-W_m}^{W_m} M_J(\nu) d\nu \stackrel{(a)}{=} \frac{N_0}{\gamma_b^2} \int_{-\infty}^{+\infty} M_J(\nu) d\nu \\
&= \frac{N_0}{\gamma_b^2} \mu_J(0) = \frac{N_0}{\gamma_b^2} J_0(0) = \frac{N_0}{\gamma_b^2}, \text{ for } |f| \leq W_m,
\end{aligned} \tag{4.41}$$

where in points (a) the band-limited nature of  $M_J(\cdot)$  was exploited, while in point (b) the aforementioned fact regarding  $\alpha(\cdot)$ . Process  $w_n(t)$  is filtered by a derivator, with frequency response  $H(j\omega) = j\frac{\omega}{2\pi}$ , to result  $w_d(t) = \frac{1}{2\pi} \frac{d}{dt} w_n(t)$ . That way the spectral density of  $w_d(t) = \frac{1}{2\pi} \frac{d}{dt} w_n(t)$  can be expressed as:

$$S_{w_d}(f) = S_w(f) |H(j\omega)|^2 = \frac{N_0}{\gamma_b^2} f^2, \text{ for } |f| \leq W_m. \tag{4.42}$$

Finally, the power of noise at the output of the receiver can be evaluated as:

$$P_{w_d} = \int_{-W_m}^{W_m} S_{w_d}(f) df = \frac{N_0}{\gamma_b^2} \int_{-W_m}^{W_m} f^2 df = \frac{N_0}{\gamma_b^2} \frac{f^3}{3} \Big|_{-W_m}^{W_m} = \frac{2N_0 W_m^3}{3\gamma_b^2}. \tag{4.43}$$

Notice that stronger carrier ( $\gamma_b$ ) of the illuminating FM station at the high SNR regime, results to smaller  $P_{w_d}$ . Having derived the noise power at the output of the receiver and using Eq. (4.16), output SINR, when operating at the high SNR regime, can be defined as:

$$\text{SINR}_{\text{high}} = \frac{k_{\text{sw}}^2 P_{\text{tag}}}{k_s^2 P_{\text{st}} + P_{w_d}}, \tag{4.44}$$

where  $P_{\text{tag}} = \mathbb{E}[\mu^2(t)]$  is the power of the tag's signal  $\mu(t)$  and  $P_{\text{st}} = \mathbb{E}[\phi_s^2(t)]$  denotes the power of the station's signal  $\phi_s(t)$ .

The denominator in Eq. (4.44) can be written in that form given that in the high SNR regime, the output noise in  $[-W_m, W_m]$  band of interest, can be considered independent of both the interference and the tag's information signal. This stems from the fact that the spectral density of noise at the output of the receiver (Eq. (4.42)), is only a function of frequency  $f$ , noise's spectral density  $N_0$  and impinged signal's amplitude  $\gamma_b$ . As per conventional FM analysis [47], this relationship (and Eq. (4.43)) effectively shows that in

FM, increasing the transmission power (and by extension the impinged power) lowers the noise level at the FM receiver's output.

### b) Low SNR Case

In the previous section, it was assumed that the noise level at the input of the receiver is at least 10 dB lower than that of the signal of interest. It can be shown [63], that when the power of noise at the input of the receiver is comparable to the signal's power, the noise at the output of the receiver has the form of shots, superimposed to the noise described in the previous section ( $P_{w_d}$ ). Following the analysis presented in [63], the power of shot noise is given by:

$$N_s = 8\pi^2 W_m \overline{|\delta f|} e^{-\text{SNR}}, \quad (4.45)$$

where  $\overline{|\delta f|}$  is the average, absolute frequency deviation, which needs to be calculated. In this work  $\delta f = k_s \phi_s(t) + k_{\text{sw}} \mu(t)$  (Eq. (4.5)). Using the triangle inequality,  $|\delta f|$  can be bounded as:

$$|\delta f| = |k_s \phi_s(t) + k_{\text{sw}} \mu(t)| \leq |k_s \phi_s(t)| + |k_{\text{sw}} \mu(t)| \stackrel{k_s, k_{\text{sw}} \geq 0}{=} k_s |\phi_s(t)| + k_{\text{sw}} |\mu(t)|. \quad (4.46)$$

The (time) average value of  $k_{\text{sw}} |\mu(t)|$  can be calculated as:

$$\begin{aligned} k_{\text{sw}} \overline{|\mu(t)|} &= \frac{k_{\text{sw}}}{T_{\text{sens}}} \int_{T_{\text{sens}}} |\mu(t)| dt = \frac{k_{\text{sw}}}{T_{\text{sens}}} \int_0^{T_{\text{sens}}} |\sin(2\pi F_{\text{sens}} t)| dt = \frac{2k_{\text{sw}}}{T_{\text{sens}}} \int_0^{T_{\text{sens}}/2} \sin(2\pi F_{\text{sens}} t) dt \\ &= \frac{2k_{\text{sw}}}{T_{\text{sens}}} \left[ \frac{-1}{2\pi F_{\text{sens}}} \cos(2\pi F_{\text{sens}} t) \right]_0^{T_{\text{sens}}/2} = \frac{2k_{\text{sw}}}{\pi}. \end{aligned} \quad (4.47)$$

For any  $t$ ,  $\phi_s(t)$  is assumed a zero mean, normally-distributed random variable (see below Eq. (4.22)). It can be shown (Sec. 8.2.2) that for any  $t$ , the associated random variable  $k_s |\phi_s(t)|$  attains a mean value of:

$$k_s \overline{|\phi_s(t)|} = k_s \mathbb{E}[|\phi_s(t)|] = \sqrt{\frac{2}{\pi}} k_s \sqrt{P_{st}}. \quad (4.48)$$

Using Eq. (4.47) and Eq. (4.48) on Eq. (4.46),

$$\overline{|\delta f|} \leq k_{\text{sw}} \overline{|\mu(t)|} + k_s \overline{|\phi_s(t)|} = \frac{2k_{\text{sw}}}{\pi} + \sqrt{\frac{2}{\pi}} k_s \sqrt{P_{st}} \triangleq \widehat{\delta f}. \quad (4.49)$$

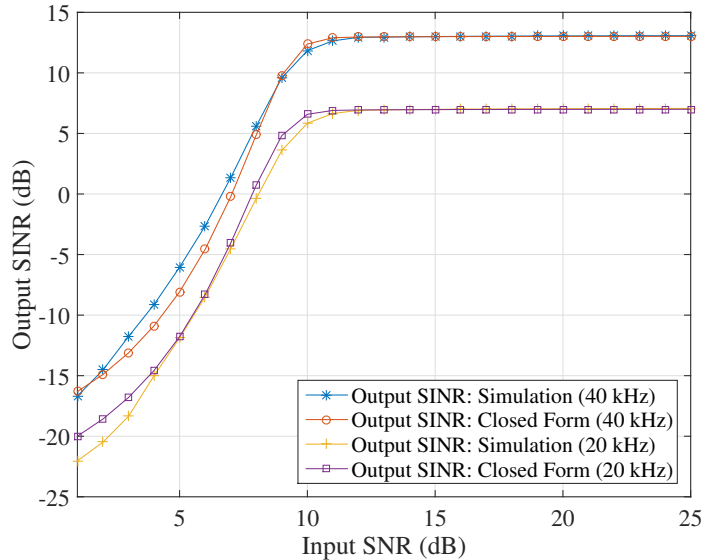


Figure 4.3: Output SINR vs input SNR for 2 different tag maximum deviation settings. The station's maximum deviation was set to 30 kHz and  $\phi_s(t)$  was a sound clip.

The upper bound  $\widehat{\delta f}$ , will be used in place of  $|\overline{\delta f}|$  in Eq. (4.45). An approximation for the power of noise  $N_s$  at the output of the FM receiver, considering an input SNR attaining values less than 10 dB, can be then given by:

$$\widetilde{N}_s = 8\pi^2 W_m \widehat{\delta f} e^{-\text{SNR}}. \quad (4.50)$$

An approximation for the SINR at the output of the receiver, can be then given as follows:

$$\text{SINR} \approx \frac{k_{\text{sw}}^2 P_{\text{tag}}}{k_s^2 P_{\text{st}} + P_{w_d} + \widetilde{N}_s} = \frac{k_{\text{sw}}^2 P_{\text{tag}}}{k_s^2 P_{\text{st}} + P_{w_d} + 8\pi^2 W_m \widehat{\delta f} e^{-\text{SNR}}}. \quad (4.51)$$

Eq. (4.51) shows that at the high SNR regime, i.e., when  $\text{SNR} \geq 10$  dB, term  $e^{-\text{SNR}}$  can be assumed zero (and result in Eq. (4.44)). However, when  $\text{SNR} < 10$  dB,  $\widetilde{N}_s$  cannot be neglected and SINR gives an approximation for the attained SINR at the FM receiver's output.

Fig. 4.3 offers the behaviour of the the receiver's output SINR, when the input SNR was varied and  $\phi_s(t)$  was a recorded audio sample from a local radio station. There are two points worth of attention in this plot. Firstly, it can be seen that around 10 dB the threshold phenomenon kicks in. Below that 10 dB threshold, the output SINR drops rapidly with respect to input SNR. This observation shows intuitively that, the more illuminating stations are available to choose from, the higher the possibility of attaining

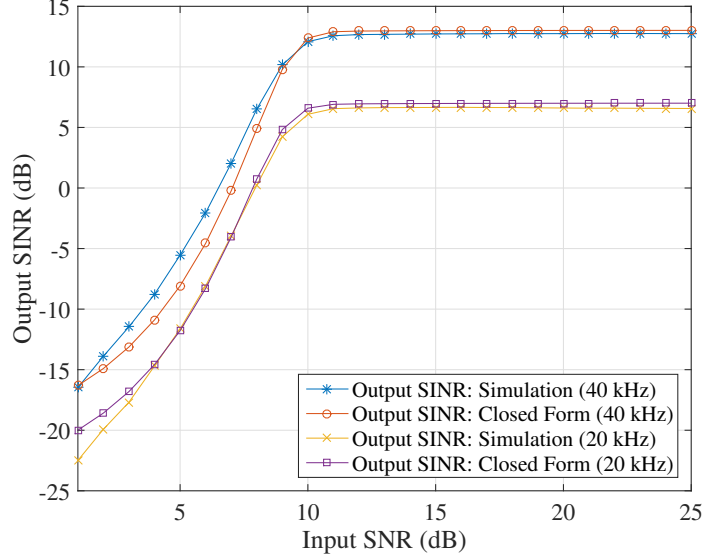


Figure 4.4: Output SINR vs input SNR for 2 different tag maximum deviation settings. The station’s maximum deviation was set to 30 kHz and  $\phi_s(t)$  was Gaussian noise.

drastically better performance, highlighting the importance of selection diversity, which will be analysed in the next section.

It can be also observed that for  $\text{SNR} > 10$  dB, the output SINR is almost constant with respect to input SNR. It must be noted that this behaviour is due to interference from station’s signal  $\phi_s(t)$ . If  $\phi_s(t) = 0$ , above the 10 dB threshold, an increase in input SNR would result a linear<sup>4</sup> increase in output S(I)NR. Fig. 4.4, repeats the simulation, with, however,  $\phi_s(t)$  modelled as Gaussian noise with same variance (i.e., equal to the power of the station’s recorded clip). The same conclusions as in Fig. 4.3 are drawn. Details for the simulation parameters are offered in Sec. 8.2.4.

### 4.1.3 Ambient Selection Diversity

As described in Chaps. (2) – (3), backscattering can be seen as a modulation operation performed in passband. Tag’s switching according to Eqs. (4.3), offers remodulated backscattered signal components at  $\{F_s \pm F_{\text{sw}}\}$ , for *all* FM stations  $s \in \{1, 2, \dots, L\}$ . Thus, a question immediately arises: from the available FM stations/illuminators  $s \in \{1, 2, \dots, L\}$ , which should the FM receiver select to tune at  $F_s \pm F_{\text{sw}}$ ? As it can be observed, there are  $2L$  possible (passband) frequencies for the utilized FM receiver to tune at, when there are  $L$  FM stations/illuminators available.

<sup>4</sup>In dB scale.

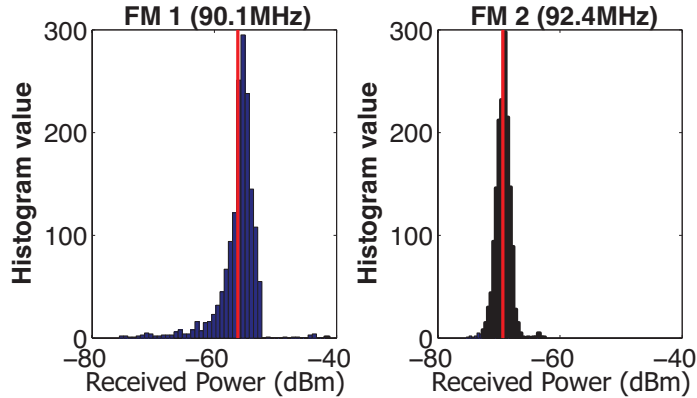


Figure 4.5: Histogram of the received power (measured at the tag's location) from 2 NLOS FM stations, 6.5 km away from the tag.

Measurements regarding the RF power offered by 2 non-line of sight (NLOS) FM radio stations, located 6.5 km away were conducted. It was found that the expected power varied significantly between the 2 stations, namely station No.1 offered  $-56$  dBm while station No.2 offered  $-69$  dBm (Fig. 4.5).<sup>5</sup>

As shown in Sec. 4.1.2, higher carrier amplitude  $\gamma_s$  results to lower impact of thermal noise at the output of the receiver. Backscatter communication is by nature link-budget limited. Thus, selecting the FM station offering the strongest received power (i.e, highest  $\gamma_s$ ) could offer better performance.

The impinged power at tag's antenna from station  $s \in \{1, 2, \dots, L\}$ ,  $\gamma_s$ , is assumed to follow a Gamma distribution with shape and scale parameters  $k_s, \theta_s$ , respectively. Similarly, the power received at the smartphone is also a Gamma-distributed random variable,  $\gamma_0$ , with shape and scale parameters  $k_0, \theta_0$ . The latter two parameters incorporate the tag fixed scattering efficiency  $s$ , as well as link-budget average loss due to tag-to-receiver (smartphone) distance  $d_0$ . The following proposition holds for the end-2-end received power  $\gamma_s \gamma_0$  of the backscattered signal at the smartphone, under selection of the stronger FM illuminator, performed among  $L$  potential FM stations:

**Proposition 4.1.** *For  $\gamma_i \sim \text{Gamma}(\cdot; k_i; \theta_i)$ ,  $i \in \{0, 1, \dots, L\}$ , the benefits of selection diversity can be assessed by the following outage probability:*

$$\Pr\left(\max_{i \in \{1, 2, \dots, L\}} \gamma_i \gamma_0 < \Theta_{RF}\right) = \frac{1}{\theta_0^{k_0}} \frac{1}{\prod_{j=0}^L \Gamma(k_j)} \int_0^{+\infty} x^{k_0-1} e^{-\frac{x}{\theta_0}} \prod_{i=1}^L \gamma\left(k_i, \frac{\Theta_{RF}}{\theta_i x}\right) dx \quad (4.52)$$

<sup>5</sup>Measurements were performed for the duration of 1 hour, every 2 sec for each station, using a portable spectrum analyzer.

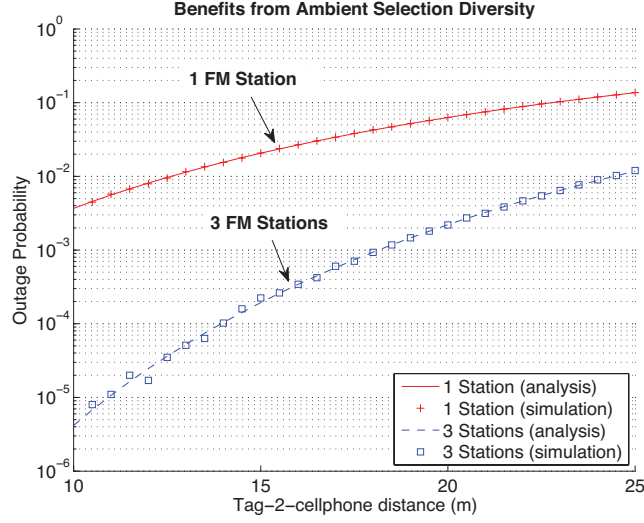


Figure 4.6: Probability of outage according to Eq. (4.52), when  $\Theta_{\text{RF}}$  corresponds to input SNR = 10 dB, value chosen according to observations in Fig. 4.3.

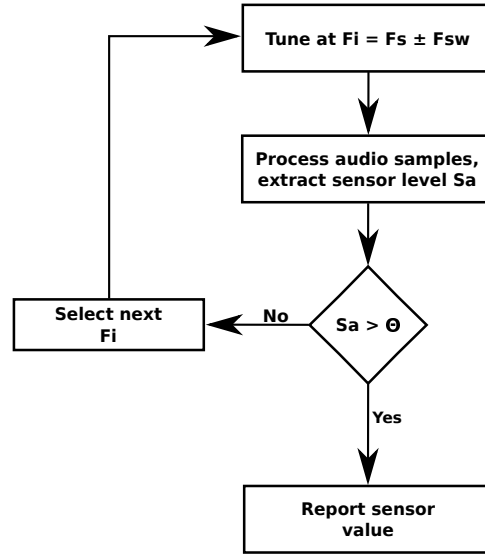


Figure 4.7: Maximizing sensor's *audio output level*.

where  $\gamma(s, x) = \int_0^x t^{s-1} e^{-t} dt$  is the lower incomplete gamma function  $\Gamma(s) = \int_0^{+\infty} t^{s-1} e^{-t} dt$  the Gamma function and  $\Theta$  is a test (fixed) threshold value. As can be seen in Fig. 4.6, the above probability decreases with increasing  $L$ . The proof is given in Sec. 8.2.3.

Nevertheless, the above selection does not necessarily minimize the interference from each FM station's own  $\phi_s(t)$  signal on the tag's signal  $\mu(t)$ . Additionally, the aforementioned selection process assumes that there is no *other* interfering signal (e.g., from another FM station) at  $F_s \pm F_{\text{sw}}$  as well as at frequencies around them.

An alternative to the above selection process, is to tune at the frequency where the demodulated sensor’s audio signal is maximized. That can be easily implemented with a single smartphone FM receiver, tuning sequentially at  $2L$  candidate frequencies  $F_s \pm F_{sw}$ ,  $s \in \{1, 2, \dots, L\}$  (for fixed  $F_{sw}$ ) and selecting the one, where the sensor’s audio tone level is above a predefined (by the user) threshold  $\Theta$ . In experiments conducted for testing the communication range (see Sec. 4.4.2),  $\Theta$  was selected 10 dB above (audio) noise (thermal and interference) floor. The described procedure is depicted in Fig. 4.7.

#### 4.1.4 Multiple Access

One way for simultaneous operation of multiple, continuous backscattering, FM remodulation tags, is to allocate the audible spectrum with non-overlapping frequency bands among the various tags, by carefully tuning the circuit producing  $\mu(t)$ .

A second way is to uniquely allocate, distinct center switching frequencies  $F_{sw}$  and frequency bands around them, among the sensors. Both ways above, essentially offer frequency division multiple access (FDMA), the first using the audible spectrum and the second using FM passband (from 88 MHz to 108 MHz).

Exploiting the capture effect inherent in the FM modulation [64], a form of spatial division multiple access (SDMA) can be also realised. The FM receiver will “lock” on the strongest (backscattered) signal. Thus, if multiple tags are placed in a given area, the receiver can be moved “near” the tag of interest in order to receive the latter’s information. Experiments showed that the slightest movement towards getting closer to a tag of interest, results in the locking of the FM receiver to the signal of said tag, despite the presence of other, backscattering tags at distances of less than 50 cm from the tag of interest.

## 4.2 Implementation

The basic tag/system idea is to design two oscillators, with the first producing sensor’s modulating signal  $\mu(t)$  (1st modulation level) and the second be driven by the first (2nd modulation level), in order to produce the FM tag signal (according to Eq. (4.3)) to be scattered back.

A capacitive  $C_s$  or resistive  $R_s$  sensing element is assumed, connected to the first oscillator, as shown in Fig. 4.8. In principle, any capacitive or resistive sensing can be utilized, as explained below. Experiments have been conducted with two different capacitive sensing elements, one for soil moisture and another for air humidity.

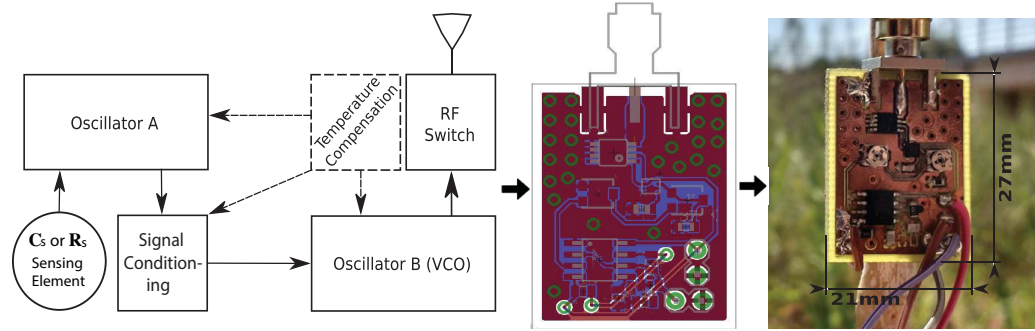


Figure 4.8: Block diagram for a tag implementing FM remodulation; the information to be backscattered is the value of a passive sensor. (Middle, Right) The PCB of the first successful prototype tag. The tag was able to measure soil moisture via a custom capacitive sensor and transmit it wirelessly at distances greater than 20 meters, while consuming  $24 \mu\text{Watts}$ .

## 4.2.1 Implementation with Discrete Components

### a) Control Circuit and Sensing Element

Oscillator A is an RC oscillator, implemented using an ultra low power version of the 555 timer, configured in astable mode, producing  $\mu(t)$  as a square wave signal; its fundamental frequency and duty cycle are determined by external components, including the value of the utilized sensors' capacitance. As discussed in Section 4.1.1, the circuit must be designed so that regardless of the sensor's value,  $\mu(t)$  will be always audible. Thus, *any* sensing capacitor can be used with the circuit, as long as the design guarantees that the output will remain audible throughout the sensor's range. In this work, a soil moisture capacitor, part of the sensor in [65, 66] was used. An environmental humidity sensing capacitor (HCH-1000), part of the sensor in [67, 68] was also tested.

Oscillator B is implemented with a Silicon Laboratories TS3002 oscillator/timer, configured as a Voltage Controlled Oscillator (VCO) (Fig. 4.8-left). VCO's control voltage is set to be  $\mu(t)$ . The oscillator produces the tag's subcarrier signal, which is FM modulated by  $\mu(t)$  (i.e., Eq. (4.3)). The maximum and minimum value of  $\mu(t)$  define the maximum and minimum frequency values produced by the VCO, which must also adhere to the required FM frequency deviation. VCO produces the FM signal with specific frequency limits/deviation; this is accomplished by scaling  $\mu(t)$  with a signal conditioning block (Fig. 4.8-Left), comprised of a resistor network. It is noted that at the time this thesis was written, TS3002 had become obsolete. In the latest prototypes, TS3002 has been substituted with Linear's LTC6906 ultra-low-power timer, configured to operate as a VCO. The latest prototypes utilize a  $F_{\text{sw}} = 300 \text{ kHz}$  and a maximum frequency deviation of  $\Delta f_{\text{max}} \approx 40 \text{ kHz}$  (for the tag).

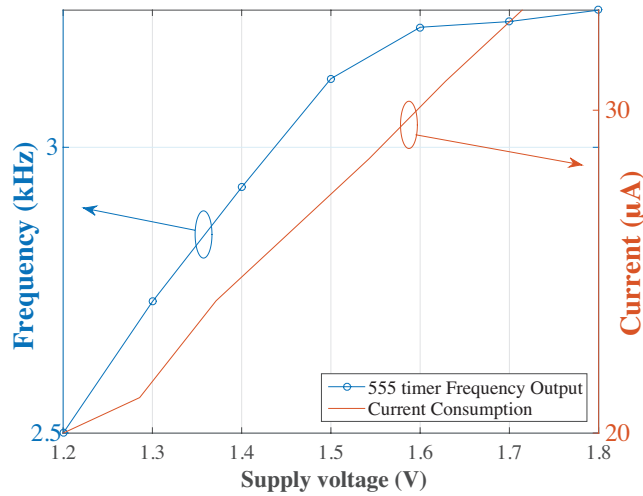


Figure 4.9: Tag’s overall current consumption/frequency drift vs supply voltage.

For fixed sensing capacitor value (sensor dry), Fig. 4.9 offers total current consumption of the overall tag, as a function of supply voltage. It can be clearly seen that the system is capable of achieving  $< 20 \mu\text{A}$  @ 1.2 V, resulting to a power consumption of **24  $\mu\text{W}$** , in *continuous* (non-duty cycled) operation. The ultra-low power consumption of the backscattering tag, allows for designing power supplies that provide power to the tag, by exploiting ambient sources of energy. A number of methods for providing power to the tag in such a way, are presented in Sec. 4.3.

For fixed Oscillator A output frequency (using a standard capacitor as sensor), Fig. 4.9 also offers the dependence of oscillator’s A fundamental frequency (i.e., of signal  $\mu(t)$ ) on supply voltage, directing the utilization of a voltage regulator, also discussed below.

### b) RF-switch

The Analog Devices ADG919 was chosen due to its ultra low power consumption ( $< 1\mu\text{A}$ ). The switch either terminates the antenna into a short-circuit ( $\Gamma_0 = -1$ ) or leaves it at an open-circuit state ( $\Gamma_1 = 1$ )

According to datasheet, its minimum operating voltage is 1.65 V. Due to the ultra low power requirements of the overall tag, the switch was tested for operating *below* its stated minimum voltage. A VNA stimulated the switch with a signal at frequency 90 MHz, power  $-10$  dBm and the reflection coefficients  $\Gamma_0, \Gamma_1$  were measured. For supply voltage 1.2 V,  $|\Delta\Gamma|_{1.2\text{V}} \triangleq |\Gamma_1 - \Gamma_0| = 1.70$  and for 1.7 V,  $|\Delta\Gamma|_{1.7\text{V}} = 1.78$ . Ignoring the expected backscattering performance degradation, the switch operates even @ 1.2 V.

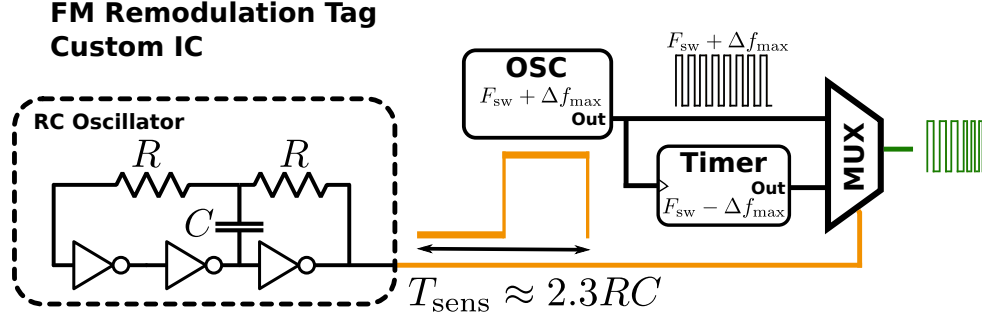


Figure 4.10: A block-level description of the single-IC implementation of FM remodulation. GreenPAK’s SLG46108 programmable matrix is used.  $\Delta f_{\text{max}}$  refers to tag’s maximum frequency deviation, while  $C$  includes the sensing capacitor. A timer is used as a frequency “prescaler”. Multiplexer’s output drives the RF switch.

## 4.2.2 Custom IC Implementation

In order to further decrease the cost of the tag, prototypes were built utilizing a single IC, integrating all the functionality required for implementing the necessary switching.

The ICs utilized for the prototypes were the one-time-programmable (OTP), mixed signal matrices of Dialog’s GreenPak series [69]. Those ICs provide resources like, for example, look-up tables, programmable logic and programmable oscillators.

The most simple among the single-IC prototypes, uses the GreenPAK SLG46108. The SLG46108 is programmed so as to implement the functionality described in the previous section, according to the block diagram of Fig. 4.8:

- **RC Oscillator:** The RC oscillator required for creating the sensor-dependent signal  $\mu(t)$ , is implemented using a ring oscillator, comprising of three inverters [70]. The oscillation frequency of the said ring oscillator, is determined by the elements of an external RC network [70]. Due to lack of information related to the internal implementation of the inverters, the oscillating frequency was experimentally measured to be  $F_{\text{sens}} = \frac{1}{2.3RC}$ , where  $R, C$  the values of the components shown in Fig. 4.10.
- **VCO:** The timer utilized in Sec. 4.2.1 produces a square wave, which is frequency modulated by  $\mu(t)$ . Because  $\mu(t)$  is also created as a square wave signal (whose fundamental frequency depends on the sensor’s value), the timer produces two signals of different frequency (the timer acts as a VCO, which is driven by a signal attaining two discrete voltage levels).

The last observation allows for the design of a VCO, using two fixed-frequency oscillators, each producing the frequency corresponding to the respective level of the RC oscillator’s output. Using a multiplexer, the input to the RF switch is chosen

among the signals of the two oscillators, by the output of the RC oscillator. The maximum frequency deviation of the tag's signal, can be adjusted by adjusting the frequencies of the two oscillators (emulating VCO).

Due to the limited resources offered by SLG46108 and to minimize the power consumption, a single, fixed frequency oscillator is utilized, with the second frequency generated by a frequency prescaler block (see Fig. 4.10).

A number of prototype FM remodulation tags have been built around the architecture shown in Fig. 4.10, and have been successfully tested. At a supply voltage of 1.8 V, the aforementioned prototypes consumed 35  $\mu\text{A}$ . The unit cost of the SLG46108 is 0.60 euros (in quantities of one).

Using SLG46533 (a programmable matrix offering more resources, compared to SLG46108), tags able to transmit a digital ID have been designed and tested, so as to facilitate ease of multiple sensor management (Sec. b)-Smartphone Application). The digital ID information is modulated on the amplitude of  $\mu(t)$  using OOK.

## 4.3 Who needs batteries?

This section studies methods for providing power, without the use of a battery, to the ultra-low-power FM remodulation tag. The energy harvesting methods include: (a) energy harvesting from ambient light using a single photodiode element (or a small solar panel) and (b) RF energy harvesting using sensitive rectenna or rectenna grids [71].

### 4.3.1 Energy Harvesting

#### a) Circuit

The operating voltage range of the tag described in Sec. 4.2 is 1.2 V to  $\sim 2$  V, while the corresponding current consumption range is 20  $\mu\text{A}$  to 40.5  $\mu\text{A}$ . Given the fact that most ambient energy harvesting elements can not directly cope with such demands, an energy management/boost converter module is necessary. In this work, the Texas Instruments BQ25504 [72] ultra low power boost converter was utilized. BQ25504 is responsible for managing the power offered by the harvesting element(s), boosting the voltage at the necessary levels and adjusting the loading of the harvesting element such that maximum power transfer is attained.

BQ25504 has integrated battery management capabilities. Energy storage elements like (super) capacitors and rechargeable batteries can be used in conjunction with the IC.

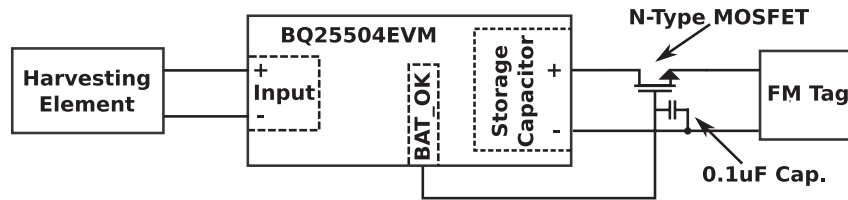


Figure 4.11: Harvesting system block diagram.

The converter also offers a storage element condition signal (BAT\_OK). The latter is set, when the voltage at the storage element is above a predefined “high” threshold and is de-asserted, when the voltage drops below a predefined “low” threshold.

When the storage element is completely discharged (below 100 mV), the boost converter must perform a cold start operation, to charge the storage element up to a specified level (set to 1.8 V). To perform the cold start operation, the input voltage (from the harvesting element) must be at least 330 mV. Once cold start has been completed, the module can manage sources offering voltages  $\leq 330$  mV.

The configuration of the boost converter module is depicted in Figure 4.11. The storage element is a 100  $\mu\text{F}$  capacitor and the nominal values for the upper and lower thresholds of the BAT\_OK signal are 2.8 V and 2.4 V, respectively. BAT\_OK drives a 5LN01SP N-Type MOSFET, which in turn connects the FM tag/load into the storage capacitor. Thus, the operating state of the tag (active/inactive) is controlled by the state of BAT\_OK signal.

A 0.1  $\mu\text{F}$  capacitor was added at the gate of the MOSFET due to oscillations observed in the BAT\_OK signal, interfering with correct operation of the tag. At first glance, the use of a single MOSFET to connect the load to the storage element, given the default configuration of the evaluation board (BQ25504EVM), seems a poor design choice. However, the use of a single MOSFET was made on purpose, to exploit the inherent drain-to-source voltage drop of  $\sim 0.8$  V such that, even under extreme conditions where the voltage at the storage element would be  $\sim 3$  V, the voltage at the tag would settle at  $\sim 2.2$  V. Such value, even though outside tag’s safe operating zone, did not affect the correct operation of the tag.

The variations of the tag’s supply voltage, can cause a variation in the frequency corresponding to the value of the sensor (Fig. 4.9). For a voltage swing of 2.4 V to 2.8 V at the capacitor side, corresponding to a swing of  $\sim 1.6$  V to  $\sim 2$  V at the tag, the frequency offset was measured in the order of 20 Hz. Depending on the application and the sensing element utilized, the aforementioned offset may not be acceptable. A solution to that problem would be to design the tag’s RC oscillator, such that the 20 Hz offset would not degrade the measurement accuracy. Another solution would be the

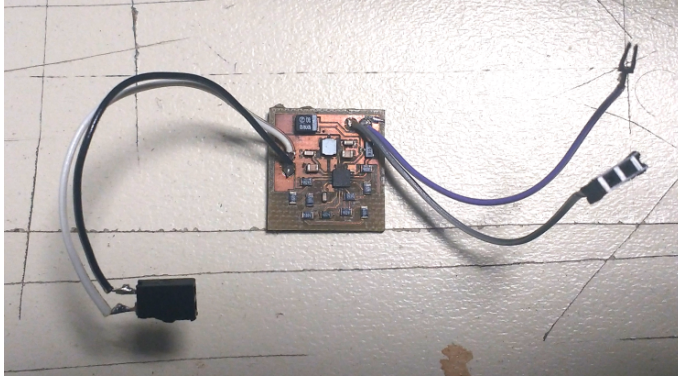


Figure 4.12: Custom, energy harvester PCB for the FM remodulation tag. The PCB can accept a number of harvesting elements.

utilization of an ultra-low power, low-dropout, voltage regulator (or a voltage reference IC that could handle the tag as a load).

Besides using the BQ25504EVM development board for testing, a PCB was designed and built in-house for further development of the proposed batteryless tags. The PCB is shown in Fig. 4.12. The aforementioned PCB represents a stand-alone power supply unit, tailored to the needs of the FM remodulation tag; the said PSU can be used in conjunction with different energy harvesting elements as will be subsequently described.

#### b) Harvesting Energy with a Photodiode

The first harvesting setup facilitates a photodiode as the element for harvesting energy from light. Examples of designing photodiodes for energy harvesting purposes, can be found in [73, 74]. A BPW34 photodiode is used, which is a PIN photodiode; an undoped, intrinsic region of silicon separates the P from the N layers, offering greater quantum efficiency compared to conventional photodiodes and higher response speeds.

The aforementioned diode can be seen as a miniature solar cell. To exploit the photodiode as a solar cell, the former is directly connected to the input terminals of the BQ25504EVM setup described earlier. Under full sunshine conditions, the photodiode was measured to provide an open circuit voltage of  $V_{oc} \simeq 0.5$  V and a short circuit current of  $I_{sc} \simeq 2.5$  mA, while the same figures for an indoor office setup, under fluorescent lighting, were  $\approx 280$  mV and  $\approx 5.4$   $\mu$ A.

**Indoor Experiments** The tag-harvester-photodiode system was tested both indoors and in outdoors. In the indoor scenario, under fluorescent lighting inside an office, the system was not able to operate, since the specific photodiode is not “tuned” for indoor lighting. As a result, the utilized boost converter could not perform its cold start

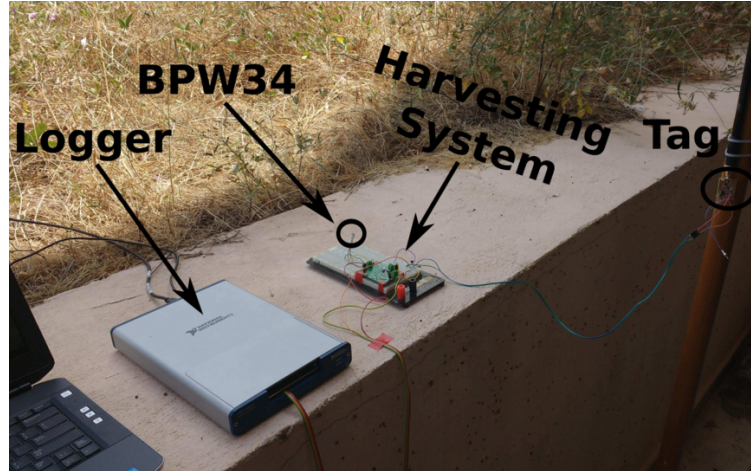


Figure 4.13: Setup for performance measurements of powering the tag using a single photodiode (partial sunshine condition).

operation, when the input voltage was below 330 mV and, as mentioned earlier, the photodiode provided only  $V_{oc} \simeq 280$  mV. It must be noted that the system would be capable to operate if a different photodiode, sensitive to indoor/fluorescent lighting, was utilized.

Nevertheless, feasibility of indoor operation was verified: the flashlight of a smartphone was used to provide light to the photodiode. Before every test, the capacitor (storage element) was short circuited in order for it to be completely depleted of charge and for cold start operation to be ensured. It was observed that, when the smartphone was located 3 cm above the photodiode, approximately one minute was needed for the system to start operation.

After the first minute, the system operated in a duty cycled fashion attaining an operational rate of 29%. When the flashlight was placed directly above the photodiode, it needed less than 1 s to begin operation and after that period, continuous operation was attained (verified by using the same phone for receiving the backscattered FM remodulated signals).

**Outdoor Experiments** The system was tested outdoors, under different illuminating conditions. The photodiode was exposed to both full sunshine and partial sunshine (Fig. 4.13) conditions. In both cases, continuous operation was attained after the cold start procedure, which lasted  $< 5$  s and  $< 20$  s for each case (full, partial sunshine, respectively). The photodiode was exposed to limited light, under cloudy conditions; after the cold start, duty cycled operation was attained with a 66% (operational) rate.

Lighting Condition	Full Sunshine	Partial Sunshine	Cloudy	Phone (3 cm)	Phone (direc.)
Cold Start Duration (sec)	4.4	17.4	28.4	63.6	0.6

Table 4.1: Time required for cold start of the system, using a photodiode as the harvesting element.

The exact times required for the system to begin operation (when the storage element is completely depleted of charge), under the various lighting conditions described above, are summarized in Table 4.1.

### c) RF Energy Harvesting Using Rectennas

To realize energy harvesting from incident RF waves, the rectenna presented in [71], in conjunction with the energy harvesting circuit described earlier, is used. The rectenna comprises of a diode-based rectifier directly connected to a bow-tie, dipole antenna. Given an input/impinging power of  $-20$  dBm, the rectenna was designed to operate within 842.2–912.1 MHz, while for the same amount of input power, the RF-to-DC conversion efficiency is 28.4% [71]. Detailed specifications and performance characterization of the utilized RF harvester can be found in [71].

As with the photodiode experiments, both outdoor and indoor scenarios were considered. The RF source was a generator configured to produce an unmodulated carrier wave centered at 868 MHz. A 3 dBi monopole antenna was used at the generator.

**RF Harvesting-Indoors** Figure 4.14 demonstrates the operation of the system, indoors, when a single rectenna is used and the generator is configured to provide 19 dBm at the antenna. The system with the rectenna was placed 1.5 m (Figure 4.14-Left) and 2.5 m (Figure 4.14-Right) away from the generator’s antenna. It can be observed that the system fails to start even after 33 minutes, when it is placed 2.5 m away from the RF source.

For 30 dBm configured at the generator, continuous operation was attained after  $< 30$  s, 1.5 m away from the generator while duty cycled operation was attained 2.5 m away after  $< 100$  s.

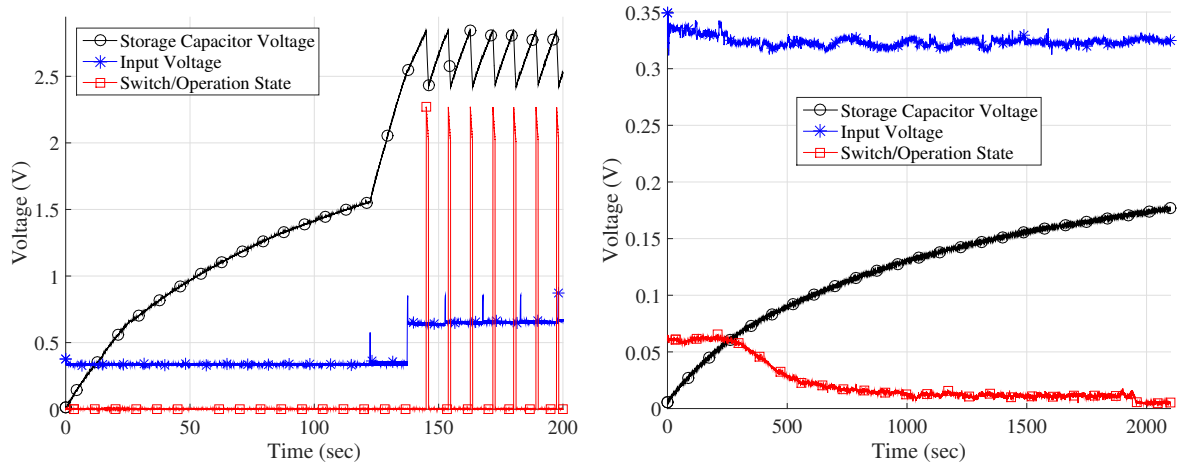


Figure 4.14: Cold start using a single rectenna (Left) 1.5 m and (Right) 2.5 m away from emitter (indoors, 19 dBm at the source’s antenna).

Experiments were also performed using an array (grid) of two rectennas. The rectennas, while being placed 17.8 cm apart, were connected to the input of the boost converter in either series or parallel configuration. Figure 4.15 offers the performance of the system (with respect to cold-start duration), when placed 2.5 m away from the generator (configured at 19 dBm). Figure 4.15-Left offers the performance for when the rectennas are connected in series, while Figure 4.15-Right the performance when connected in parallel.

It can be observed that under series configuration, the system needs more time to begin operation, compared to the respective time under parallel configuration. It can be also observed that the duty cycle rate is higher for the series configuration, compared to the parallel configuration. These observations are explained by the fact that in parallel configuration, more current is potentially available, while in series configuration more voltage is offered.

Table 4.2 offers the exact times required for the system to begin operation (due to cold start phase), when the generator is configured to 19 dBm, under various scenarios. Subsequently, Figure 4.16 depicts performance considering rectennas connected in parallel, 2.5 m away from the generator, configured at 30 dBm.

**RF Harvesting-Outdoors** Figure 4.17 offers the performance for an outdoor scenario and an array of two rectennas (located 3 m away from the RF source) connected in parallel. The generator was configured at 30 dBm. The system was able to operate up to 3 m, displaying poor performance, compared to the indoor tests. That is explained by the fact that the location where the tests were performed contained large metallic objects and the rectennas were close to the ground (as seen in Figure 4.18).

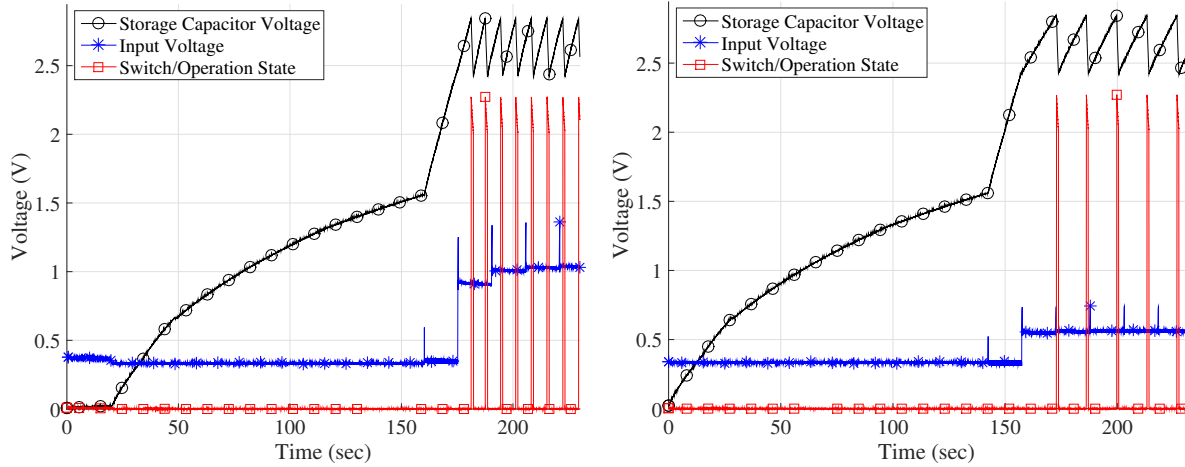


Figure 4.15: Cold start using two rectennas, 2.5 m away from emitter, in series (Left) or parallel (Right) configuration (indoors, 19 dBm at the source’s antenna).

Distance from RF source (m)	1.5	2.5
Single Rectenna	145 sec	FAIL
Two Rectennas in Series	101.2 sec	181.2 sec
Two Rectennas in Parallel	87.7 sec	172.9 sec

Table 4.2: Time required for cold start of the system using RF harvesting. The generator was configured at 19 dBm.

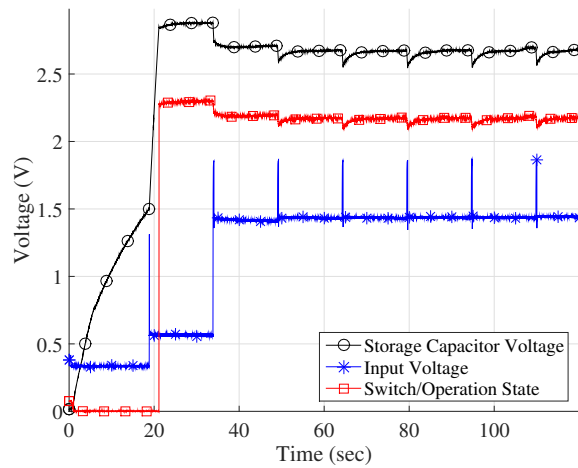


Figure 4.16: Cold start using two rectennas, 2.5 m away from emitter, in parallel configuration (indoors,  $P_{tx} = 30$  dBm).

For the experiments outdoors, the RF source was exploited as both an illuminator and a provider of energy; the tag backscattered at 868 MHz and correct operation was verified using the FM demodulation function of a spectrum analyzer.

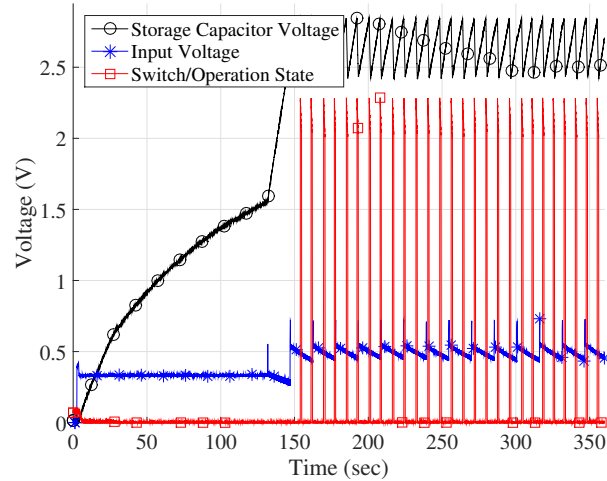


Figure 4.17: Cold start using two rectennas 3 m away from emitter in an outdoor setup (rectennas in parallel, 30 dBm at source).

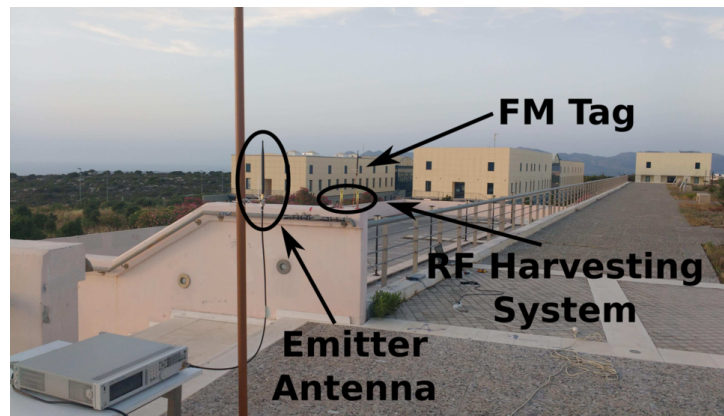


Figure 4.18: Outdoor setup for energy harvesting measurements. Two rectennas connected in parallel were used.

Given that the system has passed the cold start phase, Figure 4.19 offers the attained duty cycle rate as a function of distance from emitter, for various RF power levels configured at the generator. Figure 4.19-Left offers the duty cycle rate, when a single rectenna is used. Additionally, Figure 4.19-Left offers the impinged power at the location of the rectenna, as measured by a spectrum analyzer equipped with an antenna of same (as rectenna's) design.

As expected, the percentage of time the tag operates drops as the distance increases and follows the drop in power. At 3.5 m, a large desk was present, which might explain the peak in power and duty cycle. The last statement showcases the (inherent) sensitivity of RF harvesting performance, to the location/condition of surrounding environment. Figure 4.19-Right offers the duty cycle rate, when two rectennas are used. An interesting

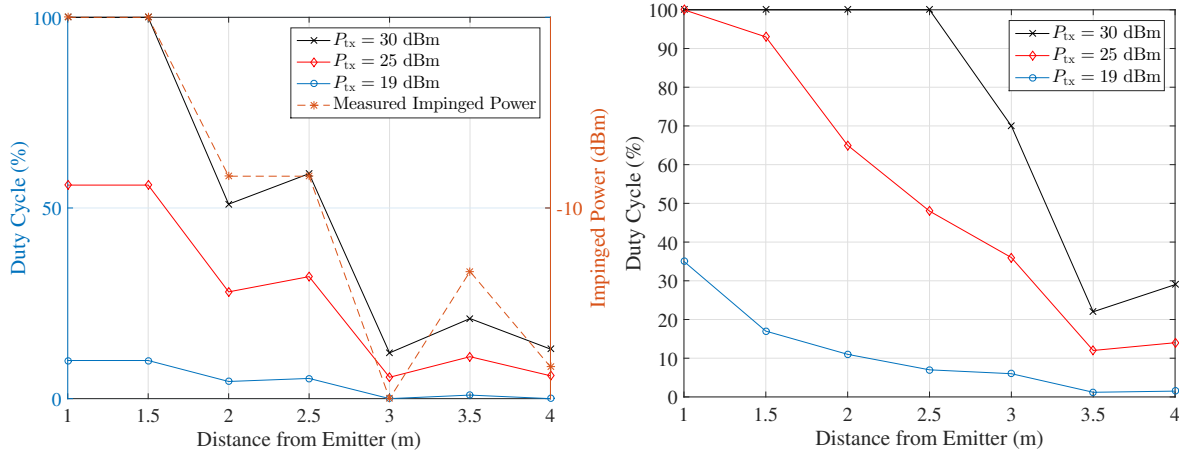


Figure 4.19: (Left) Duty cycle vs distance from carrier emitter for the case of a single rectenna. The impinged power is also displayed (generator configured at 25 dBm). (Right) Duty cycle for the case of two rectennas in a parallel configuration.

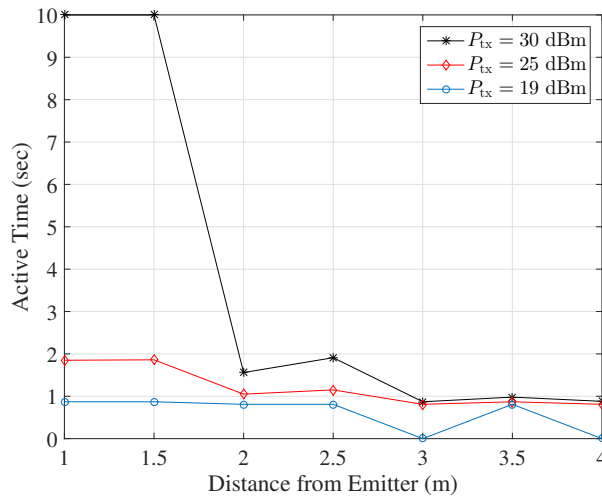


Figure 4.20: Active (operating) time vs distance from carrier emitter for the case of a single rectenna (10 s translates to continuous operation).

observation is the fact that no peak is evident, as was in Figure 4.19-Left. That might be explained by the directive characteristics resulting due to array formation caused by the two rectennas.

The time intervals for which the tag operates, as a function of distance from the RF source, are given in Figure 4.20 for a single rectenna and Figure 4.21 for two rectennas connected in parallel.

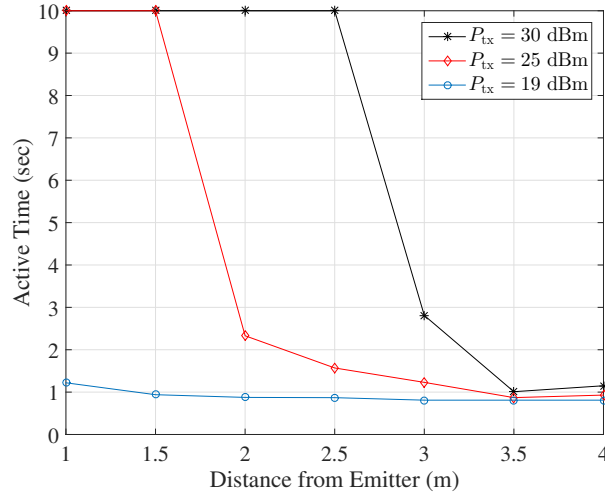


Figure 4.21: Active time for the case of two rectennas in a parallel configuration. A value of 10 s translates to continuous operation.

### 4.3.2 A Simple PSU for a Simple Tag

The selection between which of the studied harvesting methods should be utilized depends solely on the application requirements. If a backscatter network is considered, where a dedicated emitter is present and autonomous operation is required, even during the night (absence of light), then RF energy harvesting may offer the solution. When such solution is considered, one must take into account both duty cycle requirements and the fact that tags must be relatively close to the emitter, so that the sensitivity requirements of the RF harvester(s) are satisfied.

When considering a backscatter link, which exploits ambient carriers and its operation is “on demand”, i.e., a person needs to interrogate a sensor using a smartphone, the photodiode solution seems more viable, both in terms of monetary cost and practicality. Even when lighting conditions are not favourable (e.g., indoor lighting), the user can expose the photodiode to the flashlight of a smartphone and power the tag, while at the same time, the same smartphone performs sensor interrogation using ambient backscatter.

At this point one may, reasonably, ask, why use a photodiode in conjunction with an (relatively) expensive ( $\approx 4$  euros) harvesting IC, when a solar panel, combined with a low-cost, low-dropout voltage regulator, can effectively solve the same problem? Given a solar panel capable of delivering the power required by the FM remodulation tag, the problem can be solved in a ultra-low-cost manner, without any additional, (relatively) complex circuitry.

For the case of environmental sensing (e.g., outdoors, in a field), a small solar panel solves the power delivery problem, while adhering to the cost, power and complexity con-

straints. That may not be the case for other applications, where power density offered by a-relevant to application-ambient energy source (movement, RF signals, thermal gradients) would not allow “direct” exploitation of said energy source. The choice of using a harvesting IC (or custom, tailored to the application, boost converter circuitry), allows the tag to adapt in different application scenarios.

A  $31 \times 31$  mm solar has been used to power most of the tag prototypes. Under full sunlight conditions the panel was measured to provide short-circuit current  $I_{sc} = 40$  mA and open circuit voltage  $V_{oc} = 2.3$  V. The inherent solar panel output voltage variations could also cause large deviations on the received sensor value, according to Fig. 4.9. A 1.8 V voltage reference has been used to provide stable supply voltage to the tag.

## 4.4 Recovering a Sensor's Value

In the following, the tag will be assumed equipped with a custom soil moisture sensor, except where otherwise noted. The goal is to accurately recover the value of soil moisture measured by the sensor of the tag.

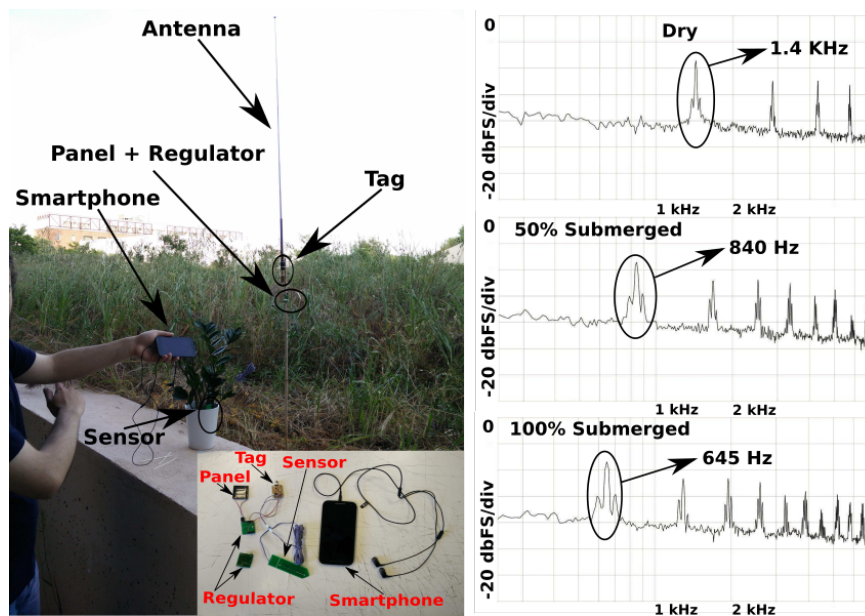


Figure 4.22: Experimental setup using a solar panel as power supply (left) and the measured spectrum of smartphone audio output; the tag sensing capacitor is being gradually submerged in a glass of water (right).

### 4.4.1 Sensor Readout Options

Any conventional FM radio receiver can be used, provided that  $\mu(t)$  is audible. The following options are readily available.

#### a) Using a Smartphone as a Receiver

A large number of smartphones is equipped with FM radio. Exploiting selection diversity and tuning at the FM station that offers the strongest demodulated tags's tone, the sensor's value can be extracted by frequency estimation of the tag's received audible tone; frequency estimation can be conducted with maximum likelihood (ML) techniques on the audio samples, using periodograms. Fig. 4.22-right shows screen captures of an audio spectrum application running on a Motorola Moto G3, while the soil moisture sensor is being gradually submerged into a glass of water. The experiment was conducted indoors, with tag supplied at 1.2 V and tag-smartphone distance of 1 m. Clearly, the water level can be detected.

#### b) Computer

If a computer (e.g., embedded microprocessor) is needed to read the sensor, two options are offered. First, any conventional FM radio receiver can be connected to the computer's audio in/microphone input. Alternatively, a software-defined radio (SDR) receiver, such as a RTL dongle, can be tuned at the FM band, perform demodulation, process the audio samples and recover sensor's information as described above.

Second, a dedicated carrier, other than the ambient FM signals, can illuminate the tag. Eq. (4.4) shows that the tag's operation is indifferent with respect to the carrier used. A computer equipped with a SDR receiver can perform FM demodulation and recover the sensor's value. To verify the last statement, experiments have been performed under illumination from an unmodulated carrier on 868 MHz. The receiver used was a low cost RTL dongle and the FM demodulation/sensor readout was performed in GNU radio. The only additional requirement of this technique is that tag's antenna should be able to receive both at the FM as well as 868 MHz UHF band.

### 4.4.2 Communication Range

Range performance of the tag-smartphone system is tested in both indoor and outdoor scenarios. The strength of the demodulated audio signal is reported, exploiting the Advanced Spectrum Analyzer PRO application, running at the smartphone. This application

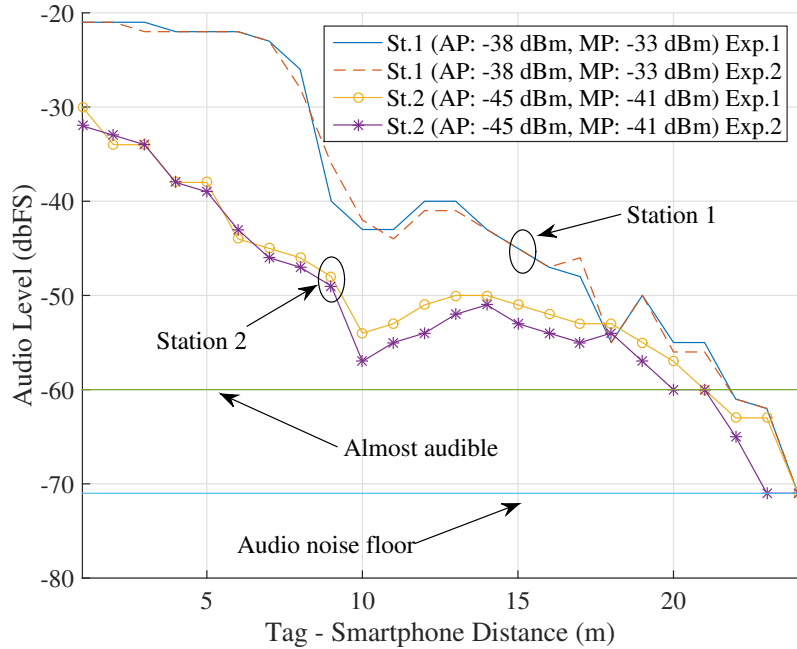


Figure 4.23: Outdoor Performance, for 2 different radio stations. AP denotes the average power and MP the maximum. dbFS is the audio level with respect to full scale microphone input (at the smartphone).

reports audio level in a scale of dbFS, which measures the audio level with respect to Full Scale audio input. Anything above  $-20$  dbFS is almost unbearable (using earphones) and anything below  $-70$  dbFS is noise.

During the tests, a standard-value capacitor was utilized as the sensing capacitor, offering a fixed (fundamental) frequency for  $\mu(t)$  at  $F_{\text{sens}} = 3.2$  kHz. That was done to ease the process of acquiring measurements by ensuring a constant “sensor value” to be estimated at the smartphone/reader. For the same reason, the tests were conducted using a 1.5V AA battery. The measurements reported audio level at 3.2 kHz, using the smartphone application’s markers. The power of FM stations’ received signal at the location of the tag was measured with a spectrum analyser.

Outdoor performance results are offered for 2 FM stations in Fig. 4.23; it can be seen that the tag achieves at least **23 meters** before the audio tone power drops below  $-60$  dbFS, i.e., 10 dB above noise, resulting to demodulated backscattered signal SINR of 10 dB. The performance was tested for two different FM stations, offering different RF power levels; for each FM station, the test was repeated twice (Experiment 1 and 2) to showcase the slight variation in the measurements, due to wireless fading in the end-2-end link from FM station-to tag-to smartphone.

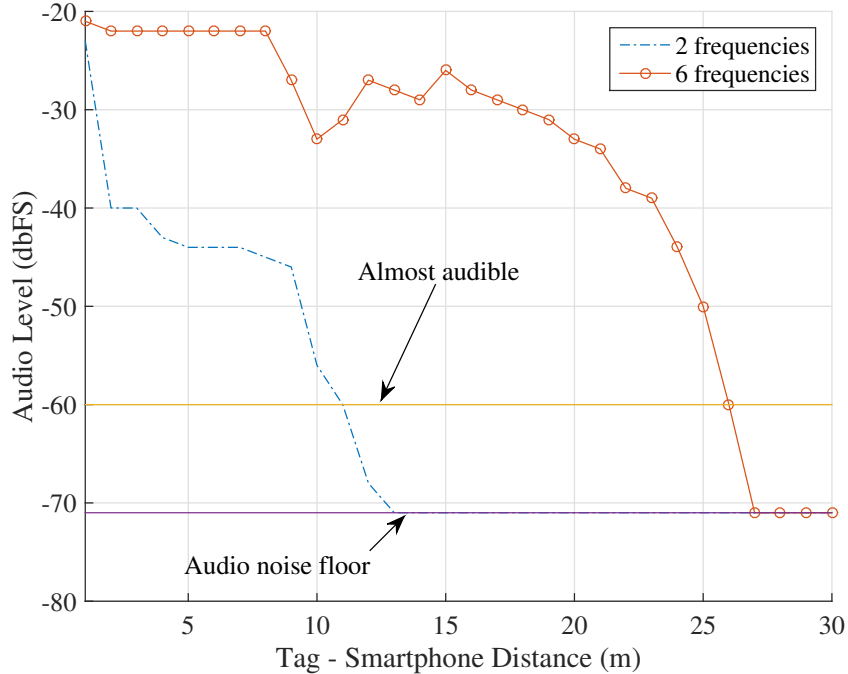


Figure 4.24: Selection among up to 3 FM stations.

The experimental results presented in Fig. 4.23, come in agreement with the analytical/simulation results offered in Fig. 4.3; both the output saturation (small tag-2-smartphone distances, up to 8 meters) and the exponential decrease can be observed in Fig. 4.23. Indoor performance tests were performed in a hallway. The communication range achieved was 16 meters exploiting an impinged power of  $-55$  dBm.

Fig. 4.24 repeats the same experiment as in Fig. 4.23 outdoors, where the smartphone selects the maximum demodulated audio sensor’s output signal power among  $L = 3$  FM stations (i.e., the smartphone tunes at  $2L = 6$  frequencies and the strongest measurement is reported). The results show significant reception improvement, offering range up to 26 m. When selection is performed among two fixed frequencies, performance is weaker, highlighting again the importance of selection diversity; the latter comes for free for backscatter radio, given that the tag switches the loads of its antenna and information is modulated on top of all impinged signals (from all illuminating stations, at tag’s antenna).

### A Note on Frequency Deviation

It was stated in Sec. 4.1.1 (and shown in Eq. (4.51)) that increasing the tag’s frequency deviation, can lead to better reception of the tag’s information signal  $\mu(t)$  at the receiver.

The effect of varying the tag’s maximum frequency deviation ( $\Delta f_{\max} = k_{\text{sw}}|\mu(t)|$ ) of the tag’s switching signal, was studied both analytically/via simulations and experimen-

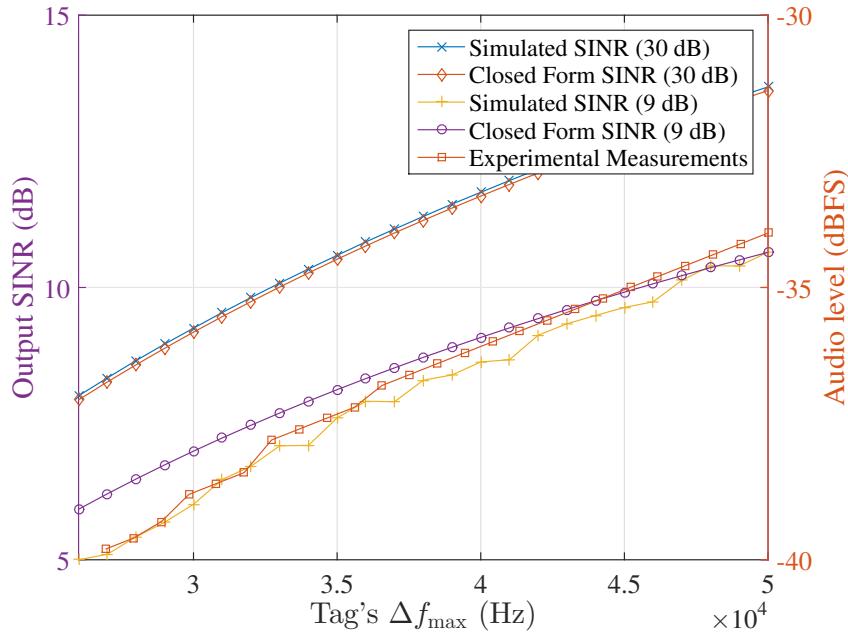


Figure 4.25: Output SINR vs tag's maximum frequency deviation  $\Delta f_{\max} = k_{\text{sw}} \max |\mu(t)|$  for input SNR of 30 and 9 dB. The station's maximum deviation was 30 kHz and  $\phi_s(t)$  a recorded sound clip. The experimental measurements correspond to the right y-axis.

tally. Experimental results were acquired using a function generator acting as the tag and adjusting the deviation setting accordingly. The generator provided both the information signal  $\mu(t)$  and the modulated subcarrier (tag's switching signal). Audio level was measured using the smartphone (the audio analyser application mentioned earlier was used) at a distance of  $\approx 30$  cm (indoors, office setting).

The results of the experiment are presented in Fig. 4.25. The simulations verify the experimental tests, where by increasing the maximum frequency deviation in the tag's VCO, higher audio levels (for the tag's signal) at the output of the receiver were observed. No threshold effect was observed (in simulations) for the deviation values utilized. That may be explained by the fixed noise bandwidth as well as the small frequency deviation values (for the utilized values of  $k_{\text{sw}}, k_s$ ), attained from Eq. (4.5) compared to that bandwidth. Linear interpolation was applied between measurements, which appeared constant due to lack of decimal digits in the reported measurement (at the smartphone). Details on how the simulations were performed are offered in Sec. 8.2.4.



Figure 4.26: Current prototypes of FM remodulation, soil moisture wireless sensors. The wireless sensors are powered using a solar panel. During the night, they can be powered using a conventional flash-light (e.g., using the flash-light of the smartphone).

## 4.5 Prototype Development

While any passive sensor (capacitive or resistive) can be used with the proposed FM remodulation tags, the work focuses on using the technology for the purposes of environmental sensing and more specifically precision agriculture. The ultra-low-cost, batteryless, easy-to-use tags, allow for any farmer to introduce the technology into his/hers empirical farming practices. Such an act can lead to better use of resources and promote sustainable farming practices. That is the reason for using soil moisture and air humidity sensors for testing the tags.

### a) Wireless Soil Moisture Sensor

**System Design** Using the FM remodulation technology, several ready-to-use, wireless soil moisture sensor nodes have been developed. The latest prototypes consist of two PCBs; upper PCB includes the RF switch (with the antenna), the voltage regulator and the solar panel, while the lower PCB comprises the actual soil moisture sensor (multi-finger, microstrip capacitor) and is inserted in the soil of interest. The upper and lower units/PCBs are connected with a 3-conductor cable. The components of the tag's controller (RC Oscillator, VCO and associated passive components), are also populated in the sensor's (lower) PCB. One of the prototypes is shown in Fig. 4.26.

The choice of populating the control circuitry in the sensor's PCB, was made to exploit the thermal insulation provided by the soil (the sensor is buried in the soil). The thermal insulation provided by the soil limits the effects of environmental temperature variations to the circuit itself, variations which could lead in significant measurement errors (due to the temperature sensitivity of electronic components).

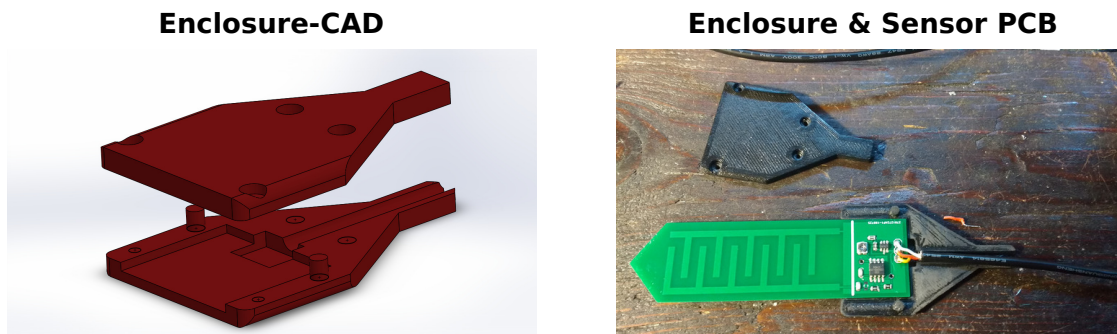


Figure 4.27: (Left) CAD-view of the enclosure designed for the lower (sensor) PCB. (Right) 3D printed enclosure with sensor PCB prior to sealing.

**Backscattering Antenna** When FM radio is used in a smartphone, a message appears so as to connect the earphones. That is because, the earphones are used as the antenna for the smartphone’s FM radio receiver. The latest prototypes exploit the same logic for lowering the cost and design complexity of the tags. A cable of appropriate length (experiments and measurements lead to a length of  $\approx 1.2$  meters) is used as the backscattering antenna. Besides lowering the cost, a flexible antenna (cable) allows for easier shipping of the tag.

**Enclosures** Both the enclosure for the upper part of the tag and the solar panel providing power, are harvested from commercially available solar garden lamps (Fig. 4.26). The utilized lamps have a cost of 1 euro/lamp. The enclosure of the lower PCB, must be fully waterproof and able to withstand the environment of the soil. It was designed in Solidworks (Fig. 4.27) and built in a 3D printer using PET-G filament (a recyclable, thermoplastic polyester, commonly used in plastic water bottles [with added glycol]).

The enclosure consists of two parts, which enclose the sensor’s PCB. The two plastic parts are sealed together (with the sensor’s PCB between them) using silicone and are mechanically held together with 4 screws. General purpose epoxy is applied on the surface of the enclosure to prevent any water leakage through the 3D printed plastic.

**Cost of Prototypes** The electronics BOM cost is  $\approx 5$  euros in quantities of 100. The cost of enclosures, solar panel and cable(s) is estimated at 1–2 euros. Thus, even with current tag designs, an overall cost of 7 euros/complete wireless sensor node is expected. Such a cost is already 1 order of magnitude lower compared to commercial soil moisture sensing solutions (e.g., Meter Group EC-5 sensor & acquisition system).

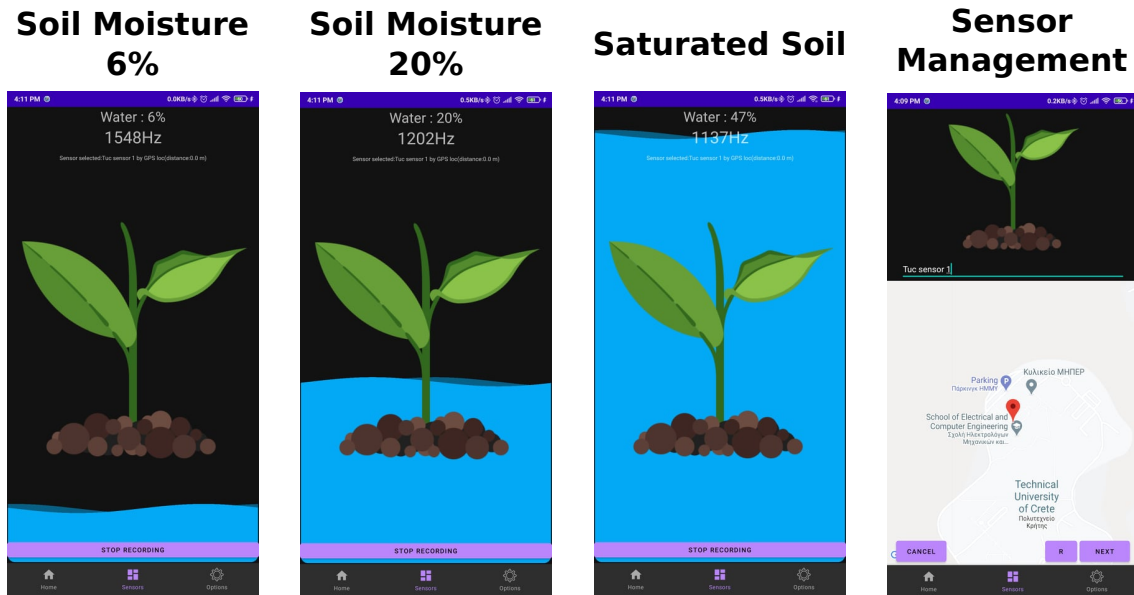


Figure 4.28: Screen captures from an android smartphone, interrogating a wireless soil moisture sensor adopting FM remodulation.

Further reduction of the overall cost is expected with newer designs that utilize the single-IC architecture described in Sec. 4.2.2. With those designs, the prototypes can be built with an electronics BOM cost of  $\approx 2$  euros.

## b) Smartphone Application

As discussed earlier, the sensor’s value can be inferred qualitatively by just hearing the pitch of the noise at the speakers of the smartphone. However, in order to provide a quantitative picture of the sensor’s actual measurement, an android application has been developed by Nick Ntantidakis. Screen captures from a smartphone running the application are offered in Fig. 4.28.

The application developed for the tag(s), like the audio spectrum analyser app mentioned earlier, processes the audio samples from the smartphone’s FM radio, so as to track the sensor’s received audio tone in the frequency domain. The frequency of the “tracked” tone is then translated into a soil moisture measurement, using an appropriate calibration curve.

The calibration, i.e., association of audio tone’s frequency with the measured soil moisture, is performed using polynomial, least squares-based, curve fitting. The calibration is performed by providing the application with known, frequency-soil moisture pairs. Using GPS information, a number of sensors can be managed through the application.

# Chapter 5

## Tags as an Antenna Array: Direction of Arrival Estimation

In the previous chapters, backscattering by switching loads at a tag (at a rate of  $F_{\text{sw}}$ ), was exploited for aiding the tag towards achieving its goal. The tag’s goal was the transmission of digital or analog information, while minimising the requirements for infrastructure, monetary cost and energy.

In this chapter, the principles presented in the previous chapters will be exploited for aiding the receiver side of a backscatter radio setup. More specifically, tags will aid the (single-antenna) receiver towards being able to solve problems, that would otherwise require it to be equipped with an antenna array (and multiple RF front-ends).

A number  $M$  of backscattering tags, each switching between its loads at a rate  $F_{\text{sw}}^{(m)}$ ,  $m \in \{1, 2, \dots, M\}$ , backscatter a signal originating from a source. As a result of the backscattering operation, multiple copies of the source’s signal “appear” in the frequency domain (see Chapter 3). If the receiver is able to discriminate those signals, problems requiring multiple independent observations of a signal (commonly solved using antenna arrays) can be solved in a ultra-low-complexity, cost and power manner.

While a number of problems requiring multi-antenna processing can be cast and solved using the the multi-tag, backscatter switching-based solution, the problem of finding the angle-of-arrival (AoA) of the source’s signal will be considered as a case-study.

### 5.1 System Model

The setup for estimating the AoA of a signal using backscatter radio is depicted in Fig. 5.1. A RF source emits modulated signals towards a single-antenna receiver. A number of single-antenna, backscattering tags are deployed in the area between the RF source and

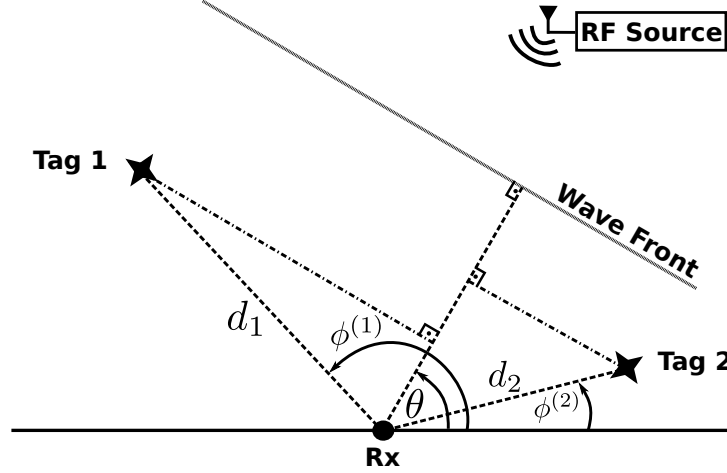


Figure 5.1: A system for estimating the angle of arrival of a signal originating from a single source, using low cost backscattering tags. The case of using  $M = 2$  tags is depicted.

the receiver. The goal for the tags-receiver system, is to find the angle with which the signal of the RF source impinges on the receiver's antenna.

Conventionally, such an estimation problem would be solved utilizing the outputs of a number of antennas, in an appropriate estimation algorithm [49]. However, such an antenna system/receiver requires a number of expensive and relative complex RF front-ends. To that end, in the following, a method will be described so as to solve the estimation problem using a number of low-cost backscattering tags.

As already stated,  $M$  backscattering tags are used. The source's signal  $\Re \{m(t) e^{j2\pi F_c t}\}$ , arrives at each tag  $m$  after time:

$$\tau_m = \tau_R - \Delta\tau_m, \quad \Delta\tau_m = \frac{d_m \cos(\phi^{(m)} - \theta)}{c}, \quad (5.1)$$

where  $\tau_R = d_R/c$  is the source-to-receiver propagation delay,  $d_R$  is the source-to-receiver distance and  $c$  is the speed of light. The tag to receiver distance is denoted by  $d_m$  and  $\phi^{(m)}$  is the associated angle. The angle of arrival of the wavefront w.r.t. the receiver is denoted by  $\theta$ . The impinged, at tag  $m$ , signal can be expressed as (see Sec. 2.3.1):

$$\Re \{c_m(t)\} = \Re \left\{ a_m m(t - \tau_m) e^{j2\pi F_c (t - \tau_m)} \right\} \approx \Re \left\{ a_m m(t) e^{j2\pi F_c t} e^{-j\phi_{CR}} e^{j2\pi \frac{d_m \cos(\phi^{(m)} - \theta)}{\lambda}} \right\}, \quad (5.2)$$

where  $a_m$  denotes the amplitude attenuation of the transmitter-to- $m^{\text{th}}$  tag link, while  $\phi_{CR} = 2\pi F_c \tau_R$ ;  $\approx$  is used due to the narrowband assumption (Sec. 2.3.1).

The signal of each of those tags can be mathematically modelled as follows (Sec. 3.2.1):

$$\mathbf{x}_{\text{tag}}^{(m)}(t) = m_{\text{dc}}^{(m)} e^{j\theta_{\text{dc}}^{(m)}} + m_{\text{tag}}^{(m)} e^{j\theta_{\text{tag}}^{(m)}} \cos\left(2\pi F_{\text{sw}}^{(m)} t + \varphi_m\right). \quad (5.3)$$

Definitions of  $m_{\text{dc}}^{(m)} e^{j\theta_{\text{dc}}^{(m)}}$ ,  $m_{\text{tag}}^{(m)} e^{j\theta_{\text{tag}}^{(m)}}$ , can be found below Eq. (3.6). As it can be seen, in contrast to the way it was designed in Sec. 3.2.2, the tag(s') switching subcarrier(s) is unmodulated. Considering homodyne reception, the model derived in Sec. 2.3.1 can be used to mathematically describe the received signal:

$$y(t) = a_{\text{CR}} e^{-j\phi_{\text{CR}}} \mathbf{m}(t) e^{-j2\pi\Delta F t} + \sum_{m=1}^M y_m(t) + n(t), \quad (5.4)$$

where  $a_{\text{CR}}$  is the amplitude attenuation introduced by the source-to-receiver link and  $n(t)$  denotes the additive Gaussian noise. Signal  $y_m(t)$  models the contribution of the  $m^{\text{th}}$  tag to the received signal and it can be expressed as follows:

$$\begin{aligned} y_m(t) &= \mathbf{c}_m(t) \mathbf{x}_{\text{tag}}^{(m)}\left(t - \tau_{\text{TR}}^{(m)}\right) s_m \mathbf{h}_{\text{TR}}^{(m)} e^{-j2\pi\Delta F t} \\ &\stackrel{\text{Eq. (5.2)}}{\approx} \mathbf{h}_m(\theta) a_m \mathbf{m}(t) e^{-j\phi_{\text{CR}}} \mathbf{x}_{\text{tag}}^{(m)}\left(t - \tau_{\text{TR}}^{(m)}\right) s_m \mathbf{h}_{\text{TR}}^{(m)} e^{-j2\pi\Delta F t}, \end{aligned}$$

where  $\mathbf{h}_m(\theta) = e^{j2\pi \frac{d_m \cos(\phi^{(m)} - \theta)}{\lambda}}$ ,  $\tau_{\text{TR}}^{(m)} = d_m/c$  and  $\mathbf{h}_{\text{TR}}^{(m)} = a_{\text{TR}}^{(m)} e^{-j\phi_{\text{TR}}^{(m)}}$  is the  $m^{\text{th}}$  tag-to-receiver channel.  $s_m$  models the scattering efficiency of the  $m^{\text{th}}$  tag. Assuming a single line-of-sight (LOS) path,  $\phi_{\text{TR}}^{(m)} = 2\pi F_c \tau_{\text{TR}}^{(m)}$ .

Similarly to Eq. (3.3.1), after performing the relevant housekeeping tasks (sampling, CFO correction), while taking into account the tags' switching subcarrier signals, the discrete baseband signal can be expressed as follows:

$$\begin{aligned} y[k] &= \mathbf{h}_d \mathbf{m}[k] + \sum_{m=1}^M \mathbf{h}_m(\theta) \mathbf{h}_{\text{TR}}^{(m)} s_m a_m \mathbf{m}[k] m_{\text{tag}}^{(m)} e^{-j\phi_{\text{CR}}} e^{j\theta_{\text{tag}}^{(m)}} \cos\left(2\pi F_{\text{sw}}^{(m)} kT_s + \Phi_t^{(m)}\right) + n(kT_s) \\ &= \mathbf{h}_d \mathbf{m}[k] + \frac{1}{2} \sum_{m=1}^M \mathbf{h}_m(\theta) \mathbf{h}_{\text{TR}}^{(m)} s_m a_m \mathbf{m}[k] m_{\text{tag}}^{(m)} e^{-j\phi_{\text{CR}}} e^{j\theta_{\text{tag}}^{(m)}} e^{j\left(2\pi F_{\text{sw}}^{(m)} kT_s + \Phi_t^{(m)}\right)} \\ &\quad + \frac{1}{2} \sum_{m=1}^M \mathbf{h}_m(\theta) \mathbf{h}_{\text{TR}}^{(m)} s_m a_m \mathbf{m}[k] m_{\text{tag}}^{(m)} e^{-j\phi_{\text{CR}}} e^{j\theta_{\text{tag}}^{(m)}} e^{-j\left(2\pi F_{\text{sw}}^{(m)} kT_s + \Phi_t^{(m)}\right)} + n(kT_s), \quad (5.5) \end{aligned}$$

where  $\mathbf{h}_d = a_{\text{CR}} e^{-j\phi_{\text{CR}}} + \sum_{m=1}^M \mathbf{h}_m(\theta) \mathbf{h}_{\text{TR}}^{(m)} s_m a_m e^{-j\phi_{\text{CR}}} m_{\text{dc}}^{(m)} e^{j\theta_{\text{dc}}^{(m)}}$  the direct link, compound channel, while  $\Phi_t^{(m)} = \varphi_m - 2\pi F_{\text{sw}}^{(m)} \tau_{\text{TR}}^{(m)}$ .

## 5.2 Processing

### 5.2.1 Emulating a Multi-Antenna Receiver

It can be seen from Eq. (5.5) that multiple, independent observations of  $\mathbf{m}[k]$  are realized through  $M$  backscattering tags and a single-antenna receiver. The aforementioned observations can be discriminated in the frequency domain due to the mixing provided by the tags' cosine term/switching operation.

The discrimination can be achieved using a set of 2 correlators, utilized in the same way as in Sec. 3.3.2:

$$r_{\mathbf{m}}^{\pm} = \sum_{k=0}^{L-1} y[k] \left( e^{\pm j2\pi F_{\text{sw}}^{(\mathbf{m})} k T_s} \right)^* . \quad (5.6)$$

Due to the aggregate of channel terms appearing in  $h_{\text{d}}$  (which can not be discriminated), the direct link term must be removed from the signal. The removal can be achieved by the correlation process if  $F_{\text{sw}}^{(\mathbf{m})} \gg \text{BW}(\mathbf{m}(t))$  (Eq. (3.14)). It is further assumed that  $|F_{\text{sw}}^{(i)} - F_{\text{sw}}^{(j)}| = \frac{k}{T_{\text{sl}}}$ ,  $i \neq j$ ,  $i, j \in \{1, \dots, M\}$ ,  $k \in \mathbb{N}$ . Parameter  $T_{\text{sl}}$  denotes the integration time window/slot duration. It is also assumed that  $F_{\text{sw}}^{(\mathbf{m})} \gg \frac{1}{T_{\text{sl}}}$ .  $L = \frac{T_{\text{sl}}}{T_s}$  is the number of samples per slot.

Under the aforementioned assumptions, similarly to Eqs. (3.16) – (3.18), the output of the  $\mathbf{m}^{\text{th}}$  correlator set for the  $l^{\text{th}}$  integration slot, takes the following form:

$$r_{\mathbf{m},l}^{\pm} = \frac{1}{2} h_{\mathbf{m}}(\theta) e^{-j\phi_{\text{TR}}^{(\mathbf{m})}} \gamma_{\mathbf{m}} e^{\pm j\Phi_{\text{t}}^{(\mathbf{m})}} \mu_{\mathbf{c}}^{(l)} + n_{\mathbf{m},l}^{\pm}, \quad (5.7)$$

where  $\gamma_{\mathbf{m}} = a_{\text{TR}}^{(\mathbf{m})} s_{\mathbf{m}} a_{\mathbf{m}} m_{\text{tag}}^{(\mathbf{m})} e^{-j\phi_{\text{CR}}} e^{j\theta_{\text{tag}}^{(\mathbf{m})}}$ ,  $n_{\mathbf{m},l}^{\pm} \sim \mathcal{CN}(0, \sigma_n^2)$ ,  $\mathbf{m} \in \{1, \dots, M\}$ ,  $n_{\mathbf{m},l}^{\pm} = \sum_{k=1}^{lL+L-1} n(kT_s) e^{\mp j2\pi F_{\text{sw}}^{(\mathbf{m})} k T_s} \sim \mathcal{CN}(0, \sigma_n^2)$ ,  $\mathbf{m} \in \{1, \dots, M\}$  and  $\sigma_n^2 = LP_n$  (see Sec. 3.3.2). Parameter  $\mu_{\mathbf{c}}^{(l)}$  is the sum of the source's samples during the  $l$ th integration window  $\mu_{\mathbf{c}}^{(l)} = \sum_{k=1}^{lL+L-1} \mathbf{m}[k]$ . Index  $l$  is omitted from the rest of the parameters by considering them invariable for the duration of  $N_s$  slots.

The phase introduced by the tags is defined as  $\Phi_{\text{t}}^{(\mathbf{m})} = \varphi_{\mathbf{m}} - 2\pi F_{\text{sw}}^{(\mathbf{m})} \tau_{\text{TR}}^{(\mathbf{m})}$ . In the context of multi-tag operation,  $\Phi_{\text{t}}^{(\mathbf{m})}$  models the synchronization error between the tags. As it will be shown in Sec. 5.3, coarse synchronization between tags is required in order for the system to offer acceptable performance. The tags must somehow be triggered to begin switching at “the same” time. Such a task can be accomplished using an energy detector (e.g., a diode envelope detector). The detector at each tag can trigger the latter, when a transmission event occurs at the source.

It is assumed that the locations of the backscattering tags are known and the associated distances can be measured up to a precision of 0.01 meters. That way, the term  $e^{-j\phi_{\text{TR}}^{(m)}}$  can be (ideally) cancelled by multiplying Eq. (5.7) with term  $e^{j2\pi F_c \hat{d}_m/c}$ , where  $\hat{d}_m$  is the (measured) distance of tag  $m$ -to-receiver. It is noted that, while the derivation has been performed under the assumption of a single LOS path, the simulated model includes statistical multipath components (block fading for  $N_s$  slots) superimposed to the LOS path (for both the source-to-tag and tag-to-receiver links).

For processing at each slot  $l$ , the following statistic is utilized:

$$r_{m,l} = r_{m,l}^+ + r_{m,l}^- = h_m(\theta) \gamma_m \cos(\Phi_t^{(m)}) \mu_c^{(l)} + n_{m,l}, \quad (5.8)$$

where  $n_{m,l} = n_{m,l}^+ + n_{m,l}^-$ . As will be subsequently explained in Sec. 5.3, using a single correlator instead of their sum is possible, but in such case the method becomes highly prone to synchronization (among tags) errors.

**Lemma 5.1.** *Under the aforementioned assumptions, the statistics from the correlators' outputs for the  $l$ th slot can be arranged in a vector as:*

$$\mathbf{r}_l = \begin{bmatrix} r_1 \\ r_2 \\ \vdots \\ r_M \end{bmatrix}_l = \mathbf{h}_p(\theta) \mu_c^{(l)} + \mathbf{n}_l, \quad (5.9)$$

where  $\mathbf{h}_p(\theta) = (\mathbf{h}(\theta) \odot \mathbf{g})$ ,  $\mathbf{h}(\theta) = [h_1(\theta), \dots, h_M(\theta)]^T$ ,  $\mathbf{g} = [\gamma_1 \cos(\Phi_t^{(1)}), \dots, \gamma_M \cos(\Phi_t^{(M)})]^T$ ,  $l \in \{0, \dots, N_s - 1\}$ ,  $\mathbf{n}_l \sim \mathcal{CN}(\mathbf{0}, 2\sigma_n^2 \mathbf{I}_M)$  and  $\odot$  denotes the element-wise product.

The above lemma shows that exploiting a number of simple, switching, backscattering tags along with the techniques proposed in Chapters 3 – 4, can lead to the emulation of a multi-antenna receiver system. That way, specific instances of problems that require such receivers can be solved in a low-complexity and cost manner.

### 5.2.2 MUSIC Processing

The autocorrelation matrix of the vector  $\mathbf{r}_l$ ,  $\mathbb{E}[\mathbf{r}_l \mathbf{r}_l^H]$ , can be expressed as:

$$\mathbf{R} = \mathbb{E}[\mathbf{r}_l \mathbf{r}_l^H] = \widetilde{\mathbf{R}} + 2\sigma_n^2 \mathbf{I}_M, \quad (5.10)$$

where  $\mathbf{I}_M$  is the  $M \times M$  identity matrix. The  $(i, j)$ <sup>th</sup> element of matrix  $\widetilde{\mathbf{R}}$  is given by:

$$\begin{aligned}\widetilde{R}_{(i,j)} &= h_i(\theta) h_j^*(\theta) \mathbb{E}[\gamma_i \gamma_j^*] \mathbb{E}[\mu_c \mu_c^*] \mathbb{E}[\cos(\Phi_t^{(i)}) \cos(\Phi_t^{(j)})] \\ &= h_i(\theta) h_j^*(\theta) \mathbb{E}[\gamma_i \gamma_j^*] \mathbb{E}[|\mu_c|^2] \mathbb{E}[\cos(\Phi_t^{(i)})] \mathbb{E}[\cos(\Phi_t^{(j)})], \quad i, j \in \{1, 2, \dots, M\}.\end{aligned}\tag{5.11}$$

It can be seen from Eq. (5.11) that, in order to avoid cross terms attaining relatively small values (compared to the diagonal entries),  $\mathbb{E}[\cos(\Phi_t^{(i)})] \mathbb{E}[\cos(\Phi_t^{(j)})]$  should be sufficiently large, compared to  $\mathbb{E}[\cos^2(\Phi_t^{(i)})]$ . This is the mathematical view of the requirement for synchronisation among the tags, described in the previous section (see below Eq. (5.7)).

In practice, matrix  $\mathbf{R}$  is not available. Thus, the processing is performed using an estimate  $\widehat{\mathbf{R}}$  of  $\mathbf{R}$ .  $\mathbf{Y} = [\mathbf{r}_1, \dots, \mathbf{r}_{N_s}]$  is defined and eigenvalue decomposition is applied to the estimated autocorrelation matrix  $\widehat{\mathbf{R}} = \frac{1}{N_s} \mathbf{Y} \mathbf{Y}^H$ :

$$\widehat{\mathbf{R}} = \mathbf{Q} \mathbf{\Lambda} \mathbf{Q}^{-1}.\tag{5.12}$$

Assuming a single RF source and  $N_s \geq M$ , the eigenvector  $\mathbf{q}_s \in \mathbb{C}^{M \times 1}$  corresponding to the largest eigenvalue spans the signal subspace. The remaining  $M - 1$  eigenvectors are arranged in a matrix  $\mathbf{Q}_n \in \mathbb{C}^{M \times M-1}$  and are utilized for the retrieval of an angle spectrum as per MUSIC algorithm [75]:

$$P(\theta) = \frac{1}{\|\mathbf{Q}_n^H \mathbf{h}(\theta)\|^2}.\tag{5.13}$$

Assuming a source having a true AoA of  $\theta_s$ , an estimate of the said AoA can be obtained as:

$$\hat{\theta}_s = \arg \max_{\theta \in [\theta_{\min}, \theta_{\max}]} P(\theta),\tag{5.14}$$

where  $\theta_{\min}$ ,  $\theta_{\max}$  are variables defining the search space.

### 5.3 Simulation Results

Simulations were performed to examine the feasibility of the proposed concept. The root mean squared error (RMSE) was considered as a performance indicator, averaged over  $10^4$  geometrically different tag and source deployments (receiver was set at the origin). Each deployment was randomly realized as  $d_m \sim \mathcal{U}[1, 20]$  m,  $\phi^{(m)} \sim \mathcal{U}[0, \pi]$ ,  $d_R \sim \mathcal{U}[20, 30]$  m, while the source's AoA was calculated as  $\theta_s \sim \mathcal{U}[0, \pi]$  (different  $\theta_s$  per experiment).

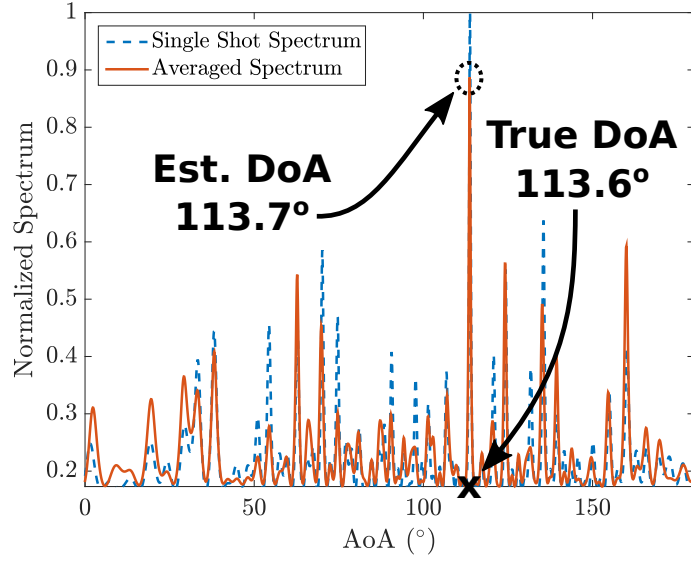


Figure 5.2: Single shot MUSIC spectrum ( $M = 5$  tags, SNR= 10dB), and averaged MUSIC spectrum over 20 packets of correlator samples.

Source-to-tags distances were calculated using the aforementioned variables. The packet length was set to  $N_s = 30$  slots. For the case of unmodulated (CW) source, the sampling rate was set to  $F_s = 1$  MHz with  $L = 10^3$ ; for the modulated source case,  $F_s = 4$  MHz with  $L = 4000$ . The aforementioned values result in a packet duration of  $N_s L T_s = 30$  ms, which satisfies the block fading requirement in minimal mobility, indoor environments.

The tag related phase  $\varphi_m$  was modeled as  $\varphi_m \sim \mathcal{N}(0, \sigma_{sw}^2)$ , where  $\sigma_{sw} = 2\pi F_{sw}^{(m)} \rho T_{sw}^{(m)}$  with  $\rho \in [0, 1]$  characterizing the tag synchronization mismatch, as a percentage of each tag's switching period. For the tag-to-reader link “cancellation”,  $\hat{d}_m$  was modelled as  $\hat{d}_m \sim \mathcal{N}(d_m, (10^{-2})^2)$ . Tag RF parameters were chosen as  $\Gamma_0^{(m)} = -\Gamma_1^{(m)} = 1$ ,  $A_s^{(m)} = 0.6047 + j0.5042$  and  $s_m \sim \mathcal{N}(\sqrt{0.1}, 0.05^2)$ .

The wireless channel parameters were statistically modelled so as to result in Rician fading. The LOS paths described in previous sections were used as the dominant paths. The Rice parameters for the involved links were set to 10. A standard pathloss model was also included with a pathloss exponent of 2.2. SNR is defined at Eq. (5.8), as the SNR of the tag attaining the minimum, combined (product of source-to-tag and tag-to-reader pathloss) pathloss.

Fig. 5.2 offers an instance of a MUSIC spectrum, acquired from a single packet of correlator samples (referred to as “Single Shot Spectrum”). In the same figure, an averaged (over 20 “packets”-sets of  $N_s$  slots) spectrum is offered. Throughout the simulations, the results are acquired after averaging the spectrum over 20 packets.

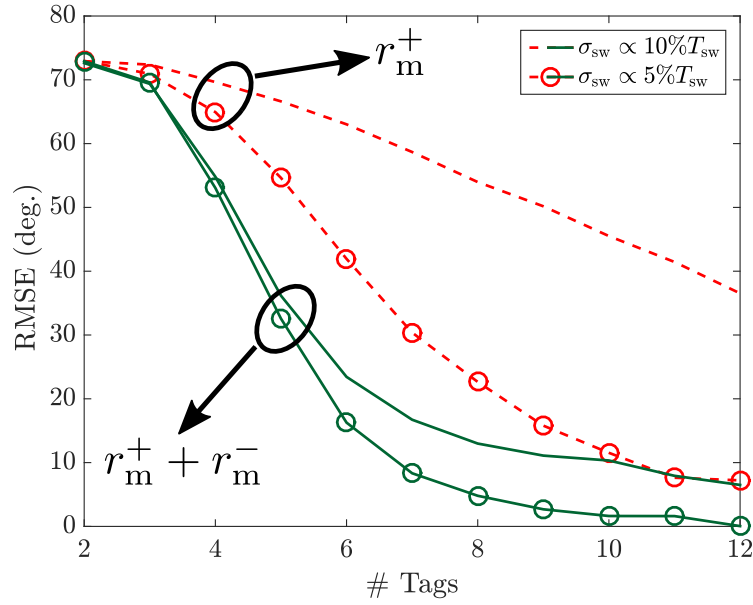


Figure 5.3: RMS error (in degrees) vs number of tags for SNR = 10 dB. Cases for two different values of  $\rho$  (modelling the synchronization mismatch among the tags) are offered, namely  $\rho = 0.1$  and  $\rho = 0.05$ . The performance for the case of exploiting only one correlator output ( $r_m^+$ ) or the sum of  $r_m^\pm$ , is also depicted.

Fig. 5.3 offers results for the RMSE performance w.r.t the number of tags utilized, for the case of  $\mathbf{m}[k] = A_c \mathbf{e}^{j\phi_c}$  (i.e., CW source). It can be seen that increasing the number of tags drastically improves the performance up to a saturation point (for  $> 9$  tags). The performance gain (w.r.t. RMSE) associated with increasing the number of tags, comes at the cost of higher bandwidth so as to facilitate the switching subcarriers ( $F_{sw}^{(m)}$ ) of the said tags.

In the same figure, the performance gap between utilizing the output of only  $r_m^+$  and utilizing the aggregate  $r_m^+ + r_m^-$  is shown. It can be seen that the gap is more pronounced for higher synchronization mismatch. The behaviour can be attributed to the fact that, utilizing only a single correlator leads to the presence of a strong diagonal component (due to the term  $\mathbf{e}^{\pm j\Phi_t^{(m)}}$ , see Eqs. (5.7),(5.11)) in  $\widetilde{\mathbf{R}}$ . The said component is constant and independent of any other variable. Thus, the combination of lower values in the cross-correlation terms (resulting from the increased synchronization mismatch) and the aforementioned constant component limits the rank deficiency of  $\widetilde{\mathbf{R}}$ . The effect can be better understood by looking at Fig. 5.4. If a single correlator is used (e.g.,  $r_m^+$ ), the diagonal term  $\mathbb{E}\left[\mathbf{e}^{j\Phi_t^{(m)}} \left(\mathbf{e}^{j\Phi_t^{(m)}}\right)^*\right] = 1$  will dominate the off-diagonal terms, as  $\sigma_{sw}$  increases.

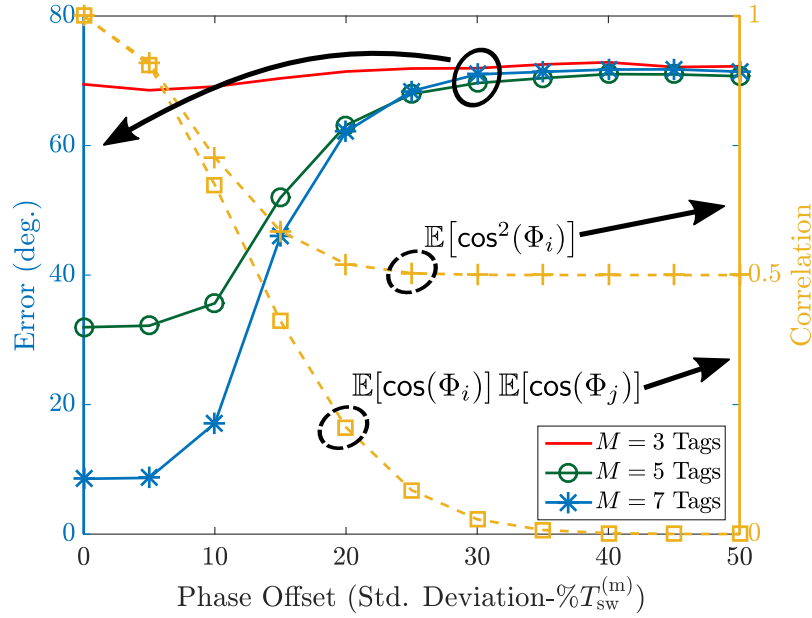


Figure 5.4: RMS error (in degrees) vs the standard deviation defining the synchronization mismatch, for SNR = 10 dB. Cases for  $M = 3, 5, 7$  tags are given. The standard deviation  $\sigma_{sw}$  is varied as a percentage  $\rho \in [0, 0.5]$  of  $T_{sw}^{(m)}$ . The analytical expressions for  $\mathbb{E}[\cos^2(\Phi_t^{(i)})]$  and  $\mathbb{E}[\cos(\Phi_t^{(i)})] \mathbb{E}[\cos(\Phi_t^{(j)})]$  are also shown. It is noted that Monte-Carlo evaluation of the aforementioned expected values, produces results that match exactly to the analytical calculations. Monte-Carlo results are omitted for reasons of figure clarity.

The performance of the proposed concept, as a function of the synchronization mismatch (stochastically varied through  $\sigma_{sw}$ , for a CW source) between the tags, is offered in Fig. 5.4. It can be seen that, depending on the number of tags and the error requirements, a synchronization mismatch of up to 10% can be tolerated. Small values of  $\sigma_{sw}$  (little to none mismatch), confine variables  $\varphi_m$  into a narrower range. Such confinement leads both the auto and cross-correlation terms (in  $\tilde{\mathbf{R}}$ ) to attain significant values, limiting the problems mentioned in the previous paragraph. It is noted that the performance degradation observed for a larger number of tags (error increases when going from 5 to 7 tags, for example) is due to the fact that it is harder for a large number of tags to be synchronized, when the mismatch deviation is increased (see Chapter 6).

As stated earlier, diagonal dominance in  $\tilde{\mathbf{R}}$  is a problem. Due to the statistical modelling of  $\varphi_m$  (and by extension  $\Phi_t^{(m)}$ ), it can be easily shown (Sec. 8.3.1) that  $\mathbb{E}[\cos^2(\Phi_t^{(i)})] = \frac{1}{2} (1 + e^{-2\sigma_{sw}^2})$  and  $\mathbb{E}[\cos(\Phi_t^{(i)})] \mathbb{E}[\cos(\Phi_t^{(j)})] = e^{-\sigma_{sw}^2}$  ( $\Phi_t^{(m)} \approx \varphi_m$ ).<sup>1</sup> It is

<sup>1</sup>Given a CW source, the switching frequencies of the tags are assumed in the order of 100 kHz. In conjunction with the distances involved, it can be safely assumed that  $2\pi F_{sw}^{(m)} \tau_m' \approx 0$  and  $\Phi_t^{(m)} \approx \varphi_m$ . To simplify the analytical expressions, the propagation term has been ignored. Including the term would not affect the behaviour of the system.

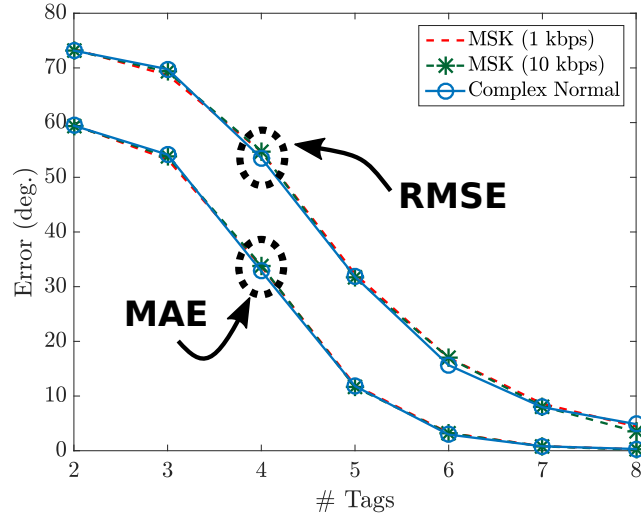


Figure 5.5: RMS & MA error (in degrees) vs number of tags for SNR = 10 dB and modulated source signals. 2 cases of MSK modulated signals are examined. The performance of when modelling the source’s baseband samples as samples drawn from a complex normal distribution is also shown.

clear from the aforementioned definitions that as  $\sigma_{sw}$  increases,  $\mathbb{E}[\cos^2(\Phi_t^{(i)})]$  will flatten out at  $1/2$ , while  $\mathbb{E}[\cos(\Phi_t^{(i)})] \mathbb{E}[\cos(\Phi_t^{(j)})]$  diminishes to zero (Fig. 5.4). Thus, the difference between the two terms (diagonal and off-diagonal) will tend to increase up to a saturation point, which explains the performance observed in Fig. 5.4.

It is worth mentioning that, even if a constant term appears in each phase  $\varphi_m$ , i.e., tags do not start at a zero phase reference/high state is modelled as non-zero mean r.v., the error behaviour remains the same. The last translates to: the tags may start at an arbitrary phase but must be synchronized to each other.

The performance of the system w.r.t. RMSE and mean absolute error (MAE) for the case of a source emitting modulated signals, is offered in Fig. 5.5. MSK of two different rates was utilized as source modulation. The case of modelling the source’s complex baseband envelope as  $\mathbf{m}[k] \sim \mathcal{CN}(0, \sigma_c^2)$  (where  $\sigma_c^2$  the source’s transmission power), was also examined. The performance of the system is similar to the performance offered in the case of an unmodulated RF source.

# Chapter 6

## Tags as an Antenna Array: Beamforming

In the previous chapter, a number of backscattering tags allowed a single antenna receiver, to solve a problem that would conventionally require the latter to be equipped with an antenna array; the backscattering tags acted like a virtual antenna array.

In this section, the same idea will be exploited so as to aid the transmitter-side of a backscatter radio setup. A number of backscattering tags will be used as distributed beamforming devices so as to aid reception of the transmitter's signals, which are subjected to severe fading conditions.

Besides lowering the complexity of beamforming by not requiring an antenna array at the transmitter, the method that will be subsequently presented, does not require any feedback from the intended receiver; the backscattering tags implement a form of distributed, *blind* beamforming.

The presence and backscattering operation of the tags, results in virtual propagation paths (that the transmitter's signal follows), which can be controlled in a blind manner. Each tag periodically alters the propagation environment, leading to constructive addition of the reflected paths at certain time intervals, offering a stronger channel and received signal at an intended receiver. Thus, instantaneous beamforming gain can be enjoyed in certain locations, at time instants when the signals from the virtual propagation paths, "align" with the signals from the "environment's" propagation paths.

The assistive tags alter the propagation environment blindly, by constantly changing the termination loads of their antennas, in a predefined pattern. Thus, beside constructive addition events, destructive interference is also probable. Depending on the application, such a problem may not pose a serious limitation.

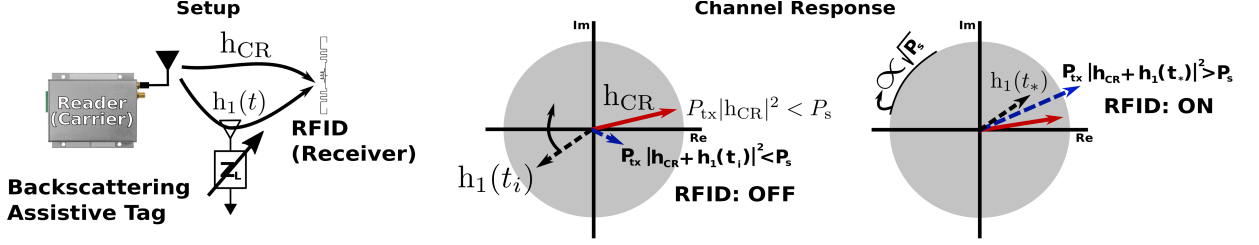


Figure 6.1: A commodity wireless transmitter-receiver link (RFID Gen2 was considered as a case-study) is aided by the presence of backscattering assistive tag(s). RFIDs that could not be interrogated due to insufficient impinging power (below sensitivity threshold  $P_s$ ), were successfully interrogated with the aid of the proposed assistive tags.

## 6.1 Basic Idea and Signal Model

A backscatter radio setup is assumed, where a transmitter illuminates a backscattering, *assistive* tag and a receiver. As a case study example, the proposed techniques will be tested on commercial Gen2 RFID protocol. In that case, the transmitter is the RFID reader, while the receiver is the RFID tag.

Flat fading is assumed, with  $h_{CR} = a_{CR}e^{-j\phi_{CR}}$  complex scale factor,  $a_{CR} \in \mathbb{R}_+$ ,  $\phi_{CR} \in [0, 2\pi)$ , characterizing the effect of multipath fading between transmitter and receiver. Assuming transmission amplitude  $\sqrt{2P_{tx}}$  at center frequency of  $F_c$ , the impinging signal at the receiver can be simplified to:

$$r_G(t) = \sqrt{2P_{tx}} \Re\{h_{CR}e^{j2\pi F_c t}\}. \quad (6.1)$$

In that case, an RFID tag receives the above signal, however the impinging power is not strong enough, and thus, tag's RF energy harvesting circuits fail to activate it. Hence, the RFID tag cannot be read from the illuminating reader (depicted in Fig. 6.1-middle).

Assume now that an “assistive” tag is placed in the vicinity of the transmitter-receiver/RFID link. That tag adds another path between transmitter and receiver, denoted through the complex coefficient  $h_1$ , altering the impinging signal at the receiver, as follows:

$$r(t) = \sqrt{2P_{tx}} \Re\{(h_{CR} + h_1(t))e^{j2\pi F_c t}\}, \quad (6.2)$$

where  $h_{CR} + h_1(t)$  expresses the overall multipath contribution to the link, introduced by the environment and the assistive tag. If the two complex coefficients  $h_{CR}$ ,  $h_1(t)$  or equivalently their representation vectors align towards the same direction, then there will be constructive addition that further enhances the impinging signal at the receiver. On the

other hand, the phases of the equivalent channel vectors may offer destructive addition, further weakening the received signal.

The assistive tag changes periodically the phase of  $h_1(t)$ , so that its vector representation rotates in the complex plane, ensuring time intervals with constructive alignment between  $h_{\text{CR}}$  and  $h_1(t)$  (depicted in Fig. 6.1-right). It is emphasized that the rotation of  $h_1(t)$  due to assistive tag's operation is necessary, as the latter is assumed to receive no feedback from the receiver, regarding the appropriate phase to be selected that offers constructive addition leading to beamforming gain.

For the special case of RFID reception, the assistive tag boosts the power of the impinged signal at the RFID's location; the RFID can then be sufficiently powered and thus, be successfully interrogated (Fig. 6.1-right) by the transmitter/RFID-reader. Such effect will be experimentally demonstrated in Section 6.4.

Despite being fixated at a location, the assistive tag can manifest such change of  $h_1(t)$ , using backscatter radio principles (Sec. 2). Specifically, the assistive tag terminates its antenna to a variable load, which in turn modifies its reflection coefficient. The latter controls the phase of the signal reflected from the assistive tag, towards the receiver (RFID). More specifically, the aforementioned factor is expressed as:

$$h_1(t) = h_{\text{CT}}^{(1)} s_1 \left( A_s^{(1)} - \Gamma_1(t) \right) h_{\text{TR}}^{(1)}, \quad (6.3)$$

where  $h_{\text{CT}}^{(1)}$ ,  $h_{\text{TR}}^{(1)}$  are the complex parameters that represent the wireless channel from transmitter (carrier, RFID reader) to assistive tag and from assistive tag to receiver (RFID), respectively. The term  $A_s^{(1)} - \Gamma_1$  controls the signal reflected from the assistive tag, while parameter  $s_1$  models the scattering efficiency (for more details, see Sec. 2).

As already discussed in previous sections, varying the assistive tag's terminating load modifies the reflection coefficient, which in turn modifies the phase of  $h_1$ . Simple, passive (i.e., without amplification) circuitry to implement such operation will be provided in Section 6.3. It is further noted that reflection may not be necessarily passive, i.e., the assistive tag may also utilize a reflection amplifier to reflect-and-amplify, simultaneously (leading to  $|\Gamma_1(t)| > 1$ ).

More than one assistive tags may be utilized and operate independently. In that scenario, the received signal at the location of the RFID tag is given by:

$$r(t) = \sqrt{2P_{\text{tx}}} \Re \left\{ \left( h_{\text{CR}} + \sum_{m=1}^M h_m(t) \right) e^{j2\pi F_c t} \right\} = \sqrt{2P_{\text{tx}}} \Re \left\{ h(t) e^{j2\pi F_c t} \right\}, \quad (6.4)$$

where  $M$  is the number of assistive tags and  $h_m(t)$  follows Eq. (6.3).

## 6.2 Analysis

### 6.2.1 Compound Wireless Channel

Denoting  $h_{\text{CT}}^{(m)} \triangleq \sqrt{L_{\text{CT}}^{(m)}} a_{\text{CT}}^{(m)} e^{-j\phi_m}$ ,  $a_{\text{CT}}^{(m)} \in \mathbb{R}_+$ ,  $\phi_m \in [0, 2\pi)$  and  $h_{\text{TR}}^{(m)} \triangleq \sqrt{L_{\text{TR}}^{(m)}} a_{\text{TR}}^{(m)} e^{-j\phi'_m}$ ,  $a_{\text{TR}}^{(m)} \in \mathbb{R}_+$ ,  $\phi'_m \in [0, 2\pi)$ , the following holds:

$$h(t) \triangleq h_{\text{CR}} + \sum_{m=1}^M h_m(t) = \sqrt{L_0} a_0 e^{-j\phi_0} + \sum_{m=1}^M \tilde{\gamma}_m(t) e^{-j(\phi_m + \phi'_m - \Theta_m(t))}, \quad (6.5)$$

where  $\tilde{\gamma}_m(t) \triangleq \sqrt{L_{\text{CT}}^{(m)} L_{\text{TR}}^{(m)}} a_{\text{CT}}^{(m)} a_{\text{TR}}^{(m)} s_m \gamma_m(t)$ ,  $\gamma_m(t) e^{j\Theta_m(t)} \triangleq (A_s^{(m)} - \Gamma_m(t))$ ,  $\gamma_m(t) \in \mathbb{R}_+$ ,  $\Theta_m(t) \in [0, 2\pi)$ . The direct link pathloss, associated with the carrier-to-RFID (reader-to-RFID) link CR, is defined as  $L_0 = G_R G_A \left(\frac{\lambda}{4\pi}\right)^2 \frac{1}{d_{\text{CR}}^2}$ , where  $d_{\text{CR}}$  the reader-to-RFID distance. Parameters  $L_{\text{CT}}^{(m)}$ ,  $L_{\text{TR}}^{(m)}$  model the pathloss of the reader-to- $m^{\text{th}}$  assistive and  $m^{\text{th}}$  assistive-to-RFID links, respectively:

$$L_{\text{CT}}^{(m)} = G_R G_A \left(\frac{\lambda}{4\pi}\right)^2 \frac{1}{d_{m,\text{CT}}^2}, \quad L_{\text{TR}}^{(m)} = G_A G_G \left(\frac{\lambda}{4\pi}\right)^2 \frac{1}{d_{m,\text{TR}}^2}, \quad (6.6)$$

where  $G_R$ ,  $G_A$ ,  $G_G$  the gains of the reader's, assistive tag's and RFID's antennas, respectively.  $\lambda = \frac{3 \cdot 10^8}{F_c}$  denotes the wavelength and  $d_{m,\text{CT}}$ ,  $d_{m,\text{TR}}$  the reader-to- $m^{\text{th}}$  assistive and  $m^{\text{th}}$  assistive-to-RFID distances, respectively.

Time is split in slots. In each slot  $k$ , a different load is connected to the antenna of the assistive tag. The duration of each slot, based on the transmitter-receiver link bit rate and packet length properties, accommodates  $N_G \geq 1$  complete transmission phases, i.e., interrogations. Each transmission phase describes one complete packet transmission, including all necessary handshaking between transmitter and receiver.

It is further assumed that all wireless channel parameters are block-constant (for each interrogation) and vary randomly between successive interrogations.<sup>1</sup> Hence, wireless channel parameters have been modified between consecutive slots and Eq. (6.5) can be expressed, per-slot, as follows:

$$h[k] = \sqrt{L_0} a_0 e^{-j\phi_0} + \sum_{m=1}^M \tilde{\gamma}_m[k] e^{-j(\phi_m + \phi'_m - \Theta_m[k])}. \quad (6.7)$$

<sup>1</sup>The circuit and antenna related parameters of the assistive tag, are assumed constant.

The maximum beamforming gain is achieved, when all of the two-dimensional vectors<sup>2</sup> involved in Eq. (6.7), align with each other. Exact alignment is not necessary. Beamforming gain can be enjoyed at RFID's location, even when the individual channel vectors align within a specific sector. However, as it will be shown in Sec. 6.2.4, a larger spread of the angles, leads to a combined channel of smaller magnitude and thus the maximum achievable beamforming gain is reduced.

Besides causing constructive addition at some slot  $k_c$ , the rotating vector (due to  $\Theta_m[k]$ ), may result in destructive addition at some other slot  $k_d$ . Since the goal is to achieve successful reception at least once (e.g., at  $k_c$ ), that drawback is not considered a serious issue. However, as will be subsequently shown through simulation results, depending on the propagation environment, several slots may be needed until an alignment event.

### 6.2.2 Phase Alignment

As stated in the previous section, beamforming gain is offered, when all the vectors (see Eq. (6.7)) add constructively or, equivalently, the angles of these vectors align within a specified sector. The above can be informally stated as follows:

$$\phi_i + \phi'_i - \Theta_i[k] \approx \phi_j + \phi'_j - \Theta_j[k], \forall i, j \in \{0, 1, \dots, M\}, \text{ with } i \neq j. \quad (6.8)$$

The aforementioned constraint can be expressed formally as:

$$\cos(\phi_i + \phi'_i - \Theta_i[k] - (\phi_j + \phi'_j - \Theta_j[k])) \geq \cos(\epsilon), \forall i, j \in \{0, 1, \dots, M\}, \text{ with } i \neq j, \quad (6.9)$$

where  $\epsilon$  defines the alignment sector angle. It is also noted that notation-wise,  $\phi_0 + \phi'_0 - \Theta_0[k] \equiv \phi_0$  ( $\phi'_0 = \Theta_0[k] = 0, \forall k$ ) since index  $m = 0$  is reserved for modelling the direct channel parameters (i.e.,  $h_{CR} = \sqrt{L_0}a_0e^{-j\phi_0}$ ).

### 6.2.3 Probability of Alignment

It is assumed that the PDF of  $\Phi_m \triangleq \phi_m + \phi'_m$ ,  $f_{\Phi_m}(\Phi_m)$  is available. Additionally, phases  $\Theta_m[k]$  are known. The analysis performed in this section, is not limited to known assistive tag phases. Randomness can be introduced to  $\Theta_m[k]$ . In such case, the characteristics of  $\Theta_m[k]$  must be taken into account in the calculation of relevant PDF and CDF. For the

---

<sup>2</sup>Each complex channel coefficient is viewed as a phasor on the complex, two-dimensional plane, as shown in Fig. 6.1.

$k^{\text{th}}$  slot,

$$\bar{\phi}_m^k = \Phi_m - \Theta_m[k]. \quad (6.10)$$

The PDF of  $\bar{\phi}_m^k$  is given by  $f_{\bar{\phi}_m^k}(\bar{\phi}_m^k) = f_{\Phi_m}(\bar{\phi}_m^k + \Theta_m[k])$  [56]. Accordingly, the CDF of  $\bar{\phi}_m^k$  is given by  $F_{\bar{\phi}_m^k}(x) = F_{\Phi_m}(x + \Theta_m[k])$ . Next,  $[0, 2\pi)$ -limited  $\tilde{\phi}_m^k = (\bar{\phi}_m^k \bmod 2\pi)$  random variables (r.v.) are defined, with PDF(s) given by [76]:

$$f_{\tilde{\phi}_m^k}(\tilde{\phi}_m^k) = \sum_{n \in \mathbb{Z}} f_{\bar{\phi}_m^k}(\tilde{\phi}_m^k + n \cdot 2\pi) = \sum_{n \in \mathbb{Z}} f_{\Phi_m}(\tilde{\phi}_m^k + n \cdot 2\pi + \Theta_m[k]). \quad (6.11)$$

The CDF of (each)  $\tilde{\phi}_m^k$  can be expressed as:

$$\begin{aligned} F_{\tilde{\phi}_m^k}(x) &= \int_0^x f_{\tilde{\phi}_m^k}(u) du = \int_0^x \sum_{n \in \mathbb{Z}} f_{\Phi_m}(u + n \cdot 2\pi + \Theta_m[k]) du \stackrel{(1)}{=} \sum_{n \in \mathbb{Z}} \int_{n \cdot 2\pi + \Theta_m[k]}^{x + n \cdot 2\pi + \Theta_m[k]} f_{\Phi_m}(\xi) d\xi \\ &= \sum_{n \in \mathbb{Z}} [F_{\Phi_m}(x + n \cdot 2\pi + \Theta_m[k]) - F_{\Phi_m}(n \cdot 2\pi + \Theta_m[k])] \\ &= \sum_{n \in \mathbb{Z}} F_{\Phi_m}(x + n \cdot 2\pi + \Theta_m[k]) - \underbrace{\sum_{n \in \mathbb{Z}} F_{\Phi_m}(n \cdot 2\pi + \Theta_m[k])}_{\text{Fixed given } n, \Theta_m[k]}, \quad x \in [0, 2\pi), \end{aligned} \quad (6.12)$$

where in (1), the substitution  $\xi = u + n \cdot 2\pi + \Theta_m[k]$  was used. Using Eq. (6.9), the probability of alignment (at slot  $k$ ) is defined as:

$$p[k] \triangleq \mathbb{P} \left( \bigcap_{i \neq j} \cos(\bar{\phi}_i^k - \bar{\phi}_j^k) \geq \cos(\epsilon) \right), \quad \forall i, j \in \{0, 1, \dots, M\}, \text{ with } i \neq j. \quad (6.13)$$

It can be shown [77], that for a collection of random variables  $\{\tilde{\phi}_m^k\}_{m=0}^M$ ,  $p[k]$  can be lower-bounded, as follows:

$$p[k] \geq \mathbb{P} \left( \max \{\tilde{\phi}_m^k\}_{m=0}^M - \min \{\tilde{\phi}_m^k\}_{m=0}^M \leq \epsilon \right). \quad (6.14)$$

For  $\epsilon < \frac{\pi}{4}$  the lower bound is tight. Exploiting the results of [77], the lower bound of Eq. (6.14) will be calculated. Let  $y = \min \{\tilde{\phi}_m^k\}_{m=0}^M$  and  $x = \max \{\tilde{\phi}_m^k\}_{m=0}^M$ . The joint PDF of the aforementioned variables is given by:

$$f(y, x) = \begin{cases} g(y, x), & y \leq x \\ 0, & \text{otherwise} \end{cases}, \quad (6.15)$$

where  $\mathbf{g}(y, x)$  is defined as [77]:

$$\mathbf{g}(y, x) = \sum_{(\beta_1, \beta_2), \beta_1 \neq \beta_2} \left[ \mathbf{f}_{\tilde{\phi}_{\beta_1}^k}(y) \mathbf{f}_{\tilde{\phi}_{\beta_2}^k}(x) + \mathbf{f}_{\tilde{\phi}_{\beta_1}^k}(x) \mathbf{f}_{\tilde{\phi}_{\beta_2}^k}(y) \right] \prod_{\beta_3, \beta_3 \neq \beta_1, \beta_3 \neq \beta_2} \left( \mathbf{F}_{\tilde{\phi}_{\beta_3}^k}(x) - \mathbf{F}_{\tilde{\phi}_{\beta_3}^k}(y) \right), \quad (6.16)$$

and  $\beta_1, \beta_2, \beta_3 \in \{0, 1, 2, \dots, M\}$ . For example, in a setup where two assistive tags are used ( $M = 2$ ), a total of  $M + 1 = 3$  random variables are involved in Eq. (6.14). In that case, function  $\mathbf{g}(y, x)$  is given by:

$$\begin{aligned} \mathbf{g}(y, x) = & \left[ \mathbf{f}_{\tilde{\phi}_0^k}(y) \mathbf{f}_{\tilde{\phi}_1^k}(x) + \mathbf{f}_{\tilde{\phi}_0^k}(x) \mathbf{f}_{\tilde{\phi}_1^k}(y) \right] \left( \mathbf{F}_{\tilde{\phi}_2^k}(x) - \mathbf{F}_{\tilde{\phi}_2^k}(y) \right) \\ & + \left[ \mathbf{f}_{\tilde{\phi}_0^k}(y) \mathbf{f}_{\tilde{\phi}_2^k}(x) + \mathbf{f}_{\tilde{\phi}_0^k}(x) \mathbf{f}_{\tilde{\phi}_2^k}(y) \right] \left( \mathbf{F}_{\tilde{\phi}_1^k}(x) - \mathbf{F}_{\tilde{\phi}_1^k}(y) \right) \\ & + \left[ \mathbf{f}_{\tilde{\phi}_1^k}(y) \mathbf{f}_{\tilde{\phi}_2^k}(x) + \mathbf{f}_{\tilde{\phi}_1^k}(x) \mathbf{f}_{\tilde{\phi}_2^k}(y) \right] \left( \mathbf{F}_{\tilde{\phi}_0^k}(x) - \mathbf{F}_{\tilde{\phi}_0^k}(y) \right). \end{aligned} \quad (6.17)$$

Finally, probability  $\mathbf{p}[k]$  can be bounded as:

$$\mathbf{p}[k] \geq \mathbf{P} \left( \max_{m=0} \left\{ \tilde{\phi}_m^k \right\}^M - \min_{m=0} \left\{ \tilde{\phi}_m^k \right\}^M \leq \epsilon \right) = \int_{y=0}^{2\pi} \int_{x=y}^{\min\{y+\epsilon, 2\pi\}} \mathbf{f}(y, x) dx dy. \quad (6.18)$$

Fig. 6.2-Left offers the exact probability of alignment, the lower bound of Eq. (6.14) and the analytical expression for the lower bound (Eq. (6.18)), for a sector size of  $\epsilon = 2.8^\circ$ . The cases of one or two assistive tags are examined.

Intuitively, the larger the number of assistive tags, the lower the probability of alignment will be. That is due to the fact that the more vectors are involved, the “harder” for all of them to align within a sector of angle  $\epsilon$ . This intuition is supported by the offered results. The average number of alignment events (see Sec. 8.4.1) per  $N_S = 10$  slots is also depicted in the figure. It is noted that multiple ( $N_G = 20$ ) interrogations are “included” in each slot. Thus,  $\lambda_a$  represents the worst-case scenario for the number of successful interrogations due to alignment.

Given a slot  $k$ , Fig. 6.2-Right offers the probability of alignment as a function of the sector size  $\epsilon$ . Intuitively, a larger sector size  $\epsilon$  offers a larger area where channel vectors can coincide, increasing the number of alignment events. Thus, a larger sector size increases the alignment probability. However, increasing the sector size reduces the achievable beamforming gain, as will be subsequently shown (Sec. c), Eq. (6.22).

The probability of alignment is given for the cases of 2 to 5 tags. It can be seen that the probability decreases by (approximately) an order of magnitude for each additional assistive tag. In Fig. 6.2, the phases introduced by each tag were randomly selected

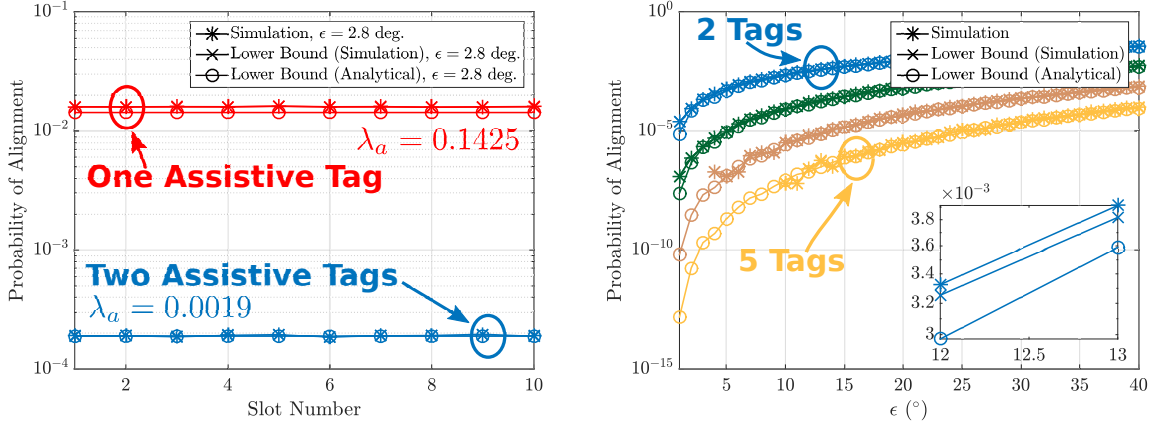


Figure 6.2: (Left) Simulated probability of alignment, the lower bound of Eq. (6.14) and the analytical expression for the lower bound (Eq. (6.18)), for  $\epsilon = 2.8^\circ$ . The cases of both a single and two assistive tags are examined. (Right) Probability of alignment as a function of sector size  $\epsilon$ , for 2 to 5 assistive tags.

(but held constant for the simulations); channel modelling is given in Sec. 8.4.2. As more assistive tags are introduced in the system, more terms appear in the product of Eq. (6.16). This fact can explain the increase in “nonlinearity” for the lower values of  $\epsilon$ . It has to be emphasized that the exact behaviour of the probability of alignment is *modelling-dependent*.

The results in Fig. 6.2-Left show that the probability of alignment is steady for the whole duration of  $N_s = 10$  slots. That is because of the symmetry of the involved distributions and the fact that channel phases can take values across the full  $[0, 2\pi)$  range; all phases follow a uniform distribution with the same parameters (Sec. 8.4.2)).

If “asymmetry” is introduced in the distribution, a different behaviour is expected. Such is the case depicted in Fig. 6.3-Right. The transient response of the system in that figure is justified by the fact that during the first slots, the rotating vector (due to  $\Theta_m[k]$ ) in conjunction with the range of the channel phases, results to a setup in the complex plane, where it is impossible for an alignment to happen. An example of such setup is depicted in Fig. 6.3-Left, for one assistive tag, at slot  $k = 1$ ; the range of possible values for the involved phases of the two vectors, corresponding to the two channels cannot coincide within the sector, for the specific slot. The above conclusion is further supported by the fact that in Setup (2), where the phase of the direct channel is limited to  $[0, \pi/2)$  (in contrast to  $[0, \pi)$  of Setup (1)), the transient in the alignment probability occupies a greater number of slots (for details on how the simulations were performed, see Sec. 8.4.2).

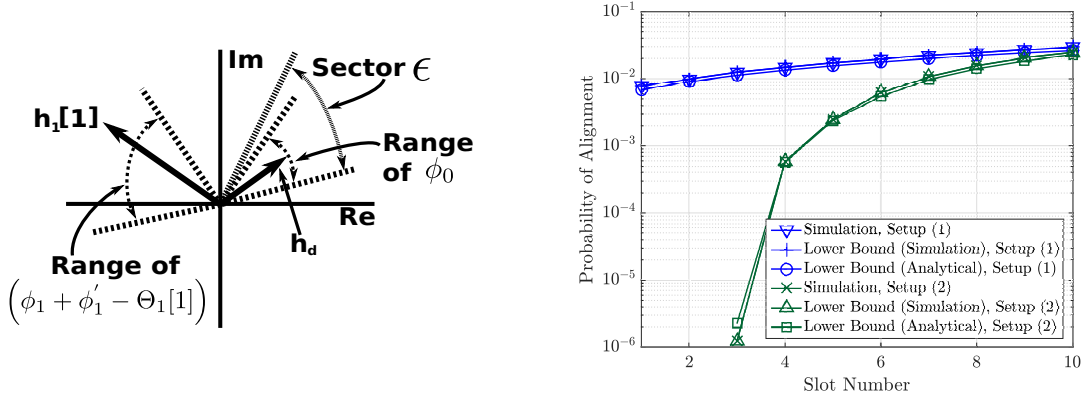


Figure 6.3: (Left) In certain slots, the range of relevant phases may deem alignment impossible (within an alignment sector  $\epsilon$ ). (Right) Behaviour of the system when phases introduced by the involved wireless channels have a limited range.

### 6.2.4 Achievable Gain

Using Eq. (6.7) and given an alignment event, the reader-to-RFID channel attains the following form:

$$h^* = \sqrt{L_0}a_0e^{-j\phi_0} + \sum_{m=1}^M \tilde{\gamma}_m e^{-j\bar{\phi}_m} = \sum_{m=0}^M \tilde{\gamma}_m e^{-j\bar{\phi}_m}, \quad (6.19)$$

where  $\tilde{\gamma}_0 e^{-j\bar{\phi}_0} = \sqrt{L_0}a_0e^{-j\phi_0}$  denotes the direct link channel  $h_{CR}$ . The (instantaneous) impinged power  $P_R$  at the RFID, can be expressed as (see Eq. (6.4)):

$$\begin{aligned} P_R &= P_{tx} |h^*|^2 = P_{tx} \left| \sum_{m=0}^M \tilde{\gamma}_m e^{-j\bar{\phi}_m} \right|^2 = P_{tx} \left| \sum_{m=0}^M \tilde{\gamma}_m \cos(\bar{\phi}_m) - j \tilde{\gamma}_m \sin(\bar{\phi}_m) \right|^2 \\ &= P_{tx} \left[ \left( \sum_{m=0}^M \tilde{\gamma}_m \cos(\bar{\phi}_m) \right)^2 + \left( \sum_{m=0}^M \tilde{\gamma}_m \sin(\bar{\phi}_m) \right)^2 \right] \\ &= P_{tx} \left[ \sum_{m=0}^M \tilde{\gamma}_m^2 + 2 \sum_{m=0}^M \sum_{i=m+1}^M \tilde{\gamma}_m \tilde{\gamma}_i \cos(\bar{\phi}_m) \cos(\bar{\phi}_i) + 2 \sum_{m=0}^M \sum_{i=m+1}^M \tilde{\gamma}_m \tilde{\gamma}_i \sin(\bar{\phi}_m) \sin(\bar{\phi}_i) \right] \\ &= P_{tx} \left[ \sum_{m=0}^M \tilde{\gamma}_m^2 + 2 \sum_{m=0}^M \sum_{i=m+1}^M \tilde{\gamma}_m \tilde{\gamma}_i \cos(\bar{\phi}_m - \bar{\phi}_i) \right]. \end{aligned} \quad (6.20)$$

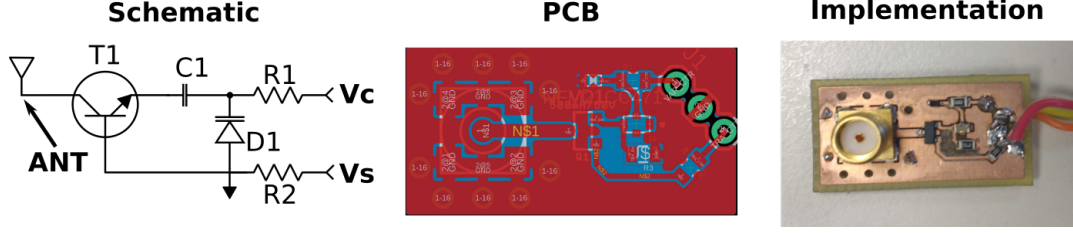


Figure 6.4: Design and printed circuit board (PCB) implementation of the assistive tag. The values of R1 and R2 are 10 k $\Omega$  and 2 k $\Omega$ , respectively.

Assuming alignment within a sector of size  $\epsilon$ , it holds that  $\cos(\bar{\phi}_m - \bar{\phi}_i) \geq \cos(\epsilon) \forall m, i \in \{0 \dots M\}$ . Thus,  $P_R$  can be lower-bounded as follows:

$$P_R \geq P_{tx} \left[ \sum_{m=0}^M \tilde{\gamma}_m^2 + 2 \sum_{m=0}^M \sum_{i=m+1}^M \tilde{\gamma}_m \tilde{\gamma}_i \cos(\epsilon) \right] = \tilde{P}_R. \quad (6.21)$$

The (instantaneous) gain can be then approximated as  $\tilde{G}_B = \frac{\tilde{P}_R}{P_{tx} L_0 a_0^2}$ . If expected values are used instead of instantaneous, the average gain can be expressed as:

$$\mathbb{E}[\tilde{G}_B] = \frac{\sum_{m=0}^M \mathbb{E}[\tilde{\gamma}_m^2] + 2 \sum_{m=0}^M \sum_{i=m+1}^M \mathbb{E}[\tilde{\gamma}_m] \mathbb{E}[\tilde{\gamma}_i] \cos(\epsilon)}{L_0 \mathbb{E}[a_0^2]}. \quad (6.22)$$

It can be seen that if a certain gain is to be satisfied (e.g., to overcome RFID's sensitivity threshold), alignment within a narrower sector (smaller  $\epsilon$ ) may be required.

It is noted that if full description of the propagation environment and knowledge of the RFIDs' locations was available, appropriate placement and loading of the assistive tags could be performed. However, acquiring such information is not straightforward and feedback to the assistive tags is also mandatory, defeating the purpose of the technique.

## 6.3 Implementation

### 6.3.1 Assistive Tag Design

A backscattering tag was designed, so as to implement the functionality described in Sec. 6.1. Using a varactor, the tag was able to alter the termination load of its antenna throughout a wide range of values (Fig. 6.4). The design is similar to the tag used in [78] for measuring the antenna's structural mode. The varactor of choice was an NXP BB179 (D1). An SMA connector was used to connect the antenna (Ettus VERT900) to an Avago AT-32033 BJT (T1) transistor and the emitter of the BJT was coupled to the varactor's

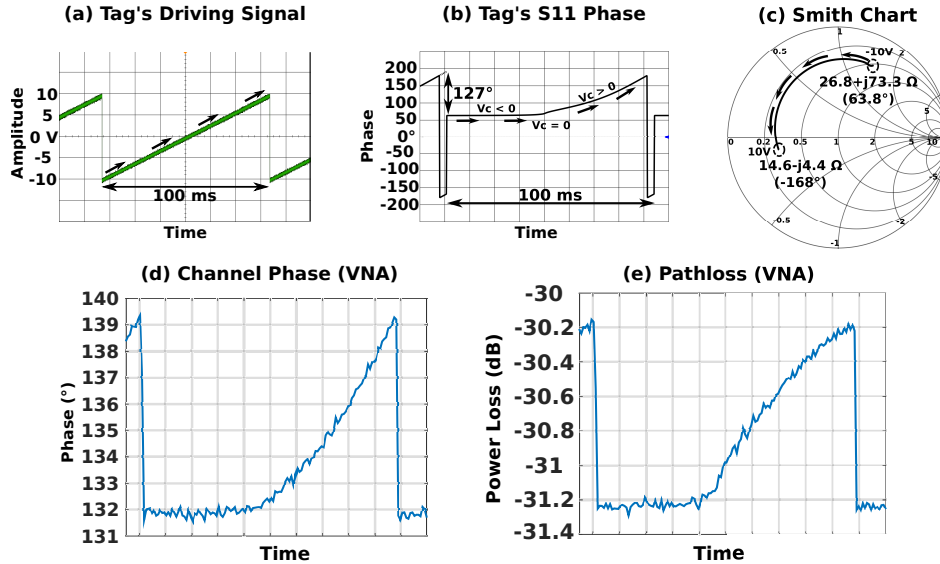


Figure 6.5: Tag is driven by the signal shown in the oscilloscope capture (a). Phase of the reflection coefficient is shown in (b) and the impedance range in the Smith Chart in (c). The phase of the reflection coefficient, does not include the phase of the tag's structural mode term ( $A_s^{(m)}$ ). The phase of the channel ( $h_{CR} + h_1(t)$ ) response is shown in (d). The pathloss of the channel is also given in (e). It is noted that the pathloss without the tag present was  $-33.8$  dB.

cathode through a Murrata 470 pF (or 220 pF for tag #2) feed through capacitor (C1, see Fig. 6.4).

Besides enabling activation and deactivation of the assistive tag, transistor T1 tunes the impedance range offered by the varactor. Different transistors were tested (e.g., NXP BFU20XRR). However, the chosen (AT-32033) offered the widest range of impedance values (as shown in Fig. 6.5). Based on the aforementioned design choices, a printed circuit board (PCB) was designed and fabricated in-house. The PCB is shown in Fig. 6.4.

### 6.3.2 Phase Control

The varactor has the ability to alter its capacitance as a function of the applied voltage. The diode has to be reverse biased in order to (properly) function as a voltage-controlled variable capacitor. A waveform generator was used to drive the cathode of the diode via resistor R1 (voltage/signal  $V_c$ , see Fig. 6.5). A linear up-ramp waveform was chosen for  $V_c$ . The voltage output swing of the generator was limited to  $20 V_{pp}$ . Thus, the varactor's potential could not be fully exploited as BB179's cathode can be driven up to the maximum value of 30 V.

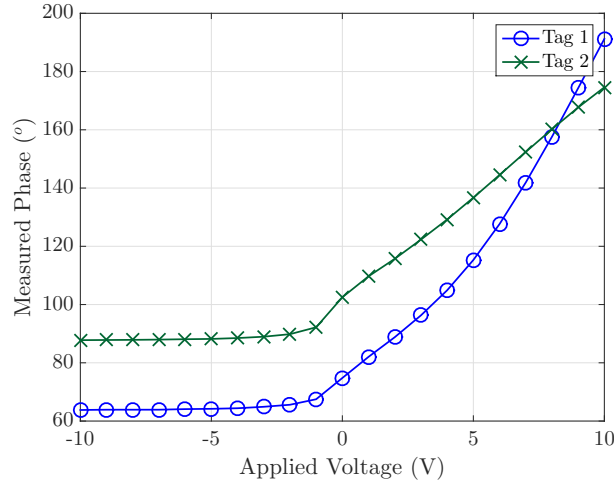


Figure 6.6: Phase of reflection coefficient  $\Gamma_m$  acquired using a VNA. The two tags use different values for the coupling feed through capacitor.

The assistive tag was connected to the generator and the impedance range was measured using a VNA. The VNA was configured to CW mode (867.5 MHz) with an output power of  $-10$  dBm. The impedance range for a full cycle of the upramp is shown in the Smith chart of Fig. 6.5. The inductive behaviour is due to the presence of the BJT. The phase of the assistive tag's reflection coefficient is also offered in the same figure, along with the channel response resulting from the operation of the assistive tag (details are given in Sec. 6.4).

The reflection coefficient phases of two different assistive tags, implemented with different coupling capacitors (C1) for various voltage values applied to R1, are given in Fig. 6.6. It must be noted that, while most of the capacitance range is offered with the diode reverse biased, a limited range of phase/impedance values was offered by forward biasing the diode up to  $10$  V (lower saturation region in Fig. 6.6); the forward current was monitored to prevent diode's damage.

While the (utilized) diode requires relatively high voltages to achieve its full capacitance range, due to its reverse bias operation it draws (ideally) no current. Thus, given a properly designed, ultra-low-power voltage boosting circuit, batteryless/wireless powered operation is feasible. Besides, as it will be shown experimentally, beamforming gain is also offered for binary loading (switching between two appropriate loads/diode voltages) of the assistive tag's antenna. The last showcases the feasibility for future RFIDs to be equipped with the appropriate circuitry that allows for instantaneous beamforming towards adjacent RFIDs.

### a) Period of Control Voltage Signal

As stated in Sec. 6.2.1, the phase introduced by the assistive tag(s) in a given slot affects multiple interrogations, while the wireless channel parameters remain block-constant for each interrogation and vary (randomly) between successive interrogations.

To avoid interference to the RFID reader, the minimum time duration of a slot must be equal to the duration of a single transmission/interrogation ( $N_G \geq 1$ ). In a different case, the assistive tag will vary the channel's phase too "fast", effectively creating a non-block-constant wireless channel.

The duration of the ramp was set to 100 ms (10 Hz). The value was chosen experimentally after observing the performance of the system. The chosen value would vary between communication systems/protocols (different from RFID Gen2) and propagation environments.

## 6.4 Experimental Results

Experiments were performed using a Thing Magic Sargas RFID reader, connected to an MTI MT-242032 7 dBi (nominal gain) antenna, via a 0.4 dB loss coaxial cable. Throughout the experiments, the reader was configured for RFID tag communication in dynamic Q mode, with backscatter link frequency (BLF) of 250 kHz and Miller-8 line coding. The distributed beamforming gain, due to the operation of backscattering tag(s) assisting interrogation of RFIDs, was showcased with two experiments, described below.

### 6.4.1 RFID Tag Interrogation

The reader was configured to output a signal at 20 dBm. A group of 5 ALN-9740 (Higgs-4) RFIDs was used. The RFIDs were randomly scattered within a radius of  $\approx 0.2$  m (see inlay of Fig. 6.8-right). Experiments were carried out at 3 random locations, 1.80 m, 2.16 m and 1.70 m away from the reader. At each of those locations, the assistive tag was placed at 4 random spots in the vicinity of the RFIDs.

The interrogation results as reported by the reader (averaged over 3, one minute-long, runs), for the first location (1.80 m away from the reader), are offered in Fig. 6.7. For each of the 4 (randomly selected) assistive tag spots, 3 cases were examined. The number of successful interrogations (reads) for each RFID in the absence of the assistive tag, is offered in the left-most bar of each spot. The middle bar offers the number of reads for the case of the assistive tag being present but not operating, while the right-most bar represents the case of the assistive tag being active.

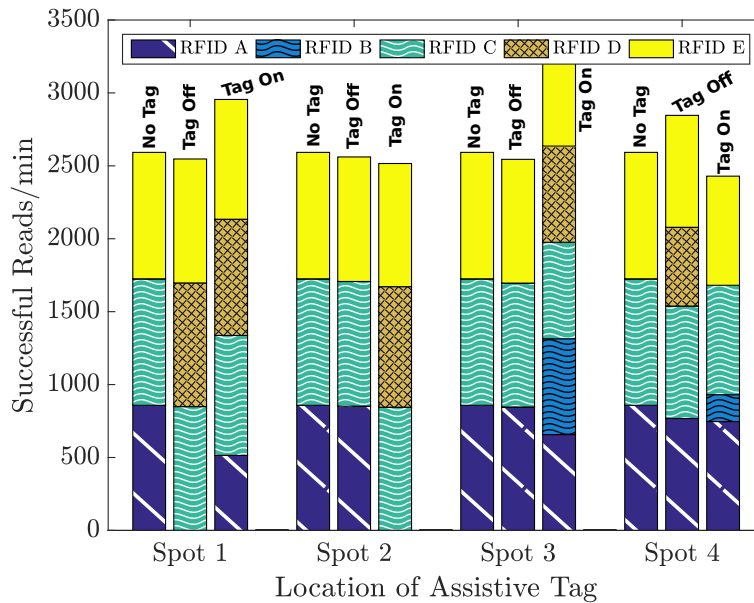


Figure 6.7: Experimental results of the interrogation performance for 5 RFIDs using one assistive tag, at a distance of 1.80 m away from the reader. Both the RFIDs’ and the assistive tag locations were randomly chosen. 3 cases per spot are examined: no assistive tag, assistive tag present but not operating, assistive tag active.

Looking into spot 3 of Fig. 6.7, the contribution of the assistive tag to the interrogation performance is evident: while in the absence of the tag only 3 RFIDs could be interrogated (A,C and E), with the assistive tag operating all RFIDs (A-E) were interrogated hundreds of times/minute ( $\approx 600$  reads/min for each RFID).

Some interesting observations are made, based on the results of Fig. 6.7. First, even when the assistive tag is inactive (middle bar), interrogation gains can be offered (see spot 4, Fig. 6.7). This is expected, as the presence of the assistive tag alters the propagation environment and RFIDs at certain locations can enjoy gains.

When inactive, the assistive’s antenna is isolated from the diode using a transistor (see Sec. 6.3). The isolation leads to the assistive introducing a phase to the channel, which is different from the phases introduced during normal operation. The “inactive” phase may offer destructive additions at some (RFID) locations (e.g., spot 1, RFID A) and constructive at others (spot 1, RFID D).

In order to maximize the number of successfully interrogated RFIDs, the operation of the assistive can be duty-cycled; while the voltage applied to the diode is swept across its full range, a square wave can be applied to the assistive tag’s transistor for periodic activation/deactivation. Operating the assistive in such a manner would result, in spot 4 for example, successful interrogations of all RFIDs.

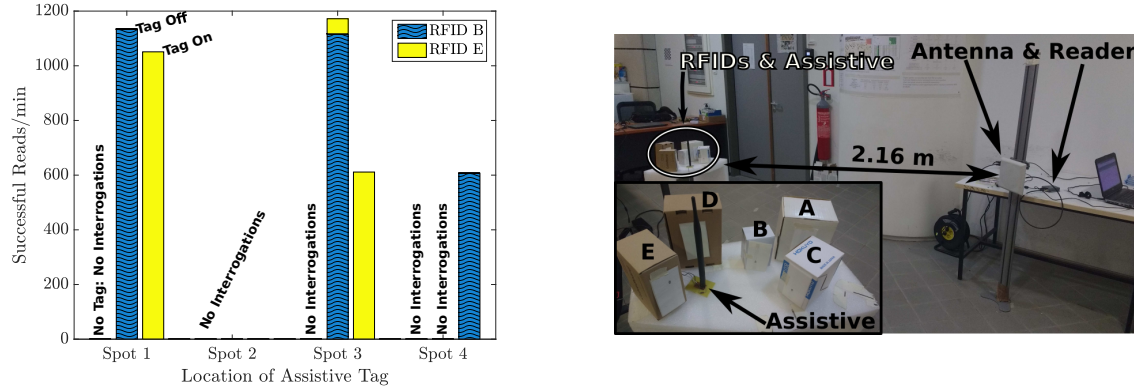


Figure 6.8: (Left) Experimental results for the interrogation performance using a single assistive tag and 5 RFIDs. (Right) Setup utilized for the aforementioned measurements, 2.16 m away from the reader.

Results from the experiments in the second location, 2.16 m away from the reader, are given in Fig. 6.8-Left, while the setup is shown in Fig. 6.8-Right. Considering spots 1, 3 & 4, it can be clearly seen that the assistive tag, despite the apparent strong multipath conditions in the location, helps the interrogation of a number of RFIDs. It is noted that after the experiments at the second location were carried out, the group of RFIDs was moved at a direct LOS spot, 2.16 m in front of the reader’s antenna. At that direct LOS location, only RFIDs A, B & E were successfully interrogated.

In the third location, 1.70 m away from the reader, no successful interrogations were reported, either with or without the assistive tag. The effectiveness of the assistive tag can be improved by further improvement of its circuit, so as to offer a wider range of capacitance (and by extension phase) values.

### 6.4.2 Channel Measurements

The effects of the assistive tags’ operation in the wireless channel, were assessed using a two-port VNA. The VNA was configured in CW mode at a frequency of 867.5 MHz with an output power of  $-5$  dBm. The transmitting antenna was connected to port 1 of the analyser and the receiving (a 1.8 dB bow-tie dipole) to port 2. The analyser was configured to report the value of the ratio  $\frac{b_2}{a_1}$ , which, assuming perfect termination of the receiving antenna (matched to port 2), is the transfer function between the transmitting and receiving antennas (i.e., the wireless channel). The setup is shown in Fig. 6.9.

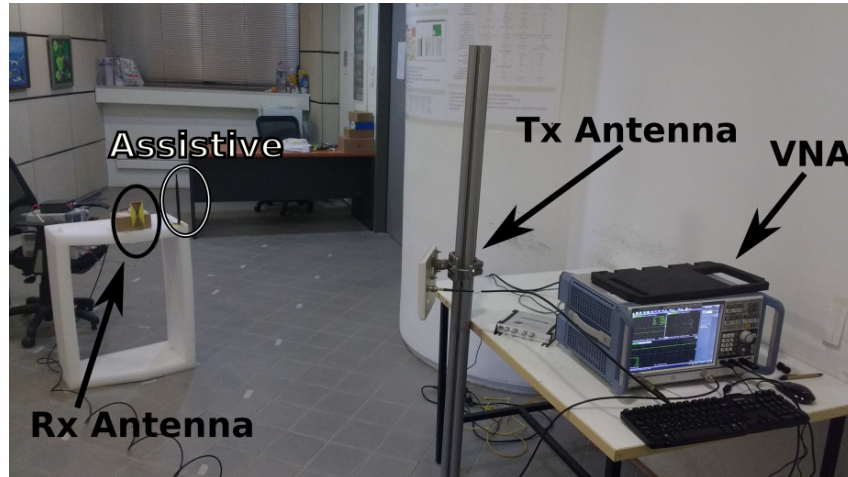


Figure 6.9: Experimental setup for the assessment of assistive tags' contribution to the wireless channel. The VNA was configured so as to measure the transfer function (channel) between the Tx antenna (port 1) and Rx antenna (port 2).

#### a) Interrogation Rate, Power Gain and Phase Alignment vs Tag Loading

An Impinj Speedway R420 RFID reader was used, with output power of 20 dBm. A RFID (ALN-9540, Higgs-2) was placed  $d_{CR} = 1.68$  m away from the transmitting antenna and the performance of the reader for a fixed amount of time (10 s) was evaluated at 1000 interrogations (i.e.,  $\sim 100$  interrogations/sec). While maintaining the same distance, the RFID was moved to a second location, where the reader could not interrogate it. The assistive tag was then placed at a distance of  $d_{TR} = 23$  cm from the RFID (the assistive-to-reader distance was  $d_{CT} = 1.77$  m). While varying the voltage of the assistive's diode, the number of successful interrogations was recorded. The results are offered in Fig. 6.10.

Having recorded the number of successful interrogations, the RFID was replaced with the Rx antenna of the VNA (reader's antenna was connected to port 1 of the VNA). The Tx to Rx pathloss without the assistive tag being present was measured at  $-33.2$  dB, while with the assistive tag being present but not operating, at  $-34.1$  dB.<sup>3</sup>

The pathloss for two states of the diode is depicted in Fig. 6.10. It can be seen that, when the assistive's diode is biased at 9 V, a gain of 1.6 dB is offered, while at 0 V, the measured gain is 0.9 dB. As it can be seen, a gain of 1.6 dB is enough for the tag to operate and be successfully interrogated multiple times.

<sup>3</sup>Measurements averaged over a 5 s time window in a environment with minimal-to-none mobility. The assistive tag being present but not operating (Tag Off) corresponds to a state, where the transistor is off, i.e., the diode is disconnected from the antenna.

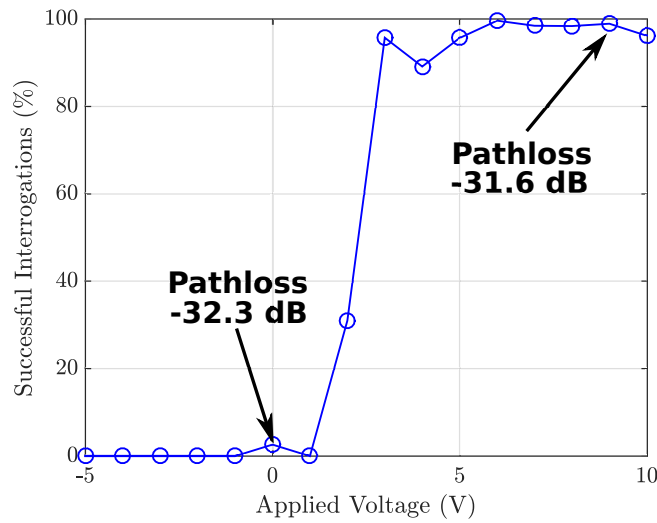


Figure 6.10: Percentage of successful interrogations (out of 1000) as a function of the reverse bias voltage applied to the assistive's diode. The interrogation rate was a result of averaging the number of successful interrogations over multiple runs (each run consisted of 1000 interrogations).

**Phase Alignment** The phase alignment models of Sec. 6.2.2 were used in the setup described above. The involved phases were modelled as  $\phi_m \sim \mathcal{U}\left[2\pi F_c \frac{d_{CT}}{c} - \delta\phi_a, 2\pi F_c \frac{d_{CT}}{c} + \delta\phi_a\right)$ ,  $\phi'_m \sim \mathcal{U}\left[2\pi F_c \frac{d_{TR}}{c} - \delta\phi_a, 2\pi F_c \frac{d_{TR}}{c} + \delta\phi_a\right)$ ,  $\phi_0 \sim \mathcal{U}\left[2\pi F_c \frac{d_{CR}}{c} - \delta\phi_a, 2\pi F_c \frac{d_{CR}}{c} + \delta\phi_a\right)$ , with  $\delta\phi_a = 0.5$  deg.  $A_s$  was set to  $A_s = 0.6047 + j0.5042$ , while  $\epsilon = 28$  deg. The reflection coefficient (as a function of applied voltage) was evaluated using the load measurements depicted in the smith chart of Fig. 6.5.

Fig. 6.11 offers the probability of alignment for the setup described in the previous paragraphs (single tag). As expected, for a significant amount of time, alignment takes place (e.g., probability of alignment is equal to 1), corroborating the experimental results provided in the previous section(s). However, one can notice an offset, with respect to when most of the alignment events take place (i.e., for which load), compared, for example, to Fig. 6.10. The last can be attributed to non-perfect modelling (multipath is not taken into account) of the phases and  $A_s$ .

It must be noted that slightly varying the placement of the assistive tag could result in zero successful interrogations which was also corroborated by the theoretical models, which offered zero probability of alignment for the specific setups.

**Switching Between Two Loads** Based on the results of Fig. 6.10, experiments utilizing switching between loads were carried out. In the first experiment the diode's voltage was switched between 0V and 9V and in the second between  $-5$ V and 5V, at a

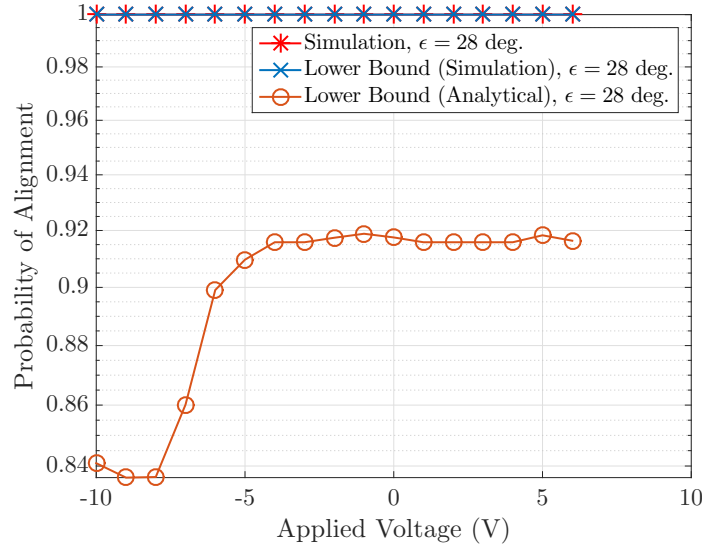


Figure 6.11: Probability of alignment for the setup described in Sec. a). The offset between simulation and analytical expression (Eq. (6.18)) is mainly due to the trapezoidal approximation of the involved integral.

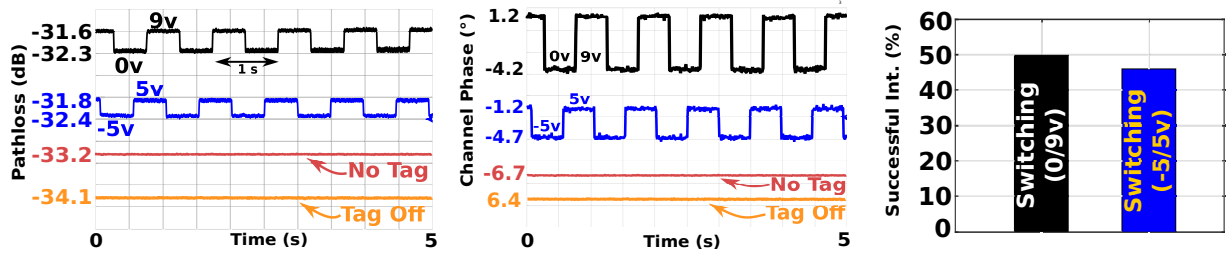


Figure 6.12: Channel pathloss (Left), phase (Middle) and successful interrogation rate (Right), for the case of switching the termination of the assistive’s antenna between two loads. A maximum gain of 1.6 dB is achieved for a reverse bias voltage of 9V. The “No Tag” label corresponds to the absence of the assistive tag.

rate of 1Hz. The interrogation rate was recorded and then the VNA was used to probe the channel. The results are shown in Fig. 6.12.

The interrogation rates depicted in Fig. 6.12-right, come in agreement with the results of Fig. 6.10: for the 0/9V switching, the assistive tag is 50% of the time in state 0V offering (on average) 2.6% successful interrogations and 50% in state 9V offering 98.9% successful interrogations. Thus, theoretically, an overall rate of 50.7% successful interrogations will be offered, which is very close to the rate of 49.8% reported by the switching experiment (shown in Fig. 6.12-right).

The VNA traces of the channel pathloss and phase, for the switching experiments, are also shown in Fig. 6.12-Left and Middle, respectively. It can be seen that, a maximum gain of 1.6 dB can be achieved while switching between appropriate loads.

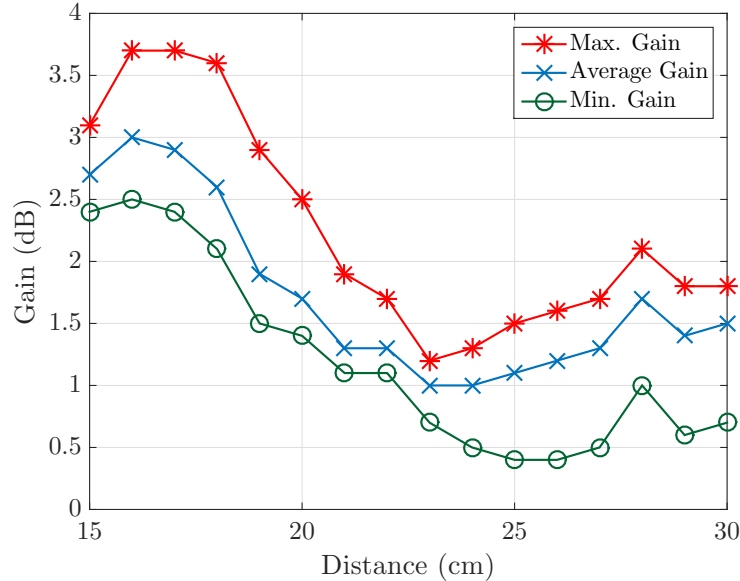


Figure 6.13: Variation of the achievable gain as a function of the Rx-to-assistive tag distance.

#### b) Achievable gain vs Assistive tag-to-RFID distance

Using the VNA for channel probing, experiments were carried out, so as to demonstrate the variability of the offered gain among different locations. It is noted that the experiments of this section were carried out in a different location from the experiments of the previous sections. The assistive tag was driven by a ramp waveform (Fig. 6.5); the assistive tag-to-Rx antenna distance was varied from 15 to 30 cm.

The resulting gain is offered in Fig. 6.13. As it is expected, gain has a decreasing oscillation as the distance increases. Therefore, the assistive tag should not be placed relatively far from the Rx antenna. Experimental results in Fig. 6.13 show gain values in the range of 0.4 – 3.7 dB.

#### c) Achievable Gain-One & Two Assistive tags

To assess the gain offered by a number of assistive tags, experiments and simulations were carried out and compared with the theoretical model of Eq. (6.22). Specifically, the cases of one and two tags were examined. The antenna gains used in the model were  $G_R = 5$  dB,<sup>4</sup>  $G_A = 3$  dB,  $G_G = 1.8$  dB. The distances utilized in the pathloss model (and in the experimental setup) were  $d_{CR} = 1.68$  m,  $d_{1,CT} = 1.65$  m,  $d_{2,CT} = 1.77$  m,  $d_{1,TR} = 0.23$  m,  $d_{2,TR} = 0.16$  m. It has to be noted that the locations of the RFID and of the two assistive

<sup>4</sup>The reader's antenna has a nominal gain (at the direction of its main lobe) of 7 dB. The Rx antenna (and the RFID) is placed at a direction lying outside its main lobe, thus the gain is reduced.

tags were arbitrarily chosen. Given a range of phases offered by the assistive tag, different setups will exhibit different gains.

Assuming an alignment event at  $t^*$ , variables  $\tilde{\gamma}_m$  are defined as in Eq. (6.5), with  $\tilde{\gamma}_0 = \sqrt{L_0}a_0$  and  $\tilde{s}_m = s_m\gamma_m(t^*) = \sqrt{0.6}$  (scattering efficiency). Fading coefficients are assumed to follow a Rician distribution:

$$a_q^{(m)} = |h_q^{(m)}|, \quad h_q^{(m)} \sim \mathcal{CN}\left(\sqrt{\frac{k_q^{(m)}}{k_q^{(m)} + 1}}\sigma_h^2, \frac{\sigma_h^2}{k_q^{(m)} + 1}\right), \quad (6.23)$$

where  $m \in \{\emptyset, 1, 2\}$ ,  $q \in \{0, \text{CT}, \text{TR}\}$ ,  $\sigma_h^2 = 1$ . The Rician factor  $k_j^{(m)}$  is set to  $k_j^{(m)} = 20$ . It can be shown that  $\mathbb{E}\left[\left(a_q^{(m)}\right)^2\right] = \sigma_h^2$  [48]. Given the definition in Eq. (6.23), the expected value  $\mathbb{E}\left[a_q^{(m)}\right]$  is given by [79]:

$$\mu_q^{(m)} = \mathbb{E}\left[a_q^{(m)}\right] = \sqrt{\frac{\pi\sigma_h^2}{4\left(k_q^{(m)} + 1}\right)} {}_1F_1\left(-1/2; 1; -k_q^{(m)}\right), \quad (6.24)$$

where  ${}_1F_1(a; b; c)$  is the confluent hypergeometric function of the first kind [62]. Eq. (6.22) can then be used to analytically offer the average gain.

The channel  $h^*$ , as per Eq. (6.19), was simulated. Alignment within a sector  $\epsilon$  was achieved by modelling the associated phases as  $\bar{\phi}_m \sim \mathcal{N}(0, \epsilon^2/2)$ . The simulated impinged power was defined as the numerical average of  $P_{\text{tx}}|h^*|^2$ , across  $10^5$  channel realizations. The gain was then calculated as the ratio of the aforementioned average power to the numerical average of  $P_{\text{tx}}|h_d|^2$ .

To experimentally measure the offered gain, the setup described earlier (utilizing the VNA) was used. The pathloss without any assistive tag present was measured at  $-33$  dB. Measurements were conducted utilizing only one tag at a time. The maximum gain offered by tag #1 was 1.8 dB, while tag #2 offered 1.5 dB (operating as in Fig. 6.5). Then, both tags were placed near the Rx antenna and unsynchronized ramp waveforms of the same parameters (see Sec. 6.3) were used to drive them (the ramp's frequency was set to 1 Hz for the VNA measurements). The maximum gain was 2.9 dB.

Fig. 6.14 offers the average gains, when using 1 and 2 assistive tags, as a function of sector size. Additionally, the experimental gains are depicted. It can be seen that the approximate average gain offered by Eq. (6.22) matches to the simulation results. The behaviour (w.r.t. sector size) of the analytical expression (and the simulation results) will depend on the modelling of the phases ( $\bar{\phi}_m$ ). Furthermore, it is evident that

the predictions from the model and the simulations, are a close match for the measurement/experimental results, with a maximum error of  $\approx 0.4$  dB.

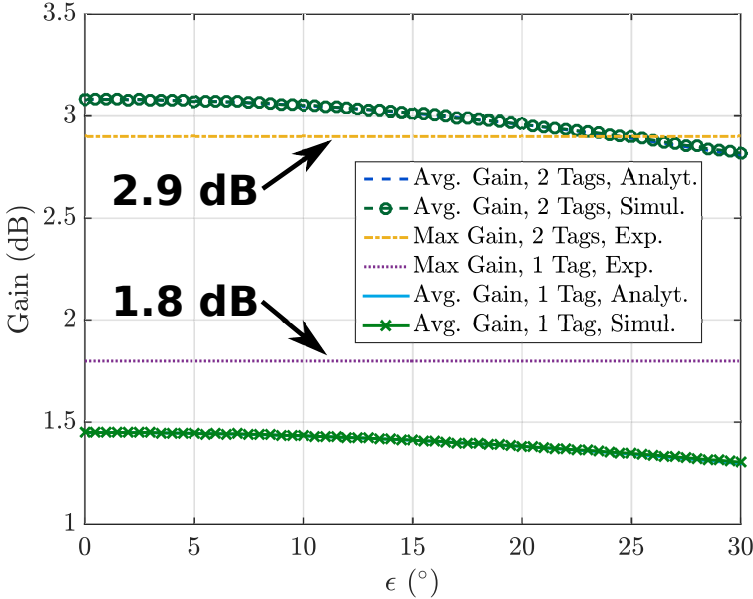


Figure 6.14: Analytical and simulated average power gain for the cases of 1 and 2 assistive tag(s) as a function of sector size ( $\epsilon$ ). Experimental power gain for the two cases is also given as measured by the VNA. The lines representing the experimentally measured gain exist only for comparison purposes.

# Chapter 7

## Conclusion

It is projected that billions of devices will be wirelessly connected in the foreseeable future. Ranging from smartphones to wireless sensing devices and RFIDs, by definition, such a number of connected devices, will have a significant socio-economic impact. A fridge can order milk, your smartphone can help you remember where you left your wallet, while a farmer is able to wirelessly check the moisture in the soil and adjust the irrigation schedule accordingly.

Those devices involve a number of risks throughout all stages of their life-cycle. From their production and use, to the time marking their end-of-life, significant impact is expected to the environment. This impact is multiplied, when someone considers the number of expected devices. To ensure a sustainable exploitation of their benefits while minimizing any negative impact to the environment, simple, elegant, engineering solutions should be provided.

The dissertation offered novel methods for achieving communication through backscatter radio, while minimizing the infrastructure, energy and monetary cost requirements. Exploiting the proposed methods, it was demonstrated that backscatter radio technology can also be used in an unorthodox way, to solve other problems in the field of wireless communication.

The proposed backscatter radio techniques and their benefits, can be used for engineering ultra-low-power, ultra-low-complexity, ultra-low-cost wireless devices. The ultra-low-power aspect of the techniques allows for the design of batteryless wireless devices, minimizing that way the maintenance cost and more importantly, the environmental impact. The life cycle of the device is extended due to its ultra-simple operation, stemming from the ultra-low-complexity of the presented techniques.

## 7.1 Wireless Transmission of Information

### 7.1.1 FM Remodulation

Besides transmitting private conversations, it was shown that backscatter radio can be used to transmit the value measured by sensors, with ultra-simple circuitry and *no battery*. In contrast to modern solutions like LoRa or Bluetooth low energy (BLE) and the involved design and manufacturing complexity, FM remodulation offers ultra-low-complexity, ultra-low-power ( $24 \mu\text{Watt}$ ), batteryless wireless communication to sensing devices, while requiring just FM radio coverage.

FM remodulation allows for an RFID-like interrogation procedure, where a person approaches (at distances  $< 26$  meters) the FM remodulation tag to recover its information. In contrast, however, to RFIDs or computational/sensing RFIDs, *no* special reader is required, just a conventional FM radio receiver, or a smartphone equipped with one.

FM remodulation revolutionizes wireless sensing technology, especially for applications in precision agriculture and environmental parameter monitoring. Commercially available soil moisture wireless sensors require infrastructure, installation effort and frequent maintenance (e.g., battery replacement). Small-scale farmers may be reluctant towards introducing new, (appearing) complex technology in their farming practices.

At a cost of less than 5 euros—at least 10 times lower than a commercial solution—a FM remodulation tag with a soil moisture sensor, requires just an FM equipped smartphone to read the moisture of the soil. The simplicity of FM remodulation-based sensing, coupled with its maintenance-free character due to its ultra-low-power consumption, allows for wide adoption of technology by small-scale farmers. With precision agriculture, valuable resources like water are consumed responsibly. Thus, widespread adoption of technology within empirical practices, can have a tremendous socio-economic and environmental impact.

### 7.1.2 Digital Modulation Schemes

Besides the analog, ambient backscatter communication scheme, digital modulation schemes were provided, along with appropriate high performance coherent, partially coherent and fully noncoherent receivers. Following a structured design approach during the derivation of the detectors (in contrast to relevant prior art), it was shown that a *modulated* illuminating signal, under certain conditions, can lead to significant performance gains for the tag communication.

From the tag's perspective, the modulations, while slightly more complicated compared to OOK, do not pose any requirement for cooperation with the ambient transmitter. Thus, the tag does not require any form of complex receiver structure for the ambient signal.

Through evaluation of recent studies on ambient backscatter, it was shown that switching based techniques, besides allowing for easy multiple access in the frequency domain, may offer performance gains, compared to conventional schemes (OOK), at the expense of slightly increased tag complexity.

The comparison demonstrated that simplified models and assumptions commonly found in prior art, related to carrier's signal structure, lead to limited performance and shall be dismissed. A mathematically sound approach to modelling the problem of digital, ambient backscatter communication, offers improved BER even with fully non-coherent detectors.

The proposed switching frequency techniques exploit existing (universal) wireless industry infrastructure and *clearly* enable ultra-low power, ultra-low-complexity tags, possibly powered by RF.

## 7.2 Virtual Antenna Array

Conventionally, to solve problems (in the field of wireless communications) requiring multiple inputs/outputs, multi-antenna arrays are considered at the receiver or the transmitter. Exploiting the proposed methods, originally intended for ultra-low-power ambient backscatter communication, an unconventional approach is attempted for solving those problems.

For the first time, it was shown that backscatter radio can be used in an unorthodox way, to attain functionality that would otherwise require the use of multi-antenna transmitters or receivers. Choosing to solve respective problems using the presented backscatter radio techniques, lowers the cost, complexity and power consumption of the solution.

### 7.2.1 Emulating a Multi-Antenna Receiver

Using the proposed switching techniques, an impinged signal on the antenna of the backscattering tag, is relayed in the frequency domain. When multiple backscattering tags are used, the said signal is relayed in multiple, distinct frequency bands. Thus, multiple observations can be made, given a receiver able to discriminate signal's copies in the

frequency domain. The receiver does not need a multi-antenna array, which significantly lowers the implementation complexity.

Combining the processing that was conventionally used for backscatter radio communication with a number of simple, low power, cost & complexity, switching backscattering tags, it was shown that a problem (DoA estimation) requiring a multi antenna receiver can be solved without the relevant cost & complexity.

### 7.2.2 Beamforming with Single Antenna Transmitter & Receiver

Exploiting the fundamental operation of a backscattering tag, it was shown that blind, *zero-feedback*, beamforming can be realized using a number of ultra-low-cost, ultra-low-complexity, ultra-low-power backscattering tags.

The proposed *assistive* tags aided the reception of signals, subject to multipath conditions. Exploiting backscatter radio principles, backscattering tags were implemented, capable of varying the phase of an impinged signal and thus, altering the propagation conditions.

It was experimentally shown that the proposed beamforming tags can offer instantaneous power gains in the range of 0.4 – 3.7 dB. In contrast to bulky RISs and their complex controllers, the proposed technique did not require any channel-related information (zero-feedback), elaborate control algorithms or large surfaces/installation effort.

By exploiting the proposed backscattering methods in the aforementioned, unconventional ways, backscatter radio finds perhaps a new area for applications and research.

## 7.3 Future Work

Using the custom-IC approach, the proposed FM remodulation-based wireless moisture sensors, are currently re-designed, so as to allow for production-ready devices. An ultra-low-complexity, analog, FM-radio based interrogation system is also going to be designed for use-cases where a smartphone is not equipped with an FM radio receiver. The last will allow for ultra-low-complexity wireless sensing, even when a smartphone or an FM radio receiver is not available.

The feasibility of extending the methods presented in Chapter 3 to wideband illuminating signals (e.g., OFDM), can be studied. Tags can be designed so as to realize the functionality described in Chapter 5. Fully passive, potentially powered using RF

harvesting, assistive tags can be also designed. The proposed tags can also benefit from designs that exploit reflection coefficient “amplification”, allowing for extending the communication range, without significant increase in power consumption.

Exploiting scatter radio relaying, the feasibility of solving other problems, different from DoA estimation and blind beamforming, for assisting “third-party” communication systems, can be studied.

# Chapter 8

## Appendix

### 8.1 Supplementary Material for Chapter 3

#### 8.1.1 SBPSK Decision Rule Derivation

Considering the case for  $H_i, i \in \{0, 1\}$ :

$$\max_{\tilde{\mu}_c^{(n)}} \ln \left[ f_{\mathbf{r}_{s,n} | H_i, \tilde{\mu}_c^{(n)}, \Phi_t}(\mathbf{r}_{s,n} | H_i, \tilde{\mu}_c^{(n)}, \Phi_t) \right] = \max_{\tilde{\mu}_c^{(n)}} \left[ 2 \ln \left( \frac{1}{\pi \tilde{\sigma}_n^2} \right) - \frac{1}{\tilde{\sigma}_n^2} \|\mathbf{r}_{s,n} - \tilde{\mu}_c^{(n)} \mathbf{x}_i(\Phi_t)\|_2^2 \right], \quad (8.1)$$

the value of the parameter  $\tilde{\mu}_c^{(n)}$  that maximizes Eq. (8.1), can be given by solving the least squares problem  $\tilde{\mu}_{c,ls}^{(n)} = \arg \min_{\tilde{\mu}_c^{(n)} \in \mathbb{C}} \|\mathbf{r}_{s,n} - \mathbf{x}_i(\Phi_t) \tilde{\mu}_c^{(n)}\|_2^2$ . The solution to the aforementioned problem can be given by [49, pp. 521]:

$$\tilde{\mu}_{c,ls}^{(n)} = \frac{\mathbf{x}_i^H(\Phi_t) \mathbf{r}_{s,n}}{\|\mathbf{x}_i(\Phi_t)\|_2^2}. \quad (8.2)$$

Substituting Eq. (8.2) to Eq. (8.1):

$$\begin{aligned} \max_{\tilde{\mu}_c^{(n)}} \left[ 2 \ln \left( \frac{1}{\pi \tilde{\sigma}_n^2} \right) - \frac{1}{\tilde{\sigma}_n^2} \|\mathbf{r}_{s,n} - \tilde{\mu}_c^{(n)} \mathbf{x}_i(\Phi_t)\|_2^2 \right] &= 2 \ln \left( \frac{1}{\pi \tilde{\sigma}_n^2} \right) - \frac{1}{\tilde{\sigma}_n^2} \|\mathbf{r}_{s,n} - \tilde{\mu}_{c,ls}^{(n)} \mathbf{x}_i(\Phi_t)\|_2^2 \\ &= 2 \ln \left( \frac{1}{\pi \tilde{\sigma}_n^2} \right) - \frac{1}{\tilde{\sigma}_n^2} \left( \|\mathbf{r}_{s,n}\|_2^2 - \frac{|\mathbf{r}_{s,n}^H \mathbf{x}_i(\Phi_t)|^2}{\|\mathbf{x}_i(\Phi_t)\|_2^2} \right). \end{aligned} \quad (8.3)$$

Using Eq. (8.3) and exploiting the fact that  $\|\mathbf{x}_i(\Phi_t)\|_2^2 = 2$ , the following is obtained:

$$\begin{aligned}
\max_{\tilde{\mu}_c^{(n)}} & \left[ 2 \ln \left( \frac{1}{\pi \tilde{\sigma}_n^2} \right) - \frac{1}{\tilde{\sigma}_n^2} \|\mathbf{r}_{s,n} - \tilde{\mu}_c^{(n)} \mathbf{x}_i(\Phi_t)\|_2^2 \right] = 2 \ln \left( \frac{1}{\pi \tilde{\sigma}_n^2} \right) - \frac{1}{\tilde{\sigma}_n^2} \left( \|\mathbf{r}_{s,n}\|_2^2 - \frac{1}{2} |\mathbf{r}^s H_n \mathbf{x}_i(\Phi_t)|^2 \right) \\
& = 2 \ln \left( \frac{1}{\pi \tilde{\sigma}_n^2} \right) - \frac{1}{\tilde{\sigma}_n^2} \|\mathbf{r}_{s,n}\|_2^2 + \frac{1}{2\tilde{\sigma}_n^2} \left| (r_{s,n}^+)^* e^{j(\Phi_t + \Phi_i)} + (r_{s,n}^-)^* e^{-j(\Phi_t + \Phi_i)} \right|^2 \\
& = 2 \ln \left( \frac{1}{\pi \tilde{\sigma}_n^2} \right) - \frac{1}{\tilde{\sigma}_n^2} \|\mathbf{r}_{s,n}\|_2^2 + \frac{1}{2\tilde{\sigma}_n^2} \left( |r_{s,n}^+|^2 + 2\Re \left\{ (r_{s,n}^+)^* (r_{s,n}^-) e^{j2(\Phi_t + \Phi_i)} \right\} + |r_{s,n}^-|^2 \right) \\
& = 2 \ln \left( \frac{1}{\pi \tilde{\sigma}_n^2} \right) - \frac{1}{\tilde{\sigma}_n^2} \|\mathbf{r}_{s,n}\|_2^2 + \frac{1}{2\tilde{\sigma}_n^2} \left( \|\mathbf{r}_{s,n}\|_2^2 + 2\Re \left\{ (r_{s,n}^+)^* (r_{s,n}^-) e^{j2(\Phi_t + \Phi_i)} \right\} \right) \\
& = 2 \ln \left( \frac{1}{\pi \tilde{\sigma}_n^2} \right) - \frac{1}{2\tilde{\sigma}_n^2} \|\mathbf{r}_{s,n}\|_2^2 + \frac{1}{\tilde{\sigma}_n^2} \Re \left\{ (r_{s,n}^+)^* (r_{s,n}^-) e^{j2(\Phi_t + \Phi_i)} \right\}. \tag{8.4}
\end{aligned}$$

Using the above equation, the decision for bit  $i_n \in \{0, 1\}$  can take the following form:

$$\begin{aligned}
i_n & = \arg \max_{i_n \in \{0,1\}} \left\{ \max_{\tilde{\mu}_c^{(n)}} \left[ 2 \ln \left( \frac{1}{\pi \tilde{\sigma}_n^2} \right) - \frac{1}{\tilde{\sigma}_n^2} \|\mathbf{r}_{s,n} - \tilde{\mu}_c^{(n)} \mathbf{x}_{i_n}(\Phi_t)\|_2^2 \right] \right\} \\
& = \arg \max_{i_n \in \{0,1\}} |\mathbf{r}_n^H \mathbf{x}_{i_n}(\Phi_t)|^2 \tag{8.5}
\end{aligned}$$

$$= \arg \max_{i_n \in \{0,1\}} \Re \left\{ (r_{s,n}^+)^* (r_{s,n}^-) e^{j2(\Phi_t + \Phi_{i_n})} \right\}. \tag{8.6}$$

## 8.2 Supplementary Material for Chapter 4

### 8.2.1 Bandwidth of $J_0(2\rho \sin(\frac{\omega_{\text{sens}} t}{2}))$

In order to obtain the occupied bandwidth of  $J_0(2\rho \sin(\frac{\omega_{\text{sens}} t}{2}))$ , where  $\omega_{\text{sens}} = 2\pi F_{\text{sens}}$ , the Fourier transform:

$$M(\omega) = \int_{-\infty}^{+\infty} J_0\left(2\rho \sin\left(\frac{\omega_{\text{sens}} t}{2}\right)\right) e^{-j\omega t} dt, \tag{8.7}$$

needs to be evaluated. Firstly  $J_0(2\rho \sin(\frac{\omega_{\text{sens}} t}{2}))$  will be expanded using [62, 9.1.10]:

$$J_n(\beta) = \left(\frac{\beta}{2}\right)^n \sum_{k=0}^{+\infty} \frac{(-\beta^2/4)^k}{k! \Gamma(n+k+1)} \stackrel{n=0}{=} \sum_{k=0}^{+\infty} \frac{(-1)^k (\beta/2)^{2k}}{(k!)^2}, \tag{8.8}$$

and  $J_0\left(2\rho \sin\left(\frac{\omega_{\text{sens}} t}{2}\right)\right)$  becomes:

$$J_0\left(2\rho \sin\left(\frac{\omega_{\text{sens}} t}{2}\right)\right) = \sum_{k=0}^{+\infty} \frac{(-1)^k \left(\rho \sin\left(\frac{\omega_{\text{sens}} t}{2}\right)\right)^{2k}}{(k!)^2} = \sum_{k=0}^{+\infty} \frac{(-1)^k \rho^{2k}}{(k!)^2} \sin^{2k}\left(\frac{\omega_{\text{sens}} t}{2}\right), \quad (8.9)$$

and Eq. (8.7) becomes:

$$\begin{aligned} M(\omega) &= \int_{-\infty}^{+\infty} \left[ \sum_{k=0}^{+\infty} \frac{(-1)^k \rho^{2k}}{(k!)^2} \sin^{2k}\left(\frac{\omega_{\text{sens}} t}{2}\right) \right] e^{-j\omega t} dt \\ &= \sum_{k=0}^{+\infty} \frac{(-1)^k \rho^{2k}}{(k!)^2} \int_{-\infty}^{+\infty} \sin^{2k}\left(\frac{\omega_{\text{sens}} t}{2}\right) e^{-j\omega t} dt. \end{aligned} \quad (8.10)$$

The term  $\sin^{2k}\left(\frac{\omega_{\text{sens}} t}{2}\right)$  can be expanded as [80]:

$$\sin^{2k}\left(\frac{\omega_{\text{sens}} t}{2}\right) = \frac{1}{2^{2k}} \binom{2k}{k} + \frac{(-1)^k}{2^{2k-1}} \sum_{i=0}^{k-1} (-1)^i \binom{2k}{i} \cos((k-i)\omega_{\text{sens}} t), \quad (8.11)$$

Eq. (8.10) then becomes:

$$\begin{aligned} M(\omega) &= \sum_{k=0}^{+\infty} \frac{(-1)^k \rho^{2k}}{(k!)^2} \int_{-\infty}^{+\infty} \left[ \frac{1}{2^{2k}} \binom{2k}{k} + \frac{(-1)^k}{2^{2k-1}} \sum_{i=0}^{k-1} (-1)^i \binom{2k}{i} \cos((k-i)\omega_{\text{sens}} t) \right] e^{-j\omega t} dt \\ &= \sum_{k=0}^{+\infty} \frac{(-1)^k \rho^{2k}}{(k!)^2} \left[ \frac{1}{2^{2k}} \binom{2k}{k} \int_{-\infty}^{+\infty} e^{-j\omega t} dt \right. \\ &\quad \left. + \frac{(-1)^k}{2^{2k-1}} \sum_{i=0}^{k-1} (-1)^i \binom{2k}{i} \int_{-\infty}^{+\infty} \cos((k-i)\omega_{\text{sens}} t) e^{-j\omega t} dt \right] \\ &= \sum_{k=0}^{+\infty} \frac{(-1)^k \rho^{2k}}{(k!)^2} \left[ \frac{1}{2^{2k}} \binom{2k}{k} \delta(\omega) + \frac{(-1)^k}{2^{2k}} \sum_{i=0}^{k-1} (-1)^i \binom{2k}{i} \Delta(\omega - (k-i)\omega_{\text{sens}}) \right], \end{aligned} \quad (8.12)$$

where  $\delta(x)$  the Dirac delta function and  $\Delta(\omega - a) \triangleq \delta(\omega - a) + \delta(\omega + a)$ . Eq. (8.12) shows that the spectrum of  $J_0(\tau_0)$  is comprised of carriers at integer multiples of  $F_{\text{sens}}$ . The bandwidth of  $J_0(\tau_0)$  can be evaluated by searching for the integer multiple of  $F_{\text{sens}}$  after which the spectral components of  $J_0(\tau_0)$  take negligible values.

Using Matlab and its fft function, the bandwidth of  $J_0(\tau_0)$  was evaluated via direct simulation. A sine wave was sampled at  $F_s = 400$  kHz with  $F_{\text{sens}} = 3.2$  kHz and  $k_{\text{sw}} = 45$

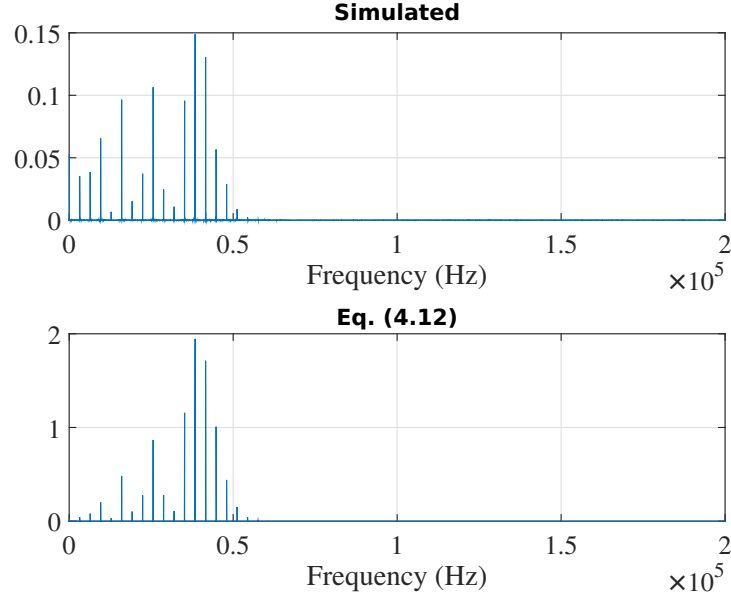


Figure 8.1: Simulated and numerically evaluated, single-sided spectrum of  $J_0(\tau_0)$ . The numerical evaluation was performed for the first 50 harmonics of  $F_{\text{sens}}$  according to Eq. (8.12). Note that no scaling has been applied to the bottom waveform.

kHz. Additionally, Eq. (8.12) was numerically evaluated for a given number of harmonics and the same parameters mentioned earlier. The simulation results can be seen in Fig. 8.1.

## 8.2.2 Expectation of The Absolute Value of a Gaussian R.V

Assuming  $x \sim \mathcal{N}(0, \sigma^2)$  then,

$$\begin{aligned}
 \mathbb{E}[|x|] &= \int_{-\infty}^{+\infty} |x| \frac{1}{\sqrt{2\pi\sigma^2}} e^{-\frac{x^2}{2\sigma^2}} dx = \int_{-\infty}^0 (-x) \frac{1}{\sqrt{2\pi\sigma^2}} e^{-\frac{x^2}{2\sigma^2}} dx + \int_0^{+\infty} x \frac{1}{\sqrt{2\pi\sigma^2}} e^{-\frac{x^2}{2\sigma^2}} dx \\
 &= \frac{2}{\sqrt{\pi}} \int_0^{+\infty} \frac{x}{\sqrt{2\sigma^2}} e^{-\frac{x^2}{2\sigma^2}} dx \stackrel{\zeta = \frac{x}{\sqrt{2\sigma^2}}}{=} \frac{2}{\sqrt{\pi}} \int_0^{+\infty} \zeta e^{-\zeta^2} \sqrt{2\sigma^2} d\zeta = \frac{2\sqrt{2\sigma^2}}{\sqrt{\pi}} \left[ \lim_{\xi \rightarrow +\infty} \left( -\frac{e^{-\zeta^2}}{2} \Big|_0^\xi \right) \right] \\
 &= \frac{2\sqrt{2\sigma^2}}{\sqrt{\pi}} \left[ \lim_{\xi \rightarrow +\infty} \left( -\frac{e^{-\xi^2}}{2} + \frac{1}{2} \right) \right] = \sqrt{\frac{2}{\pi}} \sigma. \tag{8.13}
 \end{aligned}$$

## 8.2.3 Probability of Outage Under Ambient Selection Diversity

Assume the setup illustrated in Fig. 8.2, where the tag is simultaneously illuminated by multiple FM stations.  $d_i$  with  $i \in \{1, 2, \dots, L\}$  is the distance between the  $i^{\text{th}}$  illuminating FM station and the tag.  $d_0$  denotes the distance between the tag and the smartphone/reader. The power received at the smartphone from the  $i^{\text{th}}$  station,  $P_{\text{rec}}^{(i)}$  is

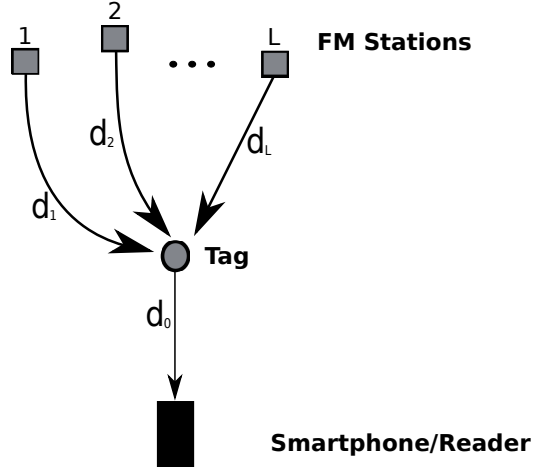


Figure 8.2: Tag is simultaneously illuminated by multiple stations, each offering different impinged RF power.

given by:

$$P_{rec}^{(i)} = P_{tx}^{(i)} \frac{\tilde{k}_i}{d_i^{v_i}} \tilde{\gamma}_i \eta \frac{\tilde{k}_0}{d_0^{v_0}} \tilde{\gamma}_0, \quad (8.14)$$

where,  $\tilde{\gamma}_j$  is a Gamma distributed random variable with shape and scale parameters  $k_j, \theta_j$  respectively.  $P_{tx}^{(i)}$  is the transmission power of the  $i^{\text{th}}$  FM station and  $\eta$  the scattering efficiency of the tag. By setting  $\gamma_i = P_{tx}^{(i)} \frac{\tilde{k}_i}{d_i^{v_i}} \tilde{\gamma}_i$  and  $k(d_0) = \frac{\tilde{k}_0}{d_0^{v_0}}$ , the received power at the smartphone, from a specific FM station  $i$  (i.e, the smartphone is tuned at the frequency that the backscattered signal, resulting from illumination by station  $i$ , is centered) is given by:

$$P_{rec}^{(i)} = \gamma_i \eta k(d_0) \tilde{\gamma}_0, \quad (8.15)$$

with  $\gamma_i \sim \text{Gamma}(k_i, \theta_i)$  and  $\mathbb{E}[\gamma_i] = k_i \theta_i$  the average power impinged at tag from station  $i$ . The PDF of the Gamma distribution is given by:

$$f_{\gamma_i}(\gamma_i) = \frac{1}{\Gamma(k_i) \theta^{k_i}} \gamma_i^{k_i-1} e^{-\frac{\gamma_i}{\theta_i}}, \quad (8.16)$$

where  $\Gamma(x)$  the Gamma function. Setting  $\gamma_0 = \eta k(d_0) \tilde{\gamma}_0$ , the received power can be defined as  $P_{rec}^{(i)} = \gamma_i \gamma_0$  with  $\gamma_i \perp \gamma_0$ . The probability of the maximum among the received

powers for each station  $i$ , to drop below a threshold  $\Theta_{\text{RF}}$  is given by:

$$\begin{aligned}
\Pr \left[ \max_{i \in \{1, \dots, L\}} \{P_{rec}^{(i)}\} < \Theta_{\text{RF}} \right] &= \Pr \left[ P_{rec}^{(1)} < \Theta_{\text{RF}} \cap P_{rec}^{(2)} < \Theta_{\text{RF}} \cap \dots \cap P_{rec}^{(L)} < \Theta_{\text{RF}} \right] \\
&= \Pr [\gamma_1 \gamma_0 < \Theta_{\text{RF}} \cap \dots \cap \gamma_L \gamma_0 < \Theta_{\text{RF}}] \\
&\stackrel{\gamma_i \perp \gamma_j, \gamma_0}{=} \mathbb{E}_{\gamma_0} \left[ \Pr \left( \gamma_1 < \frac{\Theta_{\text{RF}}}{\gamma_0} \cap \dots \cap \gamma_L < \frac{\Theta_{\text{RF}}}{\gamma_0} \middle| \gamma_0 \right) \right] \\
&\stackrel{\gamma_i \perp \gamma_j}{=} \mathbb{E}_{\gamma_0} \left[ \prod_{i=1}^L \Pr \left( \gamma_i < \frac{\Theta_{\text{RF}}}{\gamma_0} \middle| \gamma_0 \right) \right]. \tag{8.17}
\end{aligned}$$

The CDF of  $\gamma_i$  is defined as:

$$F_{\gamma_i}(x) = \Pr(\gamma_i < x) = \int_0^x f_{\gamma_i}(\gamma_i) d\gamma_i = \frac{1}{\Gamma(k_i) \theta^{k_i}} \int_0^x \gamma_i^{k_i-1} e^{-\frac{\gamma_i}{\theta}} d\gamma_i. \tag{8.18}$$

Using Eq. (8.18) and Eq. (8.16), Eq. (8.17) becomes:

$$\begin{aligned}
\Pr \left[ \max_{i \in \{1, \dots, L\}} \{P_{rec}^{(i)}\} < \Theta_{\text{RF}} \right] &= \mathbb{E}_{\gamma_0} \left[ \prod_{i=1}^L \Pr \left( \gamma_i < \frac{\Theta_{\text{RF}}}{\gamma_0} \middle| \gamma_0 \right) \right] \\
&= \int_0^{+\infty} f_{\gamma_0}(\gamma_0) \prod_{i=1}^L F_{\gamma_i} \left( \frac{\Theta_{\text{RF}}}{\gamma_0} \right) d\gamma_0 \tag{8.19}
\end{aligned}$$

The lower incomplete gamma function is defined as  $\gamma(s, x) = \int_0^x t^{s-1} e^{-t} dt$ . Using as second argument  $\frac{x}{\theta}$ :

$$\gamma \left( s, \frac{x}{\theta} \right) = \int_0^{\frac{x}{\theta}} t^{s-1} e^{-t} dt \stackrel{*}{=} \int_0^x \left( \frac{t}{\theta} \right)^{s-1} e^{-t/\theta} \frac{1}{\theta} dt = \frac{1}{\theta^s} \int_0^x t^{s-1} e^{-\frac{t}{\theta}} dt, \tag{8.20}$$

where in point \*, variable substitution was performed. That way the CDF of Eq. (8.18) becomes  $F_{\gamma_i}(x) = \frac{1}{\Gamma(k_i)} \gamma \left( k_i, \frac{x}{\theta_i} \right)$  and Eq. (8.19):

$$\Pr \left[ \max_{i \in \{1, \dots, L\}} \{P_{rec}^{(i)}\} < \Theta_{\text{RF}} \right] = \frac{1}{\theta^{k_0}} \frac{1}{\prod_{j=0}^L \Gamma(k_j)} \int_0^{+\infty} \gamma_0^{k_0-1} e^{-\frac{\gamma_0}{\theta_0}} \prod_{i=1}^L \gamma \left( k_i, \frac{\Theta_{\text{RF}}}{\gamma_0 \theta_i} \right), \tag{8.21}$$

which concludes the proof.

## 8.2.4 Details on Simulations and Experiments

### a) Simulation Parameters

Eq. (4.5) was modeled with  $F_t = 2$  MHz and  $\gamma_b$  chosen so that the “transmission power” of the tag was equal to  $-80$  dBm. To obtain different SNR values, the noise level  $P_n$  was varied, while maintaining the signal power constant. Given fixed  $B$ , noise power spectral density  $N_0$  was varied as  $N_0 = \frac{P_n}{B}$ .

Signal  $\phi_s(t)$  was a 6 second recorded clip from a local radio station.  $\phi_s(t)$  was obtained using GNU-Radio and a RTL-SDR dongle. GNU-Radio performed FM demodulation; the demodulated audio signal was sampled at  $F_{s,m} = 100$  kHz and saved to a binary file. The samples contained in the file were then imported in MATLAB and after the necessary processing, included in the model. In a second experiment,  $\phi_s(t)$  was modeled as Gaussian noise having variance equal to the power of the recorded clip.  $\mu(t)$  was created in MATLAB as defined below Eq. (4.24) with  $F_{sens} = 3.2$  kHz. Due to sampling of  $\mu(t)$  at the same rate as  $\phi_s(t)$  ( $F_{s,m}$ ), the resulting message bandwidth was set to  $W_m = 50$  kHz. After interpolating  $\phi_s(t)$  and  $\mu(t)$ , the final signal model was sampled at  $F_s = 10$  MHz. No band selection filter was used, that way the value used for  $B$  was  $B/2 = F_s/2$ . Then the receiver was implemented as described in Sec. 4.1.2. Closed form SINR was defined as per Eq. (4.51). Simulated SINR was returned by MATLAB’s `snr` [81] function using as input the receiver’s output signal.

### b) Energy Harvesting Experiments

The figures presenting voltages over time (for studying the duration of energy harvester’s cold-start times), were derived using a National Instruments USB-6366 digital acquisition system (DAQ) in conjunction with Matlab. 3 channels of the DAQ were used.

The first channel (“input voltage”) was used to log the voltage at the input of the harvesting IC, i.e., the voltage at the terminals of the harvesting element. The second channel (“storage capacitor voltage”) was used to probe the voltage at the terminals of the storage capacitor. The third channel (“Switch/Operation State”) was used to monitor state of the MOSFET’s gate and by extension, the operational state of the tag.

## 8.3 Supplementary Material for Chapter 5

### 8.3.1 Expected Value of $\cos^2(\varphi_m)$

Using trigonometric identities, the cosine term can be rewritten as  $\cos^2(\varphi_m) = \frac{1}{2}(1 + \cos(2\varphi_m))$ . The expected value can be then expressed as:

$$\mathbb{E}[\cos^2(\varphi_m)] = \frac{1}{2}(1 + \mathbb{E}[\cos(2\varphi_m)]) = \frac{1}{2}\left(1 + \frac{1}{2}\mathbb{E}[e^{j2\varphi_m} + e^{-j2\varphi_m}]\right). \quad (8.22)$$

The characteristic function  $M_x(j) = \mathbb{E}[e^{jx}]$  of a Gaussian random variable  $x \sim \mathcal{N}(\mu, \sigma^2)$ , is given by  $\mathbb{E}[e^{jx}] = M_x(j) = e^{j\mu - \frac{\sigma^2}{2}}$  [82]. If  $\varphi_m \sim \mathcal{N}(0, \sigma_{sw}^2)$ , then  $2\varphi_m, -2\varphi_m \sim \mathcal{N}(0, 4\sigma_{sw}^2)$  and the expected value can be calculated as:

$$\mathbb{E}[\cos^2(\varphi_m)] = \frac{1}{2} + \frac{1}{4}\mathbb{E}[e^{j2\varphi_m}] + \frac{1}{4}\mathbb{E}[e^{-j2\varphi_m}] = \frac{1}{2} + \frac{1}{2}e^{-2\sigma_{sw}^2}. \quad (8.23)$$

In a similar manner, it can be easily shown that  $\mathbb{E}[\cos(\varphi_m)] = e^{-\sigma_{sw}^2/2}$ .

## 8.4 Supplementary Material for Chapter 6

### 8.4.1 Average Number of Alignment Events

Assuming  $N_S$  slots, the average number  $\lambda_a$  of alignment events per  $N_S$  slots will be calculated. First, the following binary random variable is defined:

$$\delta[k] = \begin{cases} 1, & p[k] \\ 0, & 1 - p[k]. \end{cases} \quad (8.24)$$

Using Eq. (8.24) the number of successful alignment events in  $N_S$  slots is given by the random variable  $\delta_s = \sum_{k=1}^{N_S} \delta[k]$ . Using Eq. (8.24), the average number of successful alignment events per  $N_S$  slots can be expressed as:

$$\lambda_a(N_S) = \mathbb{E}[\delta_s] = \sum_{k=1}^{N_S} \mathbb{E}[\delta[k]] = \sum_{k=1}^{N_S} p[k]. \quad (8.25)$$

### 8.4.2 Simulation Parameters

Each slot affected  $N_G = 20$  transmission phases/interrogations and the simulations were performed using  $N_S = 10$  slots. As described in Sec. 6.3, a ramp was used to control the varactor at the assistive tag. Thus, in the simulation setup, based on the assistive

Phase Distribution	Fig. 6.2	Fig. 6.3 Setup (1)	Fig. 6.3 Setup (2)
Direct Channel ( $\phi_0$ )	$\mathcal{U}[0, 2\pi)$	$\mathcal{U}[0, \pi)$	$\mathcal{U}[0, \pi/2)$
Tag #1 ( $\phi_1, \phi'_1$ )	$\mathcal{U}[0, 2\pi)$	$\mathcal{U}[0, \pi/4), \mathcal{U}[\pi, 1.9\pi)$	$\mathcal{U}[0, \pi/4), \mathcal{U}[\pi, 1.9\pi)$
Tag #2 ( $\phi_2, \phi'_2$ )	$\mathcal{U}[0, 2\pi)$	-	-
Rest Tags ( $\phi_m, \phi'_m$ )	$\mathcal{U}[0, 2\pi)$	-	-

Table 8.1: Simulation parameters.  $\mathcal{U}[a, b]$  denotes the uniform distribution of support  $[a, b]$ .

tags' phases (tag #1:  $63^\circ$  to  $180^\circ$ , tag #2:  $80^\circ$  to  $150^\circ$ ), a staircase-approximated ramp consisting of  $N_S$  stairs/slots was used. Analysis results were calculated using Eq. (6.16) and the integral of Eq. (6.18) was evaluated using trapezoidal approximation. Exact and lower bound alignment probability was also estimated through Monte Carlo simulation. Channel phases were modeled as per Table 8.1 and the related PDF/CDFs were calculated according to [83].

# Bibliography

- [1] G. Brooker and J. Gomez, “Lev Termen’s Great Seal bug analyzed,” *IEEE Aerosp. Electron. Syst. Mag.*, vol. 28, no. 11, pp. 4–11, 2013.
- [2] H. Stockman, “Communication by means of reflected power,” *Proc. IRE*, pp. 1196–1204, 1948.
- [3] D. M. Dobkin, *The RF in RFID: Passive UHF RFID in Practice*. Oxford, Boston: Newnes (Elsevier), 2008.
- [4] J. Kimionis, A. Bletsas, and J. N. Sahalos, “Design and implementation of RFID systems with software defined radio,” in *Proc. IEEE European Conf. on Antennas and Propagation (EuCAP)*, Prague, Czech Republic, Mar. 2012, pp. 3464–3468.
- [5] N. Kargas, F. Mavromatis, and A. Bletsas, “Fully-coherent reader with commodity SDR for Gen2 FM0 and computational RFID,” *IEEE Wireless Commun. Lett.*, vol. 4, no. 6, pp. 617–620, Dec. 2015.
- [6] G. Vannucci, A. Bletsas, and D. Leigh, “A software-defined radio system for backscatter sensor networks,” *IEEE Trans. Wireless Commun.*, vol. 7, no. 6, pp. 2170–2179, Jun. 2008.
- [7] A. Bletsas, P. N. Alevizos, and G. Vougioukas, “The art of signal processing in backscatter radio for  $\mu$ W (or less) internet of things: Intelligent signal processing and backscatter radio enabling batteryless connectivity,” *IEEE Signal Processing Mag.*, vol. 35, no. 5, pp. 28–40, Sep. 2018.
- [8] J. Kimionis, A. Bletsas, and J. N. Sahalos, “Increased range bistatic scatter radio,” *IEEE Trans. Commun.*, vol. 62, no. 3, pp. 1091–1104, Mar. 2014.
- [9] N. Fasarakis-Hilliard, P. N. Alevizos, and A. Bletsas, “Coherent detection and channel coding for bistatic scatter radio sensor networking,” *IEEE Trans. Commun.*, vol. 63, pp. 1798–1810, May 2015.

- [10] G. Vougioukas, S. N. Daskalakis, and A. Bletsas, “Could battery-less scatter radio tags achieve 270-meter range?” in *Proc. IEEE Wireless Power Transfer Conf. (WPTC)*, Aveiro, Portugal, May 2016, pp. 1–3.
- [11] P. N. Alevizos, K. Tountas, and A. Bletsas, “Multistatic scatter radio sensor networks for extended coverage,” *IEEE Trans. Wireless Commun.*, vol. 17, no. 7, pp. 4522–4535, Jul. 2018.
- [12] V. Liu, A. Parks, V. Talla, S. Gollakota, D. Wetherall, and J. R. Smith, “Ambient backscatter: Wireless communication out of thin air,” in *Proc. ACM SIGCOMM*, Hong Kong, China, 2013, pp. 39–50.
- [13] J. Qian, F. Gao, G. Wang, S. Jin, and H. Zhu, “Noncoherent detections for ambient backscatter system,” *IEEE Trans. Wireless Commun.*, vol. 16, no. 3, pp. 1412–1422, Mar. 2017.
- [14] ———, “Semi-coherent detection and performance analysis for ambient backscatter system,” *IEEE Trans. Commun.*, vol. 65, no. 12, pp. 5266–5279, Dec. 2017.
- [15] G. Yang, Y. Liang, R. Zhang, and Y. Pei, “Modulation in the air: Backscatter communication over ambient ofdm carrier,” *IEEE Trans. Commun.*, vol. 66, no. 3, pp. 1219–1233, Mar. 2018.
- [16] D. Darsena, G. Gelli, and F. Verde, “Modeling and performance analysis of wireless networks with ambient backscatter devices,” *IEEE Trans. Commun.*, vol. 65, no. 4, pp. 1797–1814, Apr. 2017.
- [17] N. Van Huynh, D. T. Hoang, X. Lu, D. Niyato, P. Wang, and D. In Kim, “Ambient Backscatter Communications: A Contemporary Survey,” Dec. 2017. [Online]. Available: <https://arxiv.org/abs/1712.04804>
- [18] P. Zhang, D. Bharadia, K. Joshi, and S. Katti, “Hitchhike: Practical backscatter using commodity wifi,” in *Proceedings of the 14th ACM Conference on Embedded Network Sensor Systems CD-ROM*, ser. SenSys ’16. New York, NY, USA: ACM, 2016, pp. 259–271.
- [19] A. N. Parks, A. Liu, S. Gollakota, and J. R. Smith, “Turbocharging ambient backscatter communication,” in *Proc. ACM SIGCOMM*, Chicago, Illinois, USA, 2014, pp. 619–630.

- [20] A. Wang, V. Iyer, V. Talla, J. R. Smith, and S. Gollakota, “FM backscatter: Enabling connected cities and smart fabrics,” in *USENIX Symp. on Networked Systems Design and Implementation*, Boston, MA, USA, Mar. 2017.
- [21] M. A. Varner, R. Bhattacharjea, and G. D. Durgin, “Perfect pulses for ambient backscatter communication,” in *Proc. IEEE RFID*, Phoenix, AZ, USA, May 2017, pp. 13–19.
- [22] N. Kaina, M. Dupre, G. Lerosey, and M. Fink, “Shaping complex microwave fields in reverberating media with binary tunable metasurfaces,” *Scientific Reports*, vol. 4, p. 6693, Oct. 2014.
- [23] M. Dupré, P. del Hougne, M. Fink, F. Lemoult, and G. Lerosey, “Wave-field shaping in cavities: Waves trapped in a box with controllable boundaries,” *Phys. Rev. Lett.*, vol. 115, p. 017701, Jul. 2015.
- [24] M. Di Renzo *et al.*, “Smart radio environments empowered by reconfigurable AI meta-surfaces: an idea whose time has come,” *EURASIP Journal on Wireless Communications and Networking*, vol. 2019, no. 1, p. 129, May 2019.
- [25] E. Basar, M. Di Renzo, J. de Rosny, M. Debbah, M.-S. Alouini, and R. Zhang, “Wireless Communications Through Reconfigurable Intelligent Surfaces,” Jun. 2019. [Online]. Available: <https://arxiv.org/abs/1906.09490>
- [26] X. Tan, Z. Sun, J. M. Jornet, and D. Pados, “Increasing indoor spectrum sharing capacity using smart reflect-array,” in *Proc. IEEE Int. Conf. Communications*, May 2016, pp. 1–6.
- [27] C. Liaskos, S. Nie, A. Tsioliariidou, A. Pitsillides, S. Ioannidis, and I. Akyildiz, “A new wireless communication paradigm through software-controlled metasurfaces,” *IEEE Commun. Mag.*, vol. 56, no. 9, pp. 162–169, Sep. 2018.
- [28] S. Han and K. G. Shin, “Enhancing wireless performance using reflectors,” in *Proc. IEEE INFOCOM*, May 2017, pp. 1–9.
- [29] Z. Li, Y. Xie, L. Shangguan, R. I. Zelaya, J. Gummesson, W. Hu, and K. Jamieson, “Towards programming the radio environment with large arrays of inexpensive antennas,” in *Proc. USENIX Symp. Netw. Syst. Design Implement.*, Feb. 2019, pp. 285–300.

- [30] V. Arun and H. Balakrishnan, “RFocus: Beamforming using thousands of passive antennas,” in *Proc. USENIX Symp. Netw. Syst. Design Implement.*, Feb. 2020, pp. 1047–1061.
- [31] Greenerwave, last Visited 27/9/19. [Online]. Available: <http://greenerwave.com/>
- [32] G. Lerosey *et al.*, “Waveforming device and wave receiver,” May 2019, Patent FR3066665B1. [Online]. Available: <https://patents.google.com/patent/FR3066665B1>
- [33] P. del Hougne, M. Fink, and G. Lerosey, “Shaping microwave fields using nonlinear unsolicited feedback: Application to enhance energy harvesting,” *Phys. Rev. Applied*, vol. 8, p. 061001, Dec. 2017.
- [34] T. Ohira and K. Iigusa, “Electronically steerable parasitic array radiator antenna,” *Electronics and Communications in Japan (Part II: Electronics)*, vol. 87, no. 10, pp. 25–45, 2004.
- [35] A. Kalis, A. G. Kanatas, and C. B. Papadias, “A novel approach to mimo transmission using a single rf front end,” *IEEE J. Select. Areas Commun.*, vol. 26, no. 6, pp. 972–980, Aug. 2008.
- [36] A. Kalis, A. Kanatas, and C. Papadias, *Parasitic Antenna Arrays for Wireless MIMO Systems*. Springer, 2013.
- [37] C. Sun, A. Hirata, T. Ohira, and N. C. Karmakar, “Fast beamforming of electronically steerable parasitic array radiator antennas: theory and experiment,” *IEEE Trans. Antennas Propagat.*, vol. 52, no. 7, pp. 1819–1832, Jul. 2004.
- [38] C. Plapous, J. Cheng, E. Taillefer, A. Hirata, and T. Ohira, “Reactance domain music algorithm for electronically steerable parasitic array radiator,” *IEEE Trans. Antennas Propagat.*, vol. 52, no. 12, pp. 3257–3264, Dec. 2004.
- [39] P. Nikitin, “Self-reconfigurable rfid reader antenna,” in *Proc. IEEE RFID*, Phoenix, AZ, May 2017, pp. 88–95.
- [40] Y. Peng, L. Shangguan, Y. Hu, Y. Qian, X. Lin, X. Chen, D. Fang, and K. Jamieson, “PLoRa: A passive long-range data network from ambient lora transmissions,” in *Proc. ACM SIGCOMM*, 2018, pp. 147–160.

- [41] P. N. Alevizos, A. Bletsas, and G. N. Karystinos, “Noncoherent short packet detection and decoding for scatter radio sensor networking,” *IEEE Trans. Commun.*, vol. 65, no. 5, pp. 2128–2140, May 2017.
- [42] P. Alevizos, “Intelligent scatter radio, RF harvesting analysis, and resource allocation for ultra-low-power internet-of-things,” Ph.D. dissertation, School of ECE, Technical University of Crete, Chania, Greece, 2017, advisor: A. Bletsas.
- [43] R. B. Green, “The general theory of antenna scattering,” Ph.D. dissertation, Dept. Elect. Comput. Eng., Ohio State Univ, Columbus, OH, 1963.
- [44] F. Fuschini, C. Piersanti, F. Paolazzi, and G. Falciasecca, “Analytical approach to the backscattering from UHF RFID transponder,” *IEEE Antennas Wireless Propagat. Lett.*, vol. 7, pp. 33–35, 2008.
- [45] A. Bletsas, A. G. Dimitriou, and J. N. Sahalos, “Improving backscatter radio tag efficiency,” *IEEE Trans. Microwave Theory Tech.*, vol. 58, no. 6, pp. 1502–1509, Jun. 2010.
- [46] C. Balanis, *Antenna Theory: Analysis and Design*, 3rd ed. Wiley, 2005.
- [47] J. G. Proakis and M. Salehi, *Communication Systems Engineering*, 2nd ed. Upper Saddle River, NJ, USA: Prentice-Hall, 2001.
- [48] A. Goldsmith, *Wireless Communications*. New York, NY, USA: Cambridge University Press, 2005.
- [49] S. M. Kay, *Fundamentals of statistical signal processing. [Volume I]. , Estimation theory*. Upper Saddle River (N.J.): Prentice Hall, 1993.
- [50] M. Rice, *Digital Communications: A Discrete-time Approach*. Pearson/Prentice Hall, 2009.
- [51] J. G. Proakis and M. Salehi, *Digital Communications*, 5th ed. New York, NY: McGraw-Hill, 2007.
- [52] M. Ouroutzoglou, G. Vougioukas, G. N. Karystinos, and A. Bletsas, “Multistatic noncoherent linear complexity miller sequence detection for Gen2 RFID/IoT,” *IEEE Trans. Wireless Commun.*, 2019, revision submitted.
- [53] Microchip Technology Inc., “PIC16LF145X series datasheet,” <http://ww1.microchip.com/downloads/en/DeviceDoc/40001639B.pdf>.

- [54] SiTime Corporation, “SiT1576  $\mu$ Power Oscillator datasheet,” <https://www.sitime.com/datasheet/SiT1576>.
- [55] S. Kay, *Fundamentals of Statistical Signal Processing: Detection theory*. Prentice-Hall PTR, 1998.
- [56] A. Pappoulis and S. U. Pillai, *Probability, Random Variables and Stochastic Processes*, 4th ed. New York, NY: McGraw-Hill, 2002.
- [57] G. Vougioukas and A. Bletsas, “Switching frequency techniques for universal ambient backscatter networking,” *IEEE J. Select. Areas Commun.*, vol. 37, no. 2, pp. 464–477, Feb. 2019.
- [58] F. W. J. Olver, D. W. Lozier, R. F. Boisvert, and C. W. Clark, *NIST handbook of mathematical functions*. New York, NY: Cambridge Univ. Press, 2010.
- [59] G. Vougioukas and A. Bletsas, “Ambient backscatter in reality: Does illuminator signal structure matter?” in *Proc. IEEE Int. Conf. Communications*, Shanghai, China, May 2019, pp. 1–6.
- [60] D. J. Sakrison, *Communication theory : transmission of waveforms and digital information*. Wiley New York, 1968.
- [61] C. E. Rasmussen and C. K. I. Williams, *Gaussian Processes for Machine Learning*. The MIT Press, 2006.
- [62] M. Abramowitz and I. A. Stegun, Eds., *Handbook of Mathematical Functions with Formulas, Graphs, and Mathematical Tables*. U.S. Government Printing Office, Washington, D.C., 1964.
- [63] H. Taub and D. L. Schilling, *Principles of Communication Systems*, 2nd ed. McGraw-Hill Higher Education, 1986.
- [64] K. Leentvaar and J. Flint, “The capture effect in FM receivers,” *IEEE Trans. Commun.*, vol. 24, no. 5, pp. 531–539, 1976.
- [65] S. N. Daskalakis, S. D. Assimonis, E. Kampionakis, and A. Bletsas, “Soil moisture wireless sensing with analog scatter radio, low power, ultra-low cost and extended communication ranges,” in *Proc. IEEE Sensors Conf. (Sensors)*, Valencia, Spain, Nov. 2014, pp. 122–125.

- [66] —, “Soil moisture scatter radio networking with low power,” *IEEE Trans. Microwave Theory Tech.*, vol. 64, no. 7, pp. 2338–2346, Jul. 2016.
- [67] E. Kampionakis, J. Kimionis, K. Tountas, C. Konstantopoulos, E. Koutroulis, and A. Bletsas, “Backscatter sensor network for extended ranges and low cost with frequency modulators: Application on wireless humidity sensing,” in *Proc. IEEE Sensors Conf. (Sensors)*, Baltimore, MD, USA, Nov. 2013.
- [68] —, “Wireless environmental sensor networking with analog scatter radio & timer principles,” *IEEE Sensors J.*, vol. 14, no. 10, pp. 3365–3376, Oct. 2014.
- [69] Dialog Semiconductor, “GreenPak Programmable Mixed-signal Matrices,” last Visited on 19/11/2020. [Online]. Available: <https://www.dialog-semiconductor.com/greenpak>
- [70] B. Razavi, *Design of Analog CMOS Integrated Circuits*, ser. McGraw-Hill electrical engineering series. McGraw-Hill, 2001.
- [71] S. D. Assimonis, S.-N. Daskalakis, and A. Bletsas, “Sensitive and efficient RF harvesting supply for batteryless backscatter sensor networks,” *IEEE Trans. Microwave Theory Tech.*, vol. 64, no. 4, pp. 1327–1338, Apr. 2016.
- [72] Texas Instruments Inc., “Bq25504 Ultra Low-Power Boost Converter With Battery Management for Energy Harvester Applications,” last Visited on 18/11/2020. [Online]. Available: <http://www.ti.com/lit/ds/symlink/bq25504.pdf>
- [73] N. J. Guilar, T. J. Kleeburg, A. Chen, D. R. Yankelevich, and R. Amirtharajah, “Integrated solar energy harvesting and storage,” *IEEE Trans. VLSI Syst.*, vol. 17, no. 5, pp. 627–637, May 2009.
- [74] E. G. Fong, N. J. Guilar, T. J. Kleeburg, H. Pham, D. R. Yankelevich, and R. Amirtharajah, “Integrated energy-harvesting photodiodes with diffractive storage capacitance,” *IEEE Trans. VLSI Syst.*, vol. 21, no. 3, pp. 486–497, Mar. 2013.
- [75] R. Schmidt, “Multiple emitter location and signal parameter estimation,” *IEEE Trans. Antennas Propagat.*, vol. 34, no. 3, pp. 276–280, Mar. 1986.
- [76] B. B. van der Genugten, “The distribution of random variables reduced modulo a,” *Statistica Neerlandica*, vol. 26, no. 1, pp. 1–13, 1972.

- [77] A. Bletsas, A. Lippman, and J. N. Sahalos, "Simple, zero-feedback, distributed beamforming with unsynchronized carriers," *IEEE J. Select. Areas Commun.*, vol. 28, no. 7, pp. 1046–1054, Sep. 2010.
- [78] A. G. Dimitriou, J. Kimionis, A. Bletsas, and J. N. Sahalos, "A fading-resistant method for RFID-antenna structural mode measurement," in *2012 IEEE International Conference on RFID-Technologies and Applications (RFID-TA)*, Nice, France, Nov. 2012, pp. 443–448.
- [79] C. G. Koay and P. J. Basser, "Analytically exact correction scheme for signal extraction from noisy magnitude MR signals," *Journal of Magnetic Resonance*, vol. 2, pp. 317–322, 2006.
- [80] E. W. Weisstein, "Trigonometric power formulas. From MathWorld—A Wolfram Web Resource," last visited on 13/2/2018. [Online]. Available: <http://mathworld.wolfram.com/TrigonometricPowerFormulas.html>
- [81] MathWorks Inc., "snr function documentation," last visited on 13/2/2018. [Online]. Available: <https://www.mathworks.com/help/signal/ref/snr.html>
- [82] F. Oberhettinger, *Fourier Transforms of Distributions and Their Inverses: A Collection of Tables*, ser. Probability & Mathematical Statistics Monograph. Academic Press, 1973.
- [83] F. Killmann and E. von Collani, "A note on the convolution of the uniform and related distributions and their use in quality control," *Economic Quality Control - Econ Qual Contr*, vol. 16, pp. 17–41, Jan. 2001.